



Università degli Studi di Ferrara

DOTTORATO DI RICERCA IN
SCIENZE CHIMICHE

CICLO XXIII

COORDINATORE Prof. Carlo Alberto Bignozzi

**Photoelectrochemical hydrogen production
from aqueous solution employing
nanostructured semiconductors**

Settore Scientifico Disciplinare CHIM/03

Dottorando

Dott. Cristino Vito

Tutore

Prof. Bignozzi Carlo Alberto
Dott. Caramori Stefano

Anni 2008/2010

INDEX

Chapter 1 Introduction

| | |
|---|----|
| 1.1 Hydrogen Production with Nanostructured and Sensitized Metal Oxides | 3 |
| 1.2 Dye sensitized Photoanodes for water oxidation and hydrogen evolution | 14 |
| 1.3. Highly Ordered semiconductors nanostructures based on TiO ₂ | 23 |
| 1.4 Experimental conditions for electrochemical titania nanotube formation | 27 |
| 1.5 Bibliography | 33 |

Chapter 2 Functionalization of titania photoelectrodes with Group VI semiconductors

| | |
|--|----|
| 2.1 Introduction | 36 |
| 2.2 Methods of functionalization of titania substrates | 40 |
| 2.3 Bi ₂ S ₃ /TiO ₂ photoelectrodes | 42 |
| 2.4 CdS and CdSe/TiO ₂ photoelectrodes | 50 |
| 2.5 CdTe | 62 |
| 2.6 Bibliography | 65 |

Chapter 3 Photoelectrochemical Properties of Nanostructured WO₃ Prepared with Different Organic Dispersing Agents

| | |
|---|----|
| 3.1 Introduction | 67 |
| 3.2 Synth-1 and Synth-2 | 68 |
| 3.3 Morphological Properties | 72 |
| 3.4 Photo-electrochemical characterization of Synth-1 and Synth-2 | 79 |
| 3.3 Conclusions | 88 |

| | |
|------------------|----|
| 3.4 Bibliography | 89 |
|------------------|----|

Chapter 4 Efficient Photoelectrochemical Water Splitting by Anodically Grown
WO₃ Electrodes

| | |
|---|-----|
| 4.1 Introduction | 92 |
| 4.2 Experimental Section | 96 |
| 4.3 Results and Discussion | 99 |
| 4.3.1 Anodic Formation of WO ₃ | 99 |
| 4.3.2 Photoelectrochemistry | 111 |
| 4.4 Conclusions | 132 |
| 4.4 Bibliography | 133 |

Chapter 5 Photoelectrochemical behaviour of sensitized TiO₂ photoanodes in
aqueous environment: application to hydrogen production

| | |
|----------------------------------|-----|
| 5.1 Introduction | 136 |
| 5.2 Experimental Section | 142 |
| 5.3 Results and Discussion | 145 |
| 5.3.1 Organic Sacrificial Agents | 147 |
| 5.3.2. Halides | 152 |
| 5.4 Conclusion | 165 |
| 5.5 Bibliography | 166 |
| Publications | 169 |

Chapter 1: Introduction

1.1 Hydrogen Production with Nanostructured and Sensitized Metal Oxides

The phenomenology of semiconductor-liquid interfaces represent a very interesting and important area in science and technology[1], involving principles of electrochemistry, photochemistry, solid state theory and surface and interface science. The applications are varied, but most are focused on solar energy conversion schemes, through the use of regenerative photoelectrochemical cells (PEC), which convert sunlight to electricity or photoelectrolytic or photoelectrosynthetic cells in which solar energy is stored into chemical fuels[2]. Other important applications involve the development of photocatalytic processes for selective photooxidation of organic compounds and for environmental remediation.

Photoelectrolysis of water using sunlight[3-5] is extremely attractive for a number of reasons: (1) photoproducted hydrogen is a valuable fuel and energy carrier which can be stored more easily than electricity or heat; (2) it is non polluting, inexhaustible and flexible with respect to energy conversion in heat (combustion) or electricity (in fuel cells); (3) hydrogen is a valuable chemical by itself, being used in large quantities by the industry in chemical processing like ammonia synthesis and petroleum refining.

A central concept in describing the interaction of a semiconductor with an electrolyte is the equilibration of the Fermi level of the solution and of the semiconductor. Although the concept of Fermi level has been initially introduced for an electronically conducting phase, as a level for which the probability of electron occupation of a given state is $\frac{1}{2}$, in our discussion the Fermi level can be conveniently identified with the electrochemical potential of electrons in the solid and of a given redox couple (O,R) in solution, where the usual free energy relationships hold. Obviously, the solution phase does not contain free electrons, but contains available electronic states (in the form of oxidized (O) and reduced species (R) which can equilibrate with free electron in the solid. As a

consequence $\overline{\mu}_{redox} = \mu^0 + KT \ln\left(\frac{C_o}{C_R}\right)$ where $\overline{\mu}_{redox}$ and μ^0 are the electrochemical and

standard electrochemical potential of the electron and C_O and C_R are the concentrations

of the oxidized and reduced form respectively. Under equilibrium conditions $E_F(\text{solid}) = E_F(\text{solution}) = \overline{\mu_{redox}} = neU_{redox}$ where U is the redox potential of the couple and n is the number of exchanged electrons (e). Thus when a n -type semiconductor is brought in contact with a redox couple, electrons (majority charge carriers) from the solid pass to the solution until the two Fermi levels are identical. Due to the relatively small charge carrier density in the solid, a positive space charge layer of the typical thickness of 10^{-6} - 10^{-8} m [6] is formed near the surface which is balanced by negative charges in the “compact” Helmholtz layer. The field generated by these negative charges causes an upward bending of the energy band (Fig.1.1b). A conceptually similar situation is established for a p -type semiconductor, in which the majority carriers are holes instead of electrons. In that case a space charge layer of opposite sign (negative) would be created by hole transfer to the electrolyte.

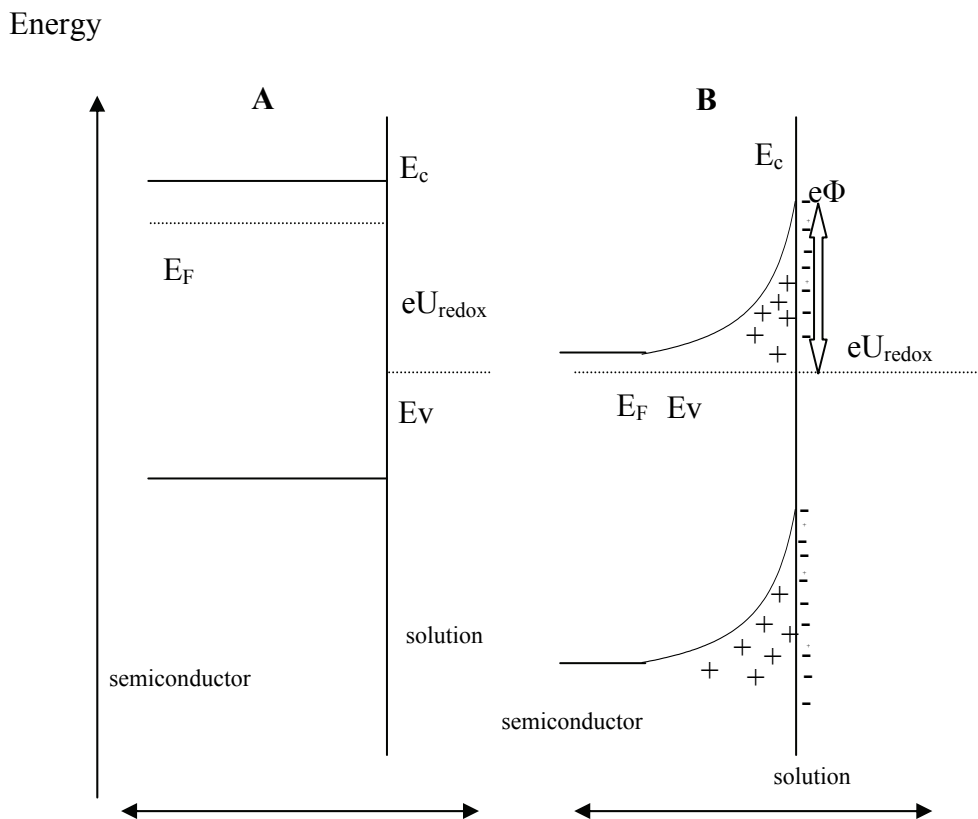


Fig.1.1 Before (a) and after (b) dark equilibration of an n type semiconductor with the electrolyte containing a redox couple of potential U .

The thermodynamic upper limit to the energy that can be extracted by the semiconductor/liquid junction is given by $e\Phi = E_c - E_F = E_c + eU_{\text{redox}}$ which is called the equilibrium barrier height. For all semiconductor/liquid junction the condition $eU_{\text{redox}} \sim E_v$ gives a barrier height approximately equal to the band gap, maximizing the power output of the system.

For semiconductors under illumination, the quantity related to Φ is the open circuit photovoltage (V_{oc}) which reflects the maximum free energy that can be harnessed by the junctions. However the usable free energy collected across a semiconductor/electrolyte junction is not purely limited by thermodynamic quantities, but also by electron transfer kinetics and transport of the photogenerated charge carriers (Fig. 1.2). The electric field inside the space charge region may have a relevant role in assisting the charge separation at the interface. Holes are attracted towards the electrolyte by the negative charge layer, while electrons are repelled from the surface. As a consequence, photooxidation reactions can take place under illumination at the surface of an n-type semiconductor, while photoreduction can be carried out at a counter electrode (either p type semiconductor or metal electrode) wired to the photoactive material. However, in many nanostructured photoelectrodes the small size of the nanocrystals and a lower charge carrier density cannot sustain a relevant electric field[7] and the charge separation is mainly determined by kinetic reasons related to the chemical nature of the redox processes at the semiconductor/electrolyte interface: the efficiency of charge separation is thus essentially determined by the different overpotentials for the oxidation and reduction reactions taking place at the semiconductor surface and by the kinetic competition between recombination and successful transfer of the charge carriers[8,9].

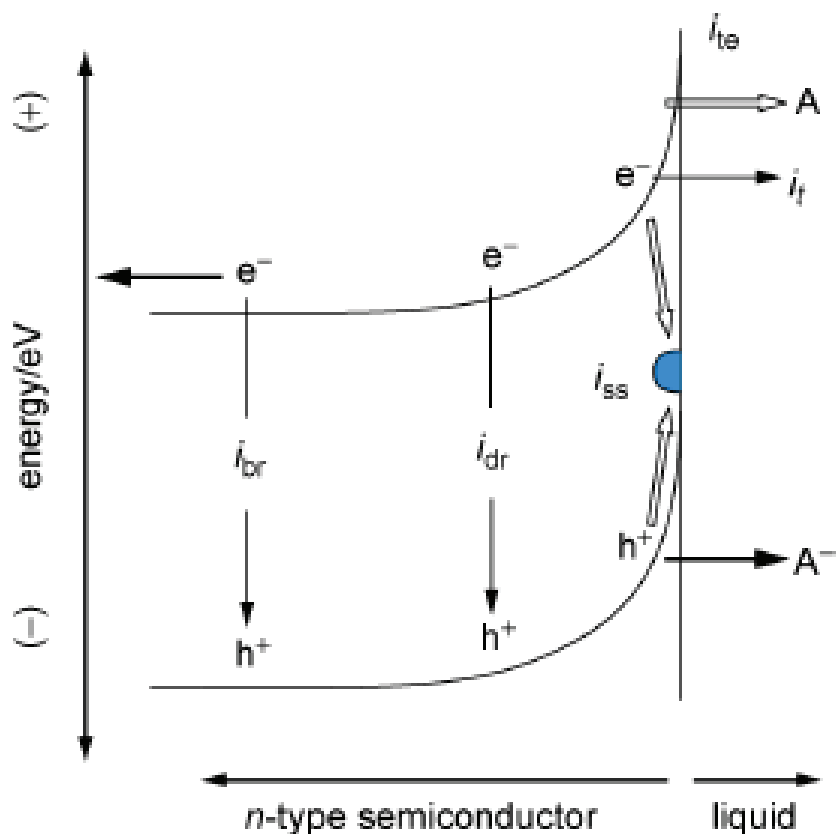


Fig.1.2. Recombination pathways of photogenerated charge carriers (e^- and h^+) in a n-type semiconductor in the presence of a space charge region and of a A/A^- redox couple. The electron/hole pair can recombine in bulk (i_{br}), depletion layer (i_{dr}) or through surface states (i_{ss}). Electron can also tunnel to the electrolyte through the barrier layer (i_t) or across the interface (i_{te}). The bold arrows indicate processes favorable to the functioning of the photoelectrochemical cell :hole transfer to the electrolyte and electron migration/diffusion through the bulk of the solid to the charge collector. From S.Maldonado et al., Nanostructured Photoelectrochemical Systems for Solar Photon Conversion, Imperial College Ed., London, 2002)

Several approaches to photoelectrolysis are possible, involving a photoactive semiconductor electrode electrically connected to a metal electrode, or photoactive anode (n-type) and cathode (p-type) acting either as separate electrodes, or coupled to form a monolithic structure called photochemical diode.

A common photoelectrolysis configuration, useful for the general scope of our discussion, is represented by the wiring of an n-type semiconductor, acting as a photoanode, to a metal counter electrode (Fig.1.3).

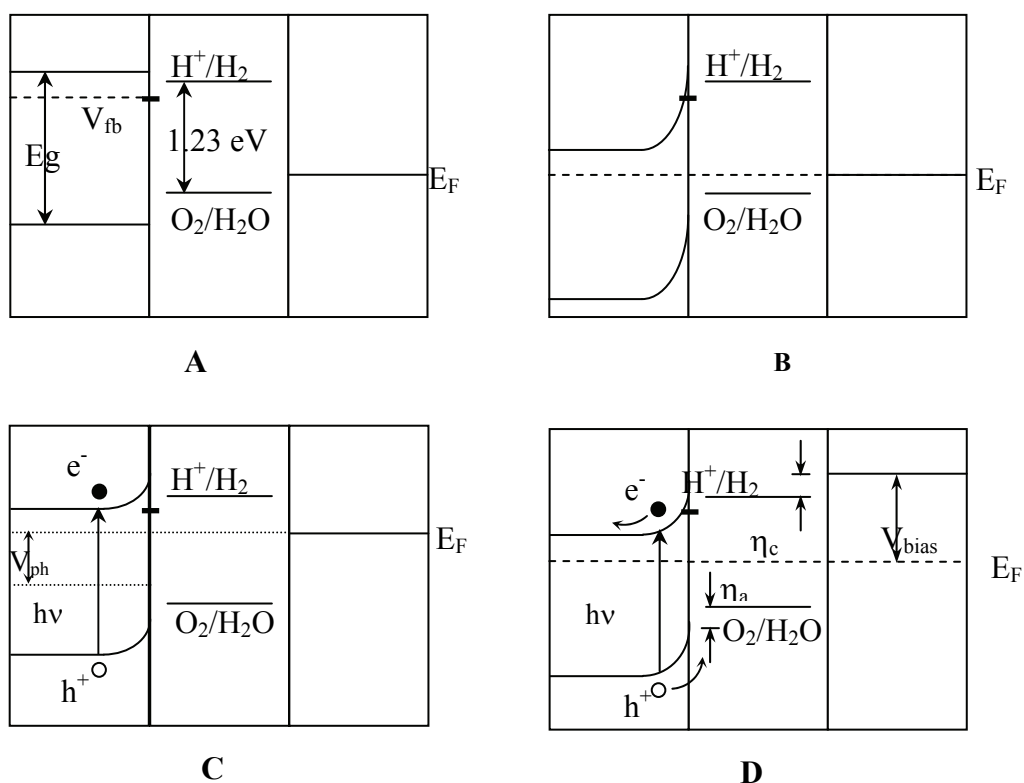


Fig.1.3 Energy level diagrams for a semiconductor-metal photoelectrolysis cell: (a) no contact, (b) equilibrium in the dark, (c) high intensity irradiation, (d) high intensity irradiation with anodic bias.

The Fermi level in the electrolyte has been left undefined since it depends on the initial relative concentrations of H_2 and O_2 in solution. Fig.1.3b shows the situation at equilibrium in the dark once the semiconductor and the metal are brought in contact with the electrolyte and a depletion layer is formed near the semiconductor surface. Fermi levels of the three phases equilibrates giving rise to a band bending in the semiconductor. When the semiconductor is irradiated with photons of energy corresponding to the band-gap, electron-hole pairs are created and the Fermi level in the semiconductor is raised towards the flat band potential V_{fb} by an amount V_{ph} which is the photopotential generated. The maximum value the Fermi level can reach in the semiconductor is the flat band potential V_{fb} which, in the case shown, is lower with respect to the H^+/H_2 redox couple. This means that hydrogen evolution cannot take place at the metal electrode even at the highest irradiation intensity. For hydrogen

evolution to occur, a positive bias must be applied to the semiconductor electrode as shown in Fig.1.3c. This bias, which is usually provided by an external voltage source, should also account for the necessary cathodic (η_c) and anodic (η_a) overvoltages in order to sustain the current flow. This situation represents a condition which is frequently met with visible absorbing semiconductor metal oxides photochemically stable in aqueous environment, like WO_3 or Fe_2O_3 .

The ideal situation would be to operate with metal oxides in which, like SrTiO_3 [10] or KTaO_3 , the flat band potential is above the H^+/H_2 potential (Fig.1.4), therefore no external bias is required to generate H_2 and O_2 . Unfortunately most of these materials have large band gaps (3.2-3.5 eV) which result in very low solar absorptivity and are inefficient for solar energy conversion.

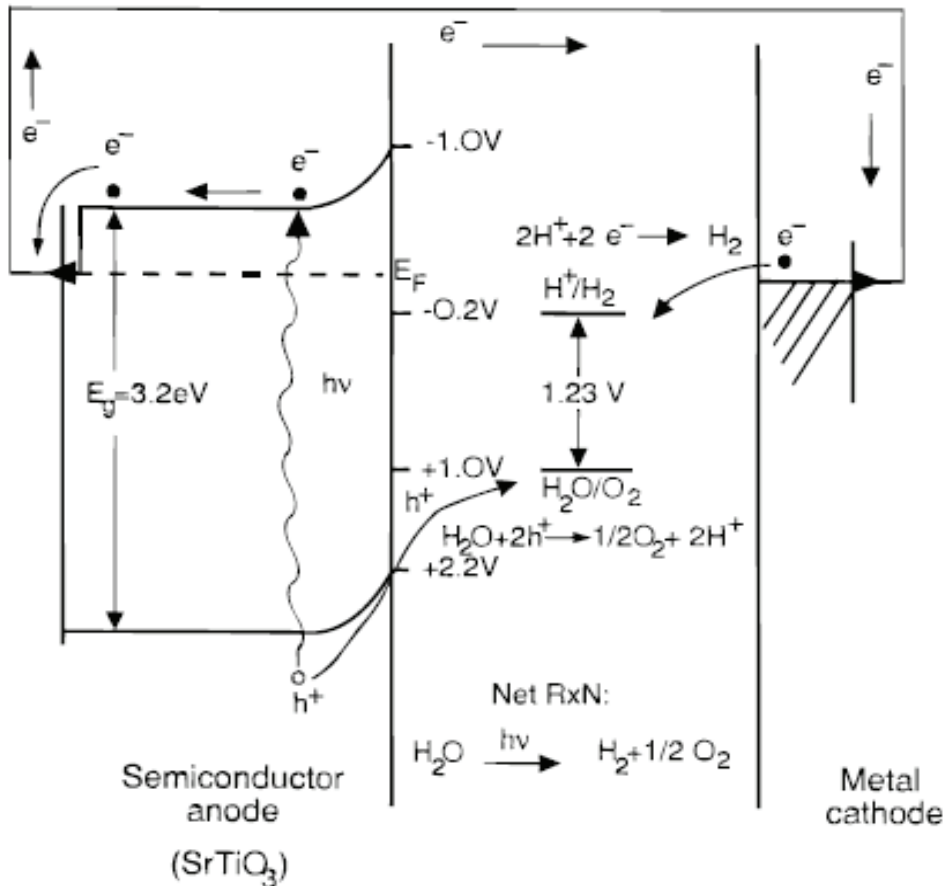


Fig.1.4 Photoelectrolysis of water using a SrTiO_3 photoanode. Due to the position of conduction and valence band edges hydrogen and oxygen are evolved without need of external bias. From A.Nozik and R.Memming, *J.Phys.Chem.*, 100, 31, 1996.

The development of a stable semiconducting material that functions efficiently under visible light, which represents almost half of the available solar spectrum, is indispensable for the practical use of solar energy. Domen et al. [11] recently reported several oxynitrides of transition metals as potential candidates for visible light induced water splitting [12-14]. The conduction band edges of these oxynitrides consist predominantly of empty orbitals of the metal, resulting in similar energy levels to those of corresponding metal oxides. On the other hand, the valence bands of oxynitrides are more negative than those of oxides due to the hybridization of N 2p with O 2p orbitals. Consequently, some oxynitride materials possess appropriate band levels for water splitting, as well as a narrow band gap allowing visible light absorption. For example, tantalum oxynitride TaON (band gap: ca. 2.5 eV, corresponding to light absorption up to 500 nm) has conduction and valence band edges at ca. -0.3 and +2.2 V vs NHE, respectively, which are suitable for both water reduction and oxidation [15]. This implies that a TaON photoelectrode has the potential to produce H₂ and O₂ from water under visible light, even without an externally applied bias. In contrast, visible light-sensitive oxide semiconductor electrodes, such as WO₃, Fe₂O₃ and BiVO₄, require a considerable applied bias to produce H₂, because their conduction band levels are too low for water reduction [16-18]. Although there have been a few reports of the fabrication of n-type photoanodes based on metal oxynitrides, such as TaON or LaTiO₂N, their efficiencies were still low [19-21]. Furthermore, all these reports demonstrated only a photocurrent, without confirming appreciable O₂ evolution.

Besides a difficult preparation route which involves the use of gaseous ammonia at high temperature (>1000K) under controlled conditions, TaON requires the use of a co-catalysts, ie. IrO₂, to successfully transfer the hole to the electrolyte. Only at these conditions the requirements of efficient photoelectrolysis are met.

Moreover, instability arises from the oxidation of nitrogen anions N₂ by photogenerated holes ($2\text{N}^{3-} + 6\text{h}^+ \rightarrow \text{N}_2$). IrO₂ loading noticeably suppressed the decreases in both photocurrent and N content. IrO₂ loading most likely resulted in hole scavenging to the IrO₂ particles, preventing self-oxidation of the TaON surface. The number of electrons passing through the outer circuit in 1 h (11.72 C, corresponding to 121.5 μmol of electrons) exceeded the molar amounts of both TaON (ca. 14.2 μmol) and IrO₂ (ca. 0.04 μmol) contained in the electrodes. This indicates that most of the photocurrent resulted

from photocatalytic water oxidation, not merely the self-oxidative decomposition of the TaON material itself (Fig. 1.5).

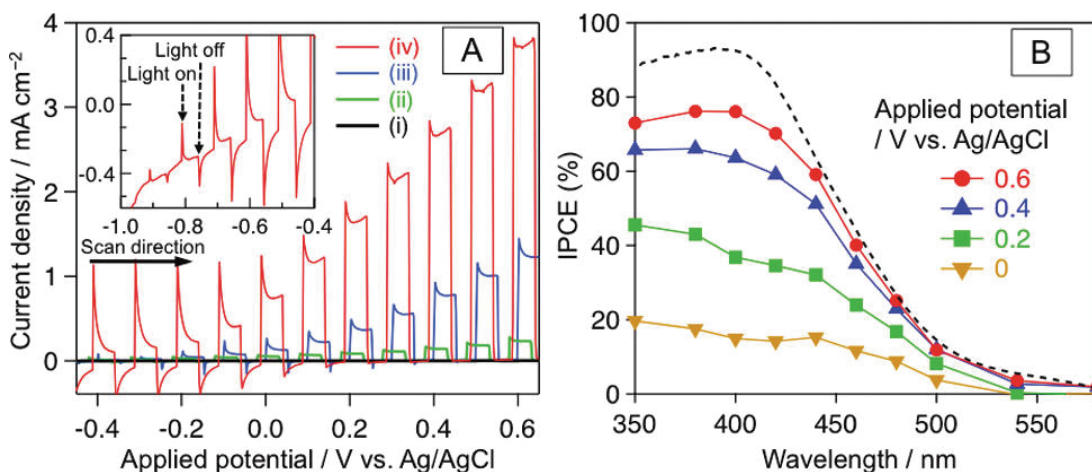


Figure 1.5. (A) Current-potential curves in aqueous 0.1 M Na₂SO₄ solution (pH 6) under chopped visible light irradiation ($\lambda > 400$ nm) for TaON electrodes as-prepared (i), treated by TaCl₅ (ii), heated in NH₃ (iii), and loaded with IrO₂ (iv). (B) Incident photon to current efficiency (IPCE) spectrum of IrO₂-TaON electrode with various applied potentials (1 M Na₂SO₄, pH 6) and absorption spectrum of TaON (dashed line).

Other materials for stable overall water splitting under visible light are GaN and ZnO that is expressed as (Ga_{1-x}Zn_x)(N_{1-x}O_x) [22–24]. Both GaN and ZnO are well-known III–V and II–VI semiconductors that have been the target of extensive research as functional materials in light-emitting diodes and laser diodes [25,26]. As shown in (Fig. 1.6), the (Ga_{1-x}Zn_x)(N_{1-x}O_x) solid solution possesses a wurtzite crystal structure similar to GaN and ZnO, and is typically synthesized by nitriding a mixture of Ga₂O₃ and ZnO powders. As both GaN and ZnO have band-gap energies of greater than 3 eV, neither can absorb visible light in pure form. Interestingly, however, the solid solution, (Ga_{1-x}Zn_x)(N_{1-x}O_x), has a band gap smaller than 3 eV and a steep absorption onset in the visible region. As shown in (Fig. 1.7), the band-gap energy (light absorption edge) is dependent on the compositional parameter (x) that is controllable by modifying the preparation parameters, and the decrease in band-gap energy in the solid solution is due to the electronic behavior of the constituent Zn and O species [27– 29].

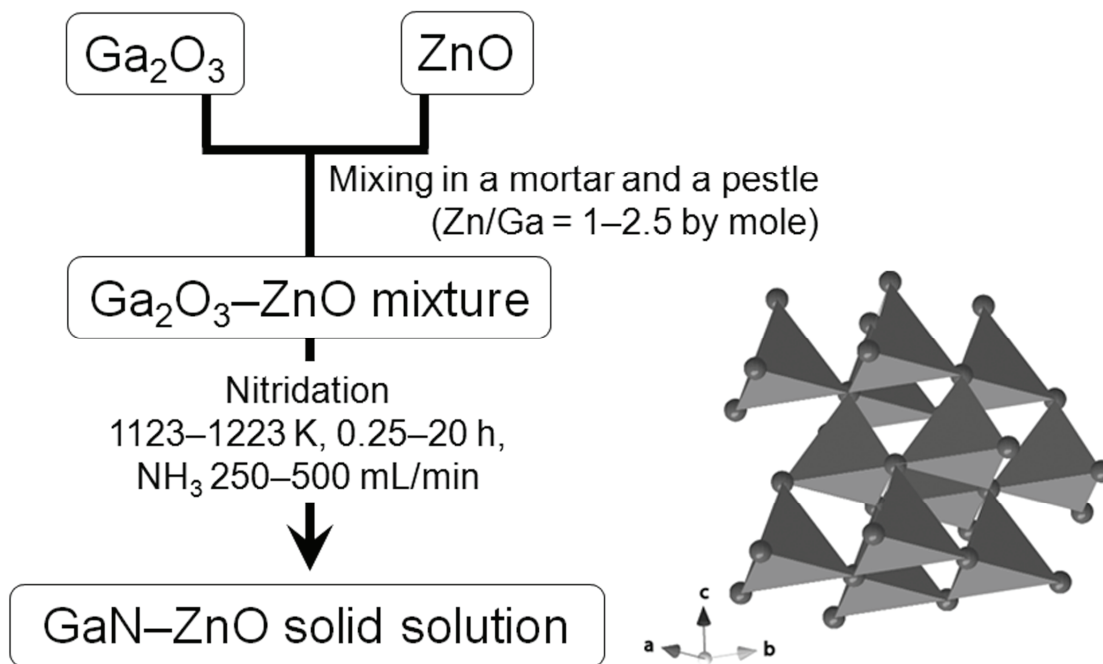


Fig 1.6 Preparation scheme of a GaN-ZnO solid solution with its crystal structure.

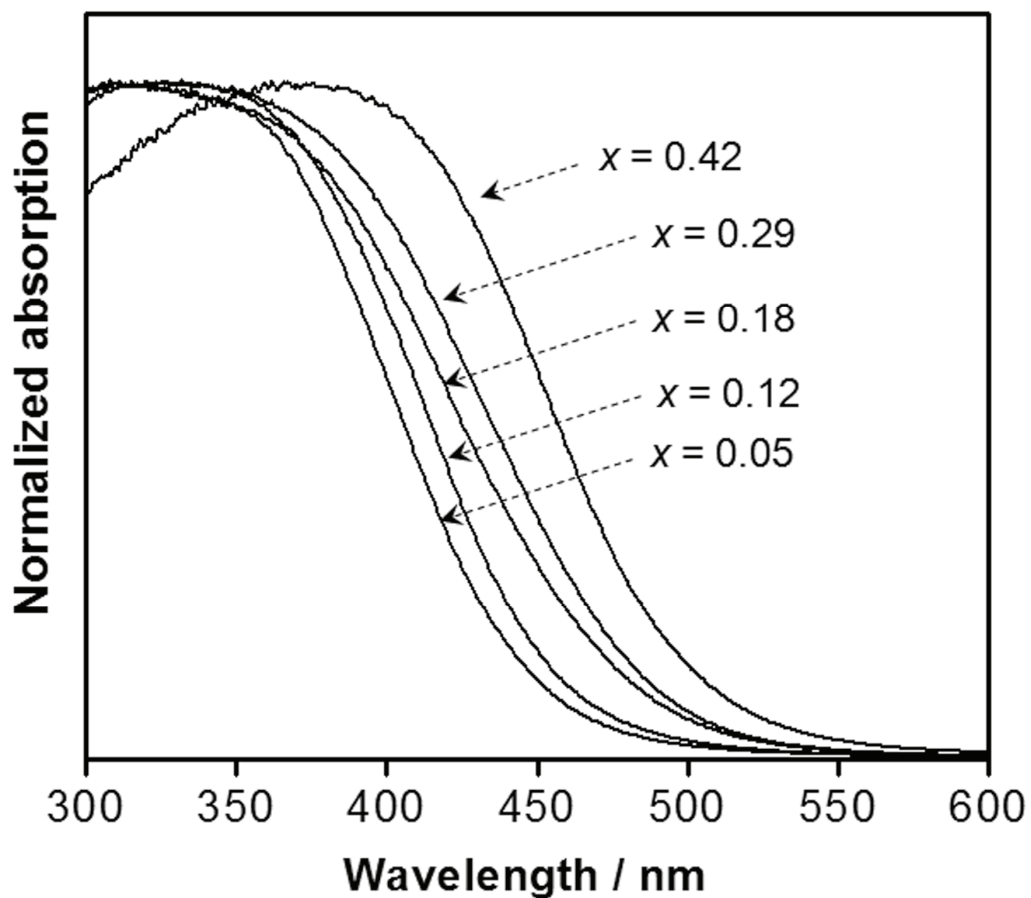


Figure 1.7 UV-visible diffuse reflectance spectra for $(\text{Ga}_{1-x}\text{Zn}_x)(\text{N}_{1-x}\text{O}_x)$ with various compositions (x).

With photoelectrochemical cells made of n-type and p-type semiconductors in contact with an electrolyte, the requirement of an external bias can be eliminated[30]. A first example of these p-n photoelectrolysis cells was reported by Nozik in 1976[31] with a n-TiO₂/p-GaP heterotype device whose efficiency at zero bias was 0.25%. The energy diagram of such a cell, also called photochemical diode, is shown in Fig. 1.8. Several other systems have been studied including n-TiO₂/p-CdTe, n-SrTiO₃/p-CdTe, n-SrTiO₃/p-GaP, n-Fe₂O₃/p-Fe₂O₃, n-TiO₂/p-LuRhO₃[32]. However, many visible absorbing p type semiconductors have shown limited stability in aqueous solvents[33], and, although power conversion efficiencies exceeding 12 % could be achieved in monolithic multijunction systems[34], the durability of many devices was low, with degradation occurring on the time scale of hours.

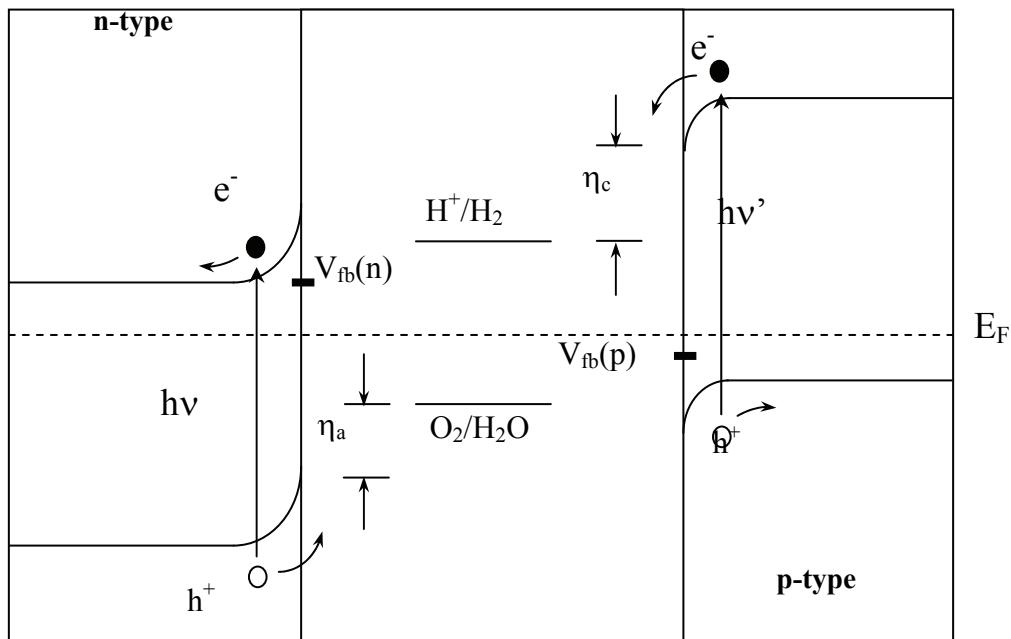


Figure 1.8 Energy level diagram for a p-n type photoelectrolysis cell.

An interesting approach to overcome limitations arising by the need of a bias while keeping an effective light absorption in the visible region is the absorption of dye molecules on the surface of a wide band gap semiconductor with an appropriate band energy, like TiO₂ for example, which, upon light excitation, can inject electrons (in n-

type materials) or holes (in p-type systems) into the acceptor states of the solid. In principle the photooxidized (photoreduced) dye can oxidize (reduce) water, while the complementary redox process can occur at the counter electrode of the cell. Although such approach has evident limitations related to the demanding 4-electron kinetics of water oxidation, some recent fundamental work pointing out the feasibility of molecular dye sensitized solar water splitting by exploiting certain specific hole transfer catalysts, are briefly reviewed in the next section. The attention will then focus on the design and characterization of newly developed photoanodes, based on anodically grown wide band gap semiconductors with improved charge transfer kinetics, as well as on the coupling of these substrates to lower band gap semiconductors.

1.2 Dye sensitized Photoanodes for water oxidation and hydrogen evolution

In a generic sensitized PEC design, the molecular excitation and excited state formation are followed by electron transfer injection into the conduction band of a semiconductor. In order to promote multi-electron transfer events like water oxidation, multiple redox equivalents must be concentrated in a single site or cluster. The working principles of the cell are schematized in Fig. 1.9, where solar energy is stored to create a photopotential for water splitting[35,36]. In principle, at the cathode, water or CO₂ reduction may occur, giving rise to the production of fuels.

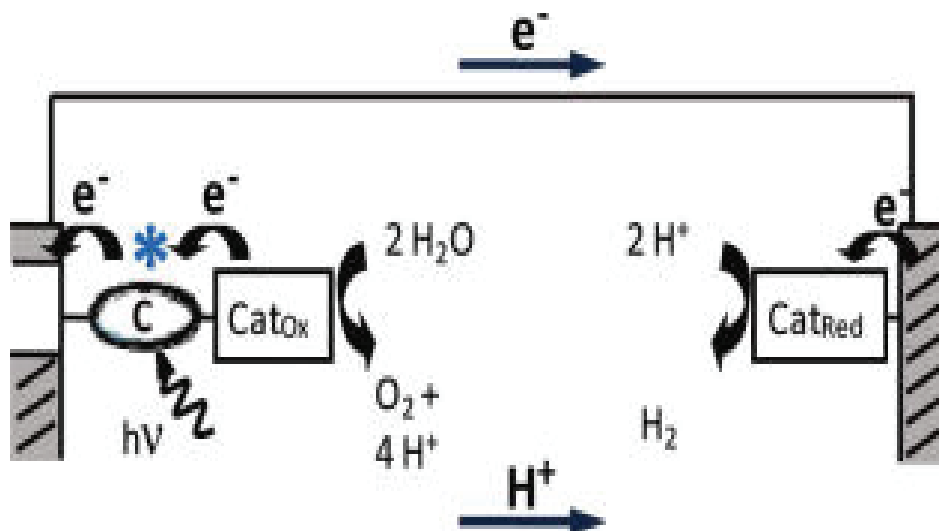


Fig. 1.9 Working principle of a sensitized PEC cell for water splitting. Cat_{ox} and Cat_{red} are catalyst for water oxidation and reduction. Acc. Chem.Res. 42, 1954, 2009.

The blue dimer *cis,cis* [(bpy)₂(H₂O)Ru(III)ORu(III)(OH₂)bpy]₂⁴⁺ (Fig. 1.10) was among the first molecular species to show a catalyzed water oxidation by Ce(IV) through a reaction mechanism which has been elucidated in detail by spectroscopic, electrochemical and chemical mixing experiment[37](Scheme 1). The key point is the 4 e⁻/4H⁺ loss to form the activated catalyst [(bpy)₂(H₂O)Ru(V)ORu(V)(OH₂)bpy]₂⁴⁺ which undergoes water attack on one of the Ru(V)=O sites to give a peroxido intermediate which releases oxygen and gives back the initial Ru(III)-O-Ru(III) species on a millisecond time scale.

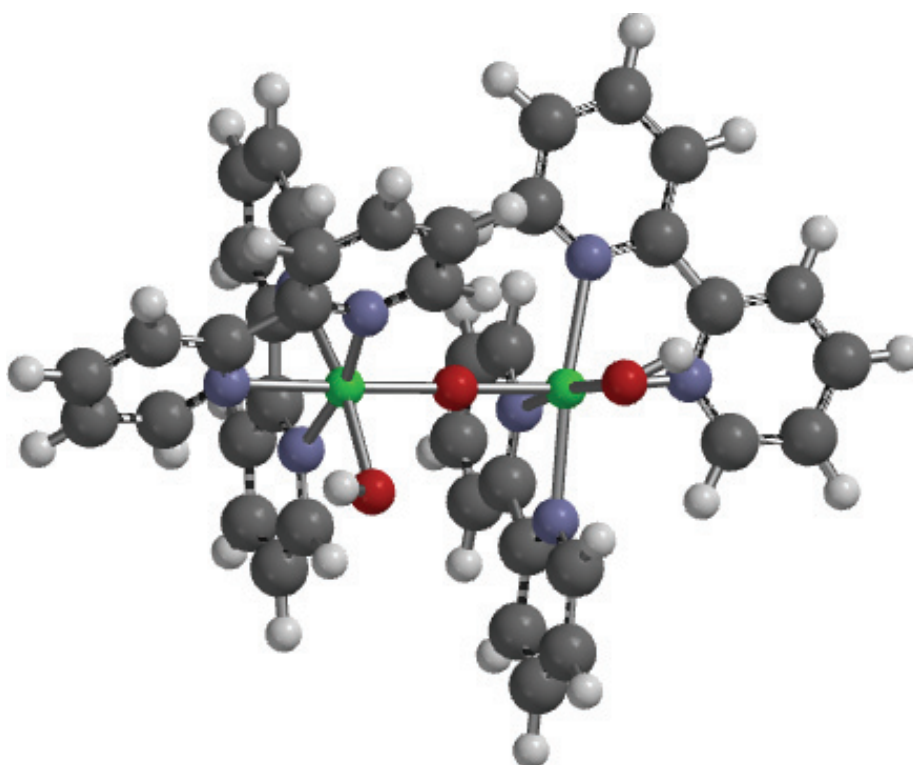
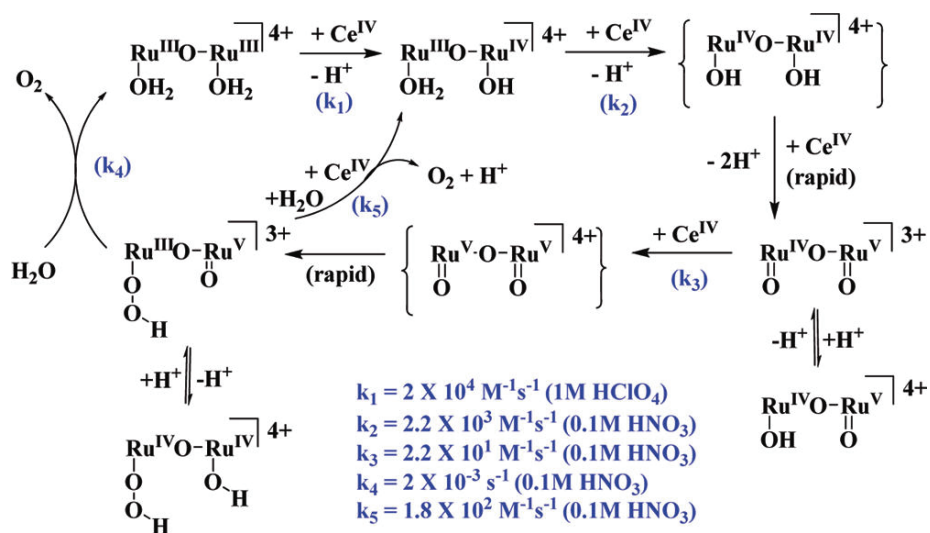


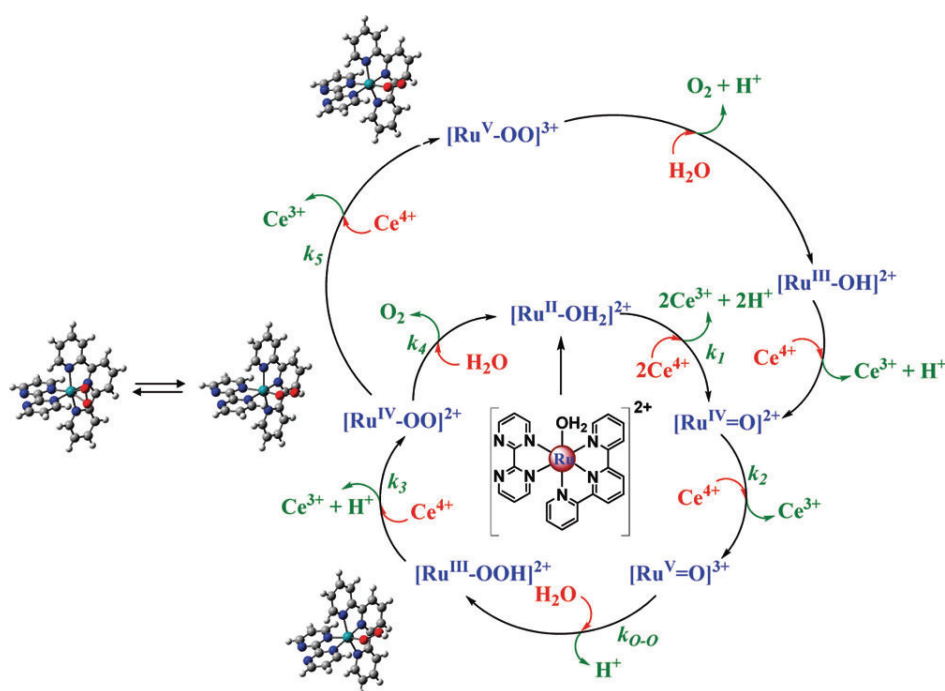
Fig. 1.10 Energy minimized structure of the “blue Ru dimer” cis,cis [(bpy)₂Ru(OH)ORu(OH)(bpy)₂]⁴⁺. The green balls are the Ru(III) centers.



Scheme 1. Mechanism of water oxidation by [(bpy)₂(H₂O)Ru(V)ORu(V)(OH₂)bpy₂]⁴⁺. Jurss et al, Inorg. Chem., 2010, 49, 3980.

As a catalyst, the blue dimer has limitations due to oxidatively induced coordination of anions which slow down the catalytic cycles. Since the O-O bond forming step occurs on single Ru(V) site, it has been demonstrated that simpler and more robust mononuclear Ru(III) aquo complexes of the type $[\text{Ru}(\text{tpy})(\text{bpm})(\text{H}_2\text{O})]^{2+}$, where tpy is the 2,2'6'2'' terpyridine and bpm is the bipyrimidine ligand, can undergo hundreds of turnovers without showing decomposition according to the cycle schematized in Scheme 2[38]. It must be noted that the Ru(III) state appears to be a “missing” state due to instability toward the disproportionation to Ru(IV) and Ru(II).

DFT and spectroscopic results indicate that, following the attack of water to the Ru(V)=O sites, one has the formation of a first intermediate described as a terminal peroxide coordinated to Ru(III) which undergoes further oxidation by Ce(IV) to give a 7 coordinated Ru(IV) complex where O_2^{2-} acts as a chelating ligand. Oxygen can be evolved both from $[\text{Ru}(\text{IV})\text{OO}]^{2+}$ and $[\text{Ru}(\text{V})\text{OO}]^{3+}$ structures following water attack.



Scheme 2. Ce(IV) water oxidation catalyzed by $[\text{Ru}(\text{tpy})(\text{bpm})\text{OH}_2]^{2+}$. Concepcion et al, Acc. Chem. Res., 2009, 1954-1965.

Although the electrocatalytic water oxidation by blue dimer has been demonstrated at FTO and ITO electrodes modified with phosphonated Ru(II) tris-bipyridine derivatives working as a redox mediator[39], the realization of an efficient dye sensitized PEC device for water oxidation has yet to be realized, but progresses are underway. Infact several issues have to be contemporarily satisfied to realize an efficient solar device: (I) effective Visible-NIR absorption by the molecular sensitizer; (II) excited state quenching by electron transfer to the semiconductor; (III) efficient and repeated single photon-single hole transfer to the catalyst to achieve the accumulation of three oxidative equivalents to give Ru(V)-OO which undergoes attack by water giving Ru(III)-OOH; after two further subsequent oxidations, one finally obtains the evolution of molecular oxygen and the recovery of Ru(III)-OH which initiates a new catalytic cycle. While oxidative excited state quenching by Ru(II) chromophores on TiO₂ have been reported to be extremely fast, the subsequent hole transfer are in critical kinetic competition with photoinjected electron (TiO₂)/hole recombination. A further complication arises from the light harvesting competition between the photoactive Ru(bpy)₃ type unit and the catalyst, which being relatively remote from the semiconductor surface does not contribute significantly to the photocurrent. Infact, APCEs (absorbed photons to electrons conversion efficiency) of the order of 3-4 % (Fig. 1.11b) and of 1-2 % have been achieved in the presence of hydroquinone and pure water repectively, by using the sensitizer/oxygen evolving catalyst dyad [(4,4'((HO)₂P(O)CH₂)₂bpy)₂Ru(II)(bpm)Ru(II)(Mebimpy)(OH₂)]⁴⁺ (Fig. 1.11a), where Mebimpy is 2,6-bis(1-methylbenzimidazol-2-yl)pyridine)[36].

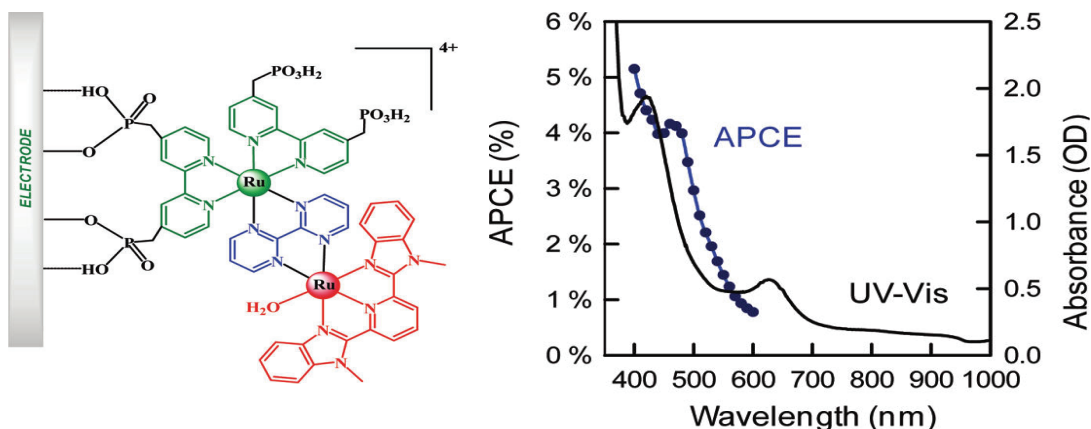


Fig. 1.11

(a) Structure of $[(4,4'((\text{HO})_2\text{P}(\text{O})\text{CH}_2)_2\text{bpy})_2\text{Ru}(\text{II})(\text{bpm})\text{Ru}(\text{II})(\text{Mebimpy})(\text{OH}_2)]^{4+}$ sensitizer/catalyst assembly anchored to a TiO_2 electrode; (b) APCE and absorption spectrum in the presence of 0.5 M hydroquinone acting as an electron donor in 0.1 M HClO_4 .

Conceptually similar approaches have been based on different molecular catalysts or nanomaterials chemically coupled to the molecular sensitizer.

In a recent interesting design[40], a manganese cage complex catalyst ($[\text{Mn}_4\text{O}_4\text{L}_6]^+$, or “*cubium*”, $\text{L} = \text{MeOPh}_2\text{PO}_2^-$) able to undergo multiple proton coupled electron transfer, is encapsulated in a nafion membrane which has the role of providing both an high local surface concentration of redox active catalyst and a reasonable coupling with the Ru(II) dye sensitizer (Fig. 1.12). The molecular level solar water splitting, recalling that occurring in natural photosynthesis was thus beautifully demonstrated, but also in this case the performances were far from a practical application of the device, with IPCEs (IPCE=number of electrons/number of incident photons) below 2 %, corresponding to a stable photocurrent, with no externally applied bias, of the order of $30\text{-}5 \mu\text{A}/\text{cm}^2$ depending on the illumination intensity and spectral bandwidth.

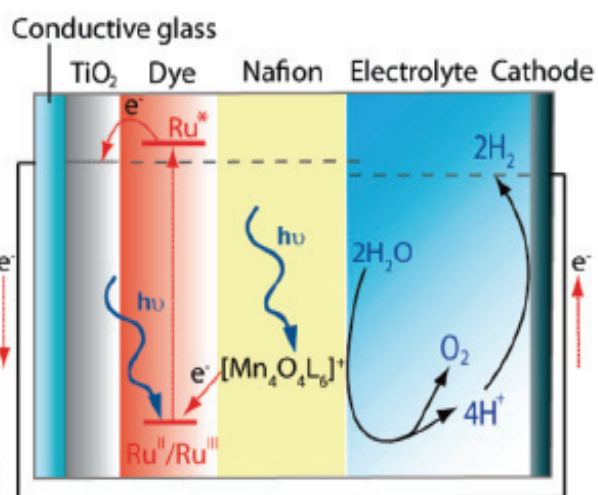
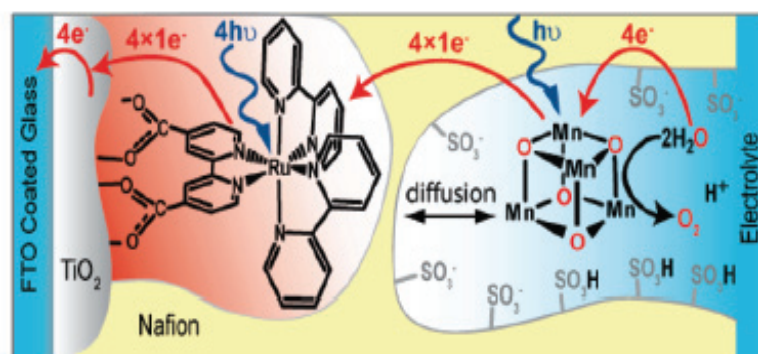
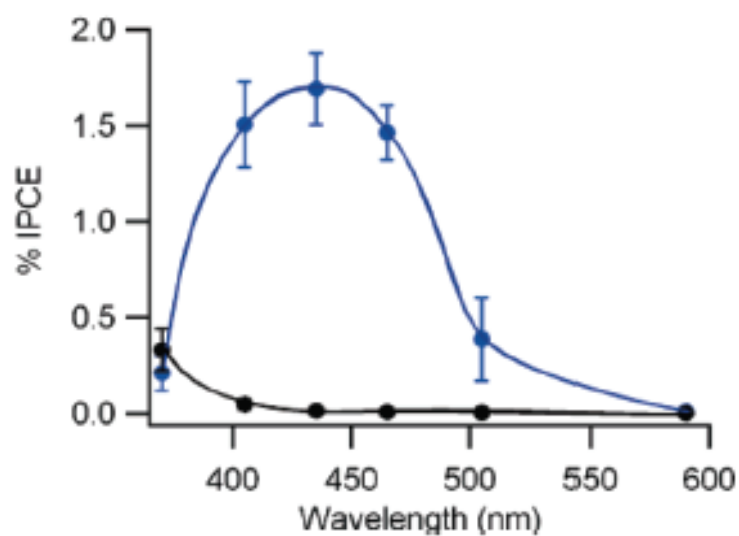


Fig. 1.12 (a) IPCE Spectrum (blue) of the sensitizer/catalyst system (b) compared to that of the plain nafion/ TiO_2 electrodes. (c) Pictorial scheme of working principles of the dye sensitized PEC for solar water splitting with no external bias. From Brimblecomb et al., JACS, 2010, 132, 2892.

Another interesting configuration, which is discussed in detail in another section of this book, involves the anchoring of hydrated IrO₂ nanoparticles to a phosphonated Ru(II) sensitizer modified with malonate binding groups (Fig. 1.13) [41,42]. The hole transfer to the IrO₂ takes place on a millisecond (2.2 ms) time scale, while charge recombination occurs on a sub-millisecond (0.37 ms) time scale. Thus, the competition between hole transfer and recombination is unfavorable to an effective charge separation. Nevertheless, under a small positive bias (≥ 330 mV) a stable photoanodic current of the order of few tens of microamperes is effectively detected, indicating the occurrence of photoinduced water oxidation under steady state conditions. Although the efficiency is low, the device represent a successful proof of concept of water splitting in a sensitized PEC device. Possible efficiency improvements could be related to synthetic modifications of the sensitizer/catalyst assembly, aimed to improve the binding between the photoactive dye and the IrO₂ nanostructures, to slow down recombination and to speed up the hole transfer to Ir(IV) for improving the turnover number which is now poor (<20).

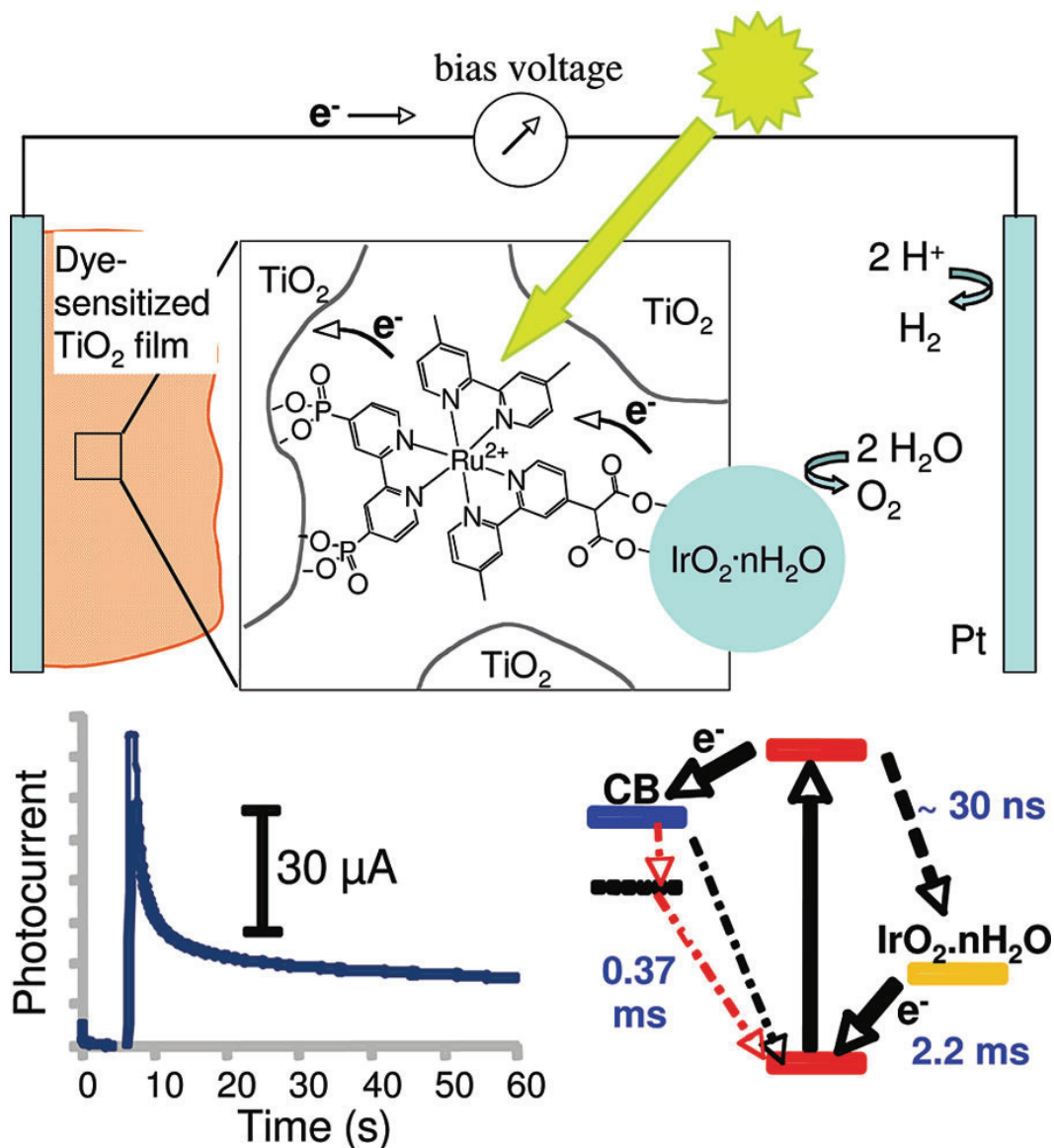


Fig. 1.13 Top: schematic diagram of a IrO_2 catalyzed water-splitting dye-sensitized solar cell. Following light excitation and oxidative quenching of the excited state of Ru(II) , the hole is transferred to Ir(IV) , activating the IrO_2 catalyst toward water oxidation. Bottom left: photocurrent transient showing a steady state photocurrent. Bottom right: energy diagram and time constants for the relevant interfacial electron transfer and excited state deactivation processes.

Unless sensitizers capable of performing directly an efficient water oxidation are designed, the use of sacrificial agents, although disadvantageous, cannot be avoided. It must be noted that there is a potentially large number of relatively abundant easily oxidizable ions and organic species that could be consumed to produce hydrogen. This type of conceptually simple sensitized photo-electrolytic cell is schematized in Fig. 1.14. In principle, photogenerated D^+ could compete with the reduction of H^+ at the

counter electrode, thus decreasing the hydrogen yield, however this process can be avoided, or at least minimized, by an appropriate choice of D (eg. irreversible couples, non electro-active oxidized species) or simply by operating the two electrodes in separate compartments connected by a glass frit, a proton permeable membrane or a salt bridge

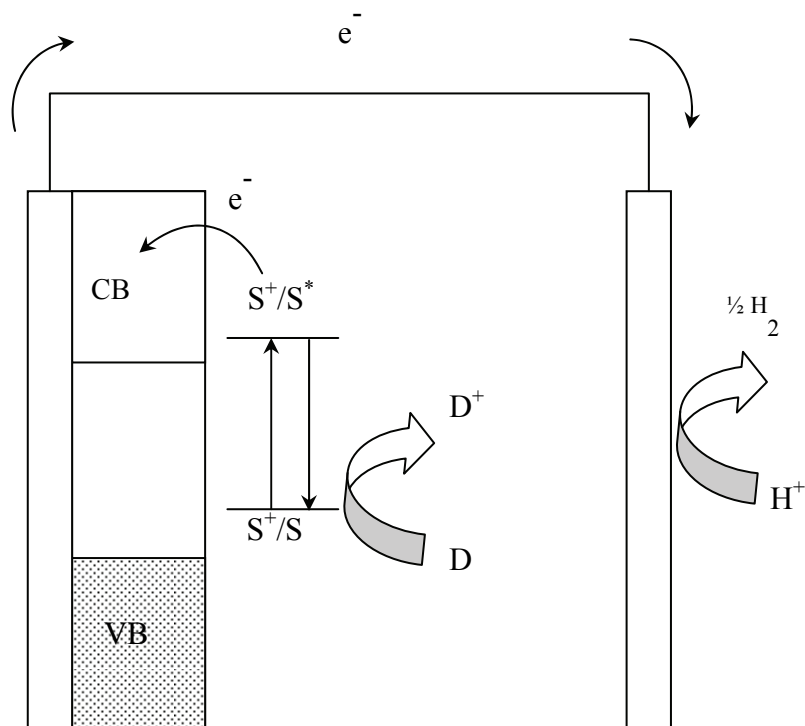


Fig. 1.14 Working principle of a dye-sensitized photoelectrolytic device based on a sacrificial agent.

1.3 Highly Ordered semiconductors nanostructures based on TiO₂

Highly organized and ordered substrates produced by electrochemical formation or by template synthesis are attracting significant interest from the scientific community[43,44]. While fundamental efforts are being directed towards the understanding of self organization phenomena, technological implications are arising from the exploitation of structure-related peculiar properties which allow for promising applications in catalysis[45], photonic materials[45] and optical waveguides[46] and, particularly, in photoelectrochemistry[47]and photovoltaics[48], since grain boundaries, normally occurring between more conventional sintered nanoparticles, can be avoided or reduced.

Although several attempts successfully achieved the production of nanotubes, their relatively short lengths (tens or hundreds of nanometers) [49] somehow limited their applications. However, in recent years, mainly P. Schmucki and C.A. Grimes have shown the possibility of growing high aspect ratio TiO₂ nanotubes of considerable length and uniform pore diameter by tailoring the electrochemical conditions during the anodization of metallic titanium foils[50-52] (Fig. 1.15).

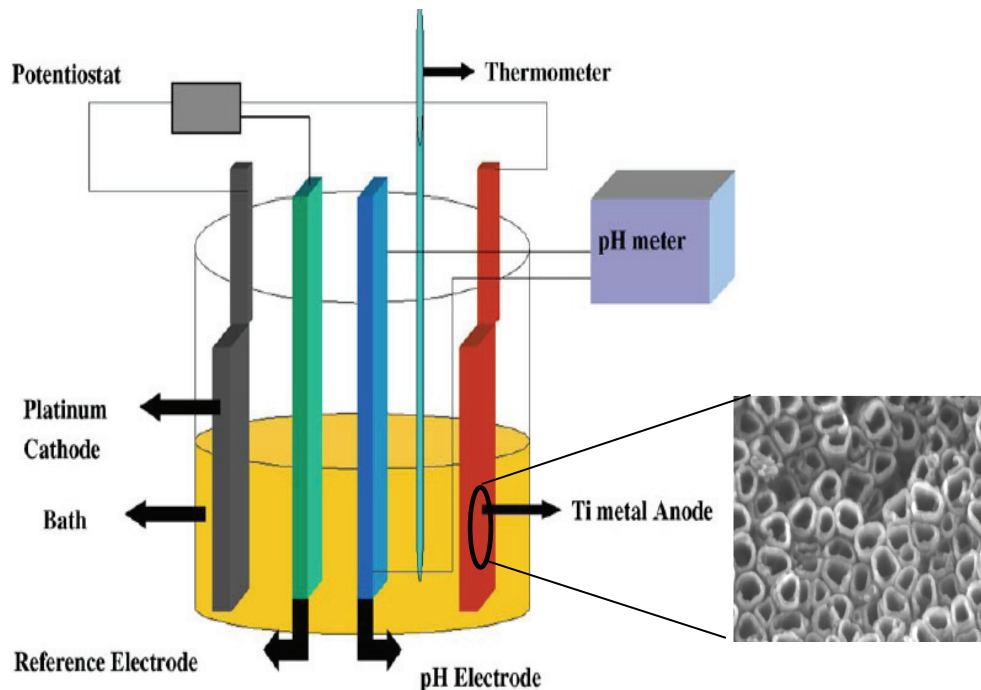
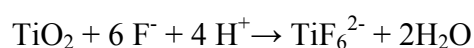


Fig. 1.15 Schematic apparatus for the electrochemical growth of titania nanotubes (right). From Grimes et.al, Sol. Energy Materials & Solar Cells, 2006, 90, 2011.

In general the key process for anodic formation of titania nanotubes are: (1) metal oxide formation due to reaction of titanium with O^{2-} or OH^- . These anions can also migrate through the initially formed oxide layer reaching the metal/metal oxide interface where they react with the metal; (2) Ti^{4+} migration from the metal to the metal oxide interface under the intense electric field; (3) field assisted dissolution of the oxide at the oxide/electrolyte interface: under the intense electric field the Ti-O bonds are polarized and weakened promoting dissolution of metal cations (Ti^{4+}); (4) chemical dissolution of titania in the HF containing electrolyte, which plays a key role in the formation of tubes rather than of an irregular mesoporous structure. Although the field assisted dissolution is initially dominating, due to the strong field across the initially thin oxide layer, it is the chemical reaction with fluorides that gives rise to localized dissolution of the oxide forming pits that act as a pore forming centers, according to



The thinner barrier layer at the bottom of the chemically etched pits leads to a localized increase of the electric field which promotes field assisted dissolution leading to pore deepening and widening, while, at the same time the density of the pits increases finally leading to the full development of a densely packed nanotube array (Fig. 1.16). When the rate of chemical oxide dissolution at the mouth of the tube (top surface) becomes equal to the rate of inward movement, the thickness of the tubular layer ceases to increase. High anodization voltages increase the oxidation and field assisted dissolution, hence a greater nanotube length can usually be achieved before equilibrating with the chemical dissolution.

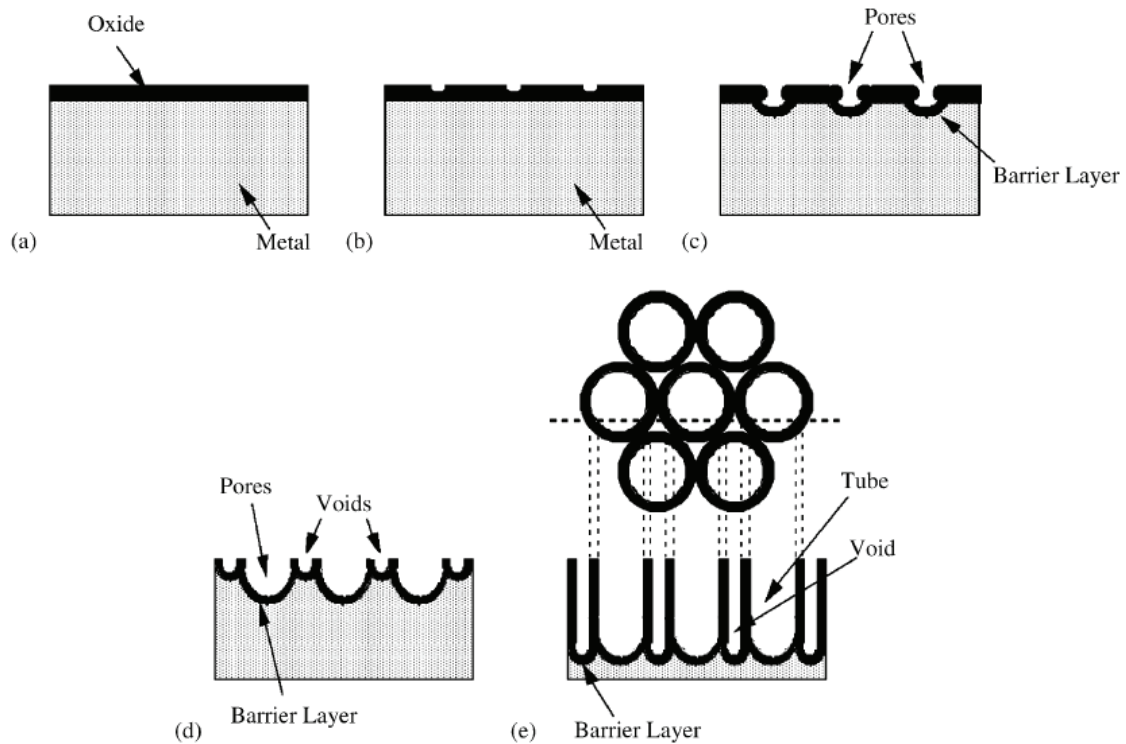
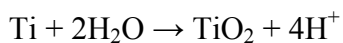


Fig. 1.16 Schematic diagram showing the nanotube on anodized titanium foil: (a) oxide layer formation; (b) pit formation; (c) growth of pit into pores; (d) regions between the pores undergo oxidation and field assisted dissolution; (e) developed nanotube array. From Grimes et al., *Sol. Energy Materials & Solar Cells*, 2006, 90, 2011.

As pointed out by Schmuki, another key parameter to achieve high aspect ratio nanotubes consists in adjusting the dissolution rate of TiO_2 at the pore bottom while a relatively protecting environment, in which the TiO_2 dissolution is slower compared to the bottom, is maintained at the walls and at the mouth of the tube (Fig. 1.17). The self acidification of the pore bottom occurs, mainly due to the electrochemical oxidation of elemental titanium, according to



Hence it is possible, by operating in a buffered solution, to produce protons where is needed by adjusting the anodic current flow to an ideal value. Thus, while lower pH values can be obtained at the tube bottom, in turn favoring chemical dissolution of the oxide due to the “in situ” formation of HF, higher pH values and, consequently, a slower oxide dissolution rate can be established at the top and at the walls of the nanotube,

thanks to the presence of pH buffering species (NH_4F , $(\text{NH}_4)_2\text{SO}_4$). The pH gradient (Fig. 1.17) has been calculated in great detail by using finite-difference numerical simulation, and it has been shown that a pH variation from 2 to 5 occurs by moving from the bottom to the top of the tube, corresponding to a 20 fold drop in the local chemical etching rate.

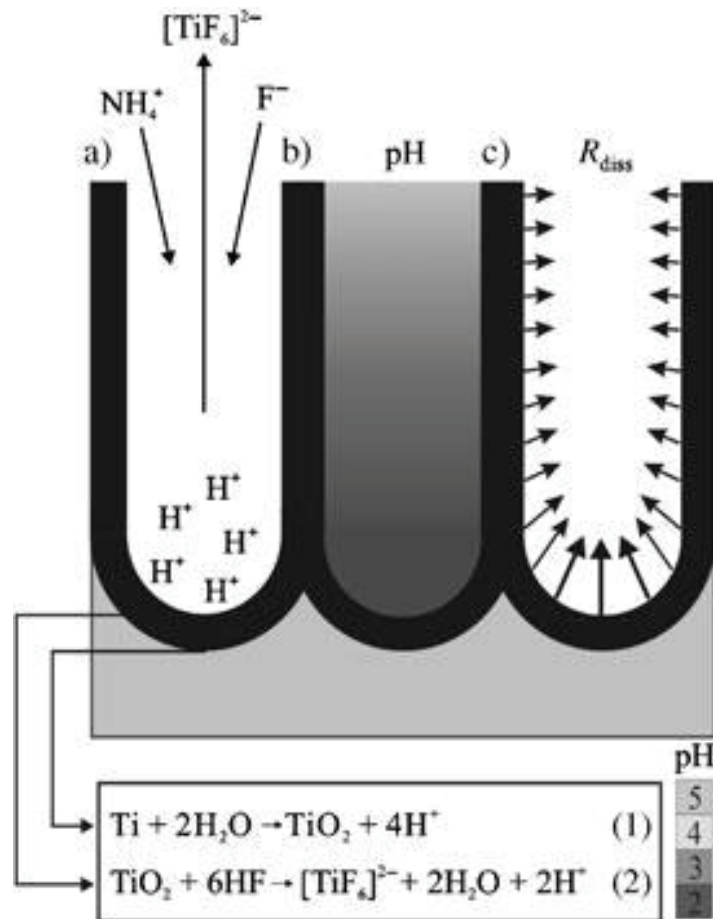


Fig. 1.17 Schematic representation of: (a) oxide formation and dissolution reactions; (b) pH profile within the pore; (c) dissolution rate (proportional to the arrow length). From Schmucki et al., *Angew. Chem.* 2005, 44, 2100.

1.4 Experimental conditions for electrochemical titania nanotube formation

In general potentiostatic or potential sweep methods are preferred over a galvanostatic approach which has the tendency to oscillate and destabilize the steady state conditions within the pore. A method devised by Schmucki et. al[50], involves the use of an aqueous electrolyte containing 1 M $(\text{NH}_4)_2\text{SO}_4$ and smaller amount of NH_4F (0.5-5% w/w). The electrochemical treatment consists in a voltage ramp from open circuit potential to 20 V, adopting various scan rates, followed by a potentiostatic treatment at 20 V for different times.

Considering, water based electrolytes, Grimes at al. [51] achieved the best results (i.e. nanotubes up to six microns long) in a solution containing either fluoride salts (NaF or KF) or HF, in the presence of buffer salts like sodium sulfate, or sodium or potassium hydrogen phosphate in a pH interval ranging from 3 to 5 (Fig. 1.18). The potential window necessary to induce nanotube formation was 10-25 volts which could be maintained for several hours, up to 25 (Tab.1). The as made nanotubes present an amorphous structure which crystallizes at high temperature ($> 280\text{ C}^\circ$) to give anatase and rutile. The rutile phase becomes dominating at temperatures higher than 620 C° .

Table.1 Electrolyte composition of KF based electrolytes and relative electrochemical treatment. V is constant voltage and t is the application time. D and L stand for nanotube diameter and length, Q stands for quality of the anodized substrates. NT denotes an homogeneous nanotube coverage, No NT partially developed/porous surfaces. pH was adjusted by addition of sulfuric acid (pH 1-2) sodium hydrogen sulfate or citric acid (2.5-6.5). From Grimes et al. Sol.Energy Materials Sol. Cells, 90, 2006,2011

| No. | Electrolyte ^a | | | | pH ^b | V (V) | t (h) | D (nm) | L (μm) | Q ^c |
|-----|--------------------------|-------------------------------|-------------------------------|-----|-----------------|-------|-------|--------|-----------|----------------|
| | F ⁻ | SO ₄ ²⁻ | PO ₄ ³⁻ | Cit | | | | | | |
| 01 | 0.1 | 1.0 | — | — | <1 | 5 | 1 | 10±2 | — | No NT |
| 02 | 0.1 | 1.0 | — | — | <1 | 10 | 1 | 40±5 | 0.28±0.02 | NT |
| 03 | 0.1 | 1.0 | — | — | <1 | 15 | 1 | 80±9 | — | NT |
| 04 | 0.1 | 1.0 | — | — | <1 | 20 | 1 | 100±11 | 0.48±0.03 | NT |
| 05 | 0.1 | 1.0 | — | — | <1 | 25 | 1 | 110±12 | 0.56±0.04 | NT |
| 06 | 0.1 | 1.0 | — | — | <1 | 30 | 1 | — | — | No NT |
| 07 | 0.1 | 1.0 | — | — | <1 | 20 | 6.5 | 100±11 | 0.43±0.03 | NT |
| 08 | 0.1 | 2.0 | — | — | <1 | 20 | 1 | 100±11 | 0.45±0.03 | NT |
| 09 | 0.1 | 1.0 | — | 0.2 | 1.3 | 10 | 20 | 30±5 | 0.32±0.03 | NT |
| 10 | 0.1 | 1.0 | — | 0.2 | 2.8 | 10 | 20 | 30±5 | 0.59±0.05 | NT |
| 11 | 0.1 | 1.0 | — | 0.2 | 2.8 | 15 | 20 | 50±5 | 1.00±0.05 | NT |
| 12 | 0.1 | 1.0 | — | 0.2 | 2.8 | 25 | 20 | 115±10 | 1.50±0.04 | NT |
| 13 | 0.1 | 1.0 | — | 0.2 | 3.8 | 10 | 20 | 30±5 | 0.80±0.06 | NT |
| 14 | 0.1 | 1.0 | — | 0.2 | 3.8 | 10 | 60 | 30±5 | 1.80±0.06 | NT |
| 15 | 0.1 | 1.0 | — | 0.2 | 3.8 | 10 | 90 | 30±5 | 2.30±0.08 | NT |
| 16 | 0.1 | 1.0 | — | 0.2 | 4.5 | 10 | 20 | 30±5 | 1.05±0.04 | NT |
| 17 | 0.1 | 1.0 | — | 0.2 | 4.5 | 25 | 20 | 115±5 | 4.40±0.10 | NT |
| 18 | 0.1 | 1.0 | — | 0.2 | 5.0 | 10 | 20 | 30±5 | 1.40±0.06 | NT |
| 19 | 0.1 | 1.0 | — | 0.2 | 5.0 | 25 | 20 | 115±5 | 6.00±0.40 | NT |
| 20 | 0.1 | 1.0 | 0.1 | 0.2 | 6.4 | 10 | 24 | — | — | No NT |
| 21 | — | 2.0 | — | — | <1 | 10 | 24 | — | — | No NT |

Table 1

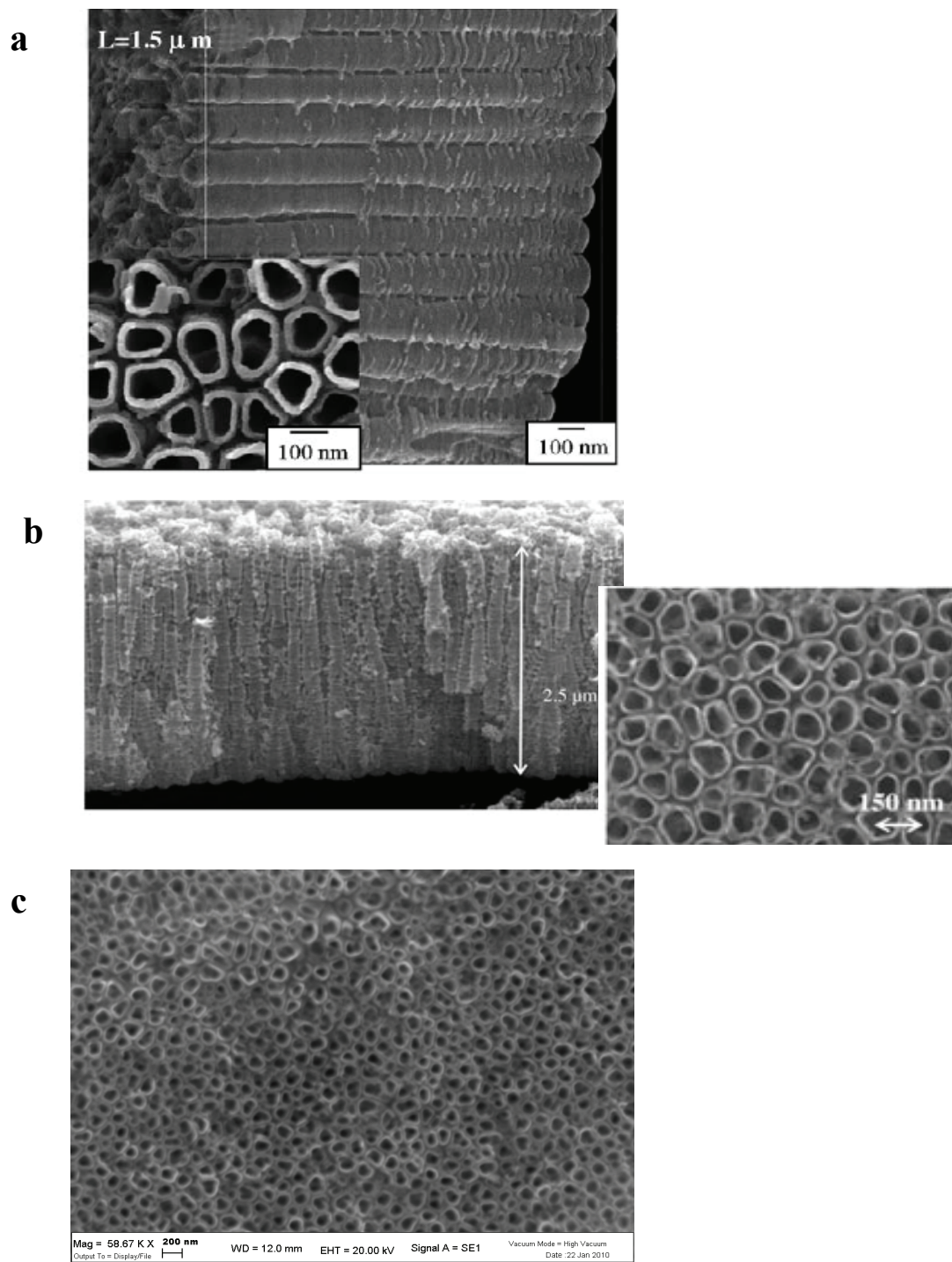


Fig. 1.18 Titania nanotubular arrays grown in various aqueous fluoride containing electrolytes. (a) 0.1 M $\text{F}^- + 1 \text{ M SO}_4^{2-}$ at pH 2.8 and at 25 V for 20 h; (b) 1 M $(\text{NH}_4)_2\text{SO}_4 + 0.5\% \text{ NH}_4\text{F}$ (w/w) by using a potential sweep from OCP to 20 V at 0.1 V/s; (c) 1M KF 0.5 M Na_2SO_4 at pH 4 at 25 V for 24 h.

Higher aspect ratio (up to an amazing 835 L/d ratio) nanotubes[52] could be obtained in organic electrolytes comprising an high dielectric constant solvent (N-methylformamide (NMF), Formamide (FA), dimethylsulfoxide (DMSO), ethylene glycol) a small percentage of water and fluoride salts of hydrofluoric acid. The highly polar FA and NMF increase dramatically nanotube length, probably due to an accelerated growth of the substrate. Infact, the dielectric constants of FA and NMF of respectively 111 and 182.4 are significantly higher than that of water (78.4). As a consequence, for any given potential the higher electrolytic capacitance induces a larger number of charges in the oxide layer, which in turn, promote an enhanced extraction of Ti^{4+} . At the same time a limited presence of water reduces the oxide dissolution rate in the fluoride containing medium aiding a longer nanotube formation.

In comparison with aqueous electrolytes, the range of applied anodization potentials over which nanotube arrays are formed is significantly extended, with an upper limit of 50 V in FA and NMF electrolytes. This is consistent with a more difficult oxygen donation in comparison with water, requiring higher overvoltages to occur. However, higher anodization potentials also imply a grater driving force for both electronic and ionic conduction within the oxide layer, both factors favoring nanotube formation and growth.

The comparison between the anodization current recorded in an aqueous electrolyte and that obtained in FA-NMF solvents is indeed striking (Fig 1.19): while in aqueous environment passivation is almost immediately established, causing a quick drop in current, in FA-NMF the current remains at an high and constant level for at least 100 s, which is consistent with the formation of a thin oxide layer of high conductivity and a low titanium oxidation rate. It is the high conductivity of the oxide layer which enables a faster inward movement of the Ti/TiO₂ interface, resulting in an improved nanotube length. Also DMSO is a suitable solvent for inducing long nanotube growth (Fig. 1.20), probably due to its protophilic properties which moderate the activity of HF. This minimize the loss by chemical dissolution from the tube mouth, allowing the tubes to grow deep into the titanium foil.

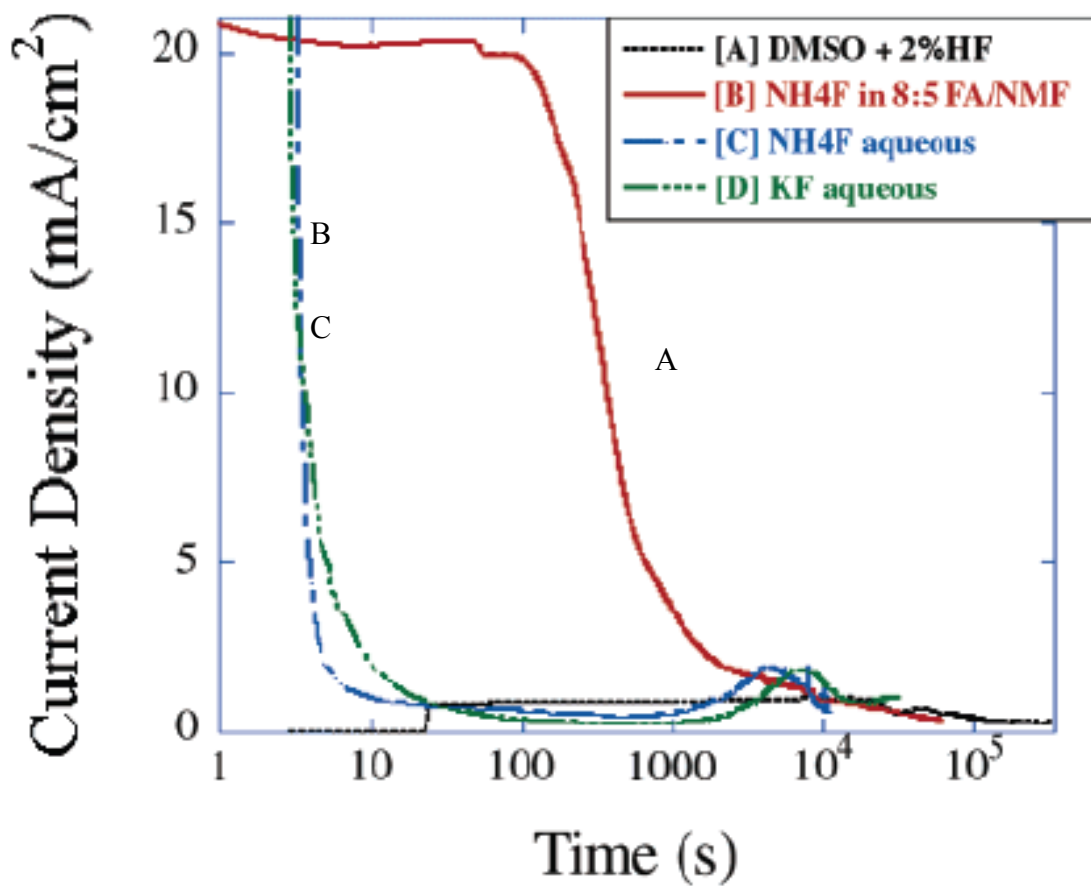


Fig. 1.19 Anodization current of Ti foil at constant 25 V in different electrolytic compositions: (A) FA-NMF + NH₄F; (B) NH₄F aqueous; (D) KF aqueous.

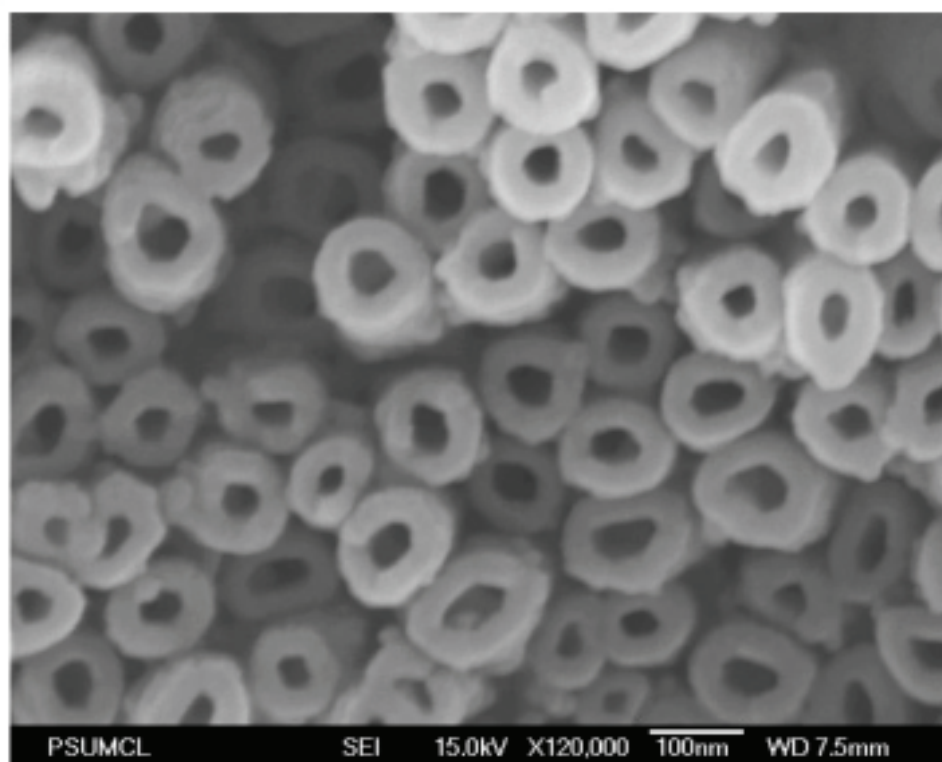
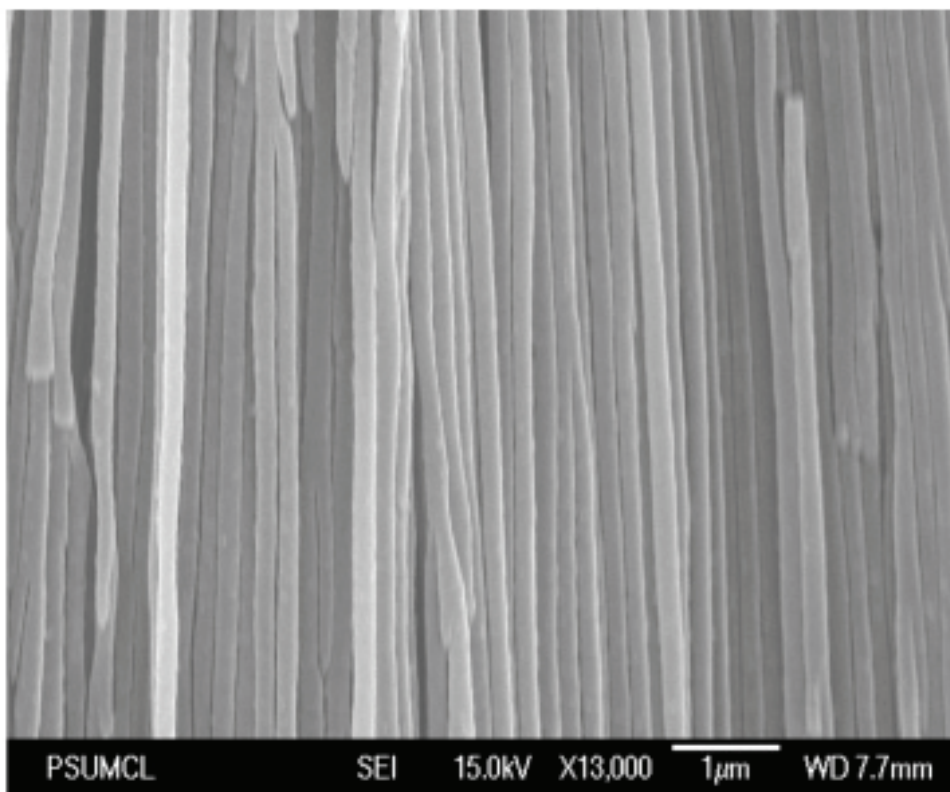


Fig. 1.20 FESEM images of anodically grown nanotubes in a FA based electrolyte at 35 V for 48 hours showing the cross section (top) and the top view (bottom) of the surface with nanotube mouths.

1.5 Bibliography

- (1) Ni, M.; Leung, M. K. H.; Leung, D. Y. C.; Sumathy, K. *Renewable Sustainable Energy Rev.* **2007**, *11*, 401.
- (2) Lewis, N. S. *Inorg.Chem.* **2005**, *44*, 6900-6911.
- (3) Eisenberg, R.; Nocera, G. D. *Inorg.Chem.* **2005**, *44*, 6799-6801.
- (4) Nozik, A. J.; Memming, R. *J.Phys.Chem.* **1996**, *100*, 13061-13078.
- (5) Fujishima, A.; Honda, K. *Nature* **1972**, *238*, 37.
- (6) Maldonado, S.; Fitch, A. G.; Lewis, N. S. *Nanostructured and Photoelectrochemical Systems for Solar Photon Conversion*; Imperial College Press: London, 2008.
- (7) Sodergren, S.; Hagfeldt, A.; Olsson, J.; Lindquist, S.-E. *J.Phys.Chem.* **1994**, *5552-5556*.
- (8) Gregg, B. A. *Coordination Chemistry Reviews* **2004**, *248*, 1215-1224.
- (9) Gregg, B. A.; Pichot, F.; Ferrere, S.; Fields, C. R. *J.Phys.Chem.B* **2001**, *105*, 1422-1429.
- (10) Kumar, A.; Santangelo, P. G.; Lewis, N. S. *J.Phys.Chem.* **1992**, 834-842.
- (11) Ryu Abe, Masanobu Higashi, and Kazunari Domen **J. AM. CHEM. SOC.** **2010**, *132*, 11828–11829
- (12) Higashi, M.; Abe, R.; Takata, T.; Domen, K. *Chem. Mater.* **2009**, *21*, 1543–1549.
- (13) Maeda, K.; Teramura, K.; Lu, D.; Takata, T.; Saito, N.; Inoue, Y.; Domen, K. *Nature* **2006**, *404*, 295.
- (14) Abe, R.; Takata, T.; Sugihara, H.; Domen, K. *Chem. Commun.* **2005**, 3829–3831
- (15) Chun, W. J.; Ishikawa, A.; Fujisawa, H.; Takata, T.; Kondo, J. N.; Hara, M.; Kawai, M.; Matsumoto, Y.; Domen, K. *J. Phys. Chem. B* **2003**, *107*, 1798–1803
- (16) Santato, C.; Ulmann, M.; Augustynski, J. *J. Phys. Chem. B* **2001**, *105*, 936 -940.
- (17) Kay, A.; Cesar, I.; Gratzel, M. *J. Am. Chem. Soc.* **2006**, *128*, 15714–15721.
- (18) Sayama, K.; Nomura, A.; Arai, T.; Sugita, T.; Abe, R.; Yanagida, M.; Oi, T.; Iwasaki, Y.; Abe, Y.; Sugihara, H. *J. Phys. Chem. B* **2006**, *110*, 11352–11360
- (19) Abe, R.; Takata, T.; Sugihara, H.; Domen, K. *Chem. Lett.* **2005**, *34*, 1162–1163.

- (20) Nakamura, R.; Tanaka, T.; Nakato, Y. *J. Phys. Chem. B* **2005**, *109*, 8920–8927.
- (21) Le Paven-Thivet, C.; Ishikawa, A.; Ziani, A.; Le Gendre, L.; Yoshida, M.; Kubota, J.; Tessier, F.; Domen, K. *J. Phys. Chem. C* **2009**, *113*, 6156–6162
- (22) Maeda K, Takata T, Hara M, Saito N, Inoue Y, Kobayashi H, Domen K (2005) *J Am Chem Soc* 127:8286
- (23) Maeda K, Xiong A, Yoshinaga T, Ikeda T, Sakamoto N, Hisatomi T, Takashima M, Lu D, Kanehara M, Setoyama T, Teranishi T, Domen K (2010) *Angew Chem, Int Ed* 49:4096
- (24) Surface Nanostructures in Photocatalysts for Visible-Light-Driven Water Splitting -Kazuhiko Maeda and Kazunari Domen-
- (25) Nakamura S, Mukai T, Senoh M (1994) *Appl Phys Lett* 64:1687
- (26) Tsukazaki A, Ohtomo A, Onuma T, Ohtani M, Makino T, Sumiya M, Ohtani K, Chichibu SF, Fuke S, Segawa Y, Ohno H, Koinuma H, Kawasaki M (2005) *Nat Mater* 4:42
- (27) Hirai T, Maeda K, Yoshida M, Kubota J, Ikeda S, Matsumura M, Domen K (2007) *J Phys Chem C* 111:18853
- (28) Jensen LL, Muckerman JT, Newton MD (2008) *J Phys Chem C* 112:3439
- (29) Wei W, Dai Y, Yang K, Guo M, Huang B (2008) *J Phys Chem C* 112:15915
- (30) Fornarini, L.; Nozik, A. J.; Parkinson, B. A. *J.Phys.Chem.* **1984**, *88*, 3238-3243.
- (31) Nozik, A. J. *Appl. Phys. Lett.* **1976**, *29*, 150-153.
- (32) Kainthla, R. C.; Zelenay, B.; Bockris, J. O. M. *J. Electrochem. Soc.* **1987**, *134*, 841-845.
- (33) Grimes, C. A.; Varghese, O. K.; Ranjan, S. *Light, Water, Hydrogen*; Springer: New York, 2008.
- (34) Khaselev, O.; Turner, J. A. *Science* **1998**, *280*, 425-427.
- (35) Alstrum-Acevedo, J. H.; Brennaman, M. K.; Meyer, T. J. *Inorg.Chem.* **2005**, *44*, 6802-6827.
- (36) Concepcion, J. J.; Jurss, J. W.; Brennaman, M. K.; Hoertz, P. G.; Patrocionio, A. O. T.; Murakami Iha, N. Y.; Templeton, J. L.; Meyer, T. J. *Accounts of Chemical Research* **2009**, *42*, 1954-1965.
- (37) Liu, F.; Concepcion, J. J.; Jurss, J. W.; Cardolaccia, T.; Templeton, J. L.; Meyer, T. J. *Inorg. Chem.* **2008**, *47*, 1727-1752.

- (38) Concepcion, J. J.; Jurss, J. W.; Norris, M. R.; Chen, Z.; Templeton, J. L.; Meyer, T. J. *Inorg.Chem.* **2010**, *49*, 1277-1279.
- (39) Jurss, J. W.; Concepcion, J. J.; Norris, M. R.; Templeton, J. L.; Meyer, T. J. *Inorg.Chem.* **2010**, *49*, 3980-3982.
- (40) Brimblecombe, R.; Koo, A.; Dismukes, C. G.; Swiegers, G. F.; Spiccia, L. *J.Am.Chem.Soc.* **2010**, *132*, 2892-2864.
- (41) Youngblood, J. W.; Anna Lee, S.-H.; Maeda, K.; Mallouk, T. E. *Accounts of Chemical Research* **2009**, *42*, 1966-1973.
- (42) Youngblood, J. M.; Seung-Hyun, A. L.; Kobayashi, Y.; Hernandez Pagan, E. A.; Hoertz, P. G.; Moore, T. A.; Moore, L. A.; Gust, D.; Mallouk, T. E. *J.Am.Chem.Soc.* **2009**, *131*, 926-927..
- (43) Kayes, B. M.; Richardson, C. E.; Lewis, N. S.; Atwater, H. A. *IEEE Photo.Spec.Conf* **2005**, 55-58.
- (44) Kayes, B. M.; Atwater, H. A.; Lewis, N. S. *J.Appl.Phys.* **2005**, *97* 114302, 1-11.
- (45) Clarke, J.; Hill, D. R.; Roberts, J. *J.Chem.Technol.Biotechnol.* **1997**, *68*, 397.
- (46) Haginoya, C.; Ishibashi, M.; Koike, K. *Appl. Phys. Lett.* **1997**, *71*, 2934.
- (47) Mor, K. G.; Shankar, K.; Paulose, M.; Varghese, O. K.; Grimes, C. A. *Nano Letters* **2005**, *5*, 191-195.
- (48) Grimes, C. A.; Mor, G. K. *TiO₂ Nanotube Arrays: Synthesis, Properties and Applications*; Springer: Dordrecht, Heidelberg, London, New York, 2009.
- (49) Varghese, O. K.; Gong, D.; Paulose, M.; Ong, K. G.; Dickey, E. C.; Grimes, C. A. *Adv.Mater.* **2003**, *15*, 624.
- (50) Macack, J. M.; Tsuchiya, H.; Schmucki, P. *Angew.Chem.Int.Ed.* **2005**, *44*, 2100-2102.
- (51) Mor, G. K.; Varghese, O. K.; Paulose, M.; Shankar, K.; Grimes, C. A. *Solar energy Materials and Solar Cells* **2006**, *90*, 2011-2075.
- (52) Paulose, M.; Shankar, K.; Yoriya, S.; Prakasam, E. H.; Varghese, O. K.; Mor, G. K.; Latempa, T. A.; Fitzgerald, A.; Grimes, C. A. *J.Phys.Chem.B. Letters* **2006**, *110*, 16179-16184

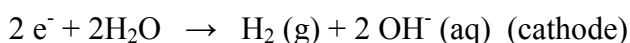
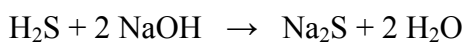
Chapter 2: Functionalization of titania photoelectrodes with Group VI semiconductors

2.1 Introduction

Group VI semiconductors, where a metal M^{n+} ($M = Cd^{2+}, Bi^{3+}, Cu^{2+}, Pb^{2+}$) is combined with S^{2-}, Se^{2-}, Te^{2-} to form an $M_2(S,Se,Te)_n$ solid may offer interesting possibilities when employed in photoelectrolytic or photoelectrosynthetic devices applied to solar hydrogen production. Although in many of these semiconductors the quasi-Fermi energy of the photogenerated hole is too low to drive an efficient water oxidation, they can be advantageously used for the photoinduced oxidation of Na_2S or of other easily oxidizable molecules or ions resulting in the concomitant production of hydrogen at the cathode of the photoelectrochemical cell[1-3].

It must be noted that H_2S and sulfides are common, abundant and harmful contaminants present in fossil fuels and in natural gas, where H_2S alone can account for up to 30 % of their total volume[4].

Thus, by exploiting solar energy and chalcogenide semiconductors, sulfides can be photoelectrochemically converted to less dangerous oxidized forms (i.e. polysulfides, S_n^{2-}) and to molecular hydrogen thanks to an energy storing cycle which can be proposed as an interesting method for the photodegradation of H_2S wastes according to the following simplified photocatalytic scheme, where CdS is chosen as an example of photoactive semiconductor:



Thus, the overall reaction is the splitting of H_2S in S (or more appropriately in S_x^{2-} , given the excess of S^{2-} in solution) and H_2 . At the end of the photoelectrolysis one also retrieves the base which has been initially used to convert H_2S into a water soluble sulfide salt, in which it is obviously easier and safer to handle.

Generally, group VI semiconductors are characterized by a relatively small band gap (from 2.4 eV for CdS to 1.4 eV for Bi₂S₃) and by intense direct transitions which allow for an efficient visible light absorption from relatively thin (few hundreds nm) layers of photoactive substrate[5]. Since in the presence of S²⁻ and at an appropriate pH, the Fermi level of these semiconductors is more negative than that of TiO₂ they can be used as photosensitizers to extend the spectral sensitivity and responsivity of TiO₂ electrodes which merely act as electron gathering mediums (Fig.2.1a). The possibility of obtaining inter-particle electron transfer has possible important implications: the deposition of group VI semiconductors onto nanocrystalline porous TiO₂ substrates (roughness coefficient 100-1000) leads to an effective light absorption from a relatively thin absorber layer (Fig. 2.1b), in which the photogenerated electron (e) and hole (h) pairs are relatively close to both the electrolytic solution containing S²⁻ (hole acceptor) and to the electron collector, with the subsequent reduction of the probability of charge recombination.

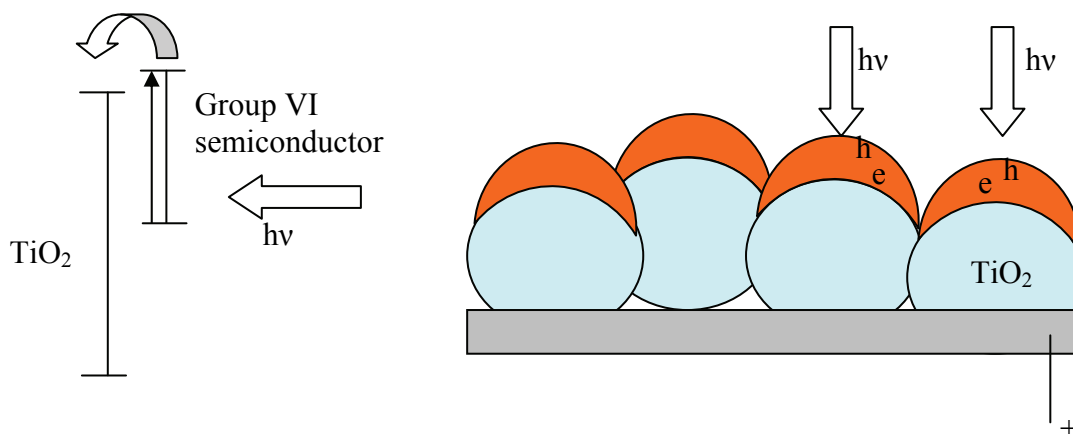


Fig. 2.1 Sensitization of TiO₂ by a visible absorbing semiconductor

Besides this effect, the coupling to TiO₂ may also have a relevant stabilizing effect against the photochemical degradation of semiconductors like CdS or CdSe. While the self oxidation of the lattice sulfides by photogenerated holes can be controlled by using a high concentration of hole scavengers, like S²⁻, the trapping of electrons, responsible for the irreversible Cd^{2+/0} reduction, can be avoided by activating the electron transfer to TiO₂. Fig. 2.2 can be taken as an illustrative example of the improvement in the photoelectrode stability obtained by coupling CdS to a TiO₂ substrate: while the fundamental CdS absorption at 500 nm is maintained in CdS/TiO₂ systems, it is lost in

pure CdS substrates after 20 minutes of intense irradiation in a sulfide containing electrolyte. The decreased reflectance at longer wavelength is indicative of the development of a grey coloration of the photoelectrode, consistent with the formation of Cd^0

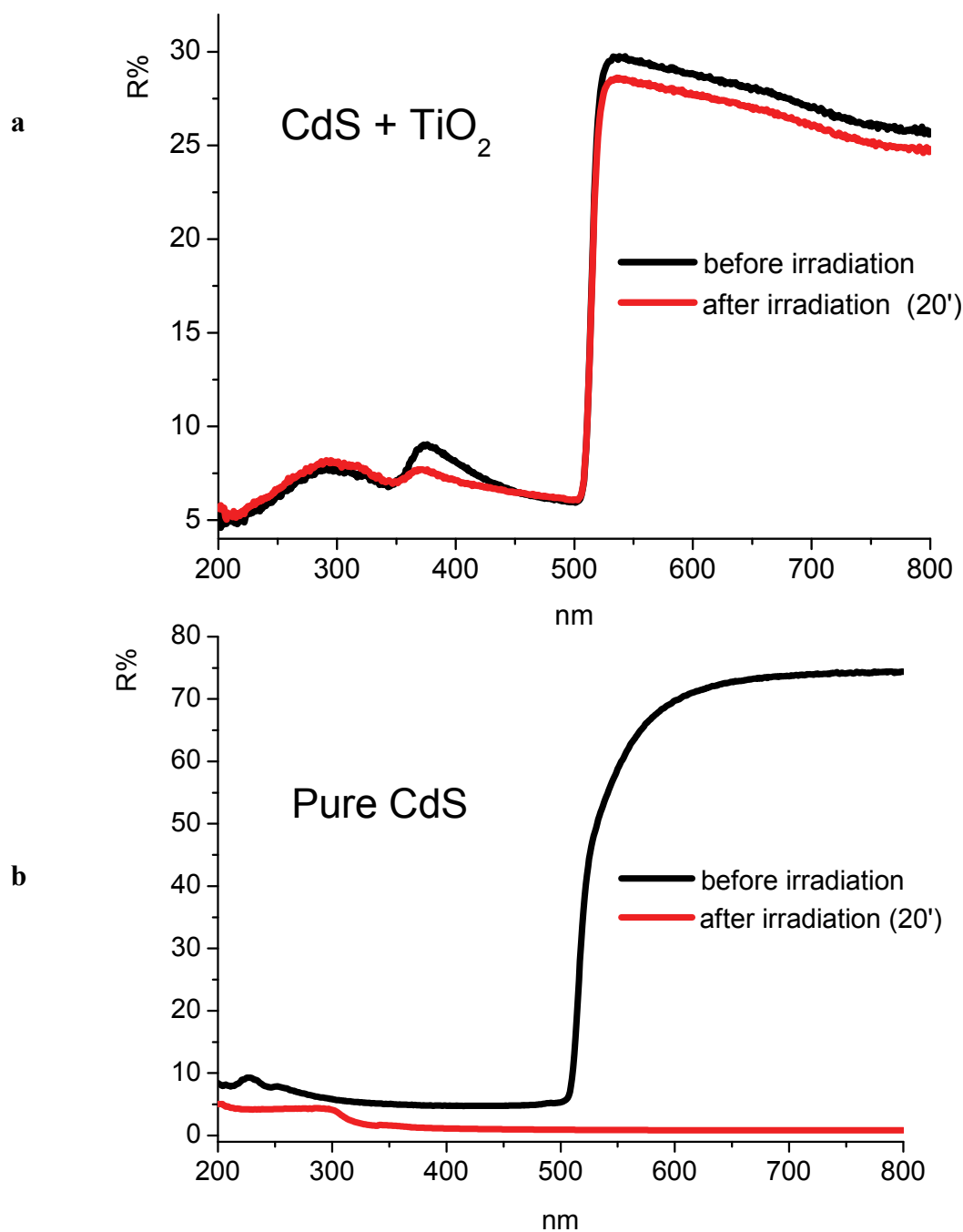


Fig 2.2 Diffuse reflectance spectra of CdS based electrodes before (black) and after (red) 20 minutes of continuous irradiation under simulated sunlight. (a) Mixed electrode: 50 % W/W nanocrystalline TiO₂ and CdS (Aldrich 99%). (b) Pure CdS 99% (Aldrich).

In a similar way, the sensitization of tubular titania structures could be equally promising, since the cylindrical geometry of the TiO_2 core may allow for the generation of the charge carriers at a short distance from the electron collector, regardless of the penetration depth of the radiation, leading to an enhancement in electron collection efficiency as it is pictorially illustrated in Fig 2.3.

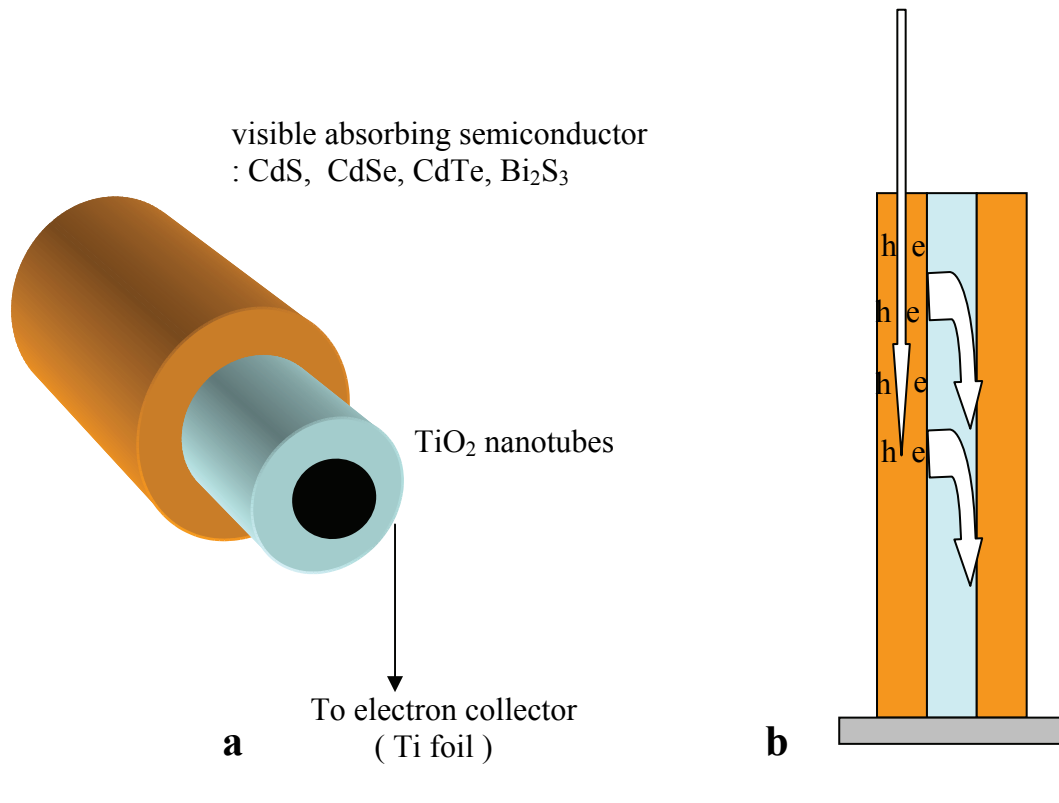


Fig.2.3 (a) TiO_2 nanotubes functionalized with group VI semiconductors; (b) generation and collection of charge carriers.

2.2 Methods of functionalization of titania substrates

Sulfur, Selenium and Tellurium have very similar chemical properties: many sulfides and selenides are insoluble compounds ($K_s(\text{CdS}) = 10^{-26}$, $K_s(\text{Bi}_2\text{S}_3) = 10^{-98}$ e $K_s(\text{CdSe}) = 10^{-33}$) hence it is possible to obtain the functionalisation of titania electrodes by a simple chemical bath deposition.

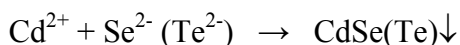
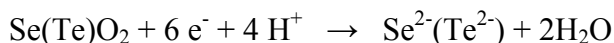
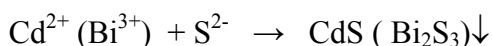
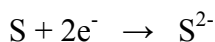
Many methods of obtaining a CdS deposition on a variety of substrates have been devised[6-8] and all of these reside in the in situ reaction of S^{2-} with Cd^{2+} , which can be obtained by alternated repeated immersion of the photoelectrodes in separate solutions containing Na_2S and $\text{Cd}(\text{NO}_3)_2$ or CdCl_2 . An analogous procedure can be adopted for depositing Bi_2S_3 , starting from $\text{Bi}(\text{NO}_3)_3$ or $\text{Bi}(\text{Ac})_3$ (Ac=acetate) solutions. A convenient and stable selenide source for CdSe deposition can be represented by sodium selenosulfite (Na_2SeSO_3) which can be obtained by reaction of elemental selenium with a 4 fold excess of Na_2SO_3 at 70-80 °C. In the presence of Cd^{2+} , SeSO_3^{2-} gives a grayish precipitate which quickly decomposes, particularly under moderate heating (ca. 50 °C) to give red-brown CdSe[9,10].

In general, a thermal treatment in air improves the performance and the stability of the photoelectrodes leading to an enhancement in crystallinity, in electrical connections between the nanostructures and to an increased hole diffusion length. In the case of CdSe a partial sublimation of the photoactive film is observed starting from 260 °C. A post treatment with CdS can be helpful for encapsulating CdSe, making it more stable at elevated temperature, improving, at the same time, the photon to electron conversion at shorter wavelengths.

Bi_2S_3 (bismuthinite, orthorhombic) electrodes thermally degrade in air at $T > 260 \text{ C}^\circ$ to form white bismuth oxide sulfate ($\text{Bi}_{28}\text{O}_{32}(\text{SO}_4)_{10}$) due to reaction with atmospheric oxygen. In nitrogen atmosphere the annealing can be carried out at 400 °C without observing decomposition. However, the best photoelectrochemical results were observed with photoelectrodes annealed in air at 220 °C for 15-20 minutes, in agreement with conditions reported by other authors in the preparation of TiO_2 (P 25) supported Bi_2S_3 nanoparticles for environmental remediation[11].

The electrochemical methods of TiO_2 surface modification by growth of lower band gap semiconductors rely on principles analogous to the chemical deposition, i.e. the

electrochemical generation of the anion (S^{2-} , Se^{2-} , Te^{2-}) in a cation (Cd^{2+} , Bi^{2+}) containing electrolyte, according to the following reactions



Compared to chemical impregnation methods, the electrodeposition may lead to more homogeneous surfaces and to a better control of the sensitizing semiconductor growth, since the anions are directly electrogenerated on the oxide surface with the desired rate.

The precursor electrolytes for CdS and Bi_2S_3 deposition are very similar, consisting in a saturated sulfur solution in DMSO to which 0.3 M or $Bi(NO_3)_3$ are added. The CdSe precursor is composed by selenium oxide solution in sulfuric acid in the presence of $Cd(NO_3)_2$ [12]. Our preferred concentrations were 10^{-2} M SeO_2 and 0.3 M $Cd(NO_3)_2$ in $4 \cdot 10^{-3}$ M H_2SO_4 .

The deposition can be performed by either potentiostatic, potentiodynamic (multiple scan) or galvanostatic procedures. In our case we have adopted a multiple scan deposition technique where the potential was linearly varied on subsequent cycles at cathodic potentials, usually between -0.3 and -1.1 V vs SCE, with a scan rate of 50 mV/s until strongly colored electrodes were obtained.

The deposition was considered complete when the maximum optical density (absorbance or, in the case of opaque substrates, spectral absorption) allowed for the absorption of at least 70% of the incident photons. A direct reliable estimate of the amount of deposited material from the integration of voltammetric waves was either difficult or impossible due to the capacitive TiO_2 contribution, to the irreversible nature of the electrochemical process and to the lack of any clearly defined diffusion limited peak.

2.3 Bi₂S₃/TiO₂ photoelectrodes

The absorption spectrum of Bi₂S₃ chemically deposited on TiO₂ nanoparticles shows a featureless continuous absorption in the whole visible region, with an estimated optical band gap of 1.4 eV (Fig. 2.4) [11,13]. Repeated (up to 40) chemical bath deposition from Bi(Ac)₃ and Na₂S leads to intensely colored electrodes with a maximum absorbance of the order of 4, allowing for an almost quantitative light absorption. Despite this, the chemical impregnation appears to be characterized by a scarce reproducibility, even by considering the same number and duration of the deposition steps, and the photoelectrochemical response in 0.1 M Na₂S is promising but also highly variable: in the presence of a 0 V vs SCE potential bias, photocurrents ranging from 7 to 4 mA/cm² (Fig. 2.5) were observed under a 0.2 W/cm² visible light irradiation (HID lamp). A modest positive polarization results however in a strong enhancement of the photocurrent, which is superimposed to the contribution of the direct electrochemical oxidation of sulfides, whose onset is located at about 0.2 V vs SCE.

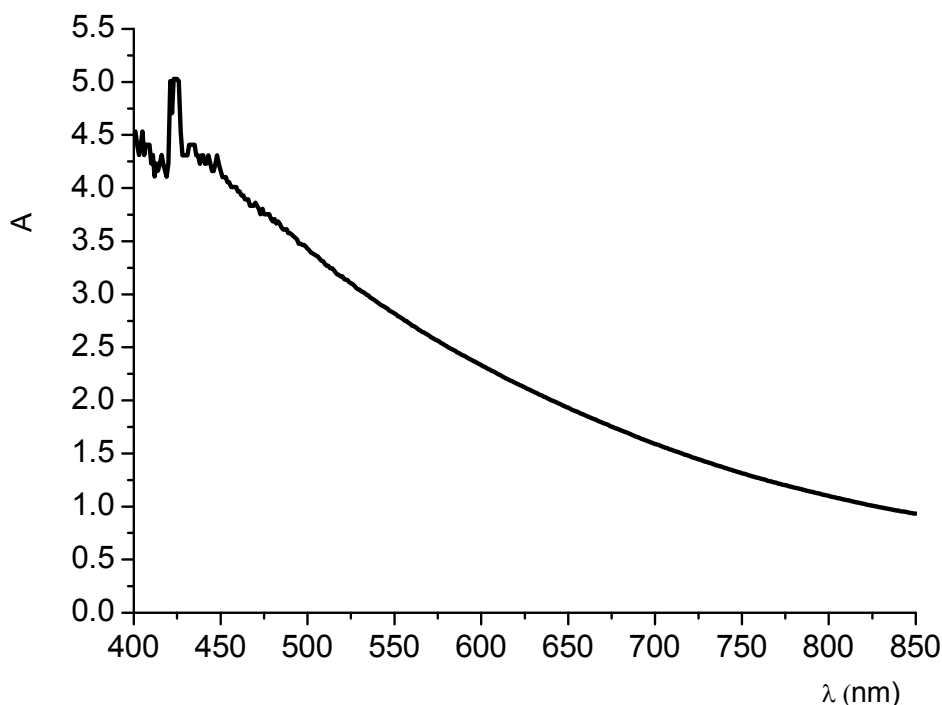


Fig.2.4 Absorption spectrum of Bi₂S₃ chemically deposited on a TiO₂ nanoparticle film.

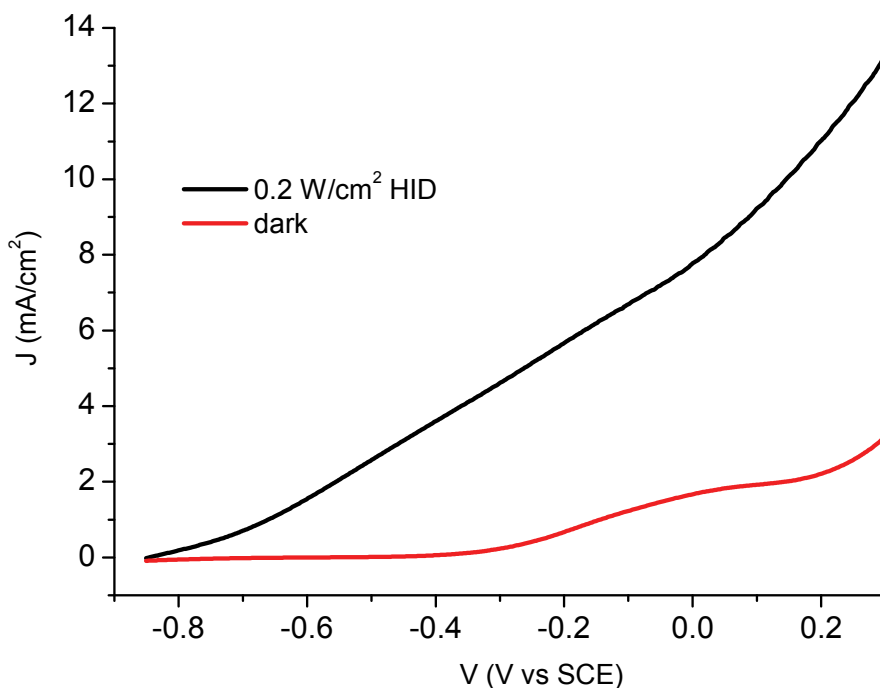


Fig. 2.5 J-V characteristics under illumination (black) (0.2 W/cm² HID lamp) and in the dark (red) of a Bi₂S₃/TiO₂ electrode in 0.1 m Na₂S.

The electrodeposition process quickly leads (2-4 potential scans) to good quality Bi₂S₃ films with a good reproducibility. Although the optical density is lower than that obtained by chemical impregnation (Fig. 2.6), the Light Harvesting Efficiency (LHE) of the photoelectrodes varies between 95% and 50 % in the spectral region between 400 and 850 nm, with a sharp rise below 400 nm due to TiO₂ absorption. The maximum photocurrent at 0 mV vs SCE is in the order of 5 ± 1 mA/cm² in the presence of an incident irradiance of 0.12 W/cm² (AM 1.5G). The advantage of having a panchromatic absorber is clearly evident from Fig. 2.7, where the UV component has been completely removed from the excitation light with a 420 nm cut-off filter. Under these conditions the photoelectrode does not undergo a substantial decrease in its performance, still reaching values of more than 3 mA/cm² at 0 V vs SCE, showing that Bi₂S₃ is effectively injecting into the conduction band of TiO₂.

Interestingly, despite the good performances, the J-V curves recorded under shuttered illumination show a notable difference between front (electrolyte) side and backside (FTO contact) illumination evidencing a more effective photocurrent generation by

backside illumination (Fig. 2.8). The effect is even more dramatic in thick electrodes, where the transients in front irradiation are about half of those recorded in backside mode, corroborating the indication of limitations arising from charge transport and collection. Although the J-V curves do not show dark cathodic features, usually originated from charge recombination mediated by surface states, the existence of a certain amount of electron recombination is also clearly suggested by the non ideally rectangular shape of the transients.

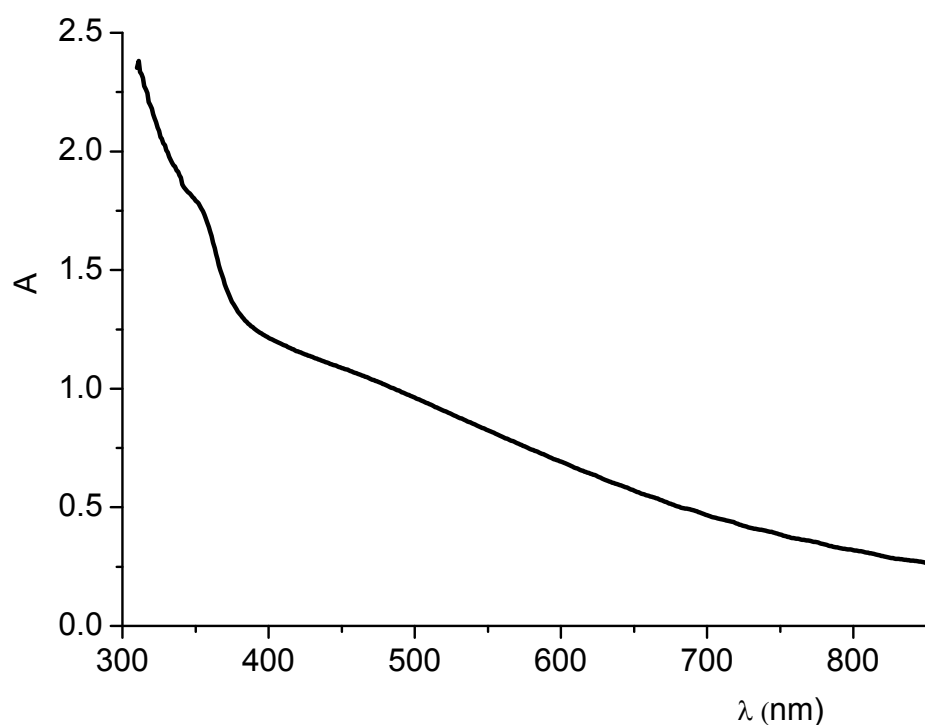


Fig. 2.6 Typical absorption spectrum of electrodeposited Bi₂S₃ on a nanocrystalline titania electrode.

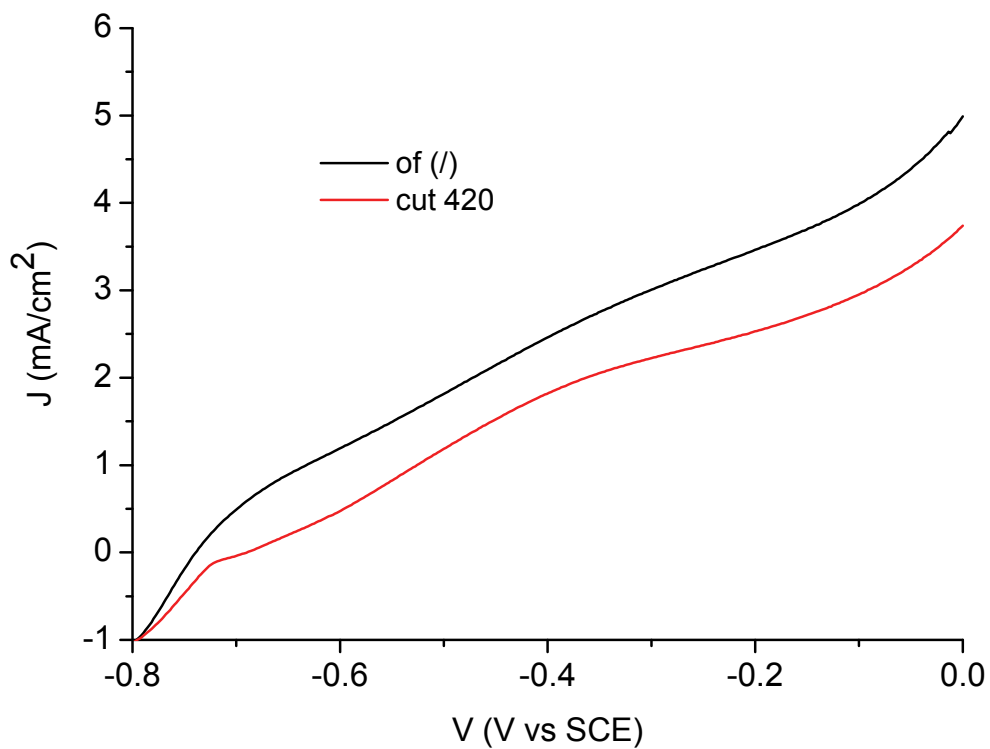
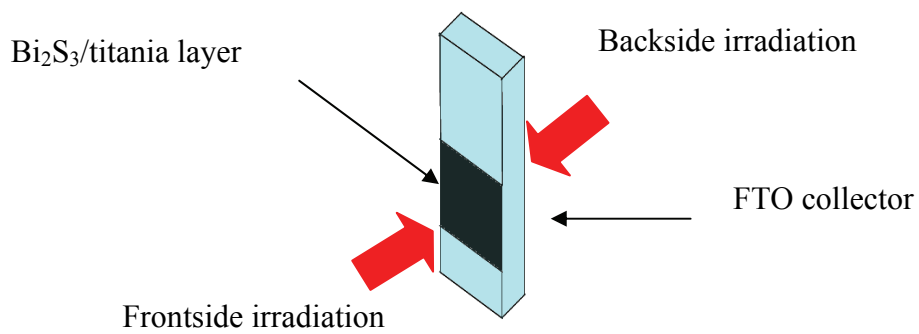


Fig. 2.7 JV curves of electrodeposited Bi_2S_3 with (red) and without (black) 420 nm cut off filter. 0.1 M Na_2 .



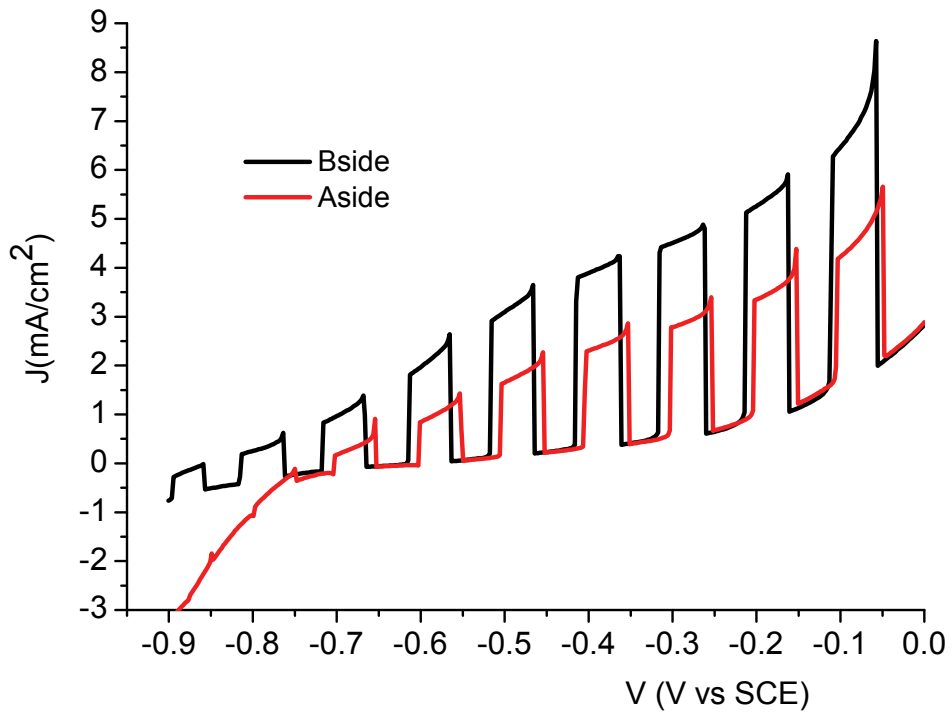
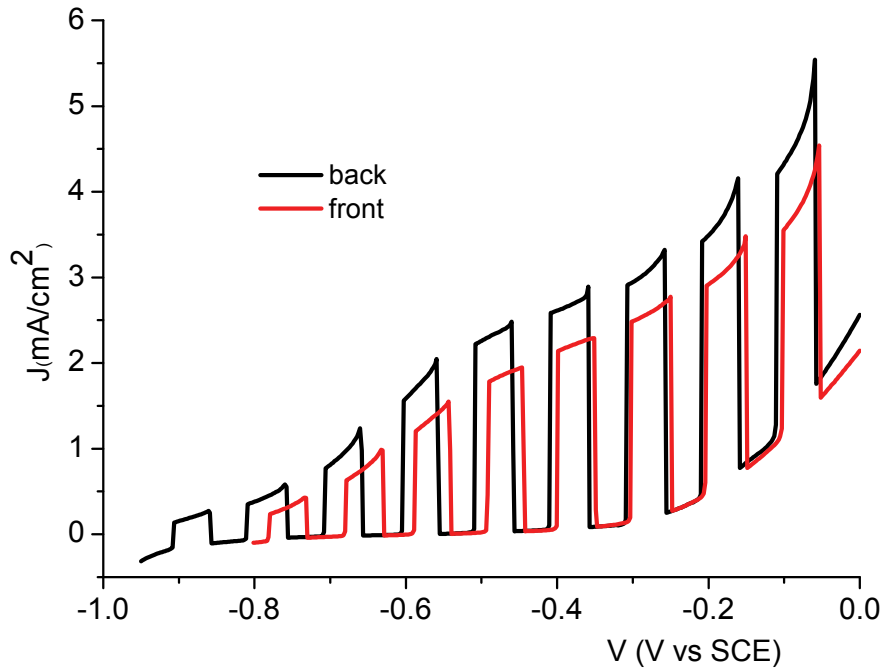


Fig. 2.8 Shuttered J-V curves of $\text{Bi}_2\text{S}_3/\text{TiO}_2$ systems in 0.1 M Na_2S under Am 1.5 G illumination. (a) thinner layer (20 deposition scans from 10^{-3} Bi^{3+} solution), (b) thicker Bi_2S_3 layer (100 deposition scans from 10^{-3} Bi^{3+} solution).

The IPCE under a potential bias of -0.5 V vs SCE is relevant when the photoelectrode is illuminated through the FTO (collector) side (backside) reaching values in the order of 30-10 % in the 350-450 nm region and extending to 830 nm (Fig.2.9). Although the UV contribution of TiO₂ cannot be completely neglected, the sharp decrease in IPCE is in contrast with the absorption spectrum of Bi₂S₃, which decline smoothly and maintains high LHE values by moving from shorter to longer wavelengths, suggesting that high energy photons with a smaller penetration depth, being absorbed in closer proximity of the back contact are more effectively converted in electrons flowing through the external circuit. By contrast, illumination to the front side leads to an almost negligible photon to current conversion, indicating that only a small fraction of electron/hole pairs generated in the outer Bi₂S₃ layer is effectively capable to escape from recombination. Actually, the difference between the photocurrent measured in front and back illumination mode under full AM 1.5 (~ 100 mW/cm²) is smaller than what could be anticipated by observing the photoaction spectra recorded under a low intensity (~ 1 mW/cm²) monochromatic light. The reason is most probably related to the fact that, due to the low excitation intensity, nearly all of the monochromatic photons in the incident beam are absorbed by the most external layers of the black absorber, where the charge collection is poor, and by a lower conductivity of Bi₂S₃ itself, which, under a sufficiently high light intensity exhibits a photoconductor behavior object of recent investigations in the field of sensor devices[14,15].

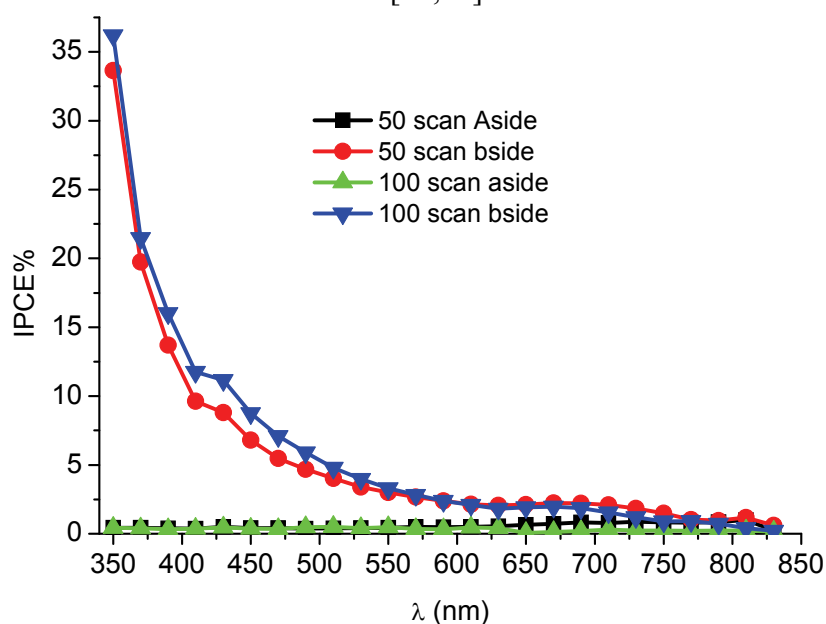


Fig. 2.9 IPCE spectra of Bi₂S₃/TiO₂ system biased at -0.5 V vs SCE. The negative bias is chosen from minimizing the dark background from electrochemical oxidation of sulfides.

In order to improve charge collection, the electrodeposition of Bi_2S_3 on titania nanotubes can be successfully performed, as demonstrated by the SEM images of the top Bi_2S_3 /nanotube structure (Fig.2.10). The multiple scan deposition at 10 mV/s from a diluted (10^{-3} M Bi^{3+}) precursor electrolyte in DMSO leads to a quite homogeneous decoration of tubular nanostructures with Bi_2S_3 , clearly evidenced by a considerable thickening of the nanotube walls, reaching a size of about 50 nm, resulting, in many cases, in the complete occlusion of the nanotube mouth. The presence of some spherical agglomerates of Bi_2S_3 with a diameter variable between 200 nm and 1 micron is also evident.

The photoaction spectra of the Bi_2S_3 /nanotubes photoelectrodes (Fig. 2.11) have distinct characteristics when compared with those found for Bi_2S_3 /nanoparticle systems: although the absolute IPCE are in the same order of magnitude, with values of 10-15% under -0.5 V vs SCE potential bias, a substantially constant photoconversion in the whole visible region is observed, as would be reasonably expected for a black absorber in which the light harvesting efficiency approaches unity. In other words, while in the planar $\text{Bi}_2\text{S}_3/\text{TiO}_2$ electrodes the light collection efficiency drops dramatically, depending on the photon penetration depth and ultimately on the distance from the collector at which electron/hole pairs are generated, in Bi_2S_3 /nanotubes the electrons are collected with analogous efficiency in both the blue and red part of the spectrum. This is consistent with the coated nanotube geometry, where, without respect to the penetration depth of the visible radiations, the charge carriers diffuse or migrate orthogonally to the tube axis[16], traversing in all cases nearly the same thickness of Bi_2S_3 before reaching the charge collector.

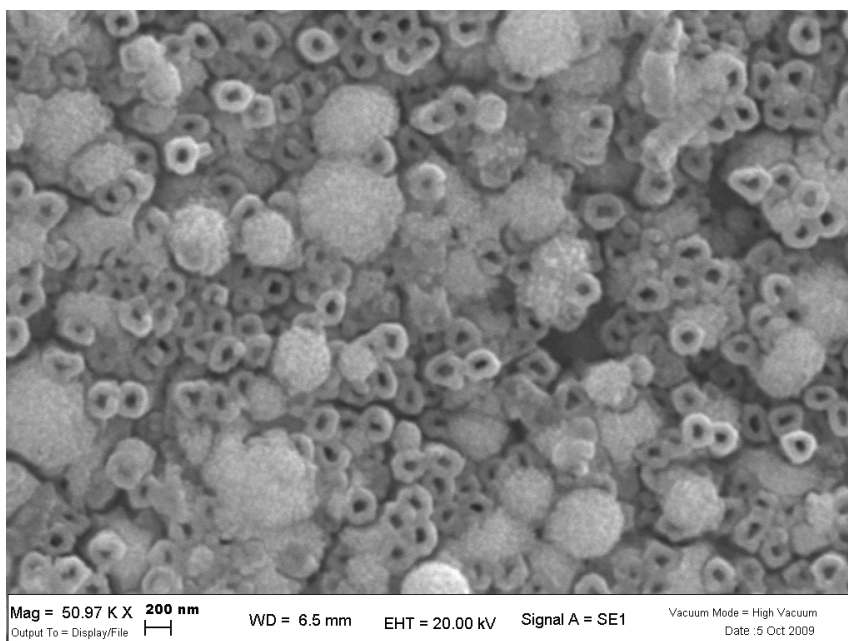


Fig. 2.10 Bi₂S₃/titania nanotubes surface obtained by multiple scan (45, 10 mV/s) electrodeposition of Bi₂S₃ from 10⁻³ M Bi³⁺ electrolytes. Sample annealed in air at 220 °C for 30’.

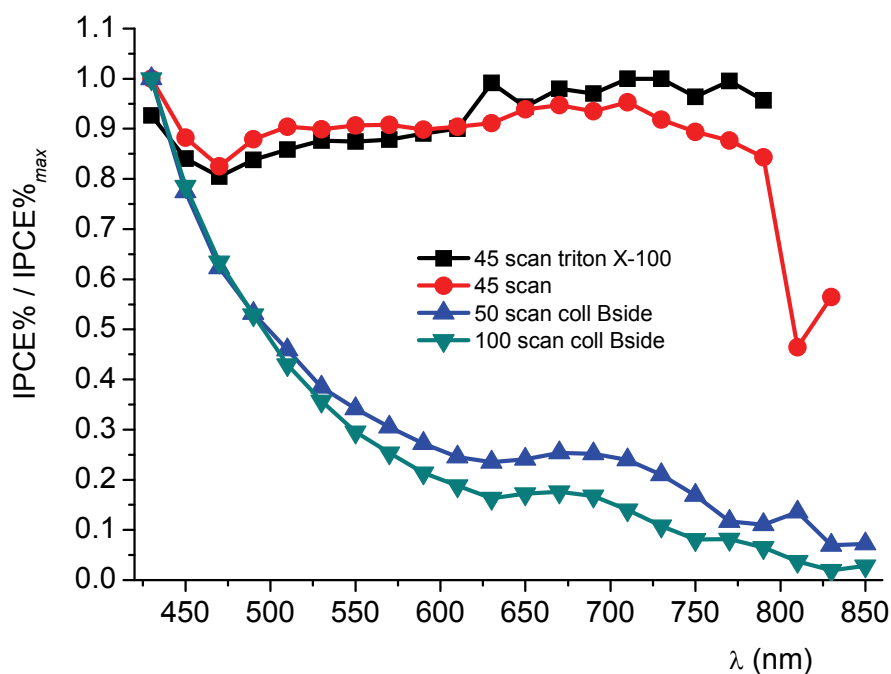
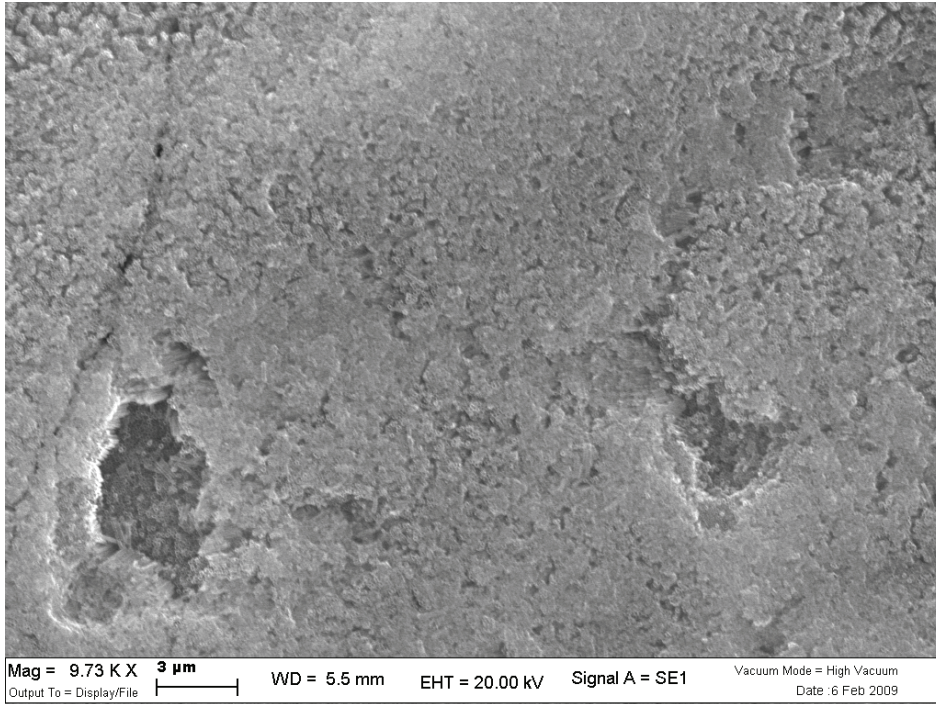


Fig. 2.11 Normalized photoaction spectra: Bi₂S₃/titania nanotubes (black and red) compared to Bi₂S₃/TiO₂ nanoparticle substrates (blue and green).

2.4 CdS and CdSe/TiO₂ photoelectrodes

The chemical bath deposition of CdS on titania nanotubes leads to photoelectrodes characterized by a satisfactory photoelectrochemical properties. SEM micrographs taken at 9700 X and at 51370 X indicate that after the annealing at 400 °C chemically deposited CdS forms a nanocrystalline network which covers and conglomerates the anatase nanotubes which have a mouth diameter of about 100 nm (Fig. 2.12). Single CdS nanostructures cannot be resolved in SEM mode, however, higher resolution transmission microscopy (HRTEM) studies carried out by Sun et. al. have confirmed that the initially formed CdS network consists of quantum dots whose size varies between 2 and 10 nm[17]. By contrast, the electrodeposition of CdS produces a much more homogeneous coating, which is actually difficult to detect in SEM imaging, simply resulting in a thickening of nanotube walls (Fig. 2.12c). Nevertheless, the diffuse reflectance spectrum (Fig. 2.12d) confirms without any doubt the presence of CdS, showing the typical steep and intense transition with onset located at about 600 nm, leading to a significant extension of the spectral sensitivity of the photoanode, with an effective absorption (75%-80%) of the photons in the 300-600 nm range.

a



b

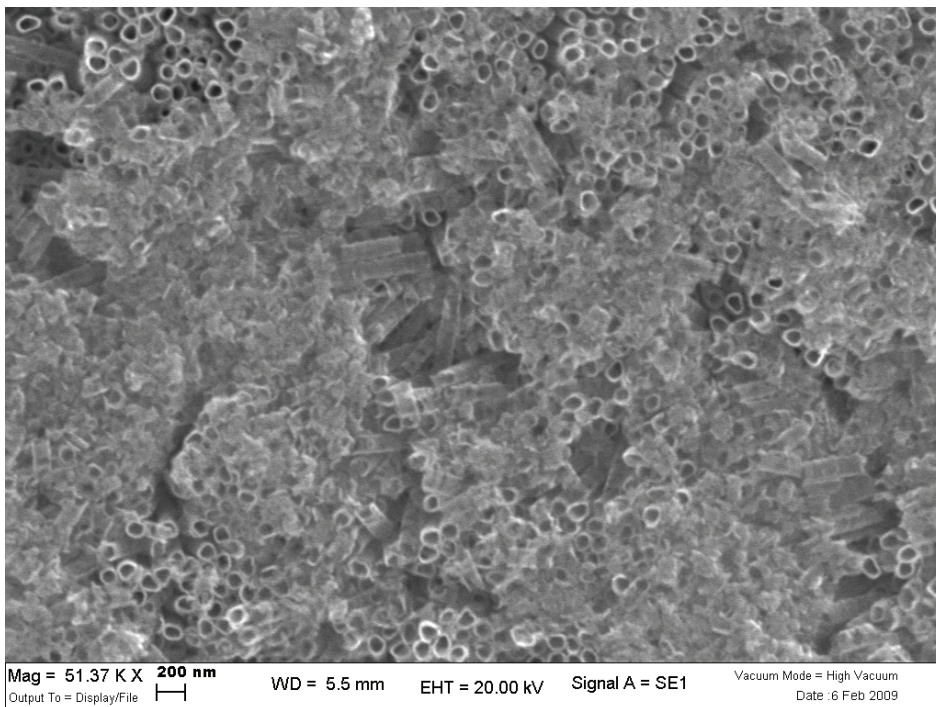
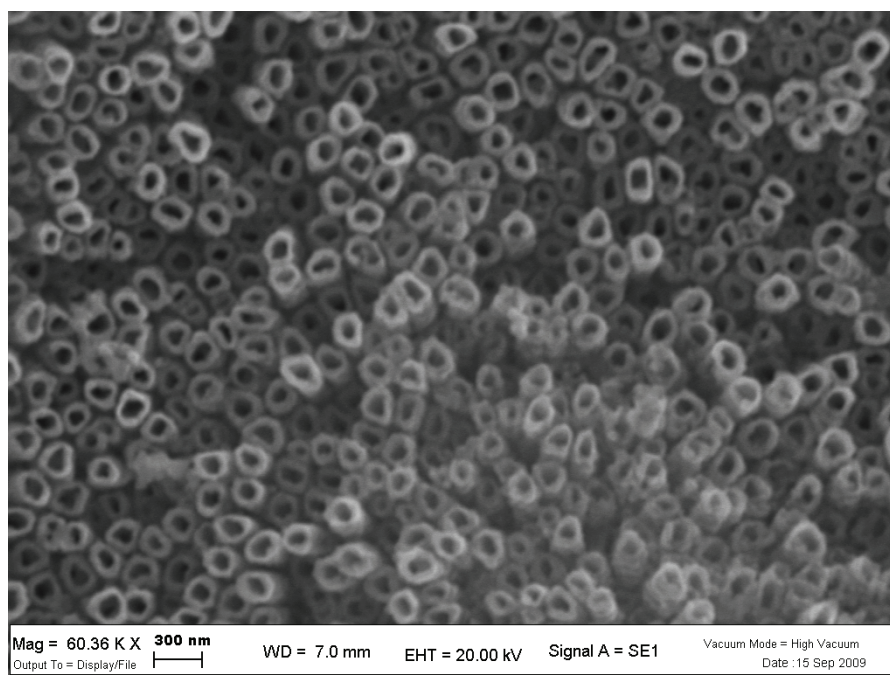


Fig. 2.12 CdS modified nanotubes by (a) and (b) chemical bath deposition and (c) electrodeposition. (d) Diffuse reflectance spectrum of the electrodeposited CdS/titania nanotubes (nt) surface compared to the unmodified titania NT surface. Titania NT were obtained from DMSO/HF anodization procedures.

c



d

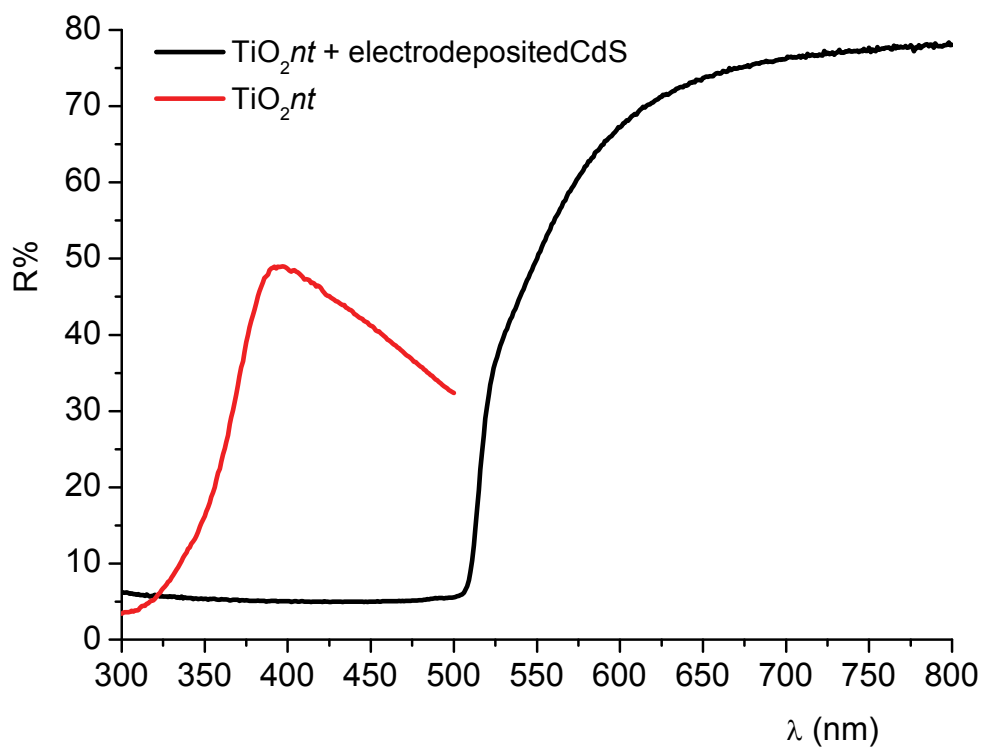


Fig. 2.12 CdS modified nanotubes by (a) and (b) chemical bath deposition and (c) electrodeposition. (d) Diffuse reflectance spectrum of the electrodeposited CdS/titania nanotubes (nt) surface compared to the unmodified titania NT surface. Titania NT were obtained from DMSO/HF anodization procedures.

The photoaction spectrum of the CdS sensitized nanotubes recorded in 0.1 M Na₂S at 0 V vs SCE shows a good conversion, approaching 50 % at 500 nm, in good agreement with the absorption spectrum of CdS, testifying an effective charge injection into TiO₂ (Fig. 2.13). The good performance is confirmed under Am 1.5 irradiation, where photocurrents of the order of 6-9 mA/cm² are recorded in 0.1 M Na₂S (Fig. 2.13). The electrodeposited CdS substrates generate higher currents (ca. 20% higher with respect to chemically deposited substrates), but display a lower fill factor. In both cases the open circuit photovoltage is ≥ 1 V vs SCE. In the presence of a formate buffer as a sacrificial donor the photocurrents are more than doubled, reaching 16-18 mA/cm² due both to a more effective hole scavenging which can be originated by HCOOH/HCOO⁻ adsorption onto the CdS/TiO₂ surface, and by secondary electron injection by highly reducing HCOO⁻ intermediates which are known to inject into the conduction band of TiO₂.

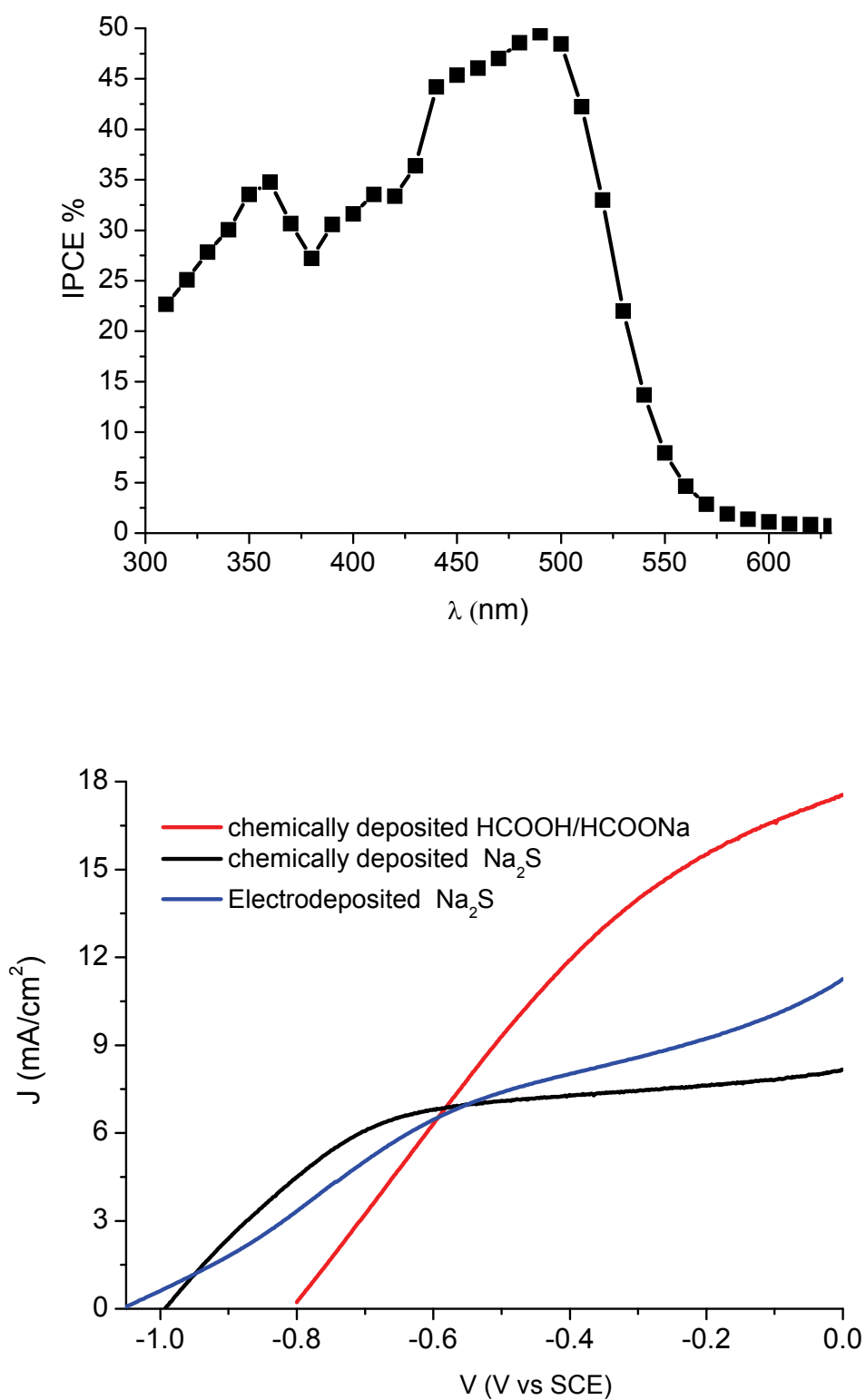
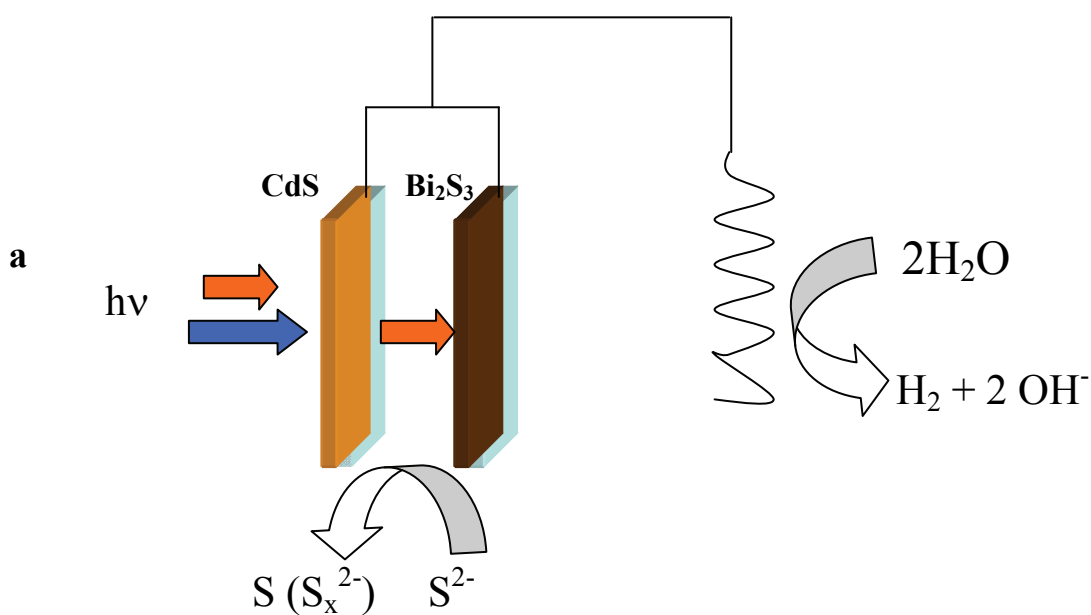


Fig. 2.13 (a) Photoaction spectrum of chemically impregnated CdS/TiO₂ nanotubes at 0 V vs SCE (b) J-V curves under Am 1.5 illumination (0.12 W/cm²) in the presence of Na₂S (black chemically deposited, blue electrochemically deposited CdS) and in 1 M 1/1 formate buffer (red).

Although in this case the sensitization of nanotubes with CdS produces good performances, comparable photocurrent densities ($J \sim 6 \pm 1 \text{ mA/cm}^2$) can be found through the sensitization via electrochemical deposition of more conventional transparent nanocrystalline electrodes made of sintered titania nanoparticles. The use of transparent CdS based electrodes has the advantage of allowing for the assembly of tandem configurations, in which two spectrally complementary photoelectrodes can be in parallel connected to sum the photocurrents (Fig. 2.14a). For example, a tandem photoanode made by a CdS/TiO₂ and by Bi₂S₃/TiO₂ heterointerfaces biased at 0 V vs SCE can generate photocurrents in the order of 12-14 mA/cm² in 0.1 M Na₂S (Fig. 2.14b) thanks to the simultaneous exploitation of the high photon to current conversion of CdS in the blue part of the spectrum (300-550 nm) and of the extended spectral sensitivity of Bi₂S₃, which is able to capture and convert photons where CdS does not absorb, starting from 830 nm.



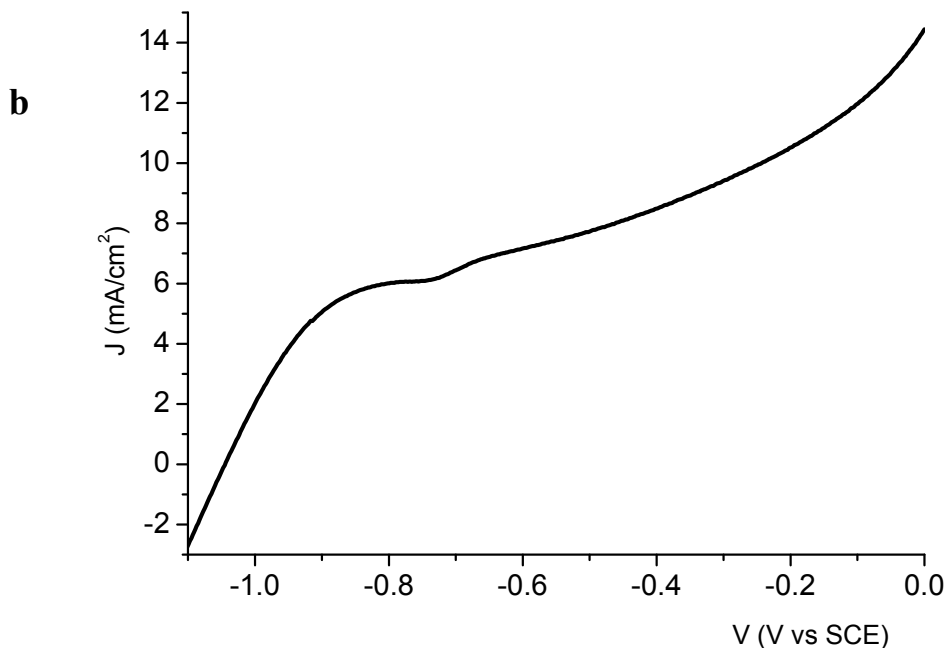
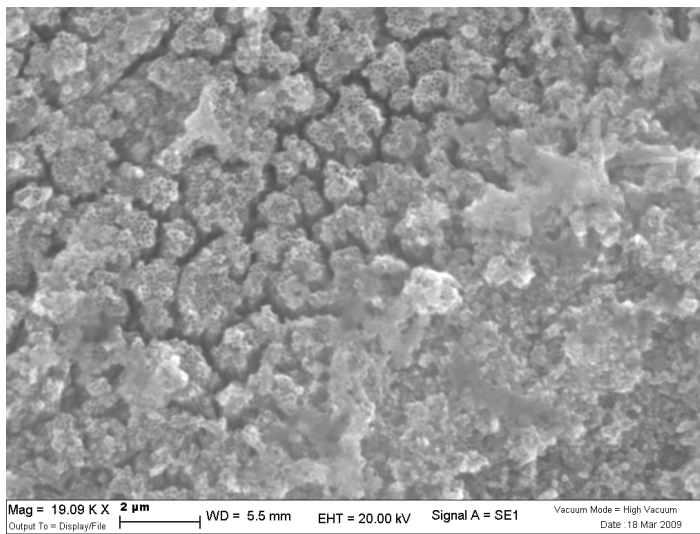


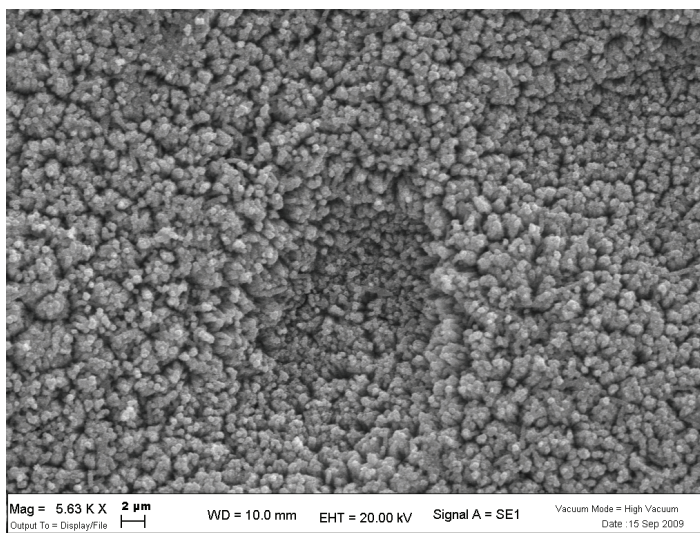
Fig. 2.14 (a) Scheme of a tandem photoelectrochemical cell based on CdS/TiO₂ and Bi₂S₃/TiO₂ heterointerfaces; (b) resulting J-V characteristic.

A panchromatic sensitization as well as a considerable efficiency in photon to electron conversion can be obtained by functionalizing titania nanostructures (nanotubes as well as nanoparticles) with CdSe. In this case both chemical and electrochemical deposition leads to morphologically similar surfaces where CdSe can be observed to decorate each nanotube. As previously observed, the electrodeposition is the preferred method for obtaining a more homogeneous coating of each nanostructure, where CdSe covers almost completely the entire length of every nanotube, occluding also their mouth (Fig. 2.15).

a



b



c

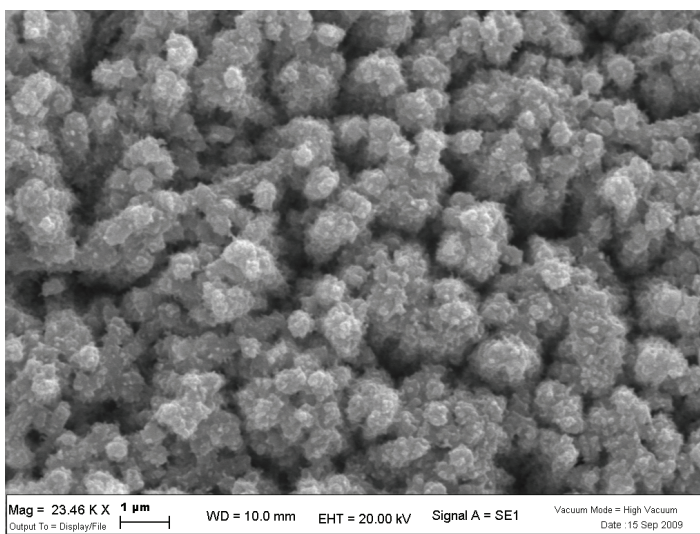


Fig. 2.15 SEM micrographs of (a) CdSe/titania nanotube heterostructures obtained by chemical bath deposition ~ 19000 X; (b) CdSe functionalized nanotubes from electrochemical deposition at 5630 X; (c) higher magnification (23460 X) of (b).

Although a relevant loss of photoactive CdSe coating occurs by sublimation during the 400 C° annealing stage in air or under inert atmosphere (N₂), the thermal treatment was found to be beneficial for both performance and stability of the photoelectrode. The optical band gap evaluated from the absorption spectrum (Fig. 2.16a) was found to be 1.65 eV, in good agreement with the literature reported values[18,19]. The IPCE extends from 310 to 750 nm keeping an almost constant plateau value which, with the annealed samples can reach 40 % (Fig.2.16b). The red shift in IPCE onset between untreated and annealed substrates is in agreement with the absorption spectra, where upon 400 C° treatment, a bathochromic shift of the absorption threshold to about 750 nm can be observed. The increased IPCE indicate an efficient charge carrier transfer and a suitable band alignment at the CdSe/TiO₂ interface. This features have been observed by other authors in CdSe/ZnO heterointerfaces[20], and have been explained by the loss of quantum confinement in CdSe nanoparticles which, due to the thermal formation of larger crystals, might facilitate the charge transport through the CdSe coating to the inner nanotube collector. Besides thermal sintering of the CdSe nanocrystals, other authors have attributed the increased reproducibility and durability of the photoelectrochemical response in cadmium chalcogenide based PEC cells to the transition from cubic zinc blende to wurtzite structures, which becomes the dominating phase at temperatures > 350 C° [21].

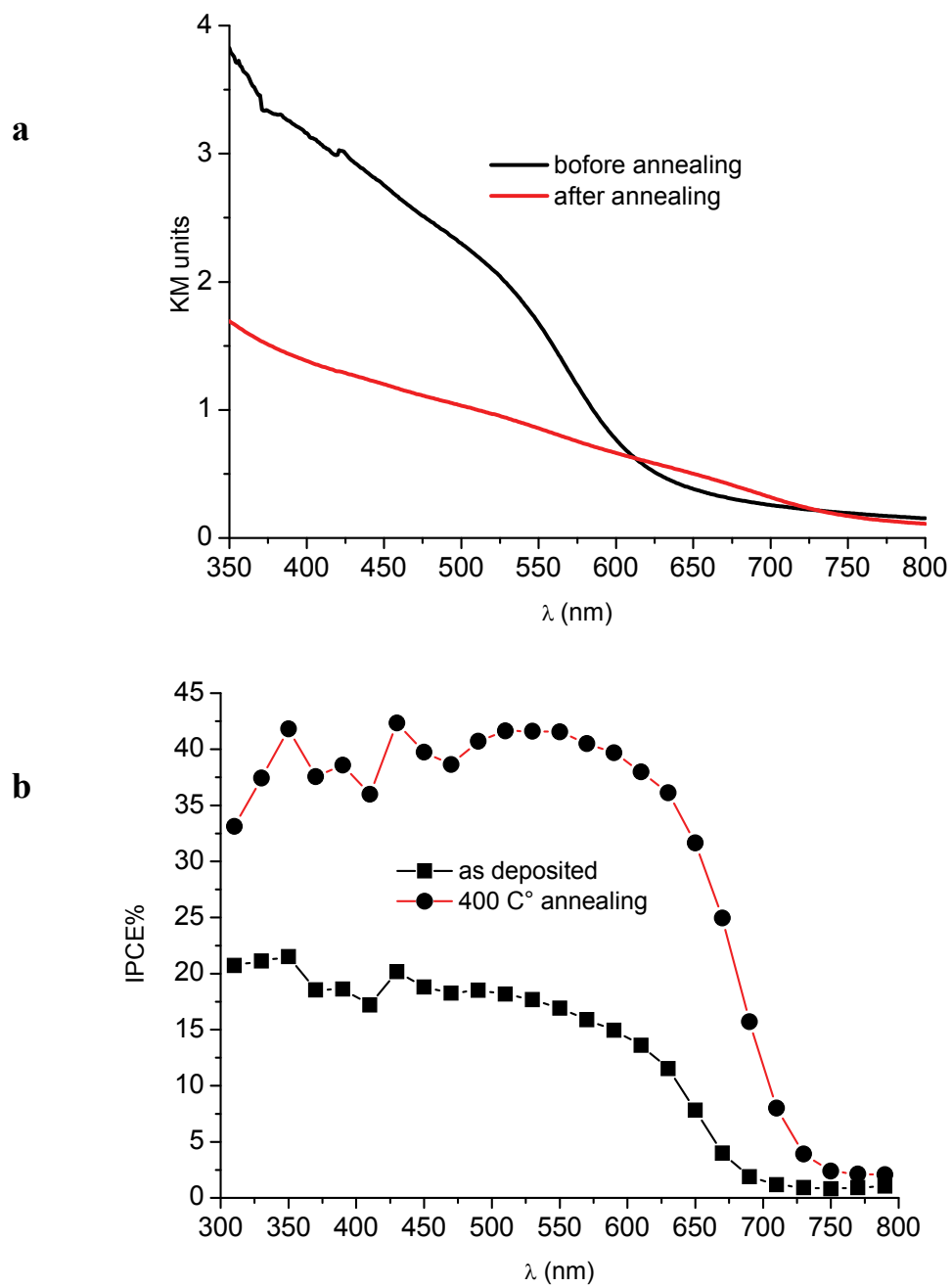


Fig. 2.16 (a) Diffuse reflectance spectra (KM units) of chemically deposited CdSe on titania nanotubes; **(b)** IPCE spectra. 0.1 M Na₂S, 0 V vs SCE.

The performances under white light are satisfactory for both chemically and electrochemically deposited CdSe substrates, showing photocurrents in the 10-11 mA/cm² range at 0 V vs SCE and a Voc > 1 V (Fig. 2.17).

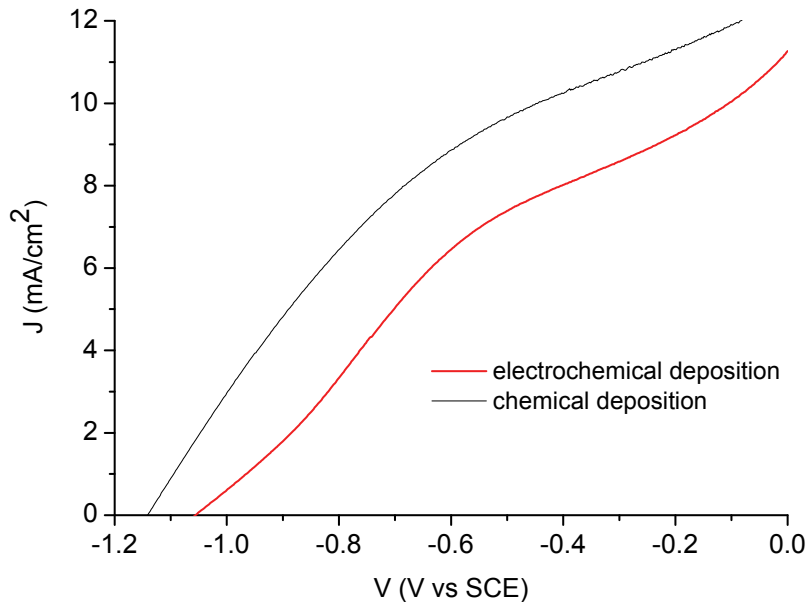


Fig. 2.17 JV curve under AM1.5G illumination (0.12W/cm²) of CdSe/TiO₂ NT photoanodes in 0.1 M Na₂S.

Sensitization by sequential electrodeposition of CdSe and CdS can be achieved with both colloidal (TiO₂ nanoparticles) and nanotube surfaces, however, as previously observed with Bi₂S₃/TiO₂ heterointerfaces, the comparison with the IPCE spectrum recorded for colloidal substrates in back (FTO collector) side illumination is consistent with a more favorable electron collection in nanotubular substrates, causing a broader photon to electron conversion and a significant IPCE maximum in the red part of the spectrum (650-700nm) clearly absent in colloidal electrodes, which, on the opposite, show a rather steep decrease in IPCE by moving from shorter to longer wavelengths (Fig. 2.18). Thus, also in this case, limitations arising from the relatively short hole diffusion length (~ 1µm in air annealed samples) [22] in CdSe may be overcome by exploiting the geometry of nanotube arrays.

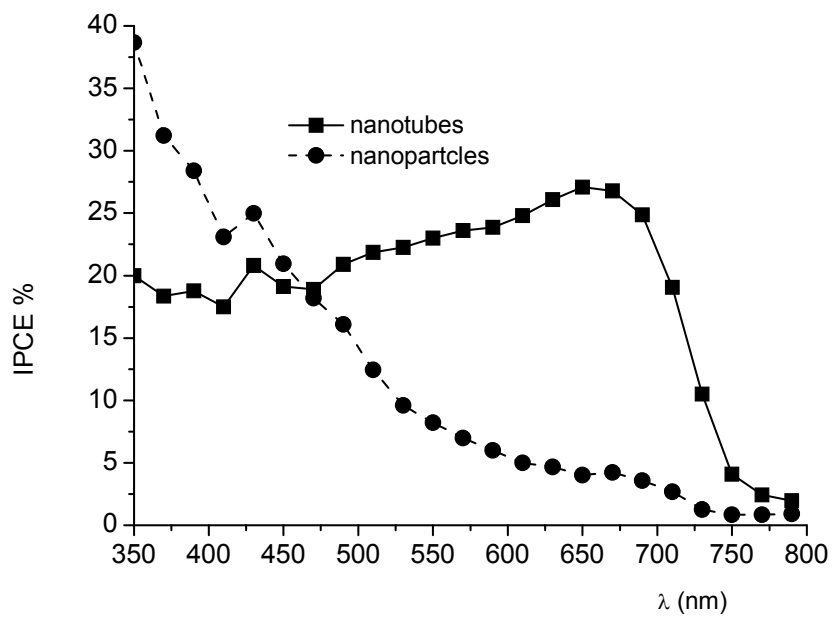


Figure 2.18 IPCE spectra in mixed CdS/CdSe/TiO₂ interfaces: nanotubes (squares) compared to nanoparticles (circles). 0V vs SCE, 0.1 M Na₂S.

2.5 CdTe

The interest in CdTe arises from its ideal band gap for solar photoconversion (1.5 eV) which, coupled to nanotube arrays, thanks to an improved charge separation and collection and to a large junction area, may lead to interesting advancements in the light to electricity (and ultimately to hydrogen) conversion. It has as already been shown that in many cases, being diffusionally favoured, the electrodeposition of cadmium chalcogenides results in the clogging of the pores before attaining a complete coverage of the internal surface of the tube with the photoactive material, thus limiting the active area which would be otherwise available for the photoelectrochemical reactions. For this reason Grimes and co-workers devised a deposition method[23] which, in principle, can be generally applied every time that a certain selectivity in the deposition of a given material has to be attained on conductive porous substrates.

Essentially, the new approach (Fig. 2.19) consists in the dipping of the nanotube electrodes in the precursor electrolytes (0.1 M CdSO₄ and 0.1 mM TeO₂ in diluted sulfuric acid at pH 1.4), where the capillary forces draw the electrolyte inside the pores. The electrode is then transferred in an inert supporting electrolyte where the electrodeposition is carried out at constant cathodic potential (-0.4 V) The procedure can be repeated until a desired amount of CdTe is deposited into the pores (Fig.2.20).

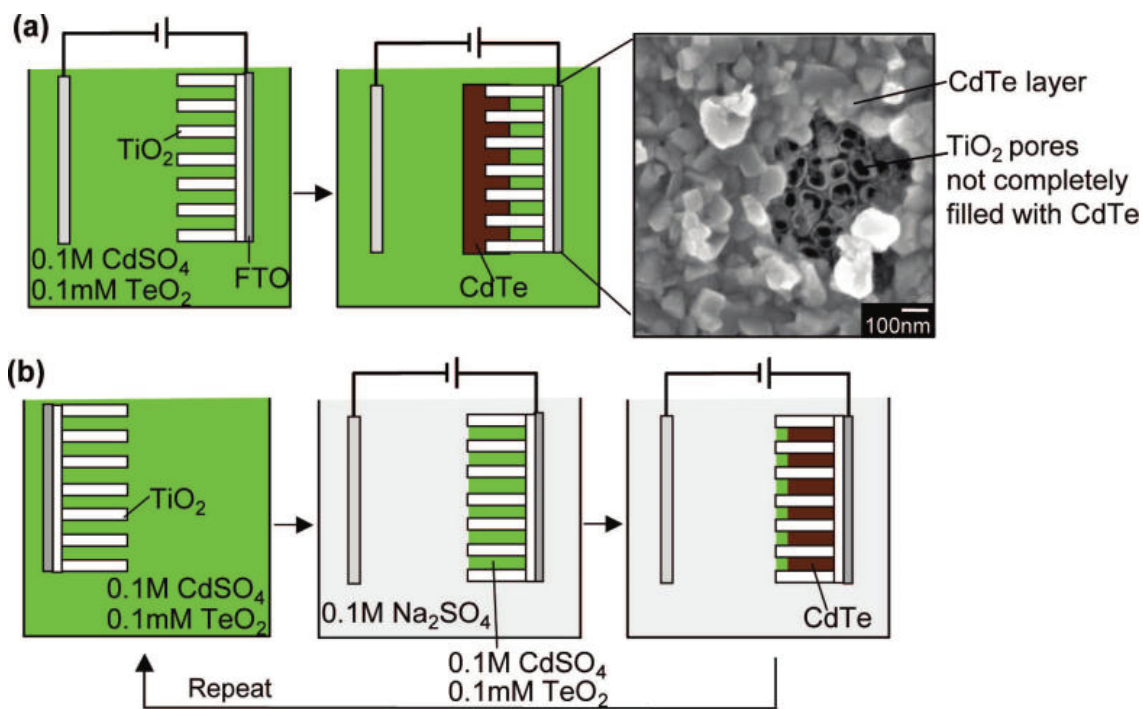


Fig. 2.19 Schematic procedure of nanotube functionalization with CdTe: (a) conventional approach; (b) dipping and deposition approach. From Chem.Mater., 2008, 20 5266-5273.

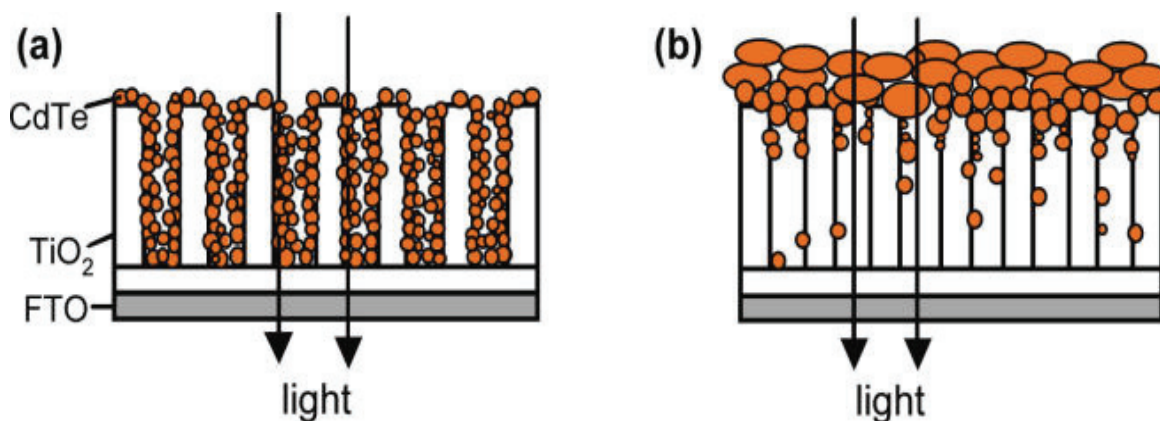


Figure 2.20 Schematic comparison of CdTe/TiO₂ heterojunctions created by dipping and deposition (a) and conventional electrodeposition (b).

The successful formation of a CdTe/TiO₂ nanotube heterojunction is testified by its n-type behavior, suggesting that electrons are more effectively transferred to the TiO₂ than to the electrolyte. The stability and the magnitude of the photoanodic current generated by the interfaces built with the newly modified procedure undergoes a general improvement, reaching 0.44 mA/cm² and nearly doubling the photoresponse of the conventional interfaces (Fig. 2.21).

Given that both (a) and (b) interfaces in Fig. 3.30 display a similar light absorption capability, the observed improvement is attributed to a reduced electron-hole recombination resulting from a thinner CdTe layer with a more even and more intimate contact with titania nanotube. For the same reason the improvement in photostability would result from the minimization of the self photooxidation of CdTe ($\text{CdTe} + 2\text{OH}^- + 2\text{h}^+ \rightarrow \text{HCdO}_2^- + \text{H}^+ + \text{Te}$) which would follow from a more effective hole transfer to the electrolyte, as a result of the enhanced electrolyte/CdTe/TiO₂ junction areas.

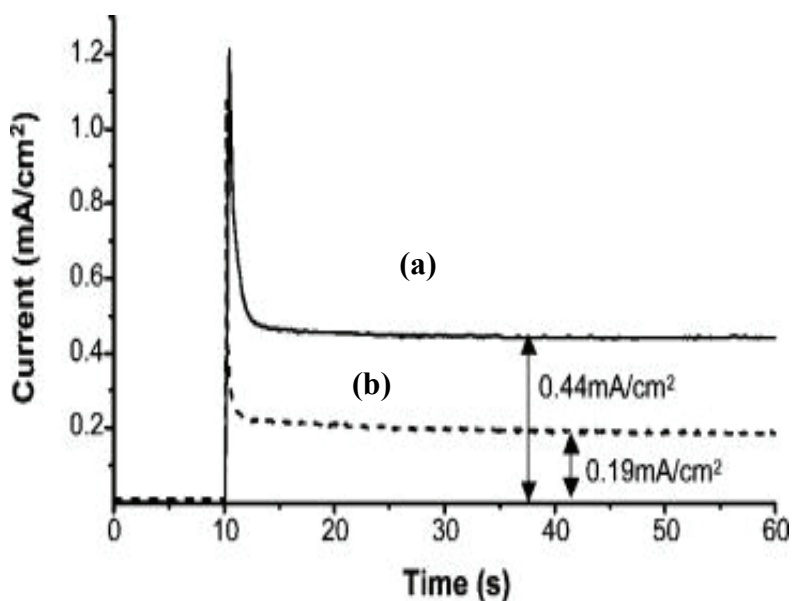


Fig. 2.21 Photocurrent transients in 0.6 M Na₂S under short circuit conditions and visible light illumination: (a) dipping/deposition (20 cycles); (b) regular deposition (30 minutes at -0.4 V vs Ag/AgCl).

2.6 Bibliography

- (1) Kamat, P. V. *J.Phys.Chem.C* **2007**, *111*, 2834-2860.
- (2) Robel, I.; Subramanian, V.; Kuno, M.; Kamat, P. V. *J.Am.Chem.Soc.* **2006**, *128*, 2385-2393.
- (3) Gopidas, K. R.; Bohorquez, M.; Kamat, P. V. *J.Phys.Chem.* **1990**, *94*, 6435-6440.
- (4) Bessekhud, Y.; Mohammedi, M.; Trari, M. *Solar Energy Materials & Solar Cells* **2002**, *73*, 339-350.
- (5) Ortuno-Lopez, M. B.; Sotelo-Lerma, M.; Mendoza-Galvan, A.; Ramirez-Bon, R. *Vacuum* **2004**, *76*, 181-184.
- (6) Blackburn, J. L.; Selmarten, D. C.; Nozik, A. J. *J.Phys.Chem. B* **2003**, *107*, 14154-14157.
- (7) Boyle, D. S.; O'Brien, P.; Otway, D. J.; Robbe, O. *J. Mater. Chem.* **1999**, *9*, 725-729.
- (8) Baranski, A. S.; Fawcett, W. R.; McDonald, A. C.; De Nobriga, R. M.; MacDonald, A. C. *J. Electrochem. Soc.: Electrochemical Science and Technology* **1981**, *128*, 963-968.
- (9) Raevskaya, A. E.; Stroyuk, A. L.; Kuchmiy, S. Y. *Journal of Colloid and Interface Science* **2006**, *302*, 133-141.
- (10) Cocivera, M.; Darkowski, A.; Love, B. *J. Electrochem. Soc.* **1984**, *131*, 2514-2517.
- (11) Bessekhud, Y.; Robert, D.; Weber, J. V. *J.Photochem.Photobiol. A: Chemistry* **2004**, *163*, 569-580.
- (12) Liu, D.; Kamat, P. V. *J.Phys.Chem.* **1993**, *97*, 10769-10773.
- (13) Medles, M.; Benramdane, N.; Bouzidi, A.; Nakrela, A.; Nakrela, A.; Tabet-Derraz, H.; Kebbab, Z.; Mathieu, C.; Khelifa, B.; Desfeux, R. *Thin Solid Films* **2006**, *497*, 58-64.
- (14) Ahire, R. R.; Deshpande, N. G.; Gudage, Y. G.; Sagade, A. A.; Chavhan, S. D.; Phase, D. M.; Sharma, R. *Sensor. Actuat.A* **2007**, *140*, 207-214.

- (15) Bao, H.; Cui, X.; Ming Li, C.; Gan, Y.; Zhang, J.; Guo, J. *J.Phys.Chem.C* **2007**, *111*, 12279-12283.
- (16) Spurgeon, J. M.; Atwater, H. A.; Lewis, N. S. *J.Phys.Chem.C* **2008**, *112*, 6186-6193.
- (17) Sun, W.-T.; Yu, Y.; Pan, H.-Y.; Gao, X.-F.; Chen, Q.; Peng, L.-M. *J.Am.Chem.Soc.* **2008**, *130*, 1124-1125.
- (18) Kale, R. B.; Lokhande, C. D. *J.Phys.Chem.B* **2005**, *109*, 20288-20294.
- (19) Soloviev, V. N.; Eichhofer, A.; Fenske, D.; Banin, U. *J.Am.Chem.Soc.* **2000**, *122*, 2673-2674.
- (20) Tena-Zaera, R.; Katty, A.; Bastside, S.; Lévy-Clément, C. *Chem.Mater.* **2007**, *19*, 1626-1632.
- (21) Hodes, G.; Manassen, J.; Cahen, D. *J.Am.Chem.Soc.* **1980**, *102*, 5964.
- (22) Szabo, J. P.; Cociviera, M. *J.Appl.Phys.* **1987**, *61*, 4820.
- (23) Seabold, J. A.; Shankar, K.; Wilke, R. H. T.; Paulose, M.; Varghese, O. K.; Grimes, C. A.; Choi, K.-S. *Chem. Mater.* **2008**, *20*, 5266-5273.

Chapter3:Photoelectrochemical Properties of Nanostructured WO₃ Prepared with Different Organic Dispersing Agents

3.1. Introduction

Photoelectrolysis uses sunlight to directly decompose water into hydrogen and oxygen and uses semiconductor materials to produce electrons and holes (carriers) by the absorption of sufficiently energetic photons. Water photoelectrolysis is a slow multielectron process that can be achieved by means of relatively large bandgap (> 2.0 eV) semiconductor materials [1]. Irradiation of the semiconductor can drive both water oxidation and reduction resulting in oxygen and hydrogen gas evolution in a two electrode photoelectrochemical cell [2-3]. Together with the optimization of the electrolyte and of the counterelectrode, the semiconducting material is the main component determining the system performance.

Nanostructured semiconductor electrodes have attracted a considerable scientific interest for a number of reasons: nanostructures combine high electro-active surfaces, good light harvesting abilities and ease of fabrication through low cost chemical methods [4-12]. Thin films based on nanocrystalline WO₃ structures can be used as high performance photoanodes for water photoelectrolysis [13-16], however, to optimize the efficiency, a highly crystalline structure should be obtained in order to minimize imperfections and surface contaminations which may lead to charge trapping and carrier recombination. The mechanical adhesion and chemical film stability are also of relevance. In particular, corrosion and dissolution of the photoanode in the electrolyte should be avoided and, in this regard, WO₃ is promising due to its photochemical stability in aqueous acidic solution up to pH 5 [16]. Since crystal size, nanoparticle necking and thickness of the photoactive layer affect the current-voltage behaviour of the photoanode, we have tried to rationalize in this work how different thermal treatments and specific organic binder/dispersing agents can control the crystal size and the morphology of nanostructured WO₃ photoanodes. Their influence on the efficiency of water oxidation in photo-electrochemical cells is investigated and discussed.

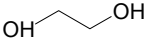
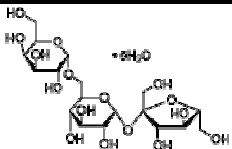
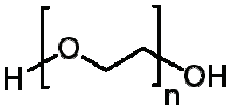
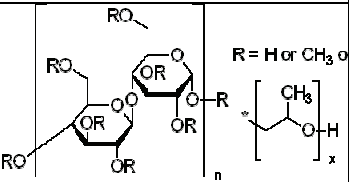
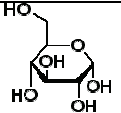
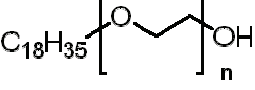
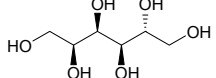
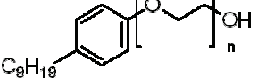
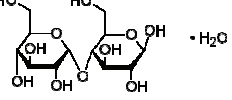
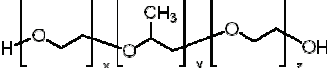
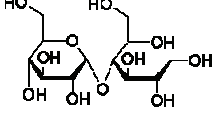
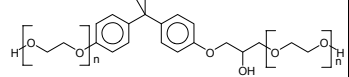
3.2 Synth-1 and Synth-2

The preparation route of nanocrystalline WO_3 was inspired by the Santato-Augustynski recipe [14]. The main difference among prepared samples is represented by the variation of dispersing agents (ethylene glycols, poly-ethylene glycols with different molecular weight, Igepal®, Brij®, sugars) as shown in Tab. 1.

According to the procedure named Synt-1, tungstic acid was obtained by passing 5 ml of an aqueous Na_2WO_4 solution (10% w/w, Carlo-Erba) through a proton exchange resin (Amberlite IR120H) and collecting the eluted solution in 5 ml of ethanol, to slow down the tungstic acid condensation. To the resulting colloidal dispersion, 0.5 g of organic dispersing agent was added and stirred until complete dissolution. Adding constant amount of organic dispersing agent, instead of constant moles, is a choice aimed to maintain similar viscosity of the colloidal solution, having a constant molar ratio between oxygen and tungsten atoms.

WO_3 photoelectrodes were obtained by blade-spreading the resulting H_2WO_4 colloidal precursor on FTO (fluorinated tin oxide, TEC 8, $8\Omega/\text{sq}$) substrates. The resulting films were annealed at 550 C° in air for 2 h. In order to study the effect of the annealing temperature on the morphology, a series of electrodes, made with PEG 300, were annealed in air at 400° , 500° , 600° C for 2 h.

Table 1 – Dispersing agents

| Dispersing agents | | Dispersing agents | |
|---|---|---|---|
| Ethylene glycol |  | D-(+)-Raffinose pentahydrate |  |
| PEG 200, PEG 300 PEG 400, PEG 1300-1600 PEG 4000, PEG 6000 PEG 20000 |  | (Hydroxypropyl)methyl cellulose |  |
| D-(+)-glucose |  | Brij® 97 (Mn 709) |  |
| D-Sorbitol |  | Igepal® CO520 (Mn 441) |  |
| D-(+)-Maltose monohydrate |  | PEG-b-PPG-b-PEG (Mn 2800) |  |
| Maltitol |  | Polyethyleneglycol Bisphenol Epichlorohydrin Copolymer (PEG-BAE) |  |

In another procedure (Synt-2) [17], devised to avoid ion exchange chromatography, 5 g of Na_2WO_4 was dissolved in 100 ml Millipore water; to this solution 20 ml of concentrated HCl was rapidly added. The resulting solid was collected by centrifugation and washed three times with water. The wet precipitate was then dissolved in 5 ml of water at 60°C in presence of 2 g of oxalic acid. The resulting colloidal suspension was weighted and Polyethylen-glycol Bisphenol A Epichlorohydrin Copolymer (PEG-BAE), in a 1:5 w/w ratio, was added. Ten drops of Triton® X-100 were finally added. WO_3 photo-electrodes were obtained by blade-spreading (scotch tape method) the colloidal precursor on FTO substrates. The resulting films were dried in air at approximately 100°C before firing at 550°C in air for 1 h.

Samples were characterized by X-Ray diffraction (XRD) by means of a Powder Diffractometer Panalytical X'Pert Pro, in Bragg-Brentano geometry using Cu K_α radiation ($\lambda=1.5416 \text{ \AA}$), with the X-ray tube set to 40 V and 40 mA. The spectra were collected in the range $5\text{-}90^\circ$ (2θ) with step size 0.02° and time acquisition set to 15 s/step. Accurate values of the coherent scattering domains lengths were obtained by means of a full profile fitting program (TOPAS) [18] based on what is called fundamental parameters approach [19]. This method perfectly models the instrumental contributions to the observed peak profiles, and a standardless refinement of sample effects, such as crystallite size and microstrain, can be performed.

The morphology of WO_3 nano-powders was characterized by using a scanning electron microscope (FE-SEM Jeol JSM 7600f) with an accelerating voltage of 15 kV. The high resolution images were collected using secondary electrons signal.

UV-Vis spectra, in the 200-840 nm wavelength range, were obtained with a JASCO V-570 spectrophotometer equipped with a Hamamatsu 928 detector.

The evaluation of the WO_3 layer thickness was not a trivial task because of the scarce area homogeneity of the layers. Thus, the thickness average values were obtained by weighing the electrodes before and after deposition and annealing. The final thickness was determined by using both WO_3 bulk density (7.16 g/cm^3) and layer area (about 5 cm^2). The surface areas and porosity were obtained by nitrogen adsorption isotherms and BJH standard analysis. The average thickness is an important parameter to be controlled as it has a strong influence on the produced photo-current [20-21].

Photoanodes were tested in both two and three electrodes photo-electrochemical cell configurations, having a Pt-grid as a counterelectrode and a saturated calomel (SCE) as a reference electrode, respectively.

Although the potentiostatic arrangement is necessary for a more accurate characterization of the electrodic material, the choice of a the two-electrode arrangement was motivated by the need of investigating the photo-electrochemical behaviour of the photoanodes in conditions similar to the operation of a real device (i.e. a commercial or industrial photoelectrolyzer), in which a potentiostatic arrangement is not a practical setup and the potential bias can be either supplied by a DC power supply or by a solar cell.

The photoelectrochemical measurements were performed either in 0.03 M or 1 M H_2SO_4 at room temperature. A Mercury ORIEL 300W lamp, adjusted to an incident irradiance of 0.3 W/cm^2 or a sun simulator (AM 1.5 G) set to 0.14 W/cm^2 were used as light sources.

J-V curves, both under illumination and in the dark, were collected by applying a linear voltage ramp with scan speeds of 10 or 20 mV/s and were found nearly independent from the scan speed, at least in the explored 2-50 mV/s interval.

Photo-action spectra were recorded by using a home built apparatus comprising a 150 W Xe light source (Applied Photo- physics), an high radiance monochromator (Applied Phophysics, f:4) and a biconvex lens (f=7cm) for focalisation. The spectral bandwidth was 10 nm and the potential (referred to SCE) was generated by an Amel Mod. 552 potentiostat in a three electrode configuration, using a platinum counter electrode. Photocurrents were measured by a Agilent 34401-A multimeter. The incident irradiance was measured with a Centronic calibrated photodiode.

In zero-current chrono-potentiometry experiments the photoelectrode was first polarized 0.5 V vs. SCE potential for 30 s then the current supply was stopped and the electrode was left to reach a stationary potential in the dark. After this was attained, usually after tens of seconds, intense full xenon light (630 mW/cm^2) was shined on the electrode.

3.3 Morphological Properties

All WO_3 nanocrystals analyzed by XRD have 100% monoclinic structure. Sample morphologies were characterized by SEM analysis. The particle diameter was obtained by averaging a total of 150 particles (at magnification X 50 000) . The good correlation (Fig. 3.1) between the coherent domains obtained by XRD analysis and the nanoparticle size, giving a linear plot with almost unitary slope, indicates that each whole particle is a crystal.

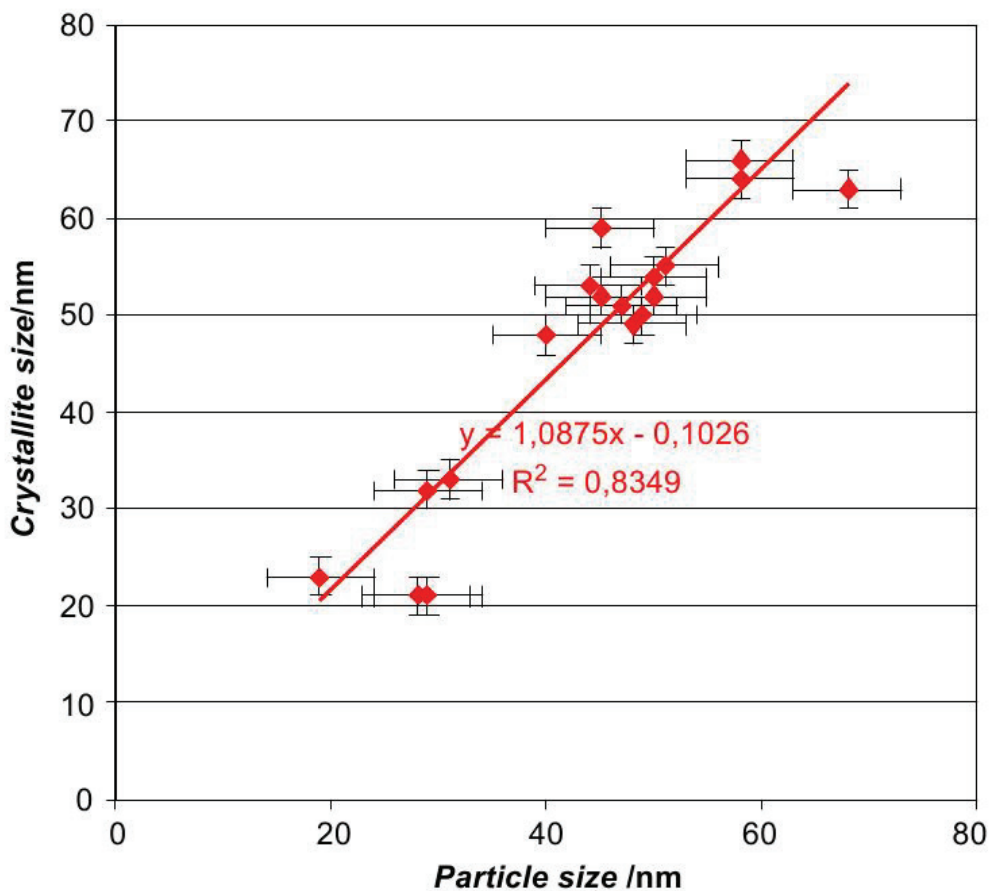


Fig. 3.1. Correlation between crystal size from XRD analysis and mean particle diameters as estimated from SEM pictures

It is well known that the annealing temperature is the most important parameter determining the final particle size [22]. The results reported in Fig. 3.2 show a considerable increase in the particle diameter starting from 773K, with a doubling in size at 873K. A fine crystallite size tuning can also be obtained by changing the

dispersing agent [20]. It can be noted that an almost logarithmic correlation between the crystal average size (XRD) and the molecular weight of dispersing agents was found (Fig. 3.3) indicating that the longer is the alcoxy-chain of the dispersing agents, the smaller is the average WO_3 particle diameter.

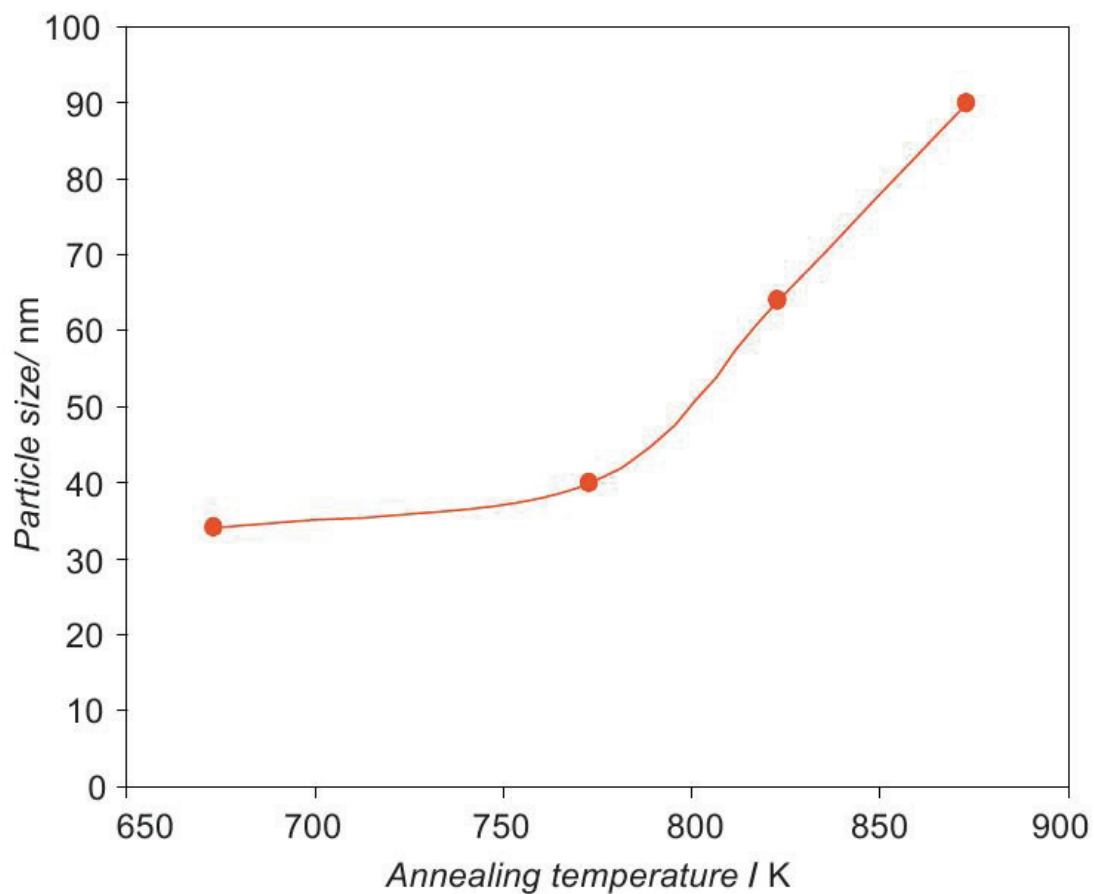


Fig. 3.2 Particle size and annealing temperature

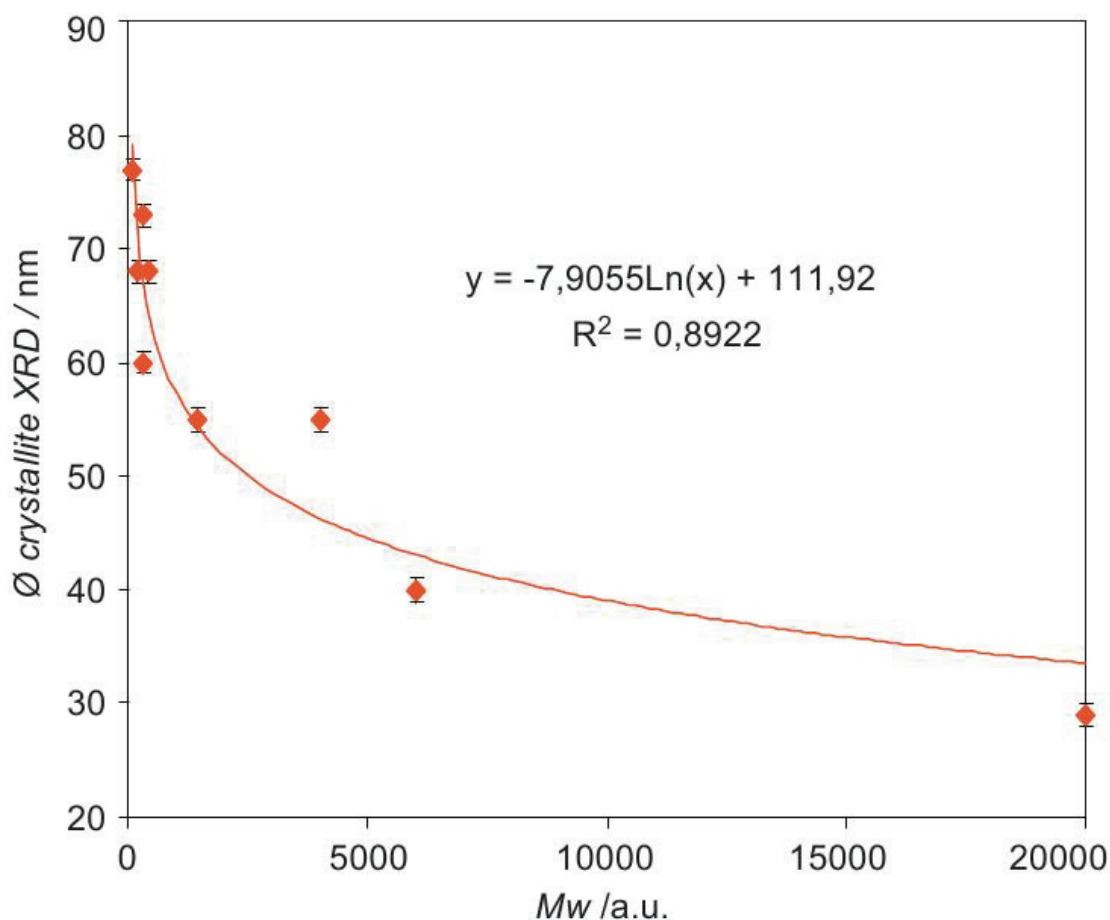


Fig. 3.3. Crystal size (XRD) as a function of the molecular correlation weight of the organic dispersing agents.

Fig. 3.5 shows a plot of photocurrent at a fixed applied voltage of 1.00 V vs. thickness of photoactive material deposited on the conductive substrate, related to samples with different dispersing agents of the PEG family. The general trend observed indicates an increase of the photocurrent with the amount of photoactive material as expected for very thin and porous electrodes (Fig. 3.4) [23-24]. For PEG-4000 sample it is shown that the initial photocurrent increase is followed by a saturation. The highest measured photocurrents were obtained with PEG 300 and 1300-1600 for estimated thickness of the order 400-500 nm.

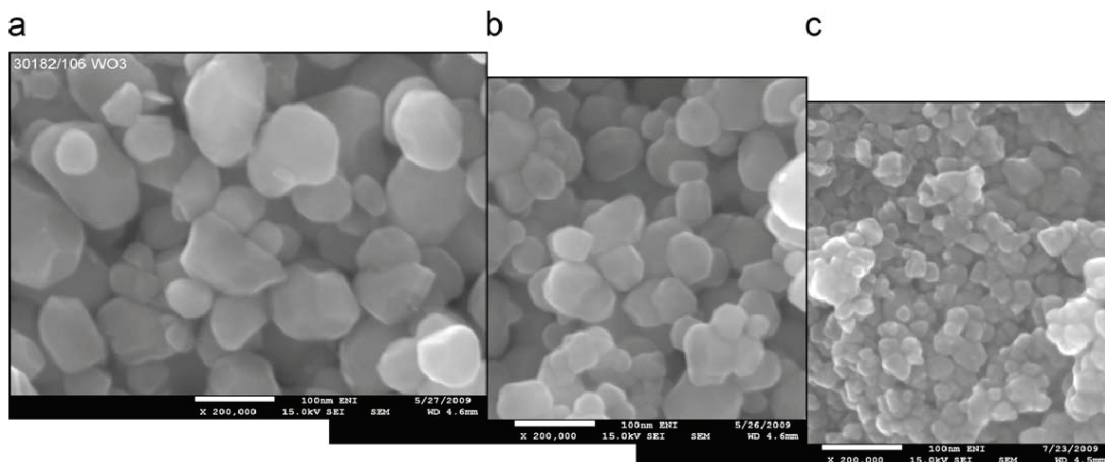


Fig. 3.4. SEM micrographs (15kV; magnification X 200 000) of WO₃ nanoparticles obtained by dispersion in: (a) ethylene glycol; (b) PEG1300-1600and (c) PEG20000.

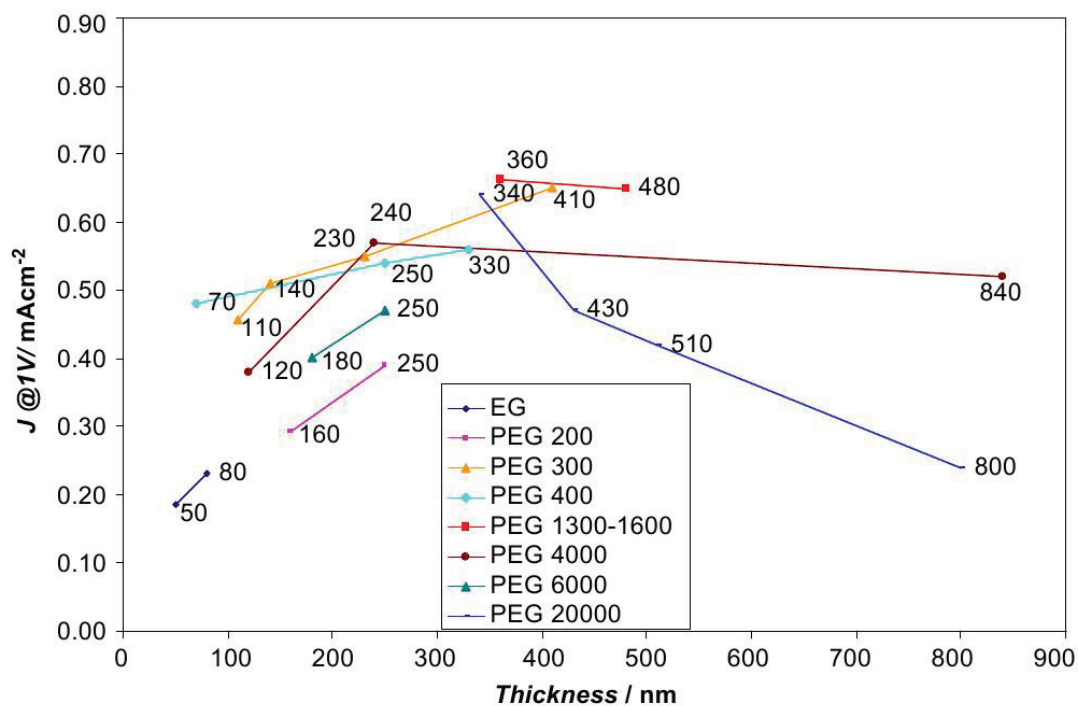


Fig. 5. Photocurrent density at 1 V vs. WO₃ layer thickness prepared with different dispersing agents (PEG)

Fig. 3.5. Photocurrent density at 1V vs. WO₃ layer thickness prepared with different dispersing agents (PEG)

The surface area of PEG-20000 sample was determined by nitrogen adsorption and resulted to be 12 m²/g; the pore specific volume was 0.14cc/g and the average pore size was 60 ± 30 nm.

The use of polysaccharides as dispersing agents was also investigated. Fig. 3.6 shows that, with respect to the PEG family, sugars lead to smaller particles. Smaller particle size, which means greater specific area, is able to increase current density as observed for sorbitol-dispersed samples (Fig.3.7).

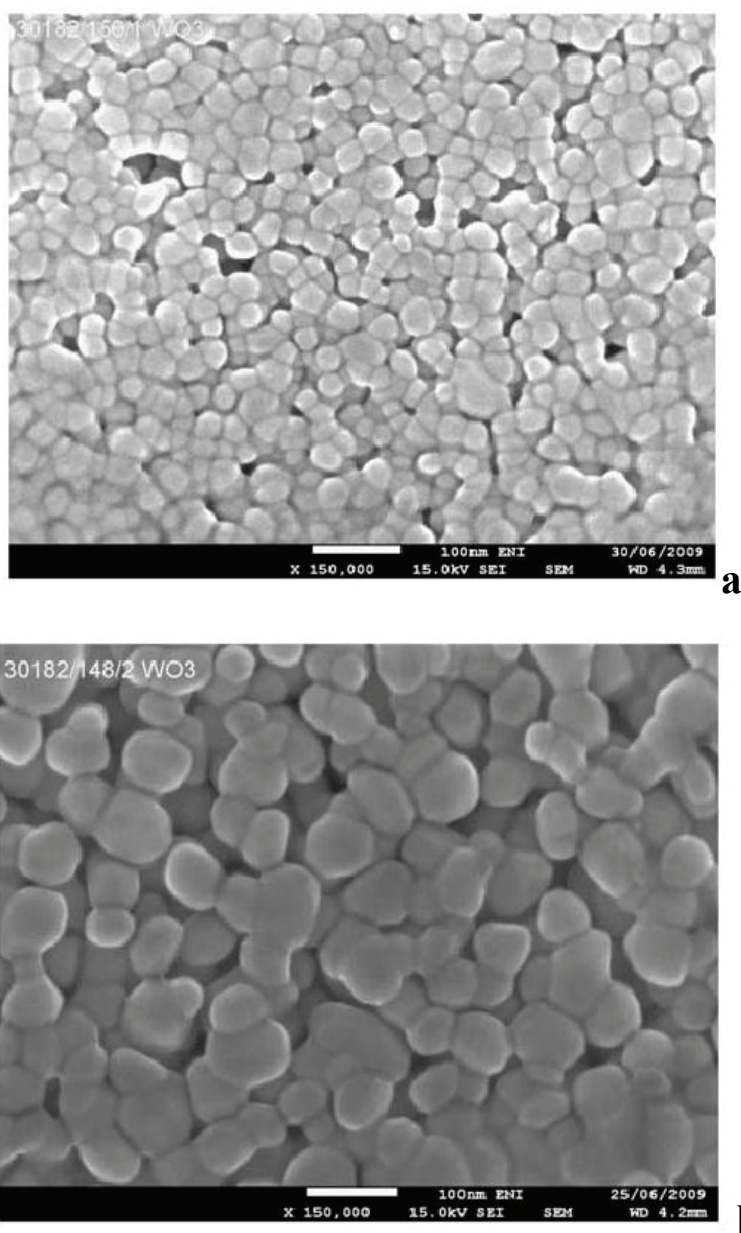


Fig. 3.6. SEM micro graphs (15kV; magnification x 150.000). Sample prepared with Sorbitol (a) and with PEG400 (b).

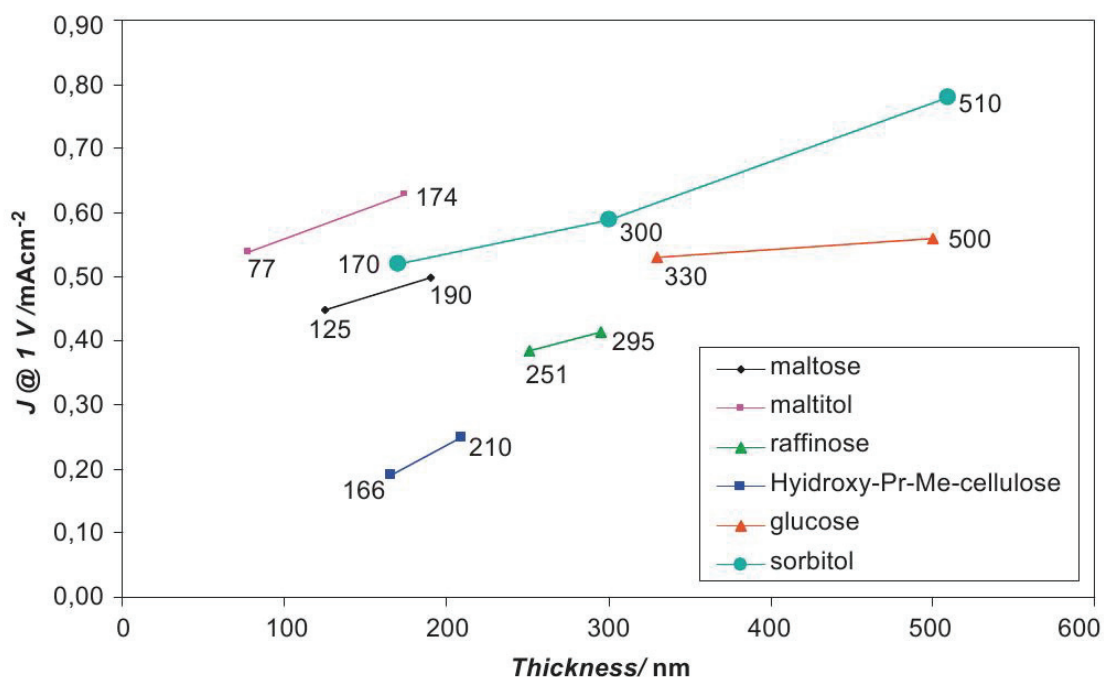


Fig. 3.7. Photocurrent density at 1V vs. WO₃ layer thickness for different sugar as dispersing agents

Fig. 3.8 shows J–V curves obtained in H₂SO₄ 0.03M at 0.3W/cm², in a two-electrode cell, for some samples prepared with different dispersing agents. As shown in the inset in the voltage range 0.85–1.05 V, curve slopes are parallel. The sorbitol sample shows the highest photocurrent in this range.

The limiting photocurrents were substantially independent of H₂SO₄ concentration in the 0.03–1M range. In the two-electrode arrangement (0.03M H₂SO₄) the dark current onset was observed at an applied voltage of 2V (the electrolysis threshold for water oxidation with WO₃/FTO anodes) while the photocurrent started in the 200–400mV interval depending on the photoelectrodes (Fig. 3.8). All examined photoelectrodes showed the expected n-type behaviour and were able to sustain a relevant photoanodic current, associated to hydrogen evolution at the cathode, by applying an external bias significantly lower than the dark current threshold.

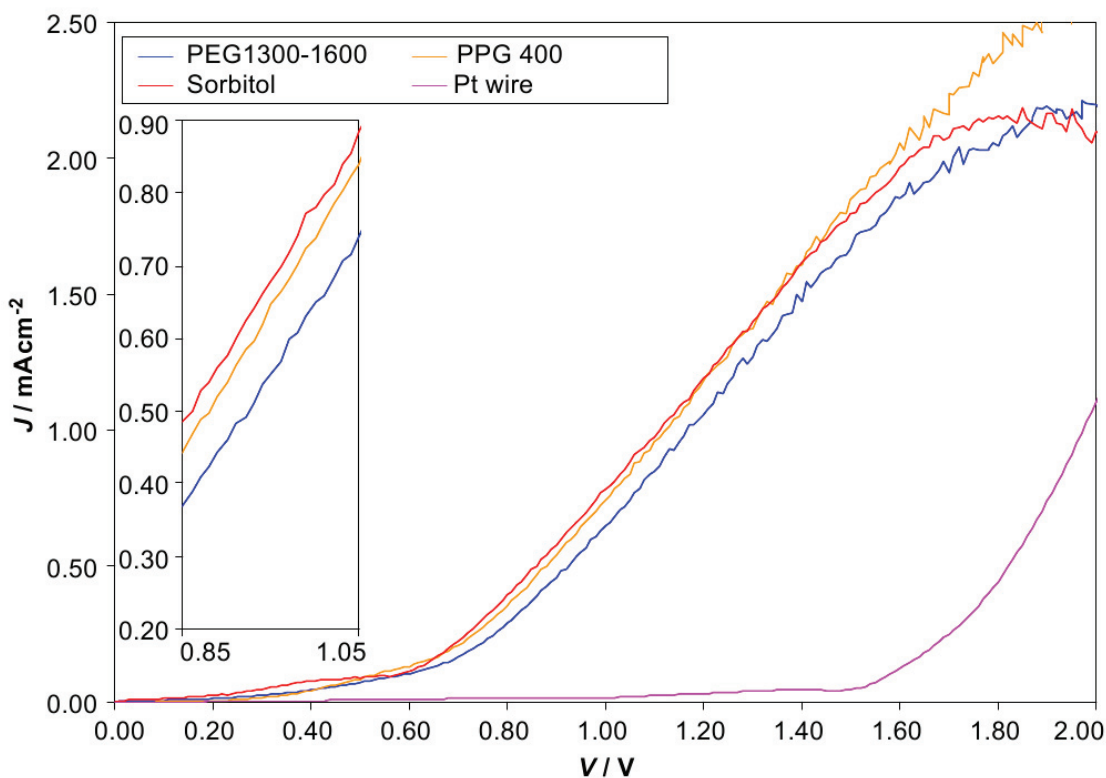


Fig. 3.8. Typical J–V curves obtained in H_2SO_4 0.03 M at $0.3\text{W}/\text{cm}^2$ in a two-electrode cell for the samples obtained with a single deposition of WO_3 .

Even when the layer thickness is increased (see Fig. 3.9), after depositing three times the same amount of WO_3 precursor, followed by thermal treatment at each step, the photocurrent slope remains unchanged but with a photocurrent plateau almost doubled. By performing multiple deposition steps it is possible to raise the thickness of the electrodes leading to an improved limiting photoanodic current for potentials 41.4 V, but no gain is achieved in the 0–1.4V region, which is the interval of major interest for practical application of photoassisted electrolysis since it allows for a real power saving with respect to conventional electrolysis. The slope of the J–V characteristic of the WO_3 photoelectrode ($2.6\text{mA cm}^{-2} \text{V}^{-1}$) is compared with a Pt–Pt system ($4.4 \text{mA cm}^{-2} \text{V}^{-1}$ in the 2.1–2.7V interval), which represents a highly conductive case.

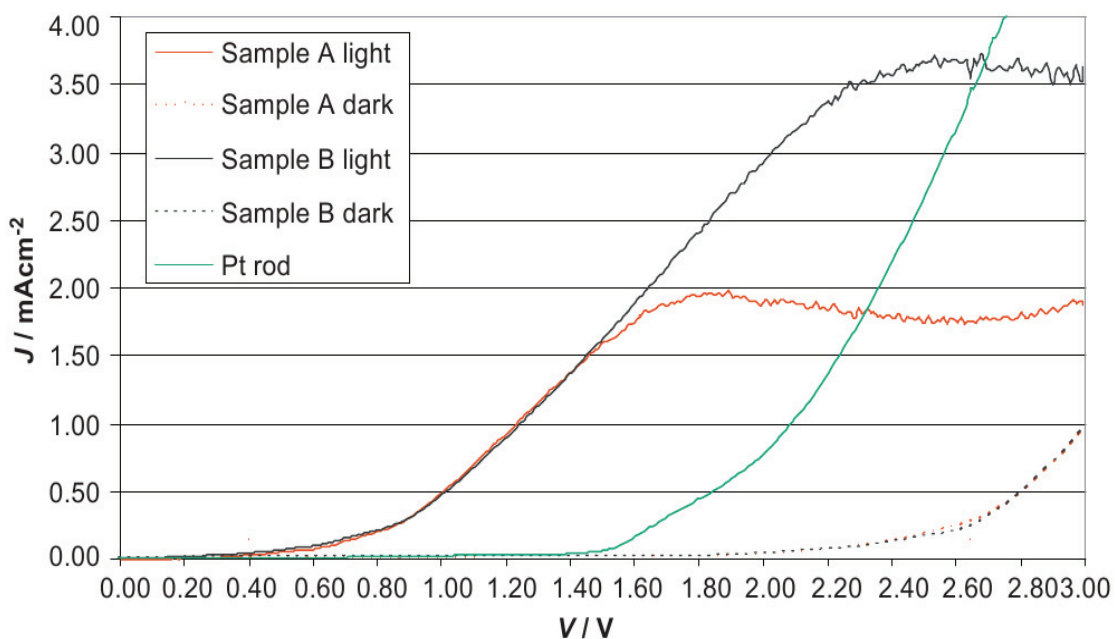


Fig. 3.9. J–V curves obtained in 0.03M H₂SO₄ at 0.3W/cm² in a two-electrode cell for a sample obtained by using D-Sorbitol as dispersing agent with one WO₃ deposition (sample A) and three WO₃ depositions (sample B). The green curve is the J–V plot during electrolysis with Pt–Pt wires.

It is well known that the hole diffusion length in WO₃ is quite short (about 150 nm, [25-26]), and that in nanostructured photoelectrodes the charge carriers are required to diffuse, in the absence of a relevant electric field, through the nanocrystal-line network to reach the collector. Although an increased thickness of the photoactive layer would imply a more effective light harvesting in thicker electrodes, the probability of electron recombination is also expected to increase since in front (electrolyte side) irradiation the carriers are generated at increasing distances from the back contact; compare models in Refs. [27-28]. Infact, Fig. 3.9 does not show any relevant improvement of the photocurrent in thicker samples, at least in the 0.1-1.4 V interval, probably due to charge transport limitations. As a consequence, a relatively thin (about 0.5 μm) nanostructured sample exhibits a good compromise between light absorption and carrier transport requirements.

3.4 Photo-electrochemical characterization of Synth-1 and Synth-2

The photo-electrochemistry of electrodes obtained with the two different preparation routes was investigated in detail [29]. In order to simplify the study, all the electrodes under comparative evaluation were obtained with a single spread of WO_3 precursor. Three of them were prepared following Synt-1, by using ethylene glycol, PEG 200, and PEG 6000, respectively, (EG-P200-P6000) as dispersing agents; the fourth sample (FE) was prepared following Synt-2 and was dispersed in PEG-BAE, as summarized in Table 2. Sample P6000 and FE had almost the same particle size (around 40 nm). Fig. 3.10 shows the UV-vis absorption spectra of the photoelectrodes: P6000 and FE display the strongest absorption in the UV region, with maximum optical density significantly greater than unity and an absorption tail extending in the visible up to 450 nm.

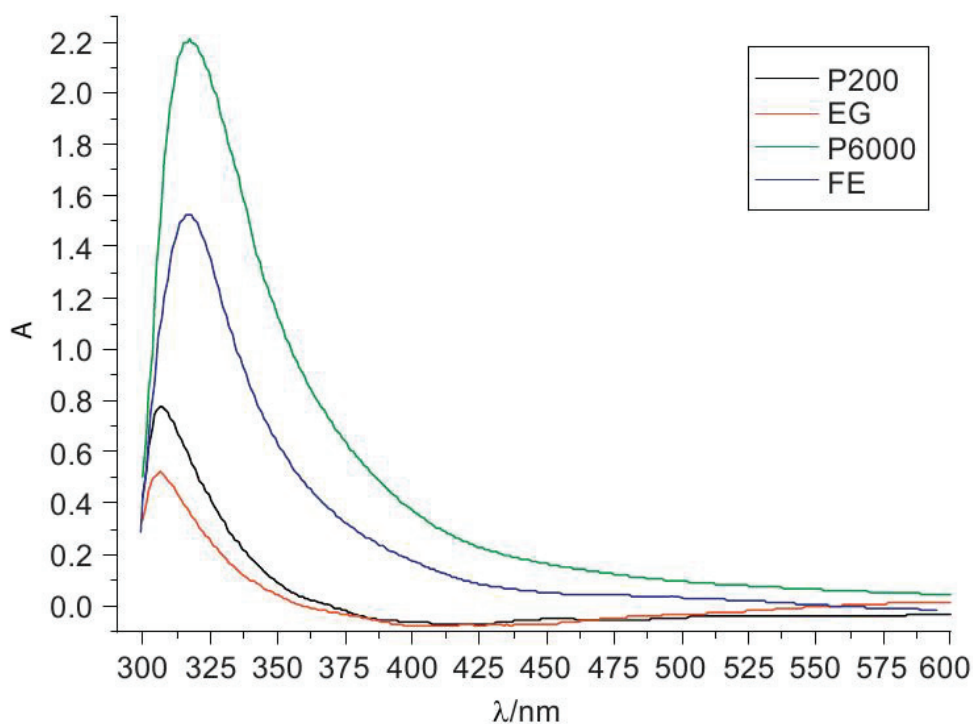


Fig. 3.10. UV-vis absorption spectra for samples at different thicknesses.

Table 2
Description of samples included in the photo-electrochemical investigation.

| Sample | Synthesis | Dispersing agent | Thermal treatment | Cristal size XRD (nm) | Thickness (nm) | J at 1 V mA cm ⁻² |
|--------|-----------|---------------------|-------------------------|-----------------------|----------------|--------------------------------|
| EG | Synth-1 | Ethylene glycol | 550 °C/2 h | 80 | 83 | 0.24 |
| P200 | Synth-1 | PEG200 | 550 °C/2 h | 60 | 160 | 0.30 |
| P6000 | Synth-1 | PEG6000 | 550 °C/2 h | 40 | 254 | 0.48 |
| FE | Synth-2 | PEG-BAE (Mw~20.000) | 100 °C/10' 550 °C/2h | 40 | 200 | 1.60 |

Fig. 3.11 shows the photocurrent density/voltage curves, obtained in a three electrode cell using a scan speed of 20 mV/s. In the three electrode arrangement (1 M H₂SO₄), where the potential was controlled by a potentiostat in relation to the reference electrode, the photocurrent started in all cases at 300 mV vs. SCE. It must be noted that the photocurrent threshold, which could be taken as a lower approximation of the flat band potential at a given pH, followed with a good approximation a nernstian behaviour (ca. 60 mV/pH). The incident irradiance, with AM 1.5 filter, was 0.14W/cm². The photo-electrode area was 1cm² for all samples. The best performances are obtained with the FE electrode which almost doubles the photoanodic current generated with the P6000 electrode. The reason for such behaviour cannot be simply explained on the basis of the light harvesting efficiency, since, for example, the absorbance of FE at all wavelength is lower than P6000.

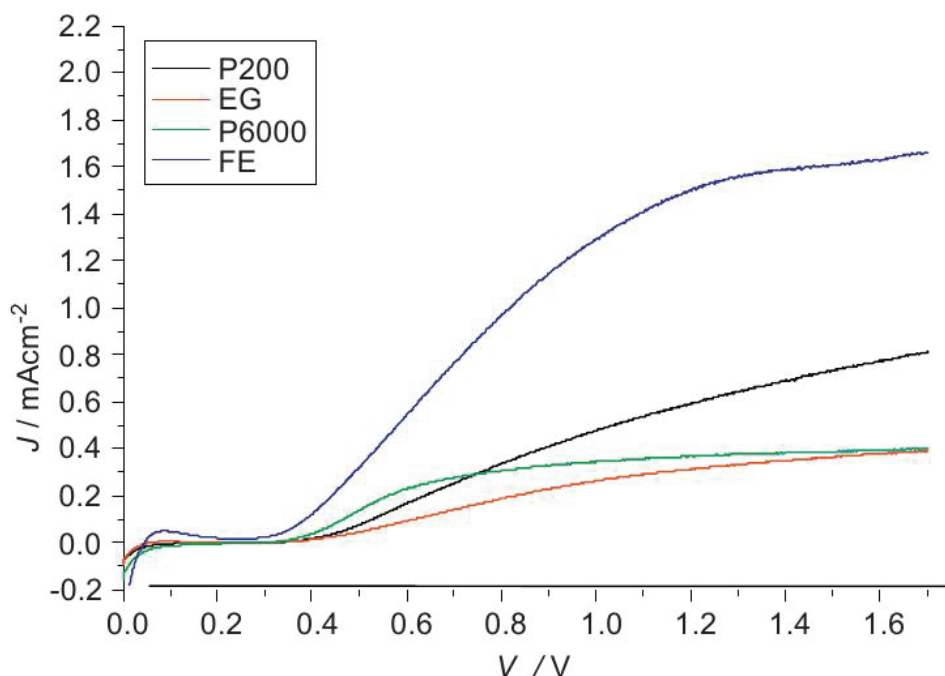


Fig. 3.11. J-V curves for a three electrodes cell. Applied potential in V vs. SCE in 1M H₂SO₄ at 0.14W/cm². Scan rate 20 mVs⁻¹.

In Fig. 3.12(a) the photo-action spectra representing the quantum efficiency (IPCE%) of each photo-electrode as a function of the wavelength are reported. These spectra are obtained with a constant and positive bias of 1.5 V and 1 V vs. SCE. In agreement with the J-V curves, among the Synt-1 electrodes, the photoanode P6000 shows the highest photo-conversion, giving rise to a maximum IPCE value of 45%, while sample P200 shows an IPCE value of 30%; the sample 106 display the poorest performance, with conversion efficiencies lower than 10%. The FE sample shows a maximum photo-conversion comparable to P6000 (40%) in the UV region (310-340 nm). However, a significantly higher photoconversion in the 350-420 nm interval, thus explaining the better performance under polychromatic irradiation. In Fig. 3.12(b) the APCE (APCE=IPCE/LHE; $LHE(1) = 1 - 10^{-A(1)}$ where A is the measured absorbance of the transparent film) for samples P6000 and FE is also reported.

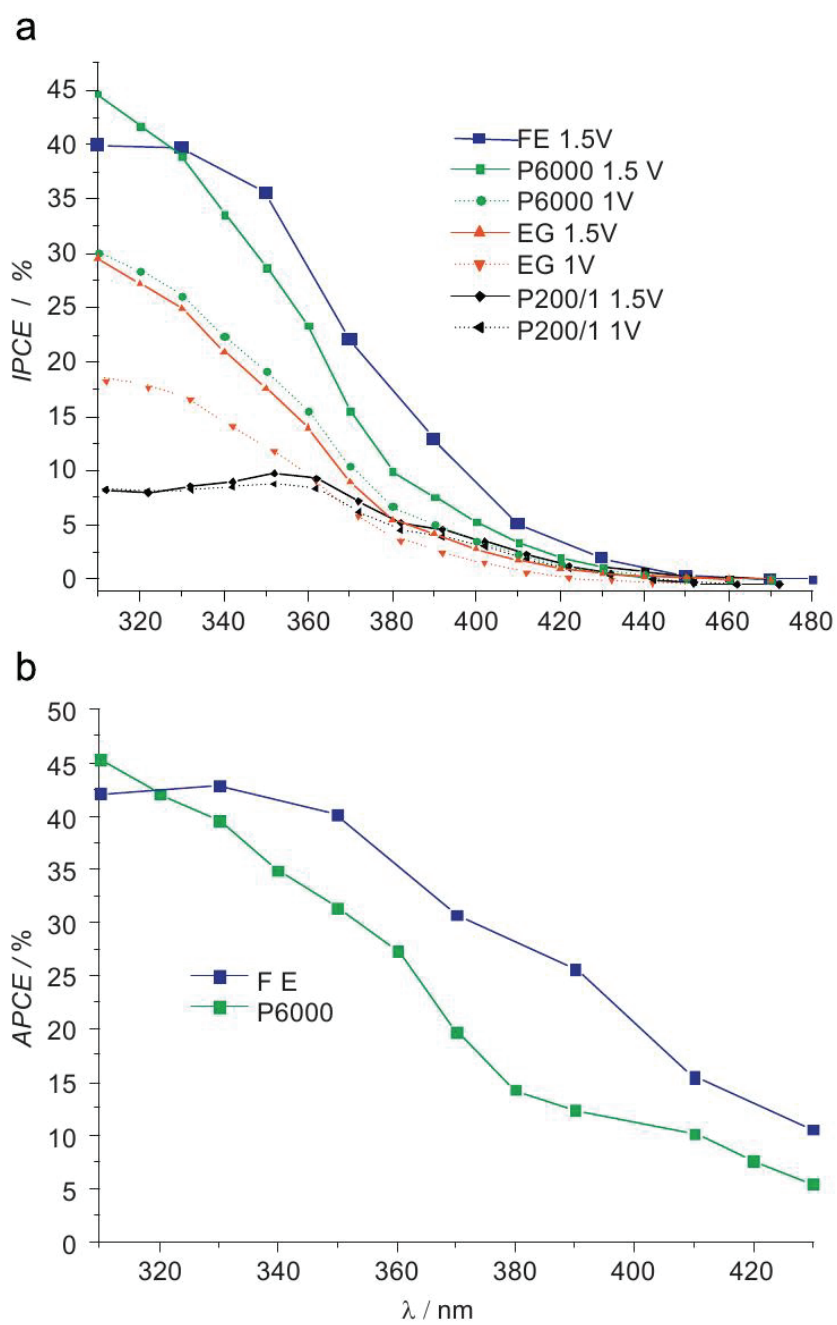


Fig. 3.12. (a) Photocurrent efficiency (IPCE) at 1.5 and 1V vs. SCE and (b) photocurrent efficiency APCE at 1.5V vs. SCE.

In the effort to rationalize the different behaviour of Synt-2 and Synt-1 electrodes, chrono-coulombometric measurements have been performed. In a potentiostatic arrangement, the applied voltage is switched between -300 mV and $+1$ V vs. SCE and the resulting current is integrated as a function of time. Upon negative polarization, electrons are injected into the conduction band of the semiconductor and the negative charge is compensated by migration/intercalation of H^+ into the nanocrystals; with positive polarization the discharging of the film is produced. Obviously, charge compensation occurs only for sites that can be effectively permeated by the solvent, therefore this method can provide a mean to probe the electro-active surface able to exchange charges with the electrolyte. In Fig. 3.13 these curves, referring to the electrodes under study, are reported. It can be seen that the FE sample shows the highest charge variation, suggesting an higher charge storing ability corresponding to a wider electro-active surface which can contribute to explain the higher photo-electrochemical performance, since a large active area in contact with the electrolyte can enhance the probability of successful hole transfer to the electrolyte.

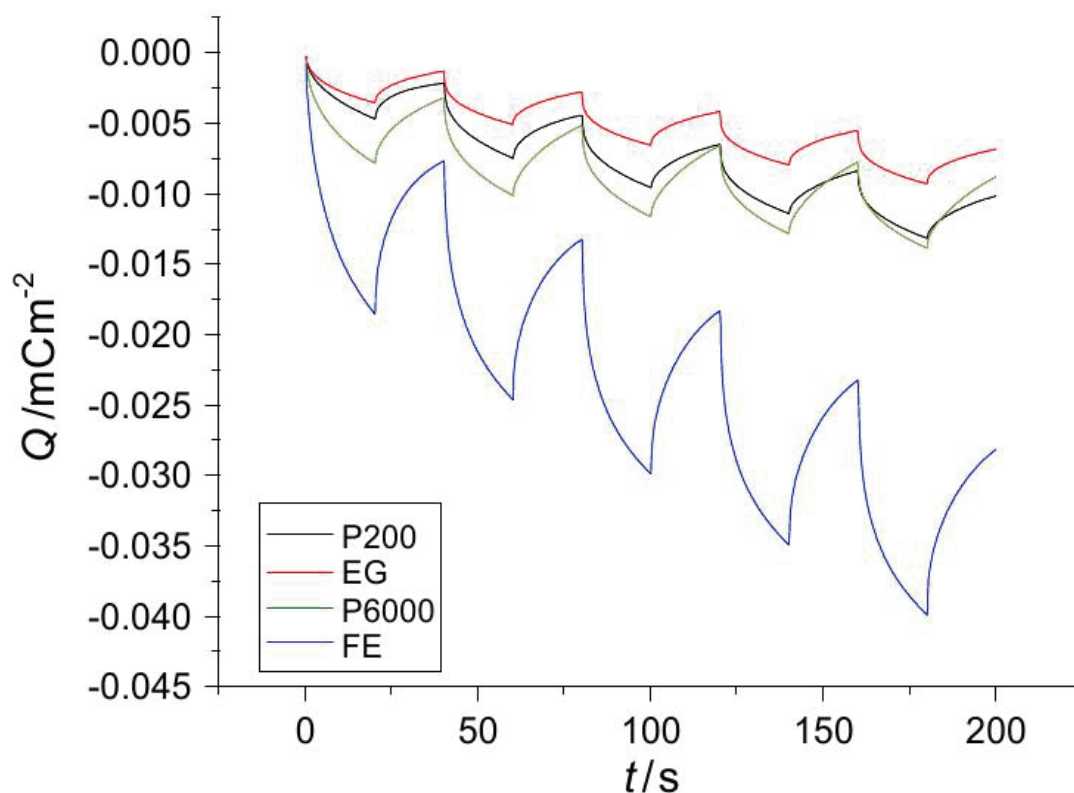


Fig. 3.13. Crono-coulombometric curves for samples EG-P200-P6000 and FE

The J-V curves of both FE and P6000 under modulated illumination (Fig.3.14) do not show transient cathodic features when light is shut off, testifying a limited hole accumulation within the mesoscopic film and minimal recombination via surface states. The shape of the voltammograms obtained by irradiating through the front (WO_3) and back contact is also very similar, suggesting that the electron transport through the film is quite effective, as it could be expected with relatively thin film photoelectrodes, however it can be observed that in the P6000 case the photocurrents obtained by irradiation through the back side are slightly higher (ca. 15%) than those obtained by irradiation through the front side (WO_3), testifying that, if the charge carriers are generated far from the collector, there is a competition between recombination and electron transport/collection at the back contact[24].

This fact can be rationalized considering that in such porous electrodes the particles are too small and too lightly doped to support an efficient depletion layer and charge separation is governed by the charge transfer kinetics involving the semiconductor/electrolyte interfaces [30-32]. Since incident light intensity is expected to decrease exponentially with the thickness of the absorber, by irradiating through the back contact, a larger number of charge carriers are photogenerated in the immediate proximity of the FTO back contact, resulting in higher probability of being collected, thus escaping charge recombination and contributing to the photocurrent [28].

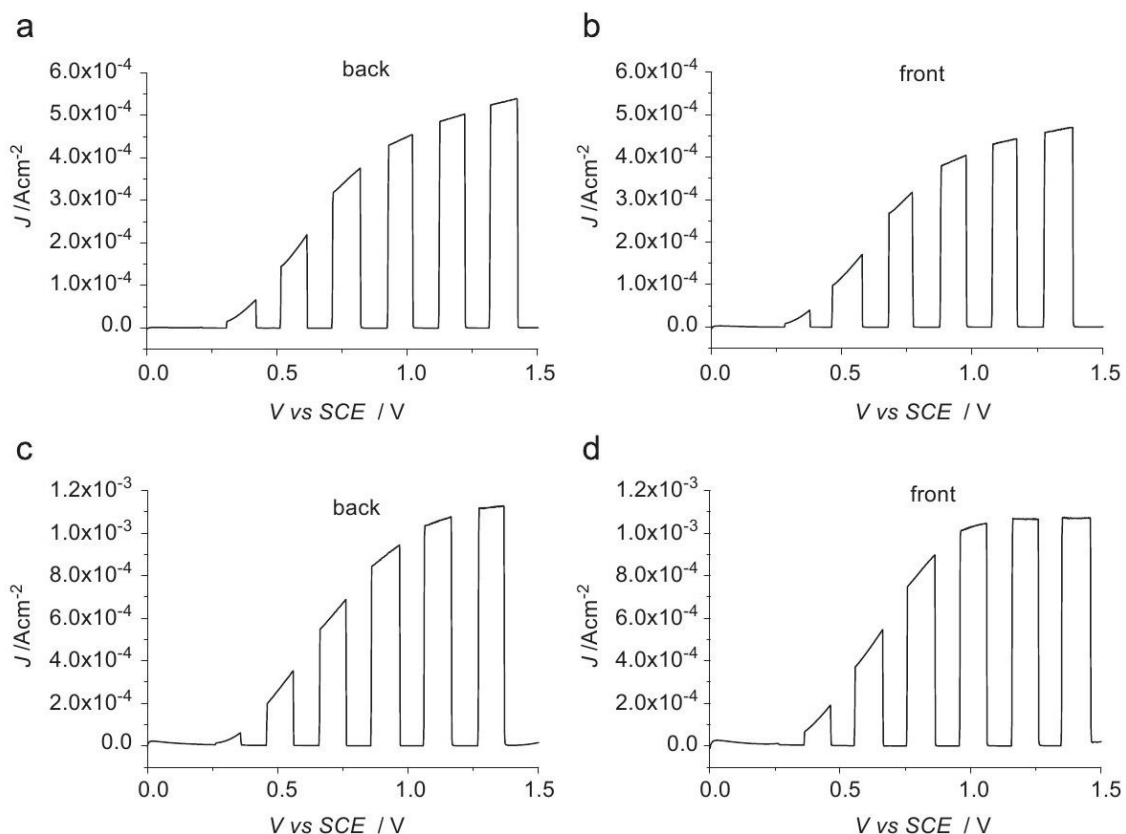


Fig. 3.14. Linear scan voltammetry under on/off modulated illumination (fullXe, $0.112\text{W}/\text{cm}^2$) in $0.03\text{M H}_2\text{SO}_4$ (a)–(b) P6000 back and front; (c)–(d) FE back and front. Back and front stand for illumination through the back FTO contact and through the WO_3 side, respectively.

The open circuit photovoltage decays (Fig. 3.15) confirm a faster recombination in P6000 electrodes. In both cases, under illumination a maximum photovoltage of 0.25 vs. SCE is attained, which can be taken as a good estimate of the flat band potential of nanocrystalline WO_3 in $1\text{ M H}_2\text{SO}_4$ (pH 0). However, when light is switched off, P6000 electrode gives rise to a considerably faster relaxation ($\tau = 35\text{ s}$) than the FE ($\tau = 130\text{ s}$) one. A slower photovoltage relaxation in FE electrode is consistent with a longer-living photogenerated electron density which should result from a more effective hole transfer to the electrolyte.

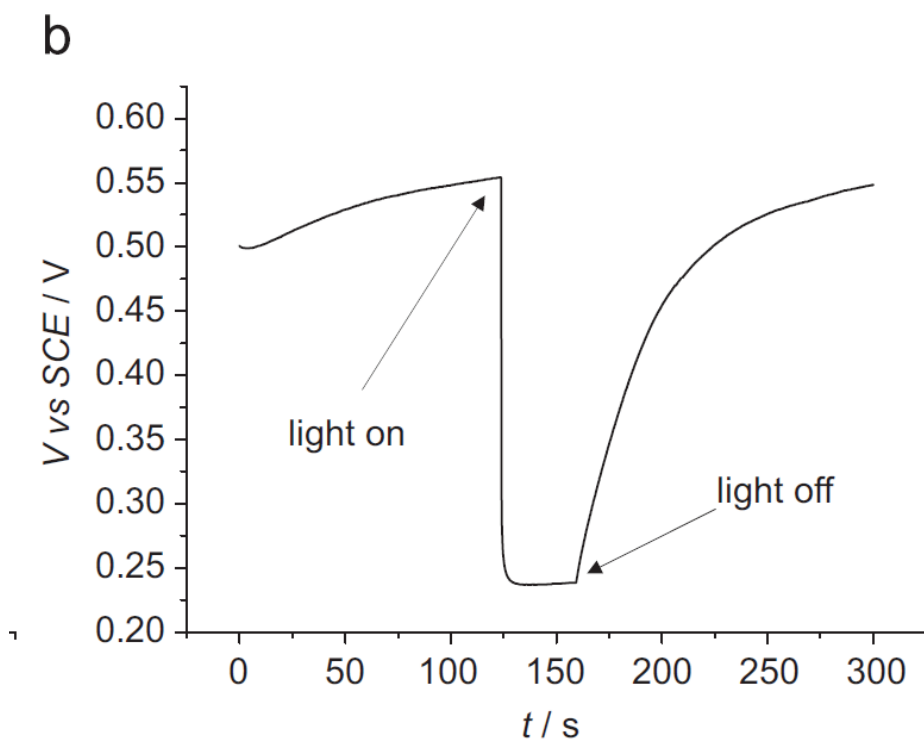
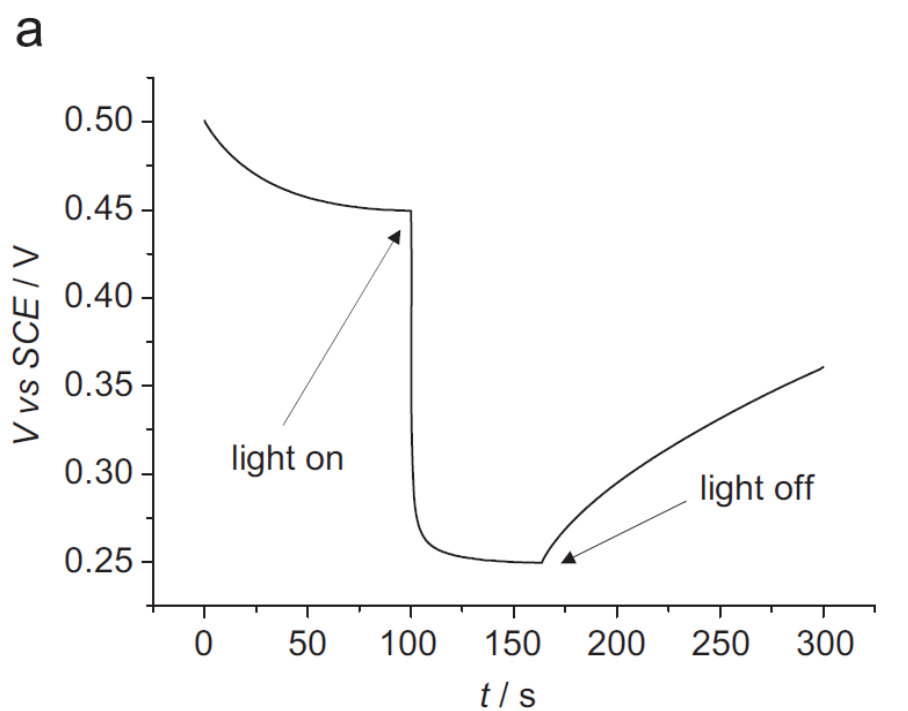


Fig. 3.15. Open circuit photovoltage decay in 1M H₂SO₄: (a) FE and (b) P6000. Incident irradiance: 630mW/cm² (full xenon).

3.5 Conclusions

Nanocrystalline WO_3 electrodes can be advantageously utilized in photoassisted water electrolysis in acidic media, since they allow for the generation of photoanodic currents at potentials considerably lower (- 0.9 V) than the thermodynamic threshold for water oxidation (1.23 V vs. NHE). This paper is divided into two parts: the first one is devoted to the correlation of the morphological properties of the nanocrystalline WO_3 (Synt- 1 only) with its photo-electrochemical performance, while, in the second one, the photo-electrochemical properties of WO_3 photo-electrodes with similar nanoparticle size, obtained from two different sol-gel routes (Synt-1 and Synt-2), are reported.

While it is known that the nanocrystal size is affected by the annealing temperature (between 40 and 80 nm, in the range 773-873 K) it has also been shown that a fine tuning of crystallite size can be obtained by changing the organic dispersing agents. For example, the use of polysaccharides results, at a given temperature (823 K), in a nanoparticle diameter ranging from 20 and 50 nm (Synt-1).

A smaller particle size, which means greater specific area, allows to increase the current density and it has been pointed out that, for a specified particle diameter and in the case of thin electrodes, the photocurrent increases by increasing the thickness of the photoactive layer. However, a thickness of 400-500 nm already achieves a good compromise between light absorption and carrier transport since thicker electrodes, obtained by multiple deposition steps, did not lead to any photocurrent improvement in the low voltage region, up to 1.4 V.

The comparison between two different preparation routes (Synt-1 and Synt-2) of nanocrystalline colloidal WO_3 pointed out that the small particle size is not the only requirement to get good photoanodes. Sample P6000 (Synth-1) and sample FE (Synth-2) show different photo-electrochemical behaviour although they have the same particle size (40 nm). Even if the absorbance of the FE electrode at all the wavelengths is lower than the P6000 one, the FE electrode almost doubles the photocurrent with respect to the P6000 one. This better performance under polychromatic irradiation may be explained by the higher photoconversion shown in the 350-420 nm interval (see Fig. 3.12a and b). The chrono-coulombometric measurement shows an higher charge storing

ability for sample FE corresponding to a larger electro- active surface per unit electrode area, able to enhance the probability of successful hole transfer to the electrolyte.

The open circuit photovoltage curves show a flat band potential of 0.25 V vs. SCE (at pH 0) for both samples and tentatively suggest a correlation between slow relaxation rate and long living photogenerated electrons. A better connectivity among crystals seems to be the reason for better photo- electrochemical performances when comparing samples with similar particle size.

3.4 Bibliography

- (1) C.K. Dyer, J. Garche, P.T. Moseley, Z. Ogumi, D.A.J. Rand, B. Scrosati (Eds.), Encyclopedia of Electrochemical Power Source. Elsevier, 2009, ISBN 9780444520937.
- (2) A. Fujishima, K. Honda, Electrochemical photolysis of water at a semiconductor electrode, *Nature* 238 (1972) 37-38.
- (3) A.J. Nozik, Photoelectrolysis of water using TiO₂ semiconducting crystals, *Nature* 257 (5525) (1975) 383-385.
- (4) M.S. Wrighton, D.L. Morse, A.B. Ellis, D.S. Ginley, H.B. Abrahamson, Photoassisted electrolysis of water by ultraviolet irradiation of an antimony doped stannic oxide electrode, *J. Am. Chem. Soc.* 98 (1976) 44-48.
- (5) G. Hodes, D. Cahen, J. Manassen, Tungsten trioxide as a photoanode for a photoelectrochemical cell (PEC), *Nature* 260 (1976) 312-313.
- (6) A.J. Nozik, p-n photoelectrolysis cells, *Appl. Phys. Lett.* 29 (1976) 150-153.
- (7) K.L. Hardee, A.J. Bard, Semiconductor electrodes, *J. Electrochem. Soc.* 122 (1975) 739-742.
- (8) L.A. Harris, R.H. Wilson, Aging effects in single crystal reduced rutile anodes, *J. Electrochem. Soc.* 123 (1976) 1010-1015.
- (9) R.M. Canda, M. Kastner, R. Goodman, N. Hickok, Photoelectrolysis of water: Si in salt water, *J. Appl. Phys.* 47 (1976) 2724-2726.
- (10) M.A. Butler, R.D. Nasby, R.K. Quinn, Tungsten trioxide as an electrode for photoelectrolysis of water, *Solid State Commun* 19 (1976) 1011-1014.
- (11) H. Gerischer, Electrochemical photo and solar cells principles and some experiments, *J. Electroanal. Chem.* 58 (1975) 263-274.
- (12) A.B. Murphy, P.R.F. Barnes, L.K. Randeniya, I.C. Plumb, I.E. Grey, M.D. Horne, J.A. Glasscock, Efficiency of solar water splitting using semiconductor electrodes, *Int. J. Hydrogen Energy* 31 (2006) 1999-2017.
- (13) C.G. Granqvist, Electrochromic tungsten oxide films: review of progress 1993-1998, *Sol. Energy Mater. Sol. Cells* 60 (2000) 201-262.
- (14) C. Santato, J. Augustynski, M. Ulmann, M. Odziemkowski, Crystallographically oriented mesoporous WO₃ films: synthesis, Characterization, and application, *J. Am. Chem. Soc.* 123 (2001) 10639-10649.

- (15) H. Wang, T. Deutsch, J.A. Turner, Direct water splitting under visible light with nanostructured hematite and WO₃ photoanodes and a GaInP₂ Photocathode, *J. Electrochem. Soc.* 155 (2008) F91-F96.
- (16) H. Wang, T. Lindgren, J. He, A. Hagfeldt, S.E. Lindquist, Photoelectrochemistry of nanostructured WO₃ thin film electrodes for water oxidation: mechanism of electron transport, *J. Phys. Chem. B* 104 (2000) 5686-5696.
- (17) Angiuli F, Argazzi R., Caramori S., Bignozzi C.A., Patent WO 2007/094019 A1.
- (18) Bruker AXS 2000:TOPAS ver 2.0: General Profile and Structure Analysis Software for Powder Diffraction Data-User Manual, Bruker AXS, Karlsruhe, Germany.
- (19) R.W. Cheary, A.A. Coelho, A fundamental parameters approach of X-ray line-profile fitting, *J. Appl. Cryst.* 25 (1992) 109-121.
- (20) A. Wolcott, T.R. Kuykendall, W. Chen, S. Chen, J.Z. Zhang, Synthesis and characterization of Ultrathin WO₃ nanodisks utilizing poly(ethylene glycol), *J. Phys. Chem. B* 110 (2006) 25288-25296.
- (21) C. Santato, M. Ulmann, J. Augustynski, Enhanced visible light conversion efficiency using nanocrystalline WO₃ films, *Adv. Mater.* 13 (7) (2001) 511-514.
- (22) S.J. Hong, H. Jun, P.H. Borse, J.S. Lee, Size effects of WO₃ nanocrystals for photooxidation of water in particulate suspension and photoelectrochemical silt systems, *Int. J. Hydrogen Energy* 34 (2009) 3234-3242.
- (23) D. Nister, K. Keis, S.E. Lindquist, A. Hagfeldt, A detailed analysis of ambipolar diffusion in nanostructured metal oxide films, *Sol. Energy Mater. Sol. Cells* 73 (2002) 411-423.
- (24) S.E. Lindquist, B. Finnstrom, L. Tegner, Photoelectrochemical properties of polycrystalline TiO₂ thin film electrodes on quartz substrates, *J. Electrochem. Soc.* 130 (1983) 351-358.
- (25) S.K. Deb, Optical and photoelectric properties and colour centres in thin films of tungsten oxide, *Philos. Mag.* 27 (1973) 801-822.
- (26) M.A. Butler, Photoelectrolysis and physical properties of the semiconducting electrode WO₃, *J. Appl. Phys.* 48 (1977) 1914-1920.
- (27) W.W. Gartner, Depletion-layer photoeffects in semiconductors, *Phys. Rev.* 116 (1959) 84-87.

- (28) S. Sodergren, A. Hagfeldt, J. Olsson, S.E. Lindquist, Theoretical models for the action spectrum and the current-voltage characteristics of microporous Semiconductor films in photoelectrochemical Cells, *J. Phys. Chem.* 94 (1994) 5552-5556.
- (29) J.O.M. Bockris, A.K.N. Reddy, M. Gamboa-Aldeco, *Modern electrochemistry*, vol. 2A, Kluwer Academic Publishers, 2002 ISBN0306461668.
- (30) B. O'Regan, J. Moser, M. Anderson, M. Graetzel, Vectorial electron injection into transparent semiconductor membranes and electric field effects on the dynamics of light-induced charge separation, *J. Phys. Chem.* 94 (1990) 87208726.
- (31) H. Lindstrom, H. Rensmo, S. Sodergren, A. Solbrand, S.-E. Lindquist, Electron transport properties in dye-sensitized nanoporous-nanocrystalline TiO₂ Films, *J. Phys. Chem.* 100 (1996) 3084-3088.
- (32) A. Zaban, A. Meyer, B.A. Gregg, Electric potential distribution and short-range screening in nanoporous TiO₂ electrodes, *J. Phys. Chem. B* 101 (1997) 7985-7990.

Chapter 4: Efficient Photoelectrochemical Water Splitting by Anodically Grown WO₃ Electrodes

4.1 Introduction

Solar energy is the only renewable and carbon neutral energy source of sufficient scale to replace fossil fuels. Direct conversion of this energy into clean fuels is one of the most important scientific challenges of the XXI century[1-3]. In this context, hydrogen production from solar water splitting, providing a potentially inexhaustible fuel source, is obviously attractive.

Although the realization of a molecular level system mimicking natural photosynthesis for the production of solar fuels[4] is certainly interesting and fascinating under a fundamental viewpoint, the practical efficiency achievements with respect to water splitting have been so far limited by a small driving force and kinetic complications arising, for example, from the need of realizing a multiple proton coupled charge transfer necessary to simultaneously overcome the demanding kinetics of water oxidation and reduction[5-7]. For these reasons either sacrificial hole or electron scavengers have been coupled to most molecular level charge separators[8].

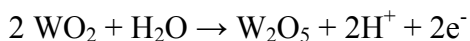
Since the experiment of Fujishima and Honda[9], the direct use of semiconductor photoelectrodes or nanoparticles, have appeared to be an alternative way for achieving photoinduced water splitting, thanks to the possibility of obtaining, with a practically unitary quantum yield, highly energetic charge carriers that can induce the required electrochemical reactions at the solid/electrolyte interface. [10-15]

Photoanodes based on n-type metal oxides like TiO₂[16], WO₃[17] and Fe₂O₃ [18-21] have been intensely studied, since, at appropriate pH, they couple ease of fabrication, high chemical stability in aqueous solution under evolving oxygen conditions, and reasonably high incident light to current generation when operated in a photoelectrochemical cell. Particularly, WO₃ electrodes show interesting properties displaying both visible absorption and good charge transport abilities[22-25].

Tungsten (together with Al, Ti, Zr, Bi, Ta, Nb) belongs to the group of the so called valve metals, which passivate and show a very high corrosion resistance in most

common aqueous media. The composition of naturally or anodically occurring tungsten oxide films is essentially coincident with that of WO_3 . Due to its electrochemical and electrochromic properties[26-29], tungsten trioxide has been employed for photoinduced water oxidation[22-25], in gas sensors[30,31], electronic displays, smart windows, sunroofs and rear and side view mirrors[26-29].

At fundamental level, considerable work has been carried out to investigate detailed mechanistic aspects of the electrochemical growth of tungsten oxide in aqueous media, but there is no universally accepted model that accounts for the complete experimental evidence[32]. According to the electrochemical and XPS evidences[33], it has been proposed that the anodic oxidation of tungsten may result in the initial formation of mixture of oxides, namely WO_2 , W_2O_5 and WO_3 , as shown by the following reactions:



However, at higher anodization potentials ($> 2\text{V}$) the dominating species is W^{6+} . The fact that passivity can still be observed in the absence of an outer/precipitated oxide layer, indicates that passivation of tungsten can be attributed to a barrier layer between the metal and the outer layer, in which transmission of ions occurs essentially by vacancy motion. EIS analysis[32] performed during the potentiostatic anodization also suggested that the migration of oxygen vacancies is the main charge transport mechanism across the growing WO_3 oxide film and that it is eventually enhanced by the accumulation of negative charges (corresponding to cation vacancies) at the film/solution interface. Thus, electrochemical anodization of metallic tungsten can be a convenient method for preparing porous photoactive substrates in which the oxide structures are tightly interconnected and strongly bound to the metal collector, both factors concurring to increase the photogenerated charge collection efficiency. It has already been shown that by this approach it is indeed possible to obtain interesting nanostructures that can find application in the field of solar energy conversion[34-36].

Besides detailed mechanistic studies, the most common route for the anodic preparation of porous WO_3 films involves the application of a constant potential to a

metallic tungsten lamina in the presence of aqueous electrolytes containing fluoride anions which establish mild oxide dissolution conditions. It is the achievement of a steady state between oxide dissolution and formation which leads to nanotubular or nanoporous structures. Some authors have also achieved a porous oxide structure (and even some small nanotubular WO_3 domains) by careful application of an appropriate overvoltage intended to reach oxide breakdown conditions in fluoride free electrolytes[35]. Basically, in order to reach breakdown conditions, made possible by the presence of a strong applied field, a harsh treatment consisting in the application of a sudden potential step of several tens of volts has to be adopted. Electrolyte temperature and compositions are also important for reaching reproducible results and a reasonable surface coverage.

Although in some contributions it appears that the monochromatic conversion in the visible region has been optimized following certain annealing conditions (pure oxygen atmosphere, 550 C°), more often are found literature reports in which the nanostructured WO_3 substrates display an high photoactivity in the UV region but give a limited response in the visible frequencies. This is consistent with the reported WO_3 indirect band gaps apparently ranging from 3.25 to 2.9 eV[36,37]. Indeed, we have also verified that, by following or slightly modifying literature approaches, relevant IPCEs in the order of 50 % or higher could be reached in the UV region, but no substantial photoactivity could be observed beyond 430 nm. We started therefore a systematic investigation on the effect of the electrolyte composition on the photoelectrochemical properties of anodized WO_3 electrodes. Our work has been largely inspired by the studies of Grimes et al. [38,39] on the anodic formation of titania nanotubes. We report here on the preparation and characterization of WO_3 electrodes which combine to a large spectral sensitivity, improved charge transfer kinetics and allow for high production yields of hydrogen in 1M H_2SO_4 under a potential bias of 1V vs SCE.

4.2 Experimental Section

Materials: Metallic tungsten foils 99.95% (0.1 mm thick), N-methyl-formamide (NMF), formamide, dimethyl sulfoxide (DMSO), N,N- dimethyl-formamide (DMF), hydrofluoric acid were from Alfa Aesar. Ammonium fluoride, Alconox, sulphuric acid, ethanol, methanol, acetone, were reagent grade products obtained from Fluka or Sigma-Aldrich and used as received.

Nanocrystalline WO_3 electrodes obtained by blading of a sol-gel precursor on fluorine-tin oxide electrodes (FTO, TEC 8, 8 ohm/sq), from Hartford Glass, USA) were prepared according to literature procedures [40-41]

Preparation of WO_3 photoanodes by anodization of metallic tungsten: prior to anodization, tungsten foils ca. 2 x 1 cm, were sonicated in an aqueous alconox solution for 10 minutes, rinsed with water and washed with ethanol and acetone. The potentiostatic anodization was carried out in a two electrode configuration in which the tungsten anode and cathode were cofacially assembled at an average distance of 3 mm. By using a DC power supply (KERT Cosmo 1500/1), the voltage was quickly risen manually to the final value of 40 V, with a rate of approximately 0.5 V/s.

The best electrolyte was composed by NMF/ H_2O 8/2 and 0.05 % NH_4F w/w. An increase in fluoride concentration up to 0.1 % led to identical results. The use of an equivalent (with respect to NH_4F) molar amount of HF instead of NH_4F did not change the structure and the performance of the resulting oxide surface. Electrolytes based on other high dielectric constant organic solvents (DMSO, formamide, DMF, ethylene glycol) were explored in an analogous ratio, i.e. organic solvent/water 8:2 in the presence of ammonium fluoride or HF (0.05 – 0.1 % w/w) with less satisfactory results. The solution was kept unstirred and the anodization was carried out for 72 hours at room temperature (20 ± 3 C°). The typical average current density during the anodization in NMF was 8-10 mA and the total charge exchanged, obtained by integration of the i-t curve was 150 ± 18 C. After the anodization process, the resulting electrodes were rinsed with water, ethanol and acetone and sonicated in water for 10' in order to remove weakly surface bound material or debris, dried under an air stream and fired at 550 C° in air for 1 hour.

X Ray diffractometry: XRD analysis was carried out with an automatic Philips X'pert $\theta/2\theta$ diffractometer using the Cu K α radiation ($\lambda = 1.5416 \text{ \AA}$). In order to eliminate the contribution from the underlying metal, a special thin film optical arrangement allowing to decouple the incidence angle (ω) from the scattering angle (θ) was employed. Thus, data acquisition was performed under a fixed incidence angle ($\omega = 1^\circ$) for 2θ varying from 5° to 90° with a 0.02° step.

Photoelectrochemical Measurements: J-V curves were recorded with an Eco Chemie PGSTAT 302/N potentiostat in a three electrode configuration by using a Pt wire counter electrode and a SCE reference electrode. The typical scan rate was 20 mV/s. Simulated sunlight irradiation was obtained with an ABET sun simulator equipped with a 150 W Xe lamp and an AM1.5 G filter. Incident irradiance was measured with a Molelectron Power Max 500 power meter.

Photon to current action spectra were obtained by using the same three electrode cell described above, by using a 150 W water cooled Xe lamp coupled to an Applied Photophysics monochromator (1200 lines/mm, f:4, band pass 10 nm). The photocurrents were recorded with an Agilent 34401A 6 ½ digits multimeter. The potential bias was generated by an AMEL mod. 552 potentiostat. Incident irradiance was measured by a Centronic OSD 7Q calibrated photodiode and IPCE, expressing the number of generated electron per number of incident photons at a given wavelength calculated according to

$$\text{IPCE}(\lambda) = 1.24 \cdot 10^3 \frac{J(\mu\text{A}/\text{cm}^2)}{\lambda(\text{nm})W(\text{W}/\text{cm}^2)}$$

where J is the photocurrent density, λ is the wavelength of the incident light, and W is the radiant power density at that given wavelength.

Potentiostatic electrochemical impedance spectroscopy (EIS) was performed by using an Eco Chemie Frequency response analyzer by applying a single sinusoidal perturbation of the amplitude of 10 mV in the $5 \cdot 10^4 - 5 \cdot 10^{-3}$ Hz frequency range. The response was acquired with the Eco Chemie Nova 1.5 program and fitted in terms of equivalent circuits with Z-Simp Win 3.22 software. In all cases the experimental data

could be satisfactorily fitted in terms of simple equivalent circuits of the type $R(QR')$ and $R(Q'R')(Q''R'')$ for the anodically grown and the nanocrystalline sol-gel WO_3 respectively, with relative errors below 8%. The capacitance of the semiconductor electrolyte interface (Helmholtz layer) was calculated from the constant phase element (Q) according to the equation $C = Q(\omega)^{1-n}$ [42] where ω is the frequency corresponding to the maximum of the imaginary part of the impedance and n is a fitting parameter. Usually in our case $0.85 < n < 1$.

Qualitative gas chromatographic detection of hydrogen was performed with a Varian CP 4900 Micro Gaschromatograph equipped with a molecular sieves column and a thermal conductivity detector. Moles of produced hydrogen were calculated by measuring the volume of hydrogen gas collected in a 1 ml graduated syringe at $T = 299$ K (26°C) and at $P = 101225$ hPa. The electrolysis yield was calculated from the ratio between the moles of collected hydrogen and those predicted on the basis of the Faraday law.

Diffuse reflectance spectra were acquired on JASCO V570 spectrophotometer and an INS 470 integration sphere.

XPS analysis: the XPS analysis in SURVEY and high resolution mode (MULTI) was performed with a Physical Electronics PHI 5800 apparatus set to explore the surface composition within 10 nm from the surface.

4.3 Results and Discussion

4.3.1 Anodic Formation of WO_3

An NMF based electrolyte was chosen because of the high dielectric constant of such solvent (182.4), which may favor, at any given potential, the formation of an higher charge density on the oxide layer, improving the extraction of W^{6+} and, ultimately favoring oxide growth. In this electrolytic composition water is required to act as an oxygen donor allowing for oxide formation, as indicated by the cyclic voltammograms in the (0-30 V range) reported below. From Fig. 4.1 (A), during the first scan at 1V/s it is clearly observable an anodic current which dramatically drops on subsequent scans as a result of the metal surface passivation induced by the formation of a barrier oxide layer; a different behavior is observed in the water free electrolyte, where a current, about one order of magnitude higher (Fig.4.1 (B)) , assigned to the anodic dissolution of the metal, is recorded with no appreciable changes upon subsequent scans.

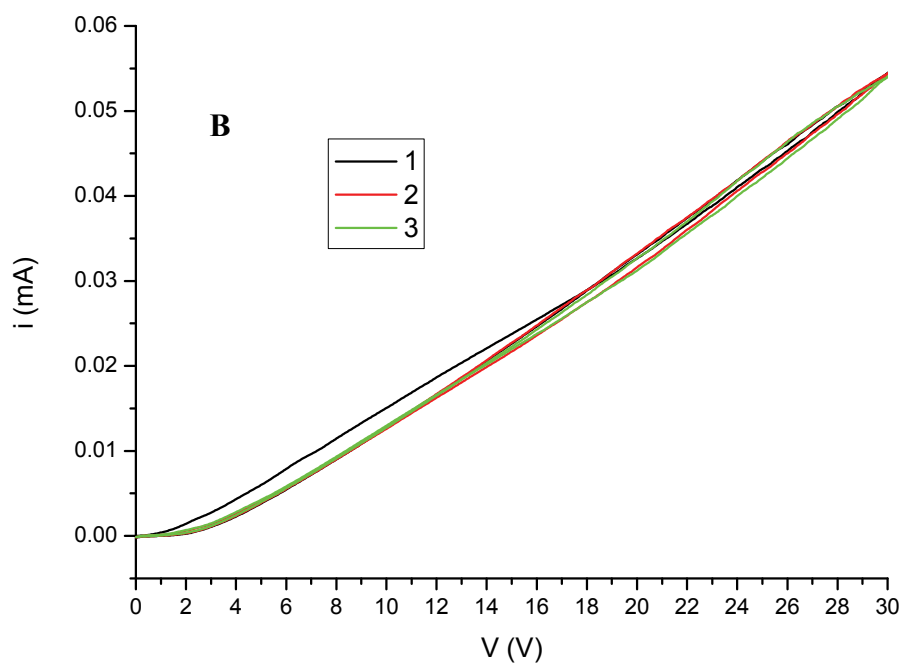
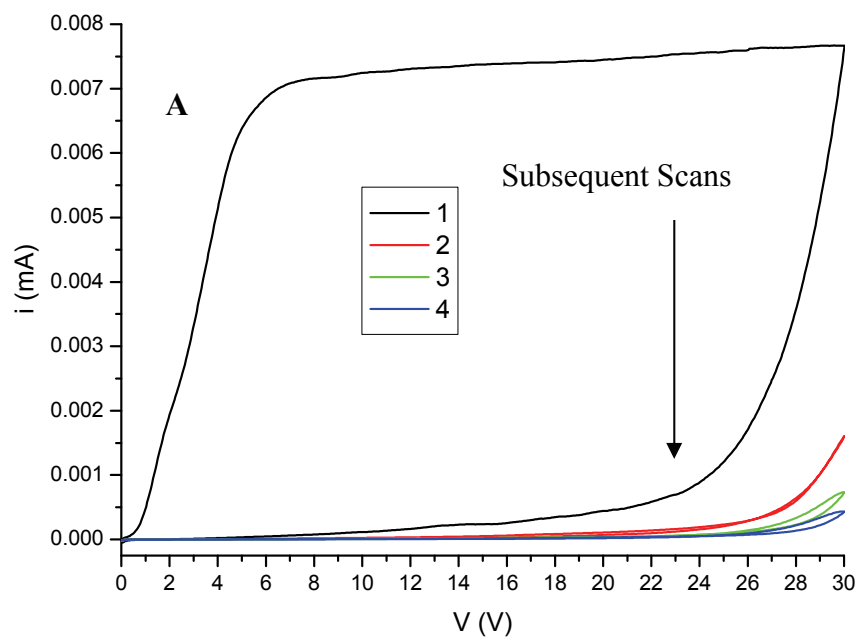


Figure 4.1. Cyclic voltammograms in a two electrode configuration of metallic W in the electrolyte comprised of NMF/water 8/2 + 0.05 % NH_4F (A); (B) NMF + 0.05 % NH_4F . The solutions were not purged with inert gas.

The potentiostatic anodization was carried out with an unstirred solution at room temperature ($20 \pm 3 \text{ C}^\circ$) for several hours (48-72). We have observed that no performance improvement of the photoanodes could be obtained by prolonging the electrolysis time beyond 72 h at a constant applied voltage of 40 V.

Fig.4.2 is indicative of the typical behavior of the current recorded during the anodization in NMF/H₂O 8/2 and 0.05 % NH₄F w/w at room temperature (17 C°). The anodization current shows an oscillating behavior characterized by alternating minima and maxima, most probably determined by the competition between oxide formation and dissolution processes: when the oxide formation overcomes its dissolution (which can be both chemical, caused by reaction with fluorides, and assisted by the intense electric field) the current drops due to a more complete passivation of the metal surface. On the contrary, the oxide dissolution leads to the exposure of fresh metal surface, which undergoes oxidation causing a new increment in the anodic current.

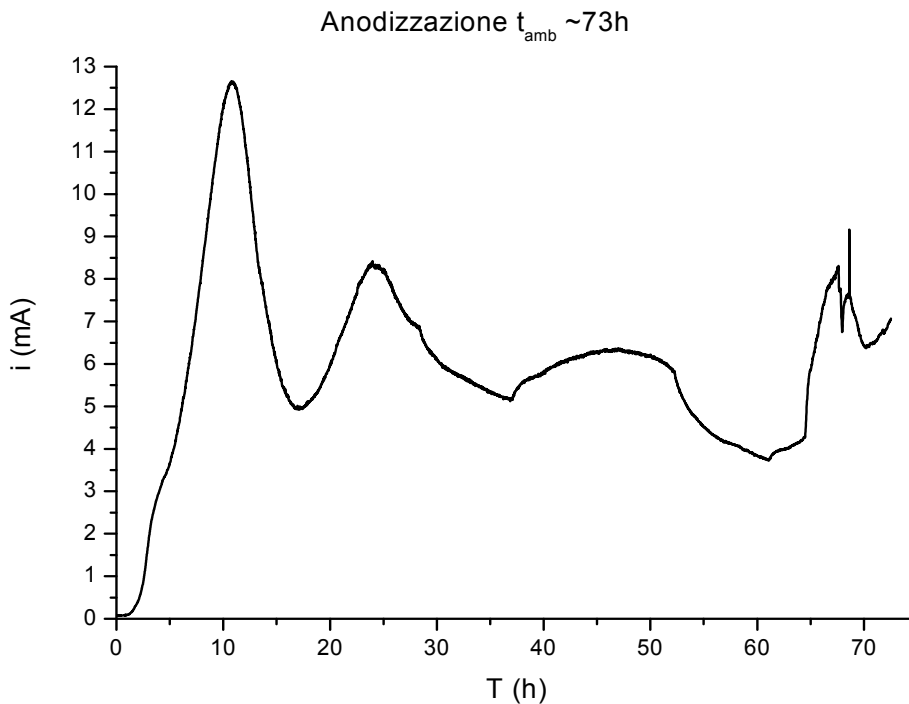


Figure 4.2. Anodization current recorded during the electrochemical tungsten oxide formation in NMF/H₂O 8/2 and 0.05 % NH₄F at 40 V

In DMF and DMSO (Fig. 4.2 and 4.3) the behavior is different: almost complete passivation, probably due to the formation of compact oxide underlayer, is reached at 40-50 h, after an intense current peak which is probably the result of the external oxide dissolution. In both cases the exchanged charge during the entire anodization process, is roughly equivalent to that calculated for the NMF case, of the order of 160 C.

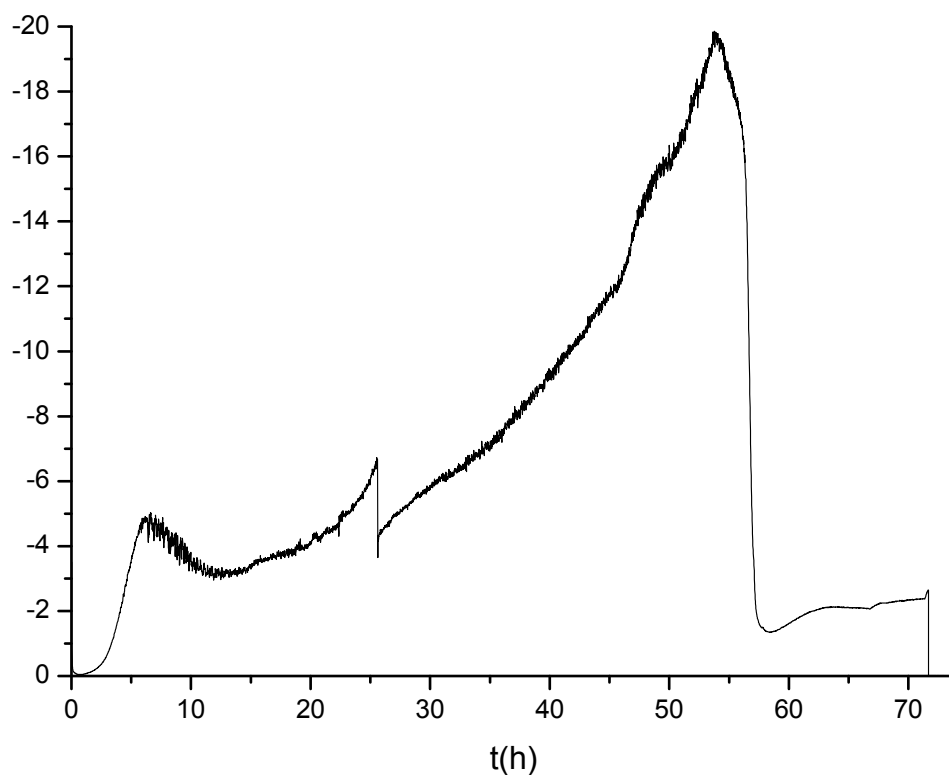


Figure 4.2. Anodization current recorded during the electrochemical tungsten oxide formation in DMSO/H₂O 8/2 and 0.05 % NH₄F at 40 V

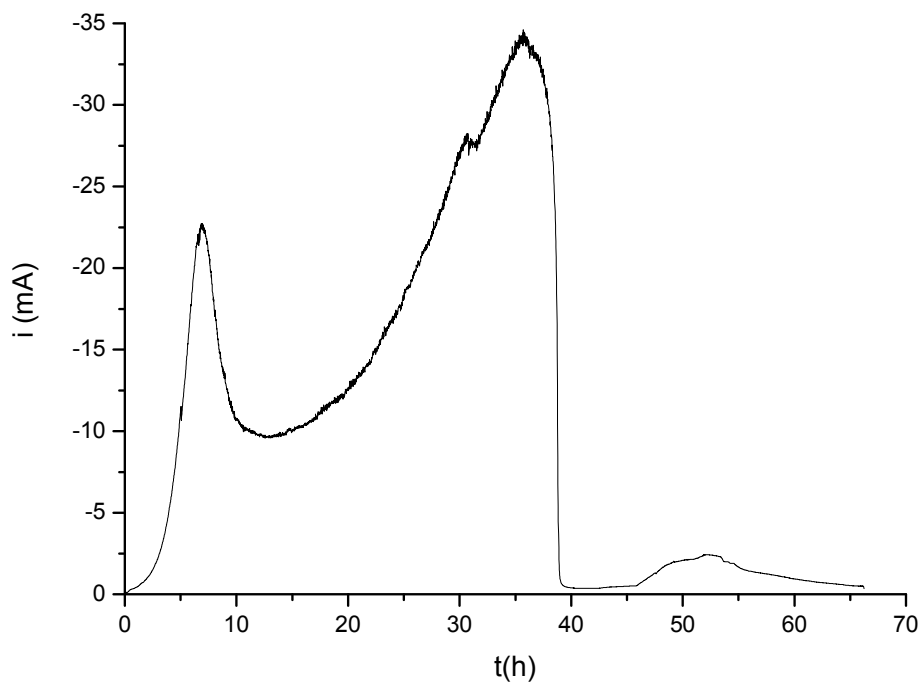
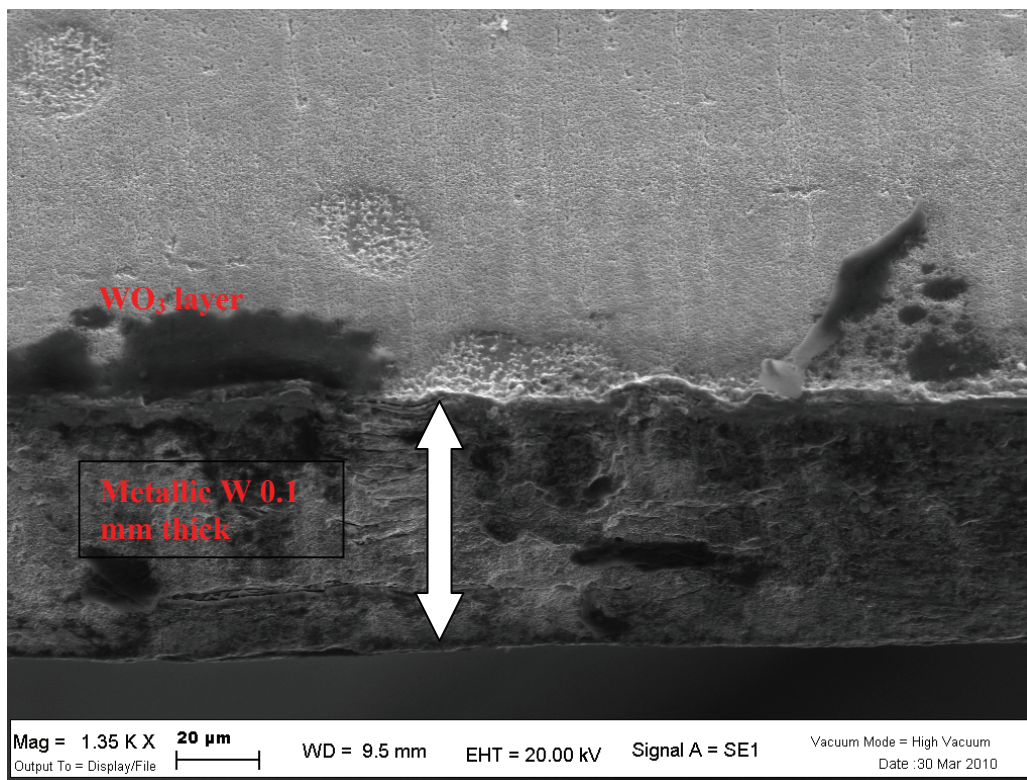


Figure 4.3. Anodization current recorded during the electrochemical tungsten oxide formation in DMF/H₂O 8/2 and 0.05 % NH₄F at 40 V

After 72 h, the anodization in NMF results in the formation of an irregular porous oxide layer 3-5 micron thick (Fig. 4.4), with bundled up structures, ca. 300 nm wide, longitudinally crossed by cracks which give to the surface an overall worm-like appearance (Fig. 4.5A).

a



b

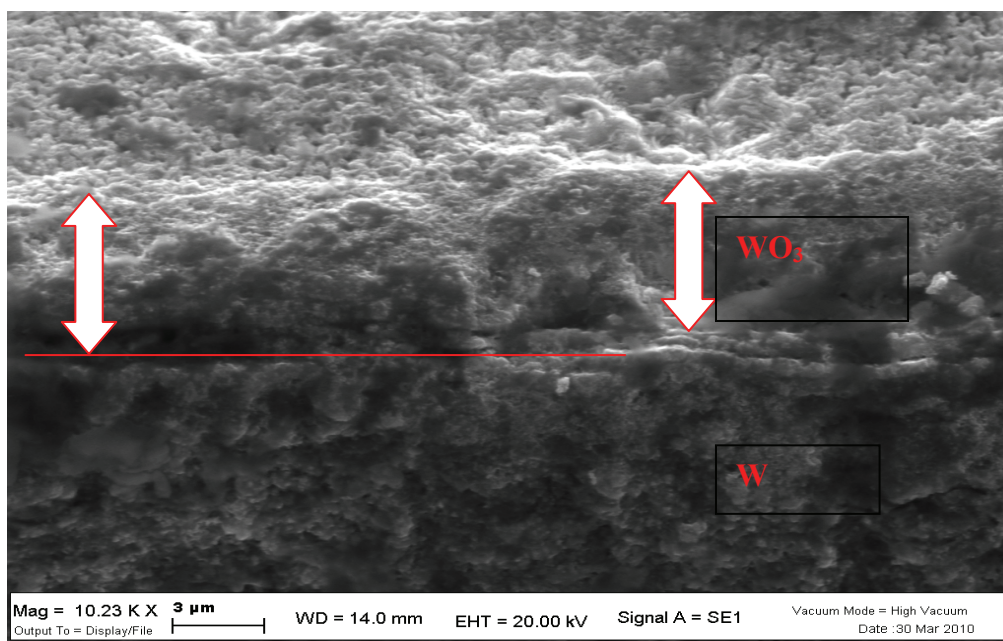


Figure 4.4 SEM cross sectional views of the anodically grown WO_3 in NMF/ H_2O / NH_4F (A) and B (higher magnification) .

AFM imaging gives the topographical picture of the surface, confirming the existence of such morphology and revealing a maximum height difference between structure crests and valleys or pores of approximately 600 nm (Fig. 4.5, (B)). As a comparison, samples anodized in DMF show a similar structure with the presence of some tubular domains (Fig. 4.6A), whereas the anodization in DMSO results in an oxide surface characterized by sintered nanoparticles (Fig. 4.6B). Without respect to the solvent used for the anodization, after a thermal treatment at 550 °C in air, necessary both to induce crystallinity and to establish or consolidate good electrical connections between the nanostructures, small angle XRD confirmed the presence of the expected monoclinic phase of WO_3 (Fig. 4.7). The coherent scattering domains obtained from the Rietveld analysis have in all cases a similar size, of the order of 20 nm. Thus even the larger structures observed in NMF and DMF are composed by nanocrystallites. In many samples a strong morphological anisotropy manifests itself as a preferential orientation of the oxide along the crystallographic planes (111) and (200). Although this feature has been documented also by other authors in different anodization conditions[36], at present we have not been able to establish any clear correlation between crystallographic anisotropy and photoelectrochemical properties of the metal oxide which, within the experimental error, do not vary appreciably.

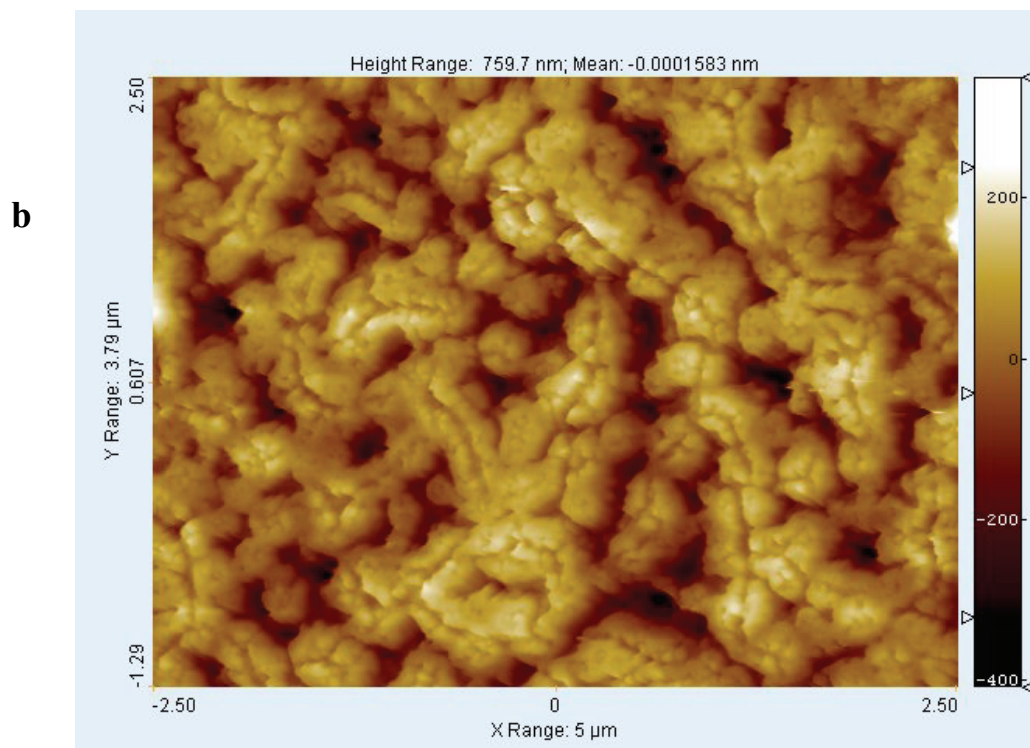
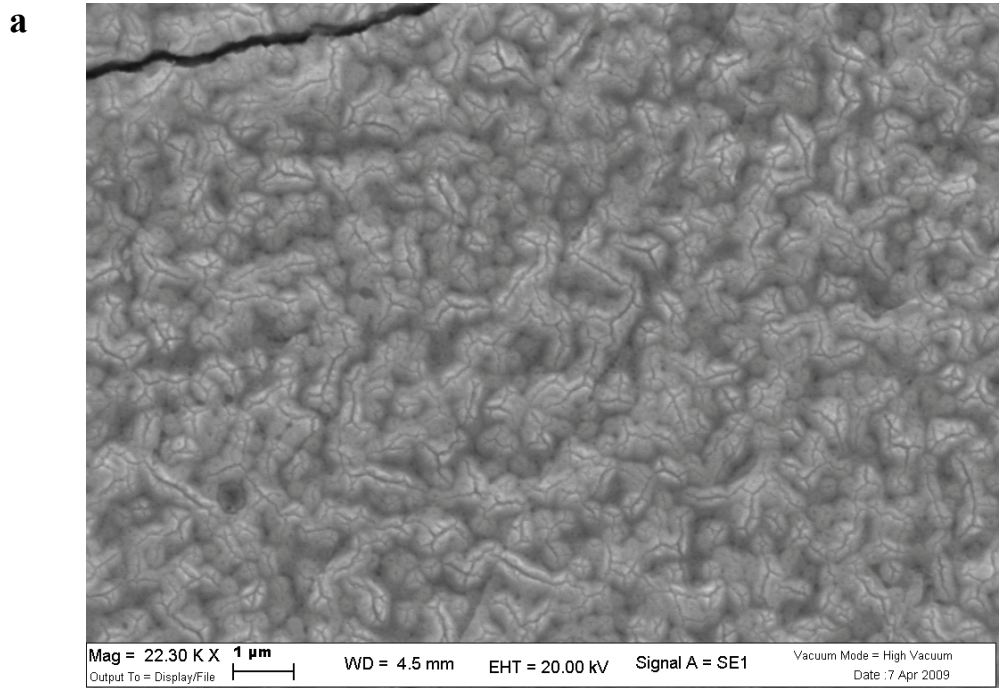
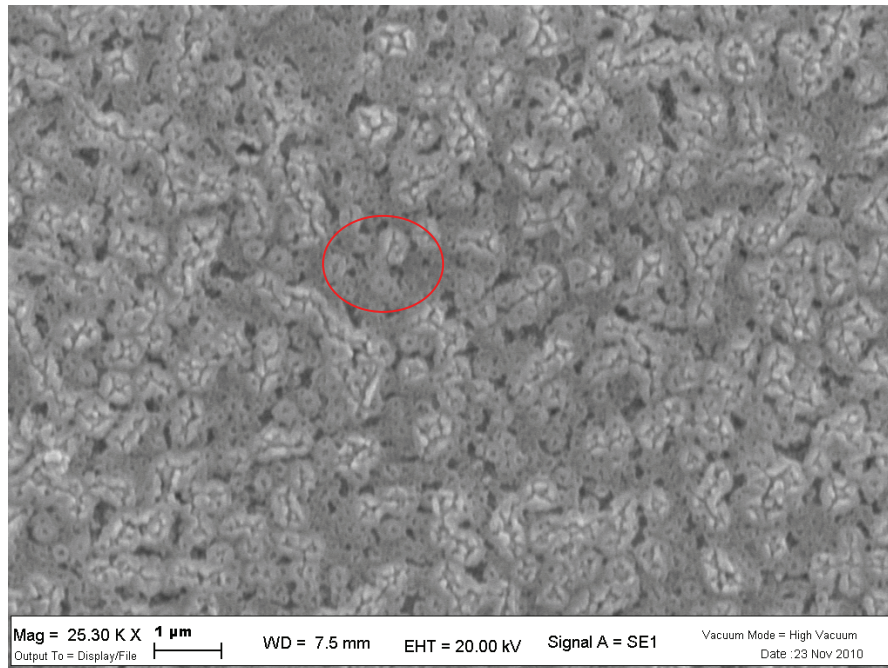


Figure 4.5. SEM (a) and AFM (b) micrographs of anodically formed WO_3 after the annealing process at $550\ \text{C}^\circ$ for 1 h in air

a



b

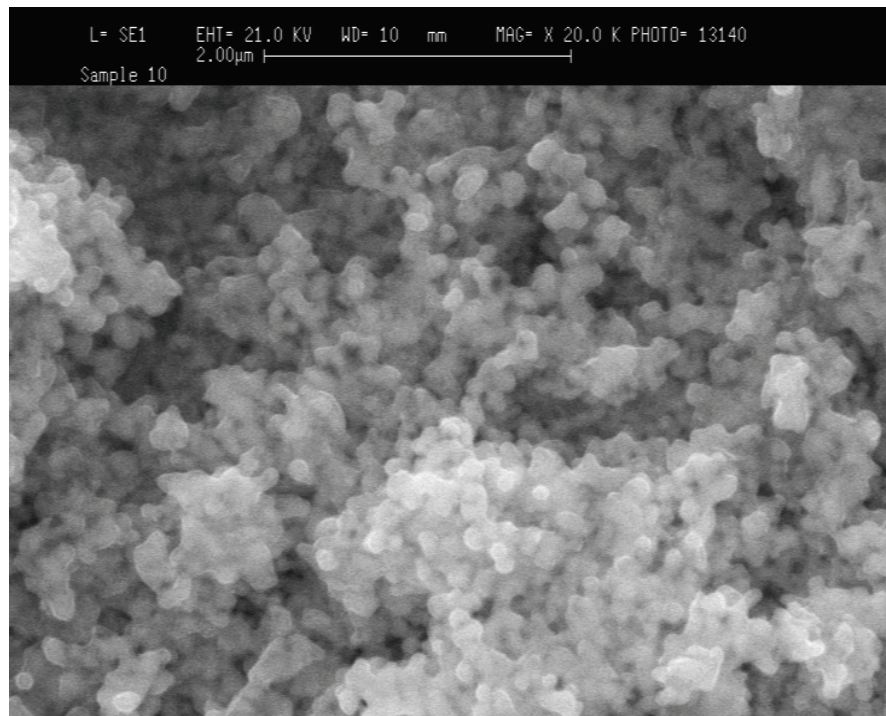


Figure 4.6. SEM micrographs of WO₃ anodized in DMF (25300 x, **(a)**); the red circle evidences some tubular mouths; WO₃ obtained in a DMSO electrolyte (20000 X **(B)**). After the annealing process at 550°C for 1 h

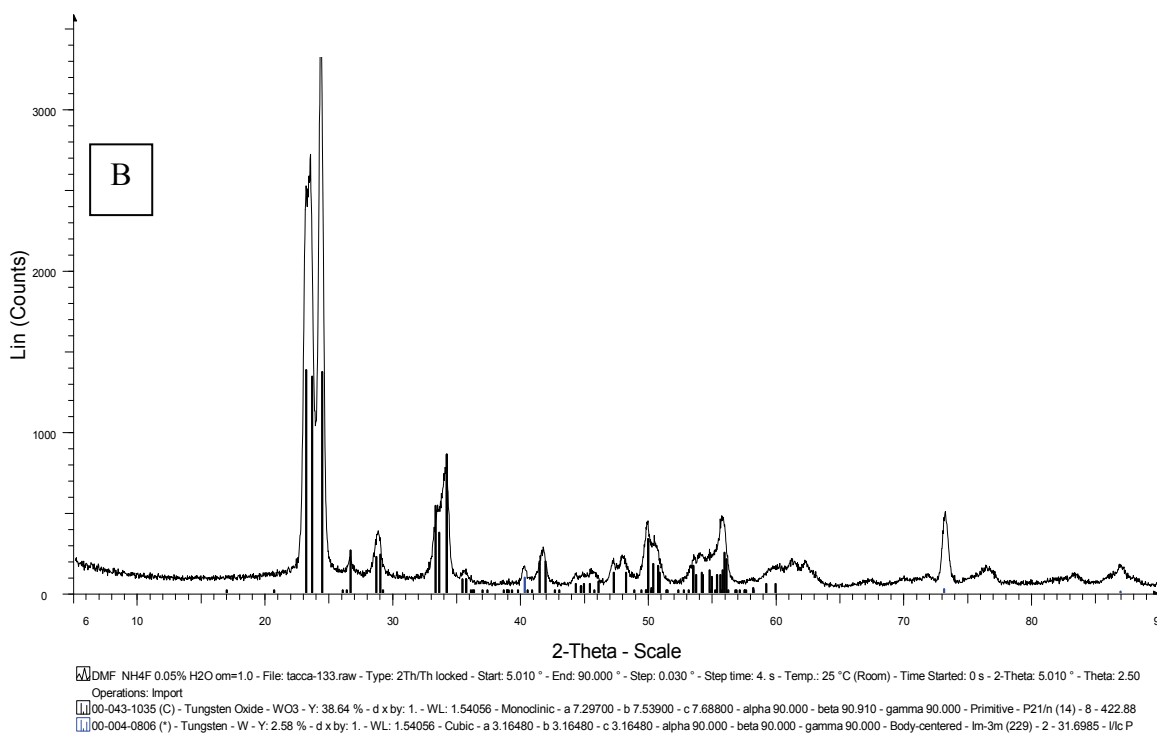
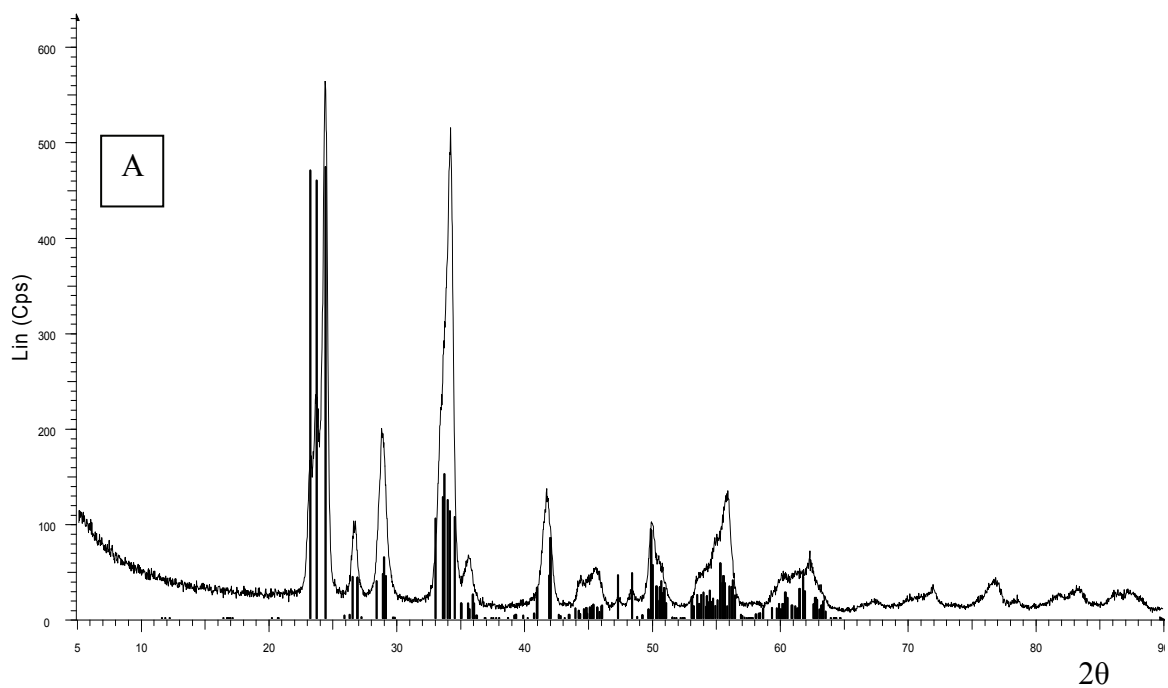


Figure 4.7. Small angle XRD pattern of the anodically grown WO_3 film obtained in: (A) NMF/water 8/2 + NH_4F 0.05 % (B) DMF/water 8/2 + NH_4F 0.05 %; (C) DMSO/water 8/2 + NH_4F 0.05 %

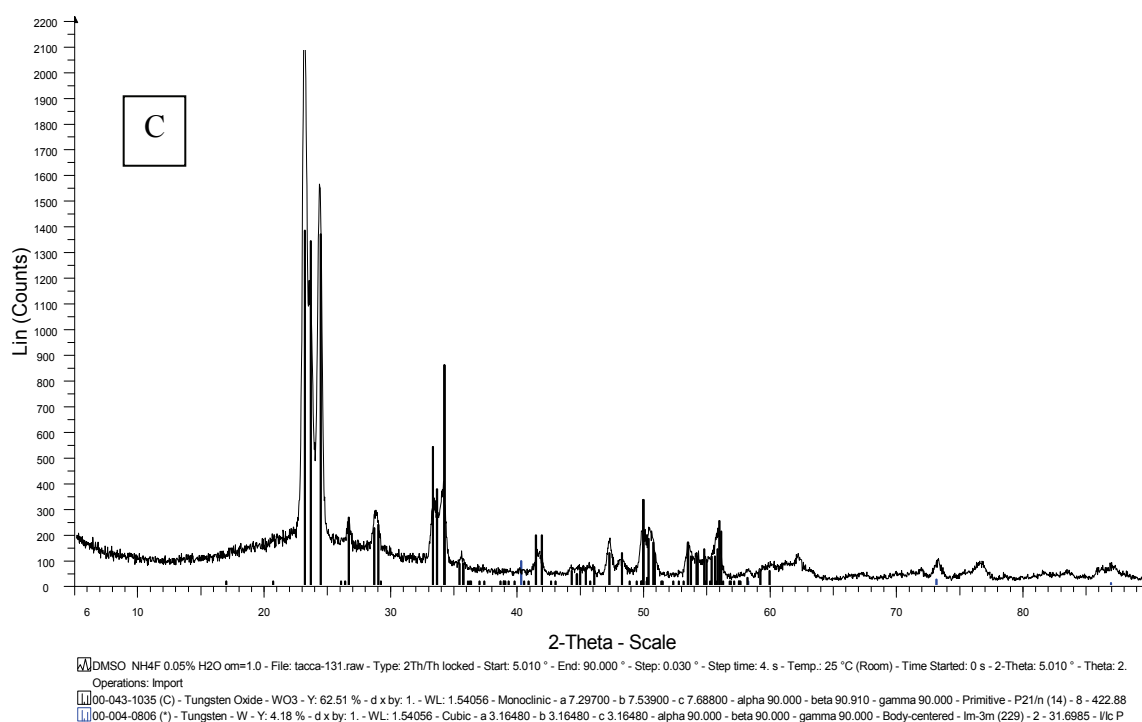


Figure 4.7. Small angle XRD pattern of the anodically grown WO_3 film obtained in: (A) NMF/water 8/2 + NH_4F 0.05 % (B) DMF/water 8/2 + NH_4F 0.05 %; (C) DMSO/water 8/2 + NH_4F 0.05 %

SEM pictures taken at progressive anodization time intervals in the NMF electrolyte provide a picture of the stages involved in the formation of the photoactive oxide. After 2 hours from the beginning of the anodization a compact oxide layer with few corrosion pits is evident (Fig.4.8). After 6 hours the number of pits is increased and thicker oxide walls are present at their borders, suggesting oxide growth and formation of deeper tubes with a circular mouth. With the progress of the anodization the of the adjacent tubes grow in numbers, their walls grow in thickness, coalesce and crack, finally resulting, after 24 hours, to the characteristic surface which is still observed after 48 and 72 hours.

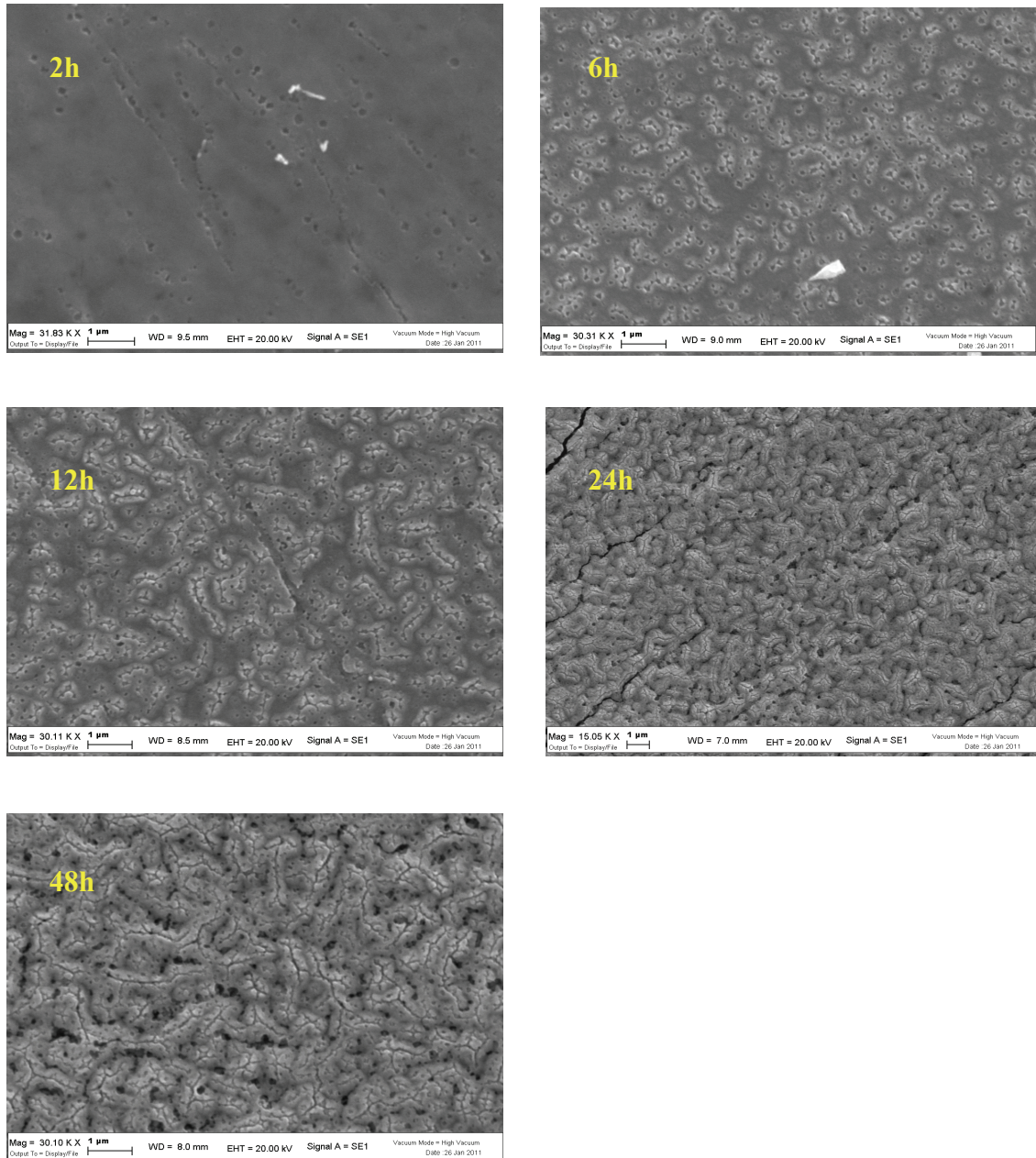


Figure 4.8 SEM micrographs of the WO₃ surface resulting from the anodization in the NMF based electrolyte at different times: 2 h, 6 h, 12 h, 24 h, 48 h. Samples annealed at 550 C° in air before SEM imaging.

4.3.2 Photoelectrochemistry

As demonstrated by the J-V characteristic recorded in 1 M H₂SO₄ (Fig.4.9 A), the typical photoelectrochemical performances of the anodically grown oxides are relevant: under an incident power of 0.15 W/cm² (AM 1.5 G) the anodized WO₃ substrates obtained in the NMF based electrolyte show the highest photocurrent, which approaching 3.5 mA/cm² at 1.5 V vs SCE is largely superior to the performances of photoelectrodes obtained from both DMF and DMSO based electrolytes. Although the surface morphology of the DMF electrodes (Fig.4.8A) is very similar to the NMF electrodes, the former perform much less satisfactorily. As can be seen, the anodized substrates in both NMF and DMSO are superior to the WO₃ electrodes obtained by blade casting of a colloidal H₂WO₄ precursor stabilized with oxalic acid. A double layer colloidal electrode obtained by two subsequent blade casting, with a thickness comparable to the NMF substrate, undergoes only a marginal improvement over the single layer, suggesting that the oxide thickness or the related light harvesting alone is not entirely responsible for the different performances. Other factors, presumably charge transport and charge transfer resistance at the interface and specific electroactive surface area are probably playing the major role in determining the photoelectrode behavior.

The other solvents chosen for the anodization (formamide, water, ethylene glycol) produce performances comparable to the DMF (data not shown), thus the main efforts in our investigations were directed to the characterization of anodically grown electrodes obtained in NMF, DMSO and DMF.

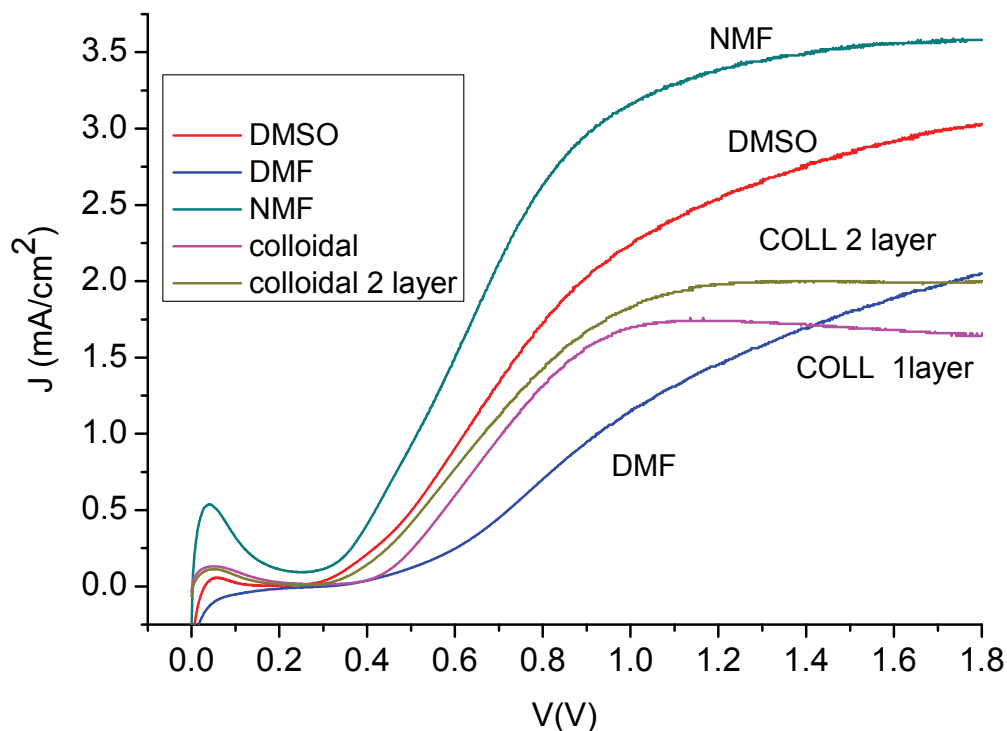


Figure 4.9. JV curves in 1M H₂SO₄ for anodized WO₃ films obtained from different electrolytic compositions : NMF (green), DMF (blue), DMSO (red), colloidal (gold and purple) . AM 1.5 G, 0.15 W/cm²

Under AM 1.5 G incident irradiation the photocurrent generated by NMF anodized electrodes, whose threshold at pH 0 is located at +0.3 V vs SCE, varies in a reasonably linear fashion with the incident irradiance, showing maximum values exceeding 9 mA/cm² under 0.37 W/cm² with an average slope of 0.013 A cm⁻² V⁻¹. The advantage of the electrochemically grown WO₃ over a more conventional WO₃ electrode obtained by standard sol-gel methods (colloidal) [40-41], can be clearly appreciated from Fig. 4.10 (B): while the performance of the two electrodes are quite similar at low power intensities, under strong illumination the anodically grown substrate does not show saturation and clearly outperforms the colloidal film almost by a factor of four.

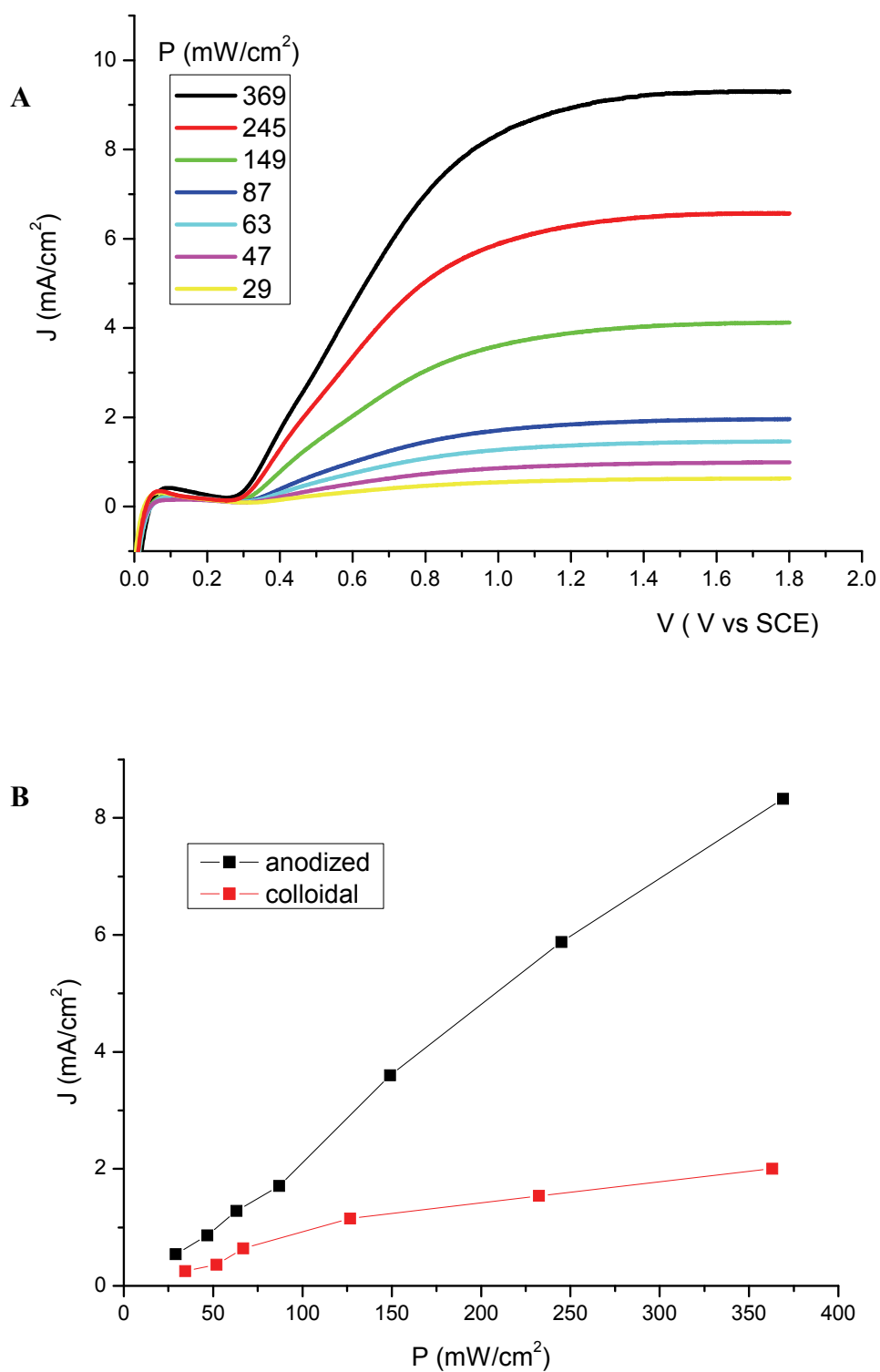


Figure 4.10. J-V curves in 1M H₂SO₄ black (A) as a function of the incident irradiance (AM 1.5 G); (B) photocurrent density taken at 1 V vs SCE vs incident irradiance: (black) anodically grown; (red) sol/gel WO₃

In the presence of an electrolyte composed by 1 M H₂SO₄/CH₃OH 8/2 the plateau photocurrents are nearly doubled, approaching, under strong illumination (ca. 0.3 W/cm²), 16 mA/cm². Concomitantly, it can be observed a negative shift of the photoanodic onset of ca. 100 mV: both effects are consistent with an improved hole scavenging by CH₃OH and/or by a known mechanism of secondary electron injection from surface adsorbed highly reducing CH₃O· intermediates[22]. The J-V curves in H₂SO₄ were found nearly independent from the scan rate in an ample interval ranging from 2 mV/s to 500 mV/s: although this is a typical behavior of a kinetically controlled process, it is also indicative of a relatively facile interfacial charge transfer, in which the steady state is maintained even in the presence of a rapidly changing potential. Referring to figure 4.11, the diffusional “bell” shaped peak at low potential (0-0.2 V interval) which, on the contrary, show a marked scan rate dependence is ascribed to the reversible W⁺⁵→W⁶⁺ oxidation, responsible for the known electrochromism of the WO₃: infact, since the flat band of WO₃ at pH < 1 is located at positive potential (ca. 0.2 V vs SCE, in reasonable agreement with the photocurrent onset at 300 mV vs SCE) a certain amount of W⁵⁺ is created each time the cell is switched on at 0 V vs SCE, at which light electron accumulation conditions in the oxide are established. W⁵⁺ is then re-oxidized as the potential is increased towards more positive values.

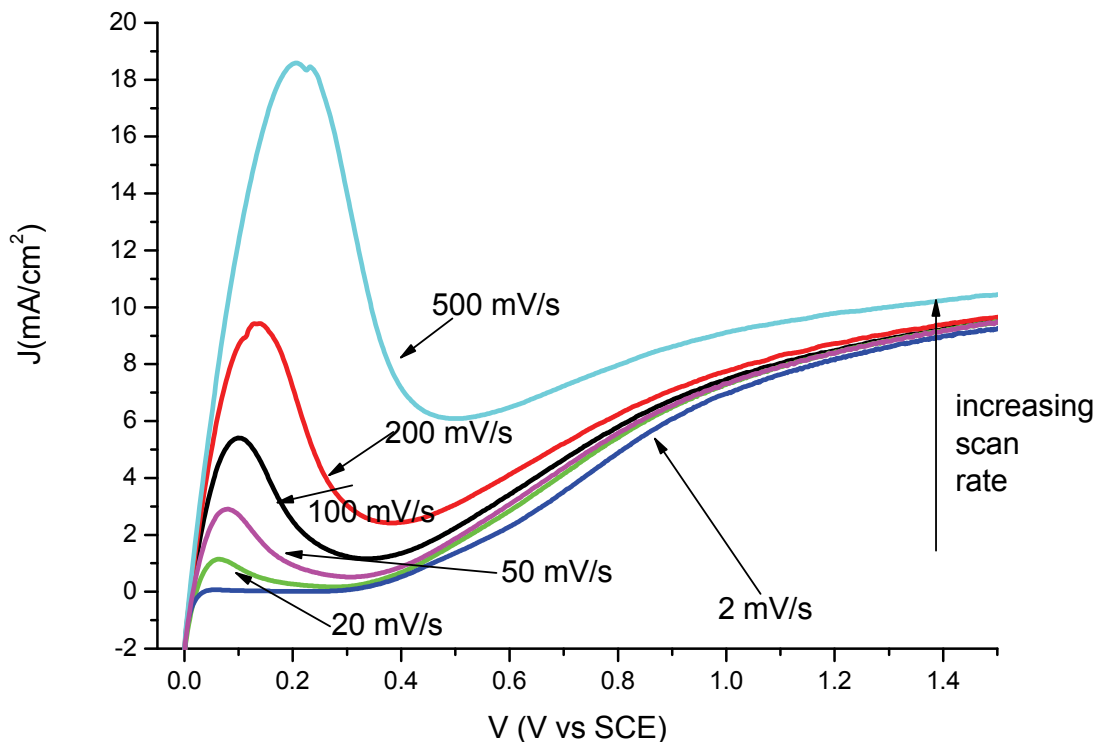


Figure 4.11 J-V curves of anodically grown WO_3 in $1\text{M H}_2\text{SO}_4$ under 0.3 W/cm^2 AM 1.5G irradiation as a function of the scan rate (2mV/s-500 mV/s interval).

In the presence of an electrolyte composed by $1\text{ M H}_2\text{SO}_4/\text{CH}_3\text{OH } 8/2$ the plateau photocurrents are nearly doubled, approaching, under strong illumination (ca. 0.3 W/cm^2), 16 mA/cm^2 . Concomitantly, it can be observed a negative shift of the photoanodic onset of ca. 100 mV : both effects are consistent with an improved hole scavenging by CH_3OH and/or by a known mechanism of secondary electron injection from surface adsorbed highly reducing $\text{CH}_3\text{O}\cdot$ intermediates[22].

A further evidence of effective charge transfer to the electrolyte, as well as of photocurrent doubling in the presence of methanol, acting as a hole scavenger, can be obtained from the J-V curves recorded under modulated (on/off) $\sim 0.1\text{ W/cm}^2$ intensity, in which the rectangular shape of the transients, the presence of small photoanodic transients in the immediate proximity of the flat band potential and the lack of cathodic features are all indicative of efficient photoinduced charge separation and transport²¹ (Fig. 4.12).

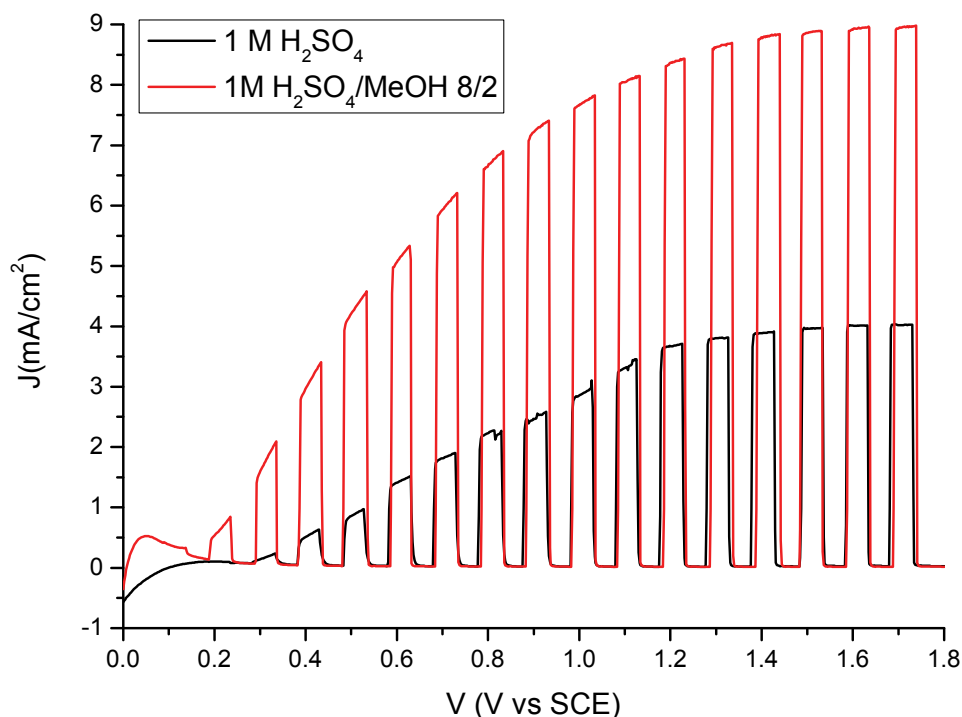


Figure 4.12. Shuttered J-V curves in 1 M H₂SO₄ (black) and 1 M H₂SO₄/CH₃OH 8/2 (red). Incident irradiance 0.120 W/cm²

The evolution of hydrogen from the cathode of the photoelectrochemical cell can be visually assessed in the presence of photocurrents $\geq 1 \text{ mA/cm}^2$. Under such conditions it is easy to collect hydrogen in a pneumatic syringe and calculate the electrolysis yield (R%) from the ratio of the moles of collected hydrogen and those theoretically predicted on the basis of the Faraday law. The rate of production of hydrogen in 1 M sulfuric acid can be calculated as $2 \text{ ml cm}^{-2} \text{ hour}^{-1}$, which is nearly tripled in the presence of CH₃OH ($\sim 6 \text{ ml cm}^{-2} \text{ hour}^{-1}$), in agreement with the enhanced photocurrent and the higher electrolysis yield which approach 100 %. It must be noted that in the presence of MeOH, due to a decreased surface tension, the detachment of hydrogen bubbles from the Pt surface of the counter electrode was faster than in pure water/sulfuric acid, where at the end of the electrolysis bubbles were observed to still adhere to the platinum spiral (Fig. 4.13)

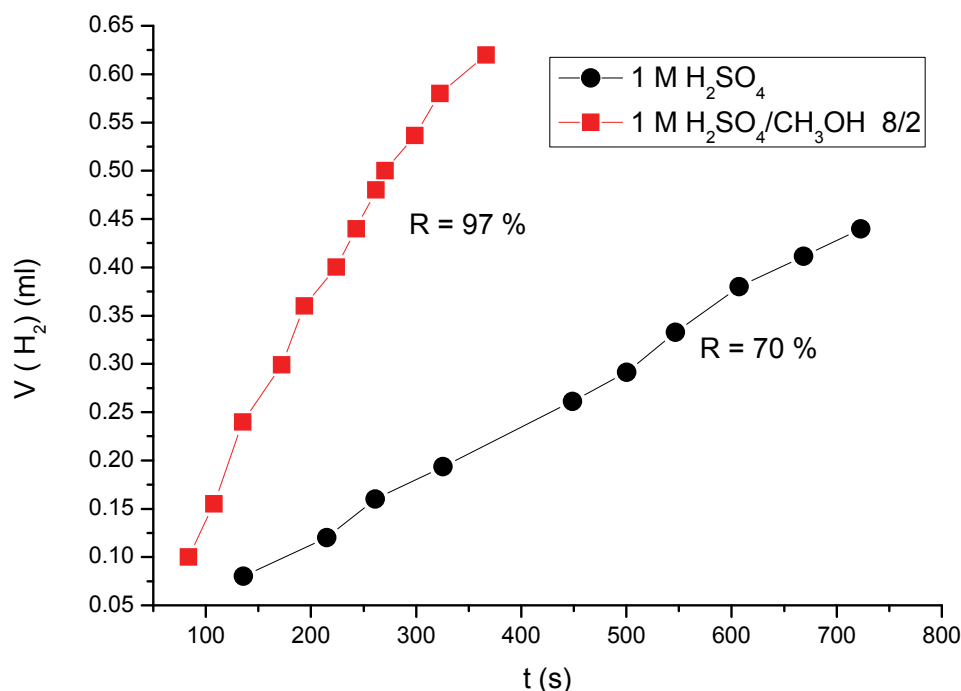


Figure 4.13. Volume of photoproduced H_2 at $T = 299$ K and $P = 101225$ hPa under 1 V potential bias and 0.25 W/cm^2 Am 1.5 G irradiation. Photoactive surface = 1 cm^2 .

The photocurrent spectrum recorded under monochromatic light under a potential bias of 1 V (Fig.4.14) shows a maximum of 280 $\mu A/cm^2$ around 390 nm and its subtended area gives an integrated photocurrent in the order of 2.5 mA/cm^2 , consistent with the photoanodic plateau observed under polychromatic light under 1 sun illumination. The photocurrent action spectra (IPCE = number of electrons/number of incident photons) (Fig. 4.15) recorded in sulfuric acid indicate an high photon to current conversion, approaching 70 % in a broad region in the UV and extending deeply in the visible region, thanks to a secondary maximum at 400 nm ($IPCE_{max} = 45$ % at 1.5 V vs SCE) whose onset is located at 490 nm. This leads to a calculated indirect band gap of 2.5 eV (Fig.4.4), which is significantly lower (by at least 0.3 -0.4 eV) than values commonly reported for other nanostructured anodically grown WO_3 substrates and agrees with those reported for monoclinic WO_3 films obtained by exploiting high vacuum technologies like thermal evaporation or radio frequency sputtering[45-46]. As a comparison, WO_3 films electrochemically produced either in water/HF/ NH_4F according to the procedure described by Guo et.al, [36] or in other organic solvents

like DMF or by sol gel methods, do not show any relevant photoconversion beyond 430-440 nm. But interestingly, electrodes produced in DMSO/water/NH₄F do show a spectral extension analogous to the NMF case, although the absolute IPCE is generally lower and its surface morphology is entirely different. Moreover, substrates produced in NMF/water/NH₄F at 50 C° show the loss of the characteristic wormlike structures which are replaced by a nanoparticle network similar to that observed in the DMSO case, but, still, a wide spectral sensitivity (fig. 4.16-4.17) is measured, with maximum IPCEs of the order of 40-50% and a photoaction onset at 480 nm which, again, bears close resemblance to that obtained in DMSO.

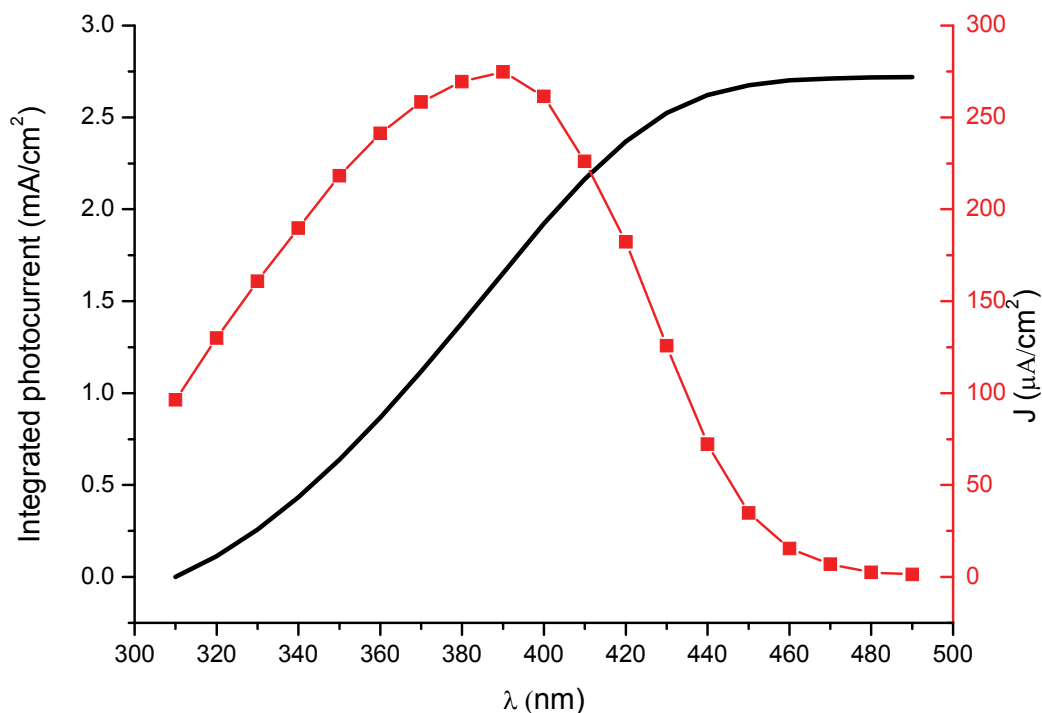


Figure 4.14. Photocurrent spectrum of a typical anodically grown WO₃ film (NMF procedure, red) and the relative integrated photocurrent (black). 1M H₂SO₄, 1 V vs SCE.

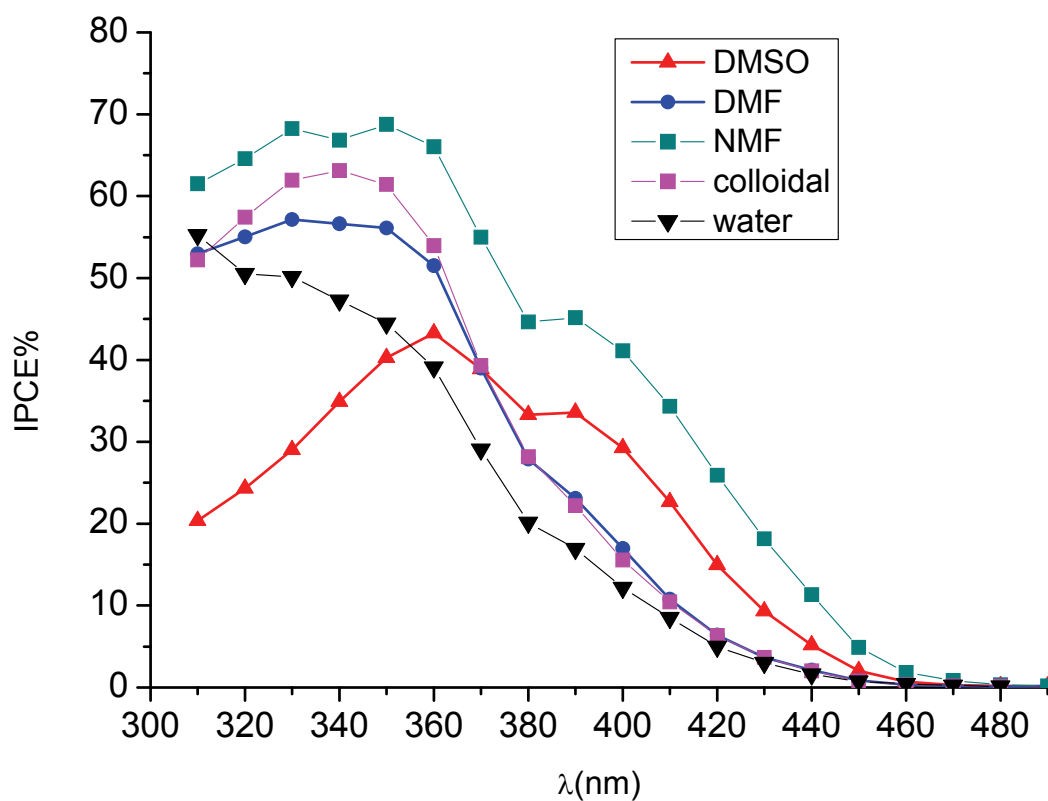


Figure 4.15. Photoaction spectra (IPCE vs λ) in 1M H_2SO_4 of a WO_3 film grown in NMF under 1.5V vs SCE potential bias, compared to a WO_3 substrate electrochemically formed in water^{36b} (black), DMF (blue), DMSO (red) and to a nanocrystalline electrode produced by sol-gel methods (violet). Values not corrected for the transmittance of the electrochemical cell

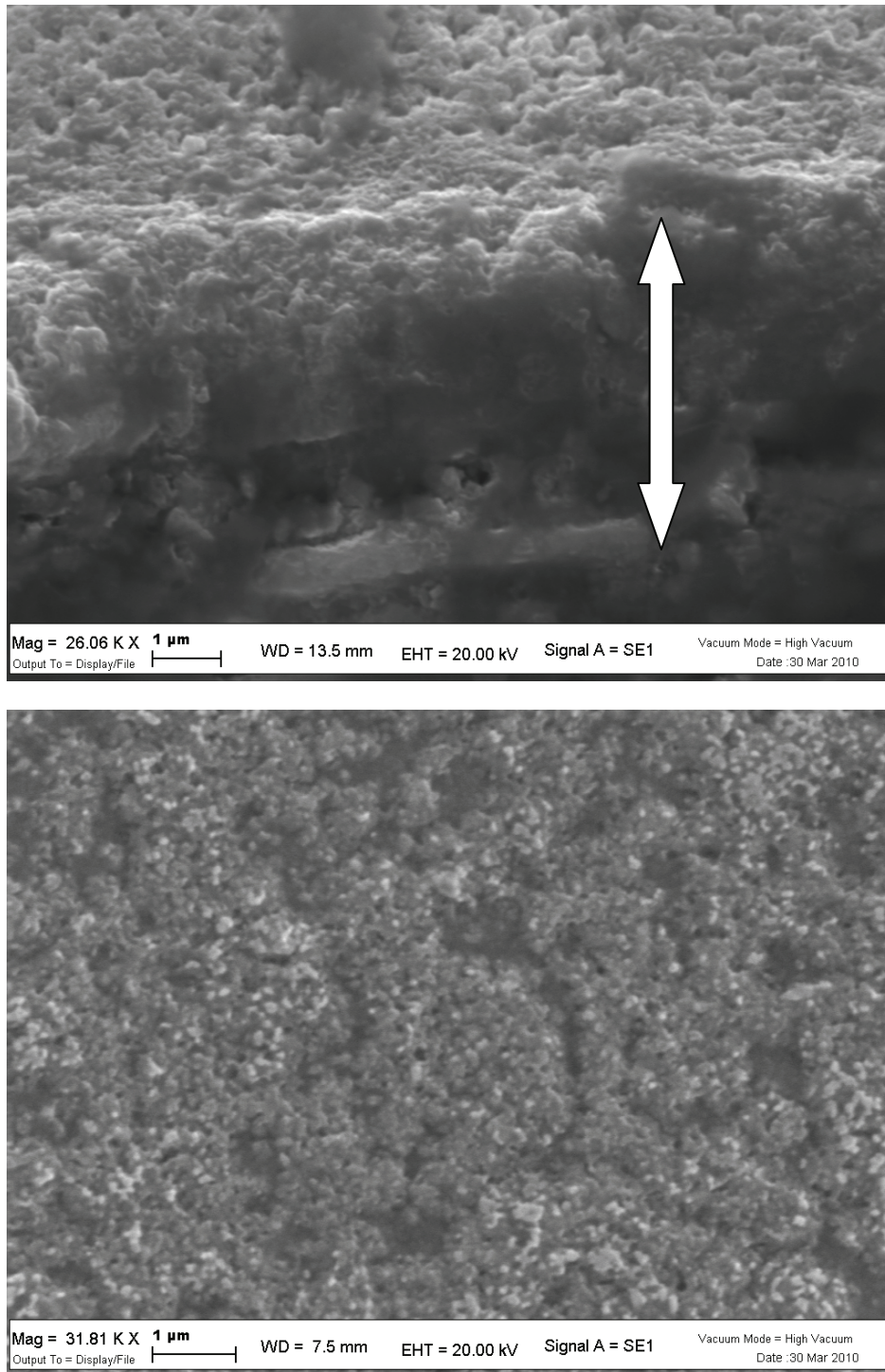


Figure 4.16. Cross sectional (Top) and top (bottom) surface view of a WO_3 electrode produced at $50\text{ }^\circ\text{C}$ in NMF/ H_2O 8/2 + NH_4F 0.5 %

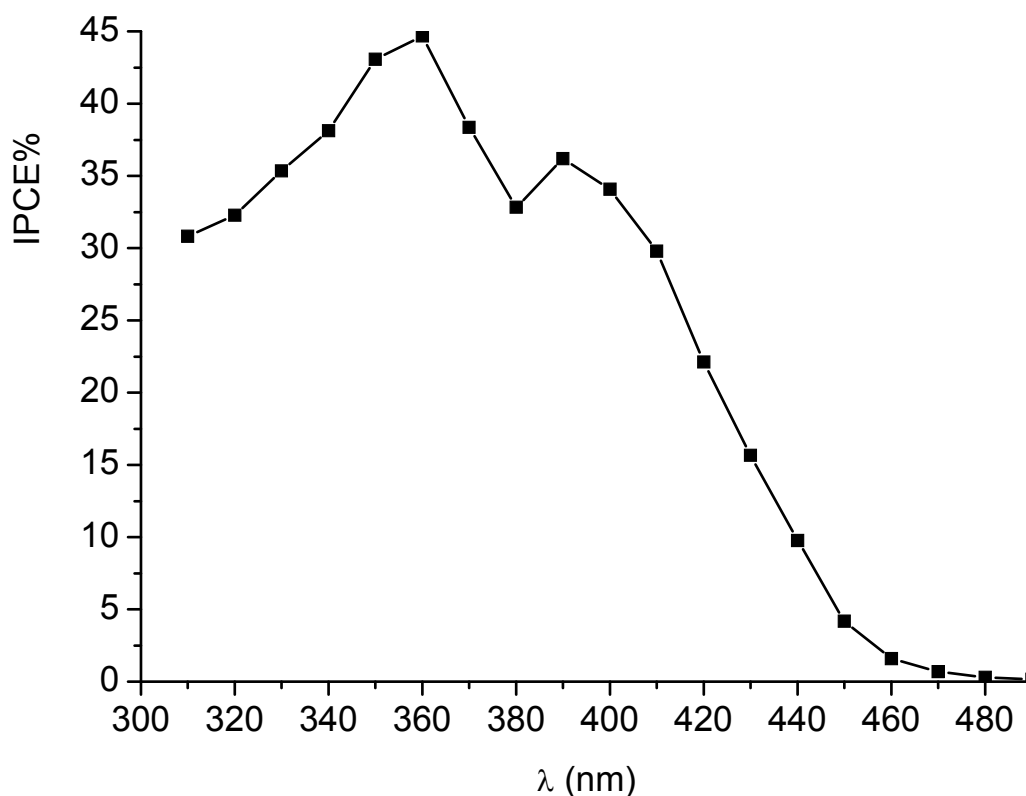


Figure 4.17. Photoaction spectrum of the WO_3 photoanode prepared by anodization at 50°C in $\text{NMF}/\text{H}_2\text{O}$ 8/2 + NH_4F 0.5 %

Thus, it is difficult to correlate the extended spectral response with purely structural and morphological data. Although, at first sight, nitrogen doping during the electrochemical growth of the oxide in the presence of nitrogen donating compounds (amides, NH_4F) could be invoked to explain the wider spectral sensitivity, the inspection of XPS data (Tab.1) lead us to believe that the presence of lattice or surface bound nitrogen atoms is not of primary importance in the determination of the photoelectrochemical performances of the WO_3 films: first, by considering the NMF anodized substrates, the relative percentage of nitrogen on the WO_3 surface is highly variable (from 1.2 % to 5%) and apparently uncorrelated with both photoconversion and spectral sensitivity; second, a lower but still comparable fraction of N is present also in substrates anodized in both water and DMF based electrolytes which, however, do not show any relevant spectral response at longer wavelengths. Moreover, although quite difficult to compare due to the metal background and to the variable thickness of

the oxide, the normalized diffuse reflectance spectra of the WO₃ substrates obtained in NMF, DMF, and DMSO (Fig. 4.18) show similar optical properties, with a reflectance minimum around 380-390 nm, corresponding to the absorption maximum of the oxide. Thus, it is probably the number of the active sites capable to undergo charge transfer to the solvent the key to understand the enhanced spectral sensitivity. This is particularly true for those wavelengths close to the visible absorption threshold of the oxide (430-470 nm) which have a longer penetration depth in the material and can create electron hole pairs in the inner part of the oxide which may not be effectively permeated by the electrolyte. Since the injection of electrons in the conduction band of the solid is compensated by protons (in the case of H₂SO₄) from the electrolyte, one simple way to probe the true electroactive area of the photoactive film in a given electrolyte relies on the estimation of the charge exchanged by subsequent WO₃ reductions and re-oxidations in the dark by a potential step chronocoulometry (Fig. 4.19), or equivalently, by integrating the cyclic voltammogram in an appropriate potential range (-300/+1000 mV vs SCE) (Fig 4.20). It is clearly evident that the amount of the exchanged charge measured for electrodes produced by the DMSO or NMF anodization route is largely superior to both colloidal and DMF samples suggesting, in this case, an equivalently larger specific electroactive surface, which enhances the possibility of successful hole transfer to the electrolyte.

Table 1. Surface composition in atomic percentage of anodized WO₃ obtained from XPS survey scan. The N peak was observed at a B.E. of 400 eV and was probably substitutional. Carbon was present as a surface contaminant. Average of five samples.

| Anodization condition | W % | O % | N % | C % | N%/W% |
|-----------------------|------------|-----------|-----------|------------|-------------|
| NMF | 22.2 ± 1.4 | 52.4± 4.9 | 3.3 ± 1.7 | 22.1 ± 5.3 | 0.15 ± 0.08 |
| DMF | 21.9±1.6 | 44.5±5.3 | 2.3±1.2 | 31.3±6.2 | 0.1 ± 0.05 |
| H ₂ O | 20.9±1.4 | 46.2± 4.8 | 1.9±1 | 31±5.8 | 0.09±0.05 |
| Ethylene Glycol | 19.2±1.7 | 39.3±3.2 | 1.7±0.7 | 39.8±3 | 0.09±0.04 |

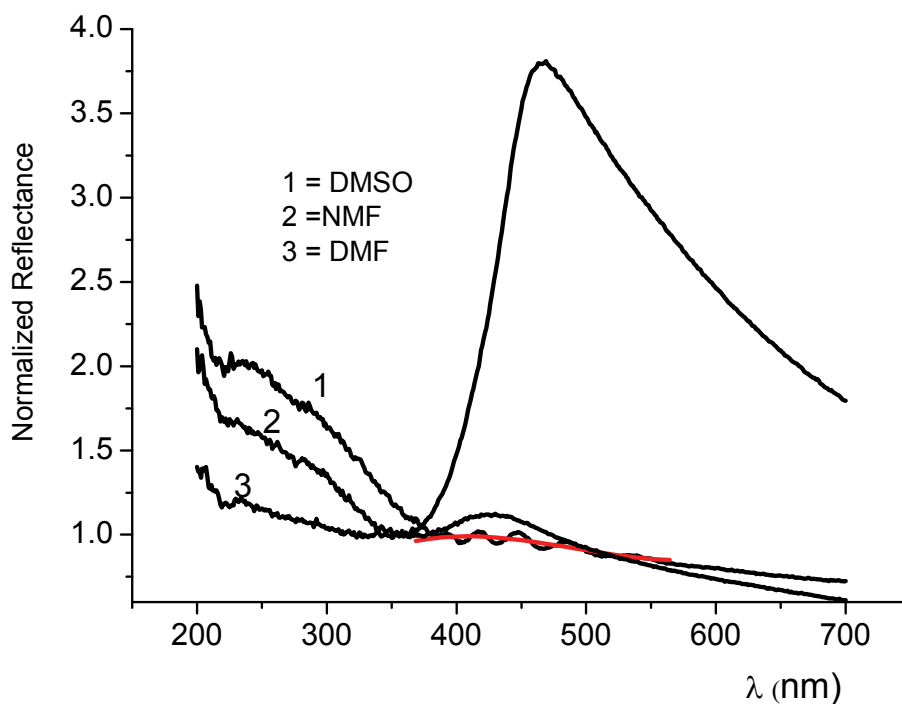


Figure 4.18. Diffuse reflectance of WO_3 substrates anodized in DMSO, NMF and DMF based electrolytes. The red line in spectrum (3) (DMF) is due to a polynomial fitting introduced to reduce the noise introduced by interference fringes.

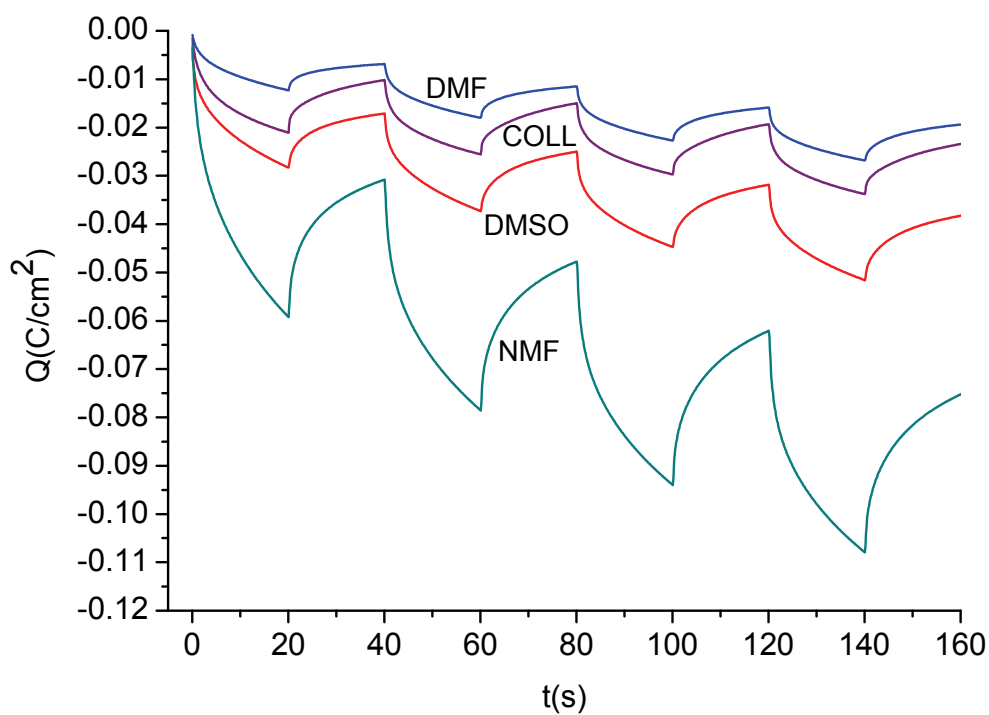


Figure 4.19. Chronocoulometry in dark conditions upon $-300 \text{ mV}/+1000 \text{ mV}$ vs SCE potential step: (NMF dark cyan), DMSO (red), colloidal (purple) and DMF (blue).

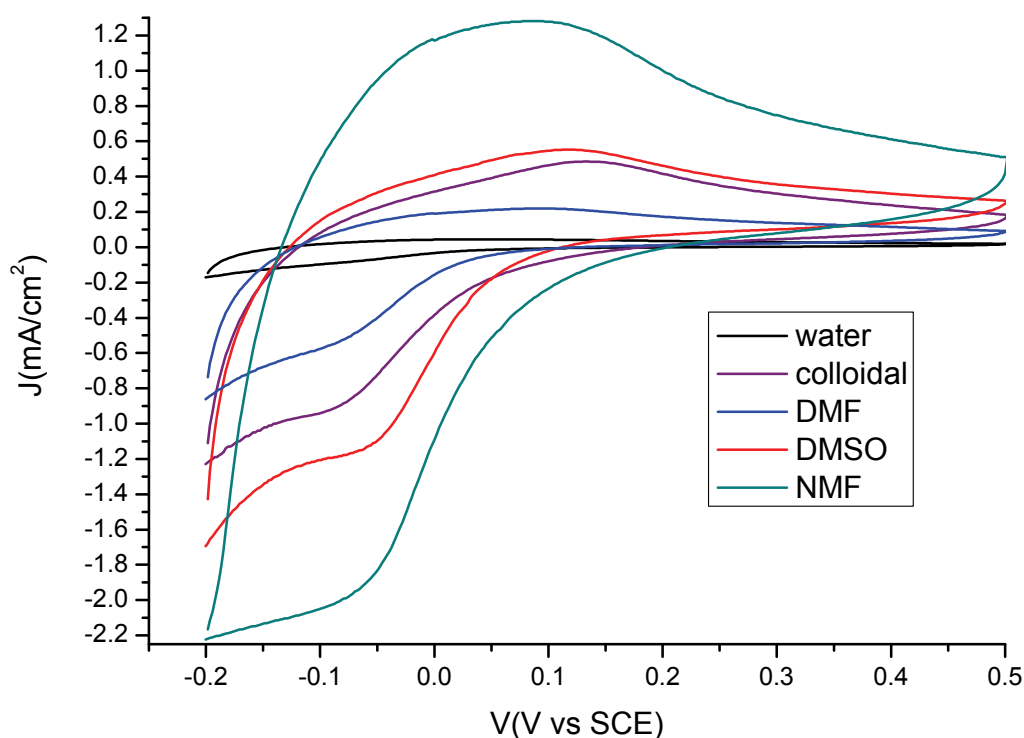


Figure 4.20. Comparative cyclic voltammetry in 1 M H_2SO_4 for a series of WO_3 electrodes obtained after 72 h anodization in NMF (dark cyan), DMSO (red), DMF (blue), pure water water (black) fluoride containing electrolytes.

The IPCE (Fig. 4.21) of the best NMF photoelectrodes undergoes a significant enhancement in the presence of sacrificial hole scavengers like methanol or formic acid, reaching a value close to 100 % in the UV region where the light absorption is complete. The secondary maximum nearly doubles in intensity, approaching values of the order of 80 %. Since, to a first approximation, the presence of a scavenger cannot influence the charge transport through the solid phase to the collector, the observed increase in IPCE is most probably the result of a more facile charge (hole) transfer process to the electrolyte (expressed by the interfacial charge transfer efficiency term η_i). This also implies an almost unitary charge transport efficiency (η_{tr}) at the interface given that, at least in the UV region, $\text{APCE} = 1 = \eta_{tr} \eta_i$ [47] and that, in pure water, limitations in interfacial kinetics may eventually represent, in this case, the primary loss mechanism.

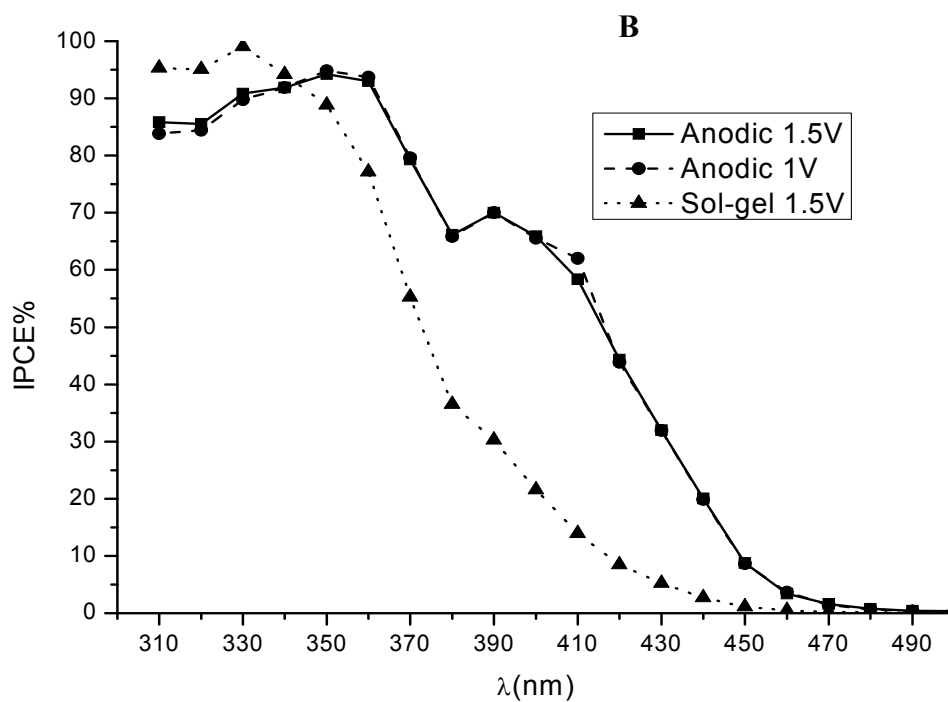
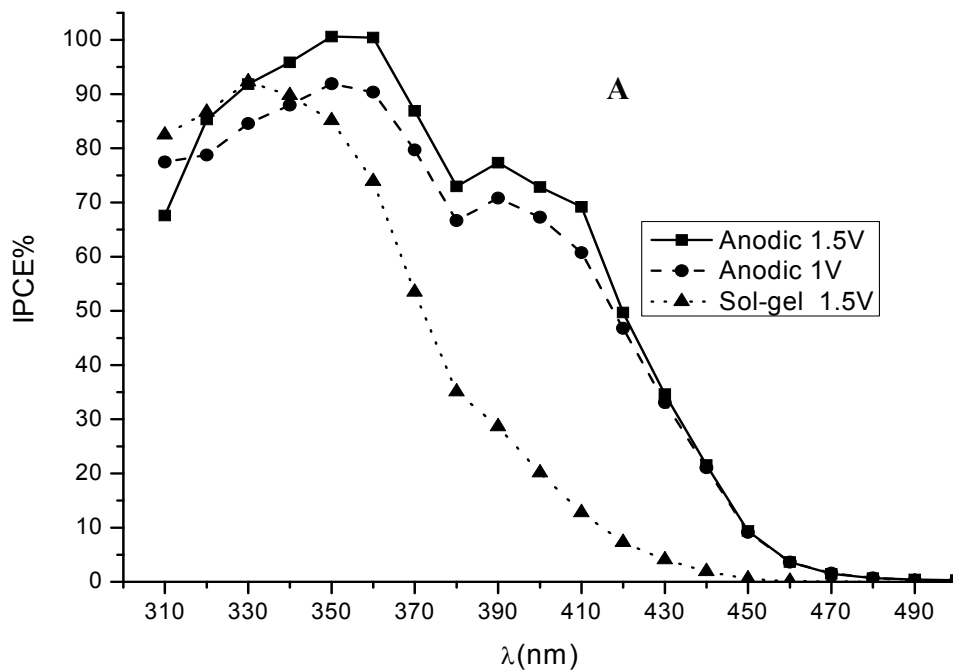


Figure 4.21. Photoaction spectra of WO_3 (NMF procedure) in the presence of sacrificial electron donors : (A) 20 % methanol in 1 M sulfuric acid; (B) 1 M formic acid/ 1 M sodium formate; squares and circles: anodically grown WO_3 films in the presence of a bias equal to, respectively, 1.5 and 1 V vs SCE compared to a sol/gel WO_3 film biased at 1.5 V vs SCE.

In fact, the impedance spectroscopy of the WO_3 photoanodes under strong illumination (ca. 0.3 W/cm^2) reveals that the photoelectrode is essentially dominated, in the complex plane, by a kinetic loop (Fig. 4.22 and Fig. 4.24): the single semicircle with a maximum in the 1-10 Hz interval (depending on the potential) can be reasonably attributed to the charge transfer across the semiconductor-electrolyte interface. It can be well fitted by a single $R(QR')$ equivalent circuit[48], where R is the ohmic contribution, Q is the constant phase element which takes into account non idealities in the capacitance of the Helmholtz layer and R' is the charge transfer resistance. The inverse of the charge transfer resistance (cm^2/Ohm) plotted as a function of the applied potential is in good agreement, in both shape and magnitude, with the derivative (slope) of the J-V curve taken under identical illumination conditions (Fig. 4.23), corroborating the correctness of our assignment. Moreover, as it would be expected in the case of an interfacial process, the charge transfer resistance is dependent upon electrolyte composition, and decreases in the presence of methanol acting as an electron donor (Fig. 4.22(B)) confirming that, effectively, the observed impedance loop is originated by the hole transfer to the electrolyte. When compared to a sol-gel nanocrystalline WO_3 substrate sintered on FTO, the anodically grown substrate exhibit a substantially decreased interfacial hole transfer resistance (64 vs 240 ohm/cm^2) and the lack of the small high frequency loop ($> 10^4 \text{ Hz}$) attributed to the FTO/ WO_3 interface, suggesting an excellent ohmic contact with the metallic tungsten (Fig.4.24). Both factors contribute to explain the good performance of the anodically grown WO_3 electrodes. A smaller charge transfer resistance can be particularly important under intense illumination, when, in order to sustain the photocurrent, large numbers of photogenerated minority charge carriers have to be efficiently injected into the electrolyte.

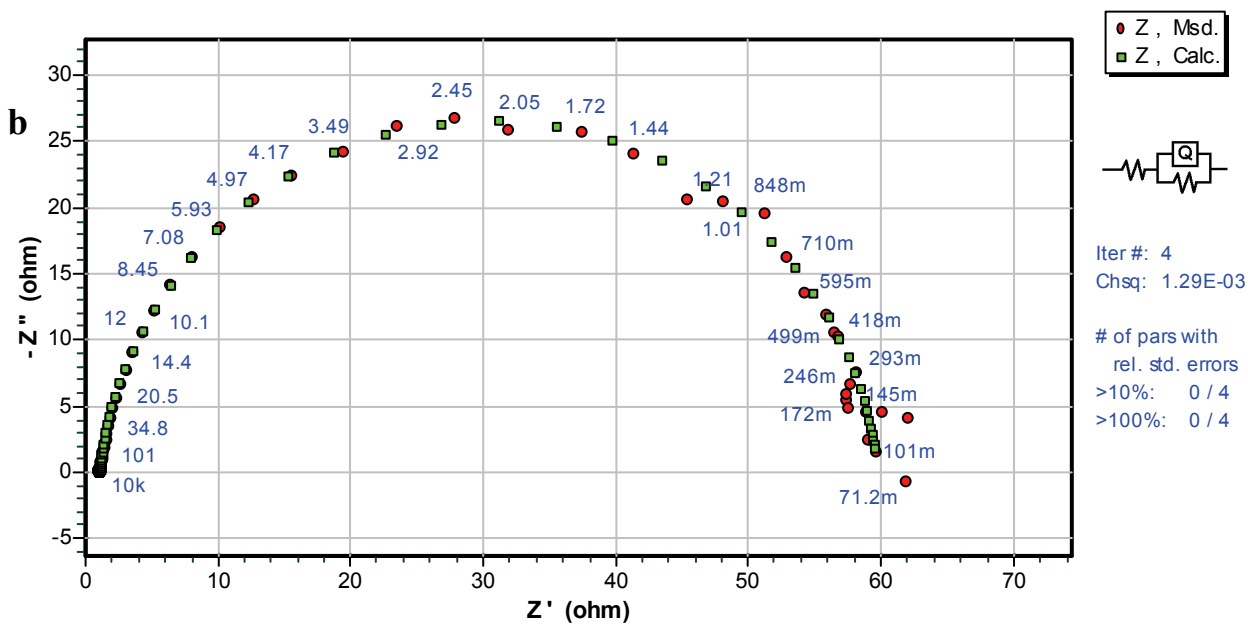
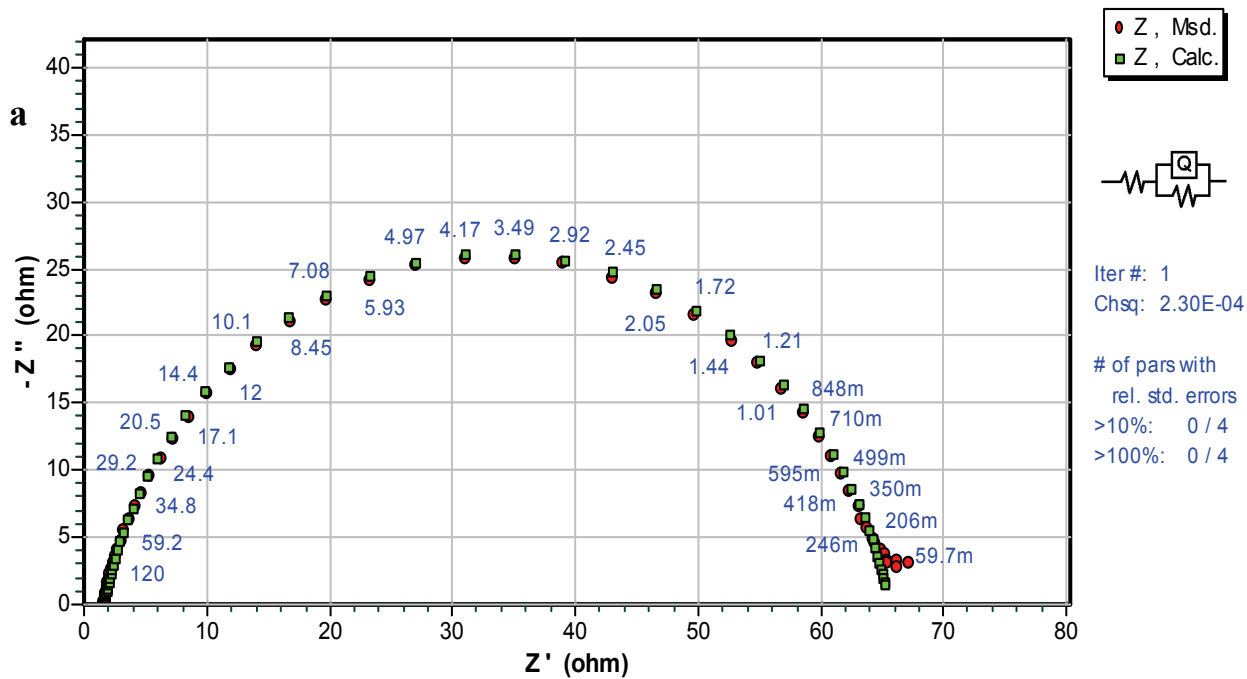


Figure 4.22. Nyquist plot of an anodically grown WO_3 photoelectrode in: (A) $1\text{M H}_2\text{SO}_4$; (B) $1\text{M H}_2\text{SO}_4 + \text{MeOH } 8/2$. Data recorded at 0.7 V vs SCE . Red dots experimental data, green dots calculated. Am 1.5 G irradiation, 0.3 W/cm^2 .

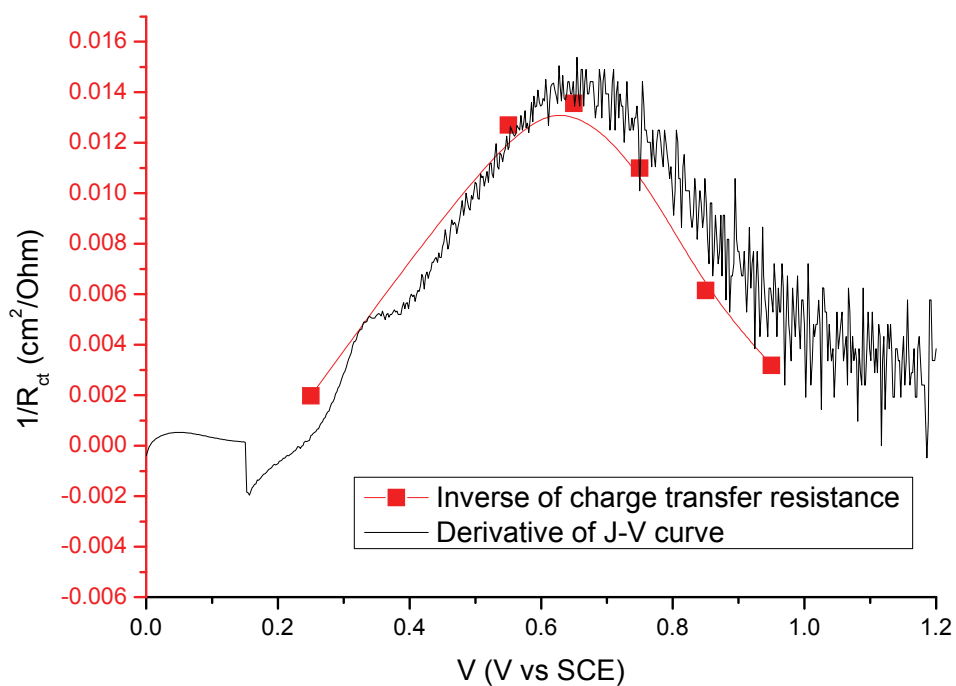


Figure 4.23 Derivative of a typical J-V curve in H₂SO₄ compared with the inverse of the charge transfer resistance (red) obtained from fitting of EIS data at different applied potentials. 0.3 W/cm² AM1.5 G irradiation in 1M H₂SO₄.

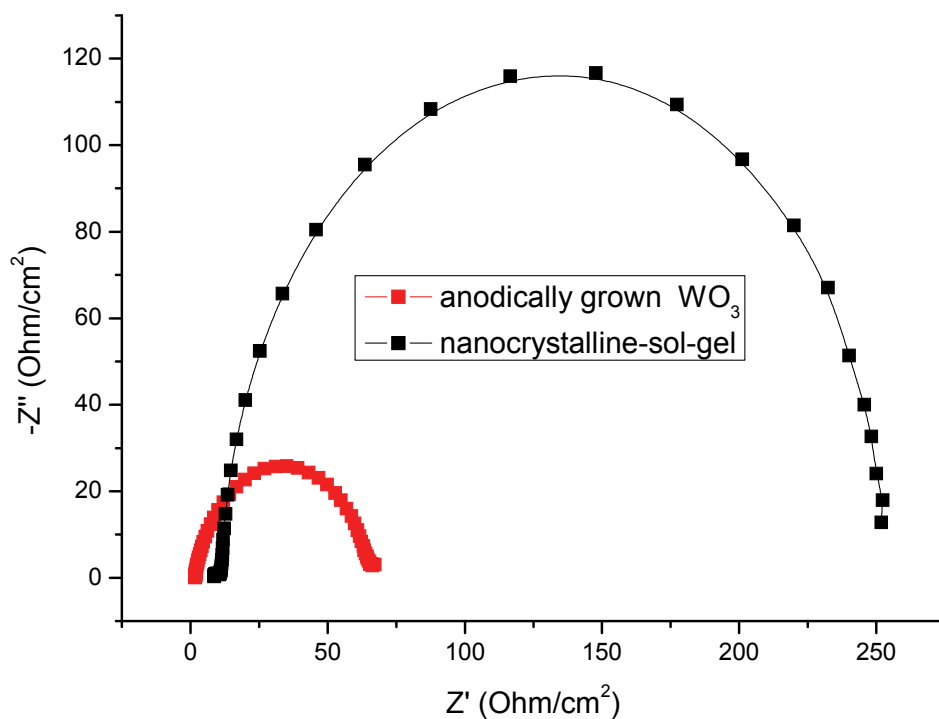


Figure 4.24. Nyquist plot of anodically grown WO₃ (NMF procedure) (red) and nanocrystalline WO₃ (black) obtained from a sol-gel route (black) under 0.3 W/cm² AM 1.5 G illumination and 0.7 V vs SCE potential bias in 1M H₂SO₄.

The capacitance of the anodic WO_3 /electrolyte interface (Helmholtz layer) under illumination was found to be up to ten times larger than that of a nanocrystalline (sol-gel) film of equivalent geometrical area obtained from sol gel routes, corroborating the evidence of the presence of an high number of electrochemically active sites which, being permeated by the solvent, are capable to undergo electron exchange with the electrolyte, contributing to explain the higher photocurrents. The capacitance was also observed to decrease exponentially with the applied voltage (Fig. 4.25). It must be recalled that, unlike a conventional capacitance, the semiconductor photoelectrode behaves essentially as a chemical capacitance[49], which is ultimately dependent on the density of occupied states in the solid at a given potential. When the electrode is illuminated under open circuit potentials, the photogenerated electrons are trapped in the solid, while holes are scavenged by the electrolyte. The resulting negative charge density is compensated by protons from the electrolyte and the capacitance should reach its maximum value. As, upon application of a positive potential, the electrons are swept from the n-type semiconductor to the counter electrode and higher occupied states are progressively emptied, the capacitance decreases. Thus the exponential dependence may be justified on the basis of the Boltzmann distribution ($\exp -qV/kT$) of electronically occupied states at a given value of applied potential.

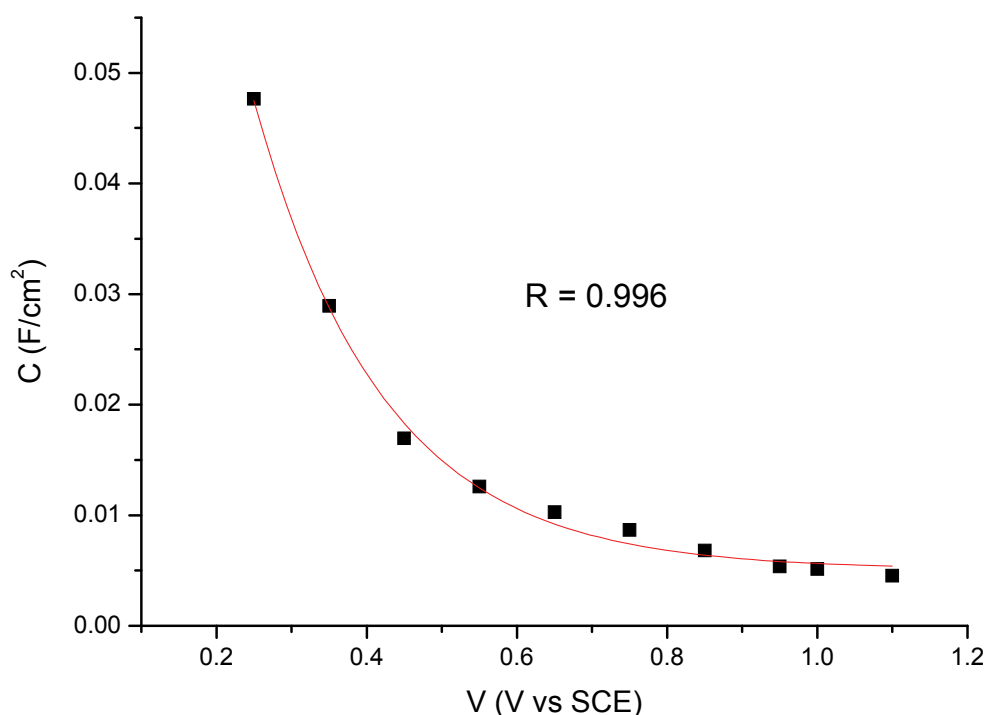


Figure 4.25. Variation of the capacitance of the WO_3 /electrolyte interface with the applied potential under 0.3 W/cm^2 AM1.5 illumination.

Since under illumination the capacitance of the double layer is populated by charge compensating protons, its measurement provides an indication which is qualitatively related to the chronocoulometry experiments in which the semiconductor is *electrochemically* reduced in the dark. Indeed also in this case it appears that at every potential the capacitance of the double layer decreases by moving from samples produced in NMF to samples produced in DMF in accordance with the observed photocurrents; for example at 0.7 V vs SCE and under 0.2 W/cm² irradiation $C(\text{NMF}) (1.27 \text{ mF/cm}^2) > C(\text{DMSO}) (0.44 \text{ mF/cm}^2) > C(\text{DMF}) (0.27 \text{ mF/cm}^2)$.

In order to understand more completely the origin of the enhanced spectral sensitivity in NMF electrolytes, IPCE spectra and impedance measurements under illumination have been recorded on samples obtained at increasing anodization intervals (2-48 h) (Fig.4.26). It can clearly be seen that from the beginning (2h) up to 12 hours of anodization time, no relevant extension of the spectral response to the visible region could be observed and that the capacitance measured at 1.5 V vs SCE under AM 1.5 illumination also remains almost constant at low values. The extended spectral response naturally emerges with time, in agreement with the abrupt increase in chemical capacitance of the photoelectrode which, in turn, is related to the active sites capable to undergo charge transfer with the electrolyte. At the same time the charge transfer resistance decreases considerably (Fig.4.27), ultimately leading to efficient photon-to electron conversion.

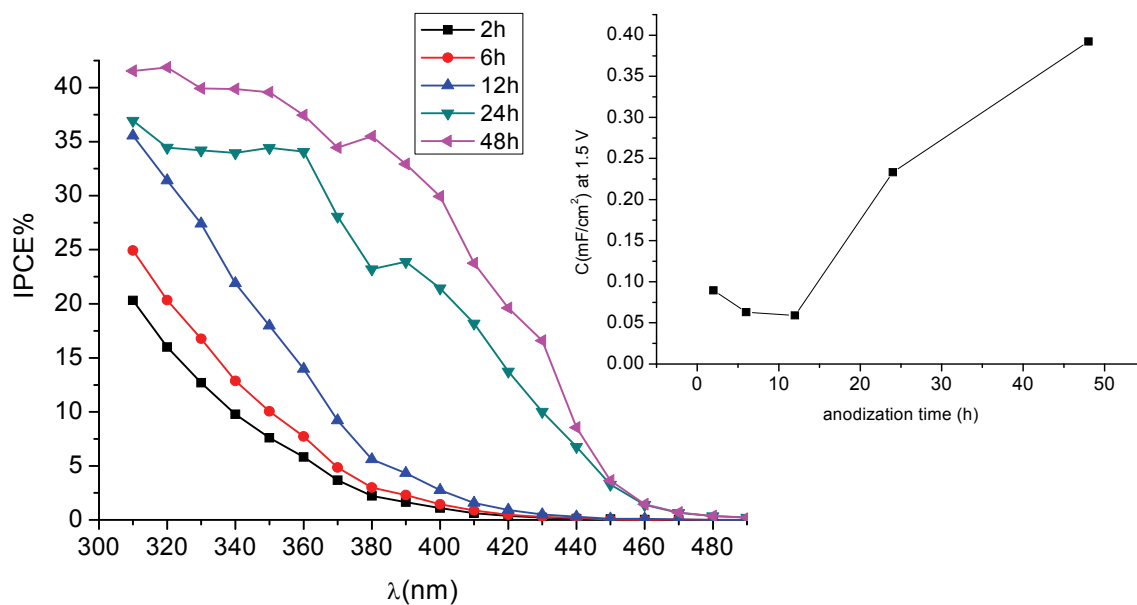


Figure 4.26. IPCE spectra of WO₃ samples obtained in the NMF electrolyte at increasing anodization intervals (2-48 h) under 1.5 V vs SCE potential bias. Inset: capacitance calculated at 1.5 V under 0.2 W/cm² illumination

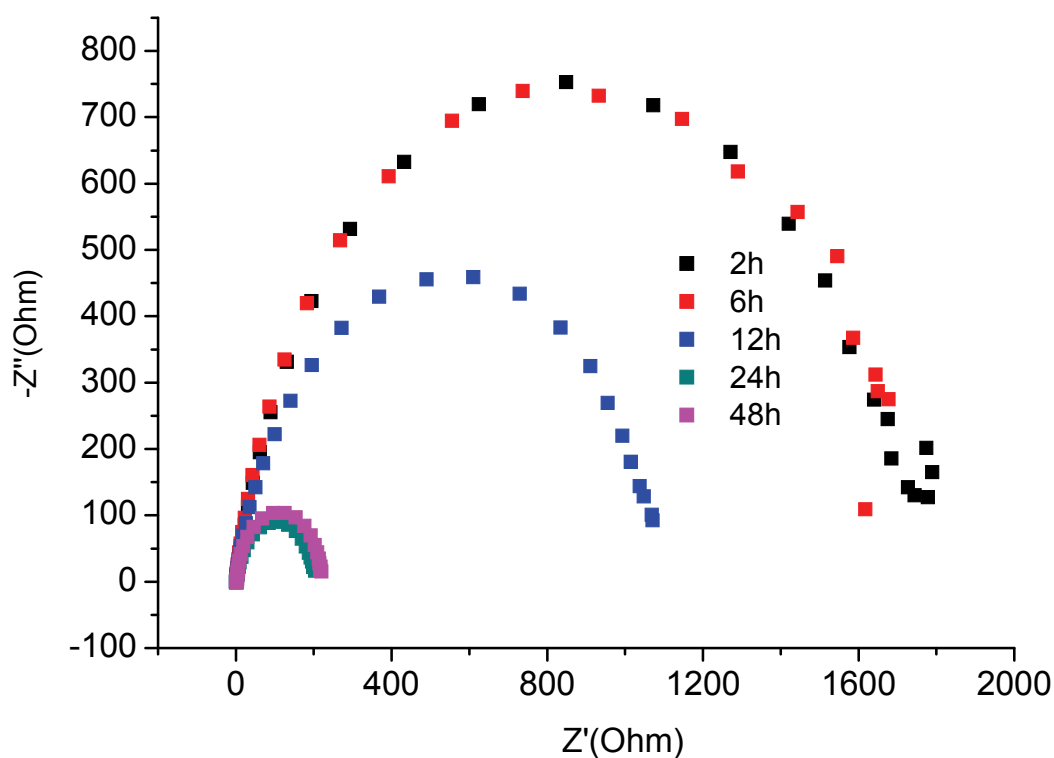


Figure 4.27. Nyquist plots recorded for a series of WO₃ photoelectrodes obtained after different anodization times (2,6,12,24,48 h). 1 M H₂SO₄ at 0.7 V vs SCE under 0.2 W/cm² illumination

4.4 Conclusions

The potentiostatic anodization of metallic tungsten has been systematically investigated as a function of electrolyte composition in order to improve the photoelectrochemical activity of the WO_3 layer for water oxidation. The work done provides a simple wet electrochemical tool to produce highly efficient WO_3 photoanodes, which, combining spectral sensitivity, high electrochemically active surface and improved charge transfer kinetics, outperform, under simulated solar illumination, most of the reported nanocrystalline substrates produced by anodization in aqueous electrolytes and by sol gel methods and are, at the very minimum, comparable to substrates produced with vacuum technologies. [50] The use of such electrodes results in water electrolysis yield of the order of 70% in 1 M H_2SO_4 under a potential bias of 1 V vs SCE and of ca 100% in the presence of methanol. Methods for speeding up photoelectrodes production through an acceleration of the anodization process of at least one order of magnitude are currently under investigation with encouraging results.

4.4 Bibliography

- (1) Eisenberg, R.; Nocera, G. D. *Inorg.Chem.* **2005**, *44*, 6799-6801.
- (2) Dempsey, J. L.; Esswein, A. J.; Manke, D. R.; Rosenthal, J.; Soper, J. D.; Nocera, G. D. *Inorg.Chem.* **2005**, *44*, 6879.
- (3) Ni, M.; Leung, M. K. H.; Leung, D. Y. C.; Sumathy, K. *Renewable Sustainable Energy Rev.* **2007**, *11*, 401.
- (4) Alstrum-Acevedo, J. H.; Brennaman, M. K.; Meyer, T. J. *Inorg.Chem.* **2005**, *44*, 6802-6827.
- (5) Youngblood, J. M.; Seung-Hyun, A. L.; Kobayashi, Y.; Hernandez Pagan, E. A.; Hoertz, P. G.; Moore, T. A.; Moore, L. A.; Gust, D.; Mallouk, T. E. *J.Am.Chem.Soc.* **2009**, *131*, 926-927.
- (6) Brimblecombe, R.; Koo, A.; Dismukes, C. G.; Swiegers, G. F.; Spiccia, L. *J.Am.Chem.Soc.* **2010**, *132*, 2892-2864.
- (7) Orlandi, M.; Argazzi, R.; Sartorel, A.; Carraro, M.; Scorrano, G.; Bonchio, M.; Scandola, F. *Chem.Commun.* **2010**, *46*, 3152-3154.
- (8) Caramori, S.; Cristino, V.; Argazzi, R.; Meda, L.; Bignozzi, C. A. *Inorg.Chem.* **2010**, *49*, 3320-3328.
- (9) Fujishima, A.; Honda, K. *Nature* **1972**, *238*, 37.
- (10) Pleskov, Y. Y.; Guerevich, Y. Y. *Semiconductor Photoelectrochemistry*; Plenum Publishing Co.: New York, 1986.
- (11) Tan, M. X.; Laibnis, P. M.; Nguyen, S. T.; Kesselman, J. M.; Stanton, C. E.; Lewis, N. S. *Progress in Inorganic Chemistry*; John Wiley & Sons: New York, 1994, 21-144.
- (12) Hagfeldt, A.; Graetzel, M. *Chem.Rev.* **1995**, *95*, 49-68.
- (13) Nozik, A. J.; Memming, R. *J.Phys.Chem.* **1996**, *100*, 13061-13078.
- (14) Maeda, K.; Higashi, M.; Lu, D.; Abe, R.; Domen, K. *J.Am.Chem.Soc.* **2010**, *132*, 5858-5868.
- (15) Yi, Z.; Ye, J.; Kikugawa, N.; Kako, T.; Ouyang, S.; Stuart Willimas, H.; Yang, H.; Cao, J.; Li, Z.; Liu, Y.; Withers, R. L. *Nature Materials* **2010**, *9*, 559-564.
- (16) Chen, X.; Mao, S. S. *Chem.Rev.* **2007**, *107*, 2891-2959.

- (17) Wang, H.; Lindgren, T.; He, J.; Hagfeldt, A.; Lindquist, S.-E. *J.Phys.Chem.B.* **2000**, *104*, 5686-5696.
- (18) Khan, S. U. M.; Akikusa, J. *J.Phys.Chem.B.* **1999**, *103*, 7184-7189.
- (19) Sartoretti, C. J.; Alexander, B. D.; Solarska, R.; Rutkowska, I. A.; Augustynski, J.; Cerny, R. *J.Phys.Chem.B.* **2005**, *109*, 13685-13692.
- (20) Sivula, K.; Le Formal, F.; Graetzel, M. *Chem.Mater.* **2009**, *21*, 2862-2867.
- (21) Sivula, K.; Zboril, R.; Le Formal, F.; Robert, R.; Weidenkaff, A.; Tucek, J.; Frydrych, J.; Graetzel, M. *J.Am.Chem.Soc.* **2010**, *ASAP PAPER*, DOI 10.1021/ja101564f.
- (22) Santato, C.; Odziemkowski, M.; Ulmann, M.; Augustynski, J. *J.Am.Chem.Soc.* **2001**, *123*, 10639-10649.
- (23) Santato, C.; Ulmann, M.; Augustynski, J. *J.Phys.Chem.B.* **2001**, *105*, 936-940.
- (24) Finlayson, A. P.; Glowacki, B. A. In *Proceedings of SPIE*, 2006; Vol. 6340, pp L1-L10.
- (25) Bard, A. J.; Park, J. H. *Electrochemical and Solid State Letters* **2006**, *9*, E5-E8.
- (26) Reichmann, B.; Bard, A. J. *J. Electrochem. Soc.* **1979**, *126*, 586.
- (27) Bellac, D. L.; Azens, A.; Granqvist, C. G. *Appl. Phys. Lett.* **1995**, 1715-1176.
- (28) Niklasson, G. A.; Klasson, J.; Olson, E. *Electrochimica Acta* **2001**, *46*, 1967.
- (29) Pennisi, A.; Simone, F.; Lampert, C. M. *Solar Energy Materials & Solar Cells* **1992**, *28*, 233-247.
- (30) Qu, W. M.; Wlodarski, W. A. *Sensor.Actuat. B* **2000**, *64*, 42-48.
- (31) Lee, H. K.; Fang, Y. K.; Lee, W. J.; Ho, J. J.; Chen, H. K.; Liao, K. S. *Sensor. Actuat.B* **2000**, *69*, 96-99.
- (32) Metikos-Hukovic, M.; Grubac, Z. *Journal of Electronanalytical Chemistry* **2003**, *556*, 167-178.
- (33) Yoshioka, H.; Habazaki, H.; Kawashima, I.; Asami, K.; Hashimoto, K. *Corros.Sci.* **1991**, *32*, 313.
- (34) Tsuchiya, H.; Macack, J. M.; Sieber, I.; Taveira, L.; Ghicov, A.; Sirotna, K.; Schmucki, P. *Electrochem. Commun.* **2005**, *7*, 295-298.
- (35) Hahn, R.; Macak, J. M.; Schmucki, P. *Electrochemistry Communications* **2007**, *9*, 947-952.

- (36) Guo, Y.; Quan, X.; Huimin Zao, N. L.; Chen, S. *Environ.Sci.Technol.* **2007**, *41*, 4422-4427.(b) The anodization in the completely aqueous fluoride containing electrolyte was prolonged up to three days at 60 V without observing any further performance improvement.
- (37) Berger, S.; Tsuchiya, H.; Ghicov, A.; Schmucki, P. *Appl. Phys. Lett.* **2006**, *88*, 203119-203121.
- (38) Mor, G. K.; Varghese, O. K.; Paulose, M.; Shankar, K.; Grimes, C. A. *Solar energy Materials and Solar Cells* **2006**, *90*, 2011-2075.
- (39) Paulose, M.; Shankar, K.; Yoriya, S.; Prakasam, E. H.; Varghese, O. K.; Mor, G. K.; Latempa, T. A.; Fitzgerald, A.; Grimes, C. A. *J.Phys.Chem.B. Letters* **2006**, *110*, 16179-16184.
- (40) Angiuli, F.; Argazzi, R.; Caramori, S.; Bignozzi, C. A. *Patent WO 2007/094019 A1*.
- (41) Meda, L.; Tozzola, G.; Tacca, A.; Marra, G. L.; Caramori, S.; Cristino, V.; Bignozzi, C. A. *Solar energy Materials & Solar Cells* **2010**, *94*, 788-796.
- (42) Hsu, C. S.; Mansfeld, F. *Corrosion* **2001**, *57*, 747.
- (43) Mor, K. G.; Shankar, K.; Paulose, M.; Varghese, O. K.; Grimes, C. A. *Nano Letters* **2005**, *5*, 191-195.
- (44) Georgeva, J.; Armyanov, S.; Valova, E.; Poulis, I.; Sotiropoulos, S. *Electrochem. Commun.* **2007**, *9*, 365-370.
- (45) Ottaviano, L.; Lozzi, L.; Passacantando, M.; Santucci, S. *Surface Science* **2001**, *475*, 73-82.
- (46) Gillet, M.; Aguir, K.; Lemire, C.; Gillet, E.; Schierbaum, K. *Thin Solid Films* **2004**, *467*, 239-246.
- (47) Chen, Z.; Jaramillo, T. F.; Deutsch, T. G.; Shwarsctein, A. K.; Forman, A. J.; Gaillard, N.; Garland, R.; Takanabe, K.; Heske, C.; Sunkara, M.; McFarland, E. W.; Domen, K.; Miller, E. L.; Turner, J. A.; Dinh, H. N. *J.Mater.Res.* **2010**, *25*, 3-16.
- (48) Wang, Q.; Moser, J.-E.; Graetzel, M. *J.Phys.Chem.B.* **2005**, *109*, 14945-14953.
- (49) O'Regan, B. C.; Scully, S.; Mayer, A. C.; Palomares, E.; Durrant, J. R. *J.Phys.Chem.B.* **2005**, *109*, 4616.

- (50) Gaillard, N.; Cole, B.; Kaneshiro, J.; Miller, E. L.; Marsen, B.; Weinhardt, L.; Bar, M.; Heske, C.; Soon Ahn, K.; Yan, Y.; Al-Jassim, M. M. *J.Mater.Res.* **2010**, *25*, 45-51.

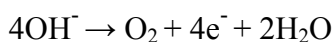
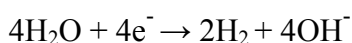
Chapter 5: Photoelectrochemical behaviour of sensitized TiO₂ photoanodes in aqueous environment: application to hydrogen production

5.1 Introduction

The use of sunlight to drive thermodynamically unfavorable reactions is the primary goal of any artificial photochemical system aimed to produce electricity or valuable materials such as fuels.

The growing demand of a sustainable and renewable alternative to fossil fuels has aroused the interest in the photodriven hydrogen production on semiconductor substrates.

A semiconductor with a band-gap higher than 1.23 eV would be required to photogenerate electron-hole pairs with sufficient driving force to carry out the two redox reactions for water splitting:



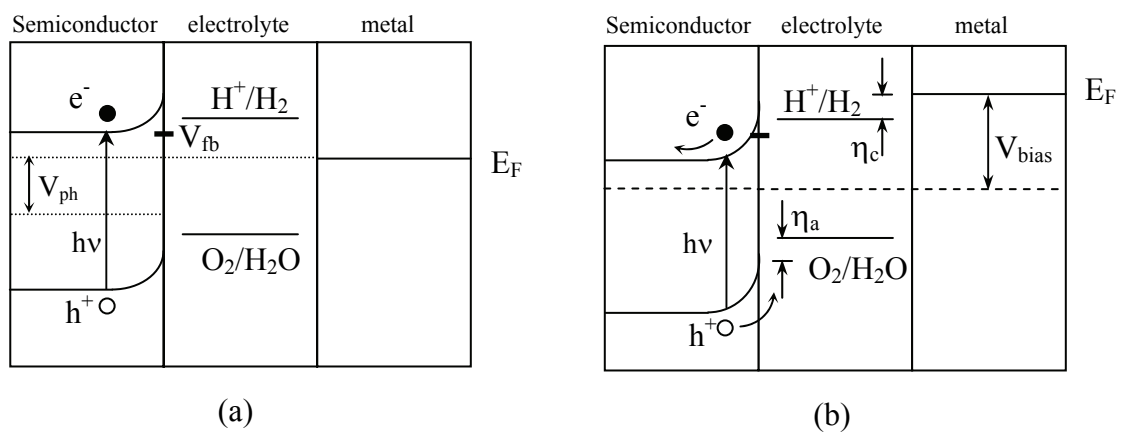
These reactions are multi-electron transfer processes which can efficiently occur on the surface of a semiconductor provided that: (a) the band edges match the redox potentials for water reduction and oxidation, (b) the charge transfer processes at the interface are fast and (c) the stability requirements under irradiation are met.

The simplest method to use sunlight to produce hydrogen and oxygen from water consists in a direct electrolysis of an aqueous solution by means of a solid state photovoltaic device (e.g. silicon solar cells appropriately connected in series to reach the required overpotential for water electrolysis), however the high cost of the solar generated power, ca. 4 \$/Wp[1], limits the feasibility of this approach. An interesting alternative is to integrate the power generating module and the electrolyzer in a single device, simplifying the construction and reducing size and cost. This implies that the semiconductor electrode has to be immersed in solution and resistant to photochemical

degradation. A device of this type, making use of a multi-junction semiconductor electrode, has been shown to reach 12.4% efficiency with a 20 hr lifetime[2].

Systems based on the semiconductor oxide-liquid electrolyte interface[3-6] have been studied for three decades starting from the pioneering work of Fujishima and Honda in 1972 on single crystal TiO₂ electrodes[7]. The main reasons for using wide band-gap oxide semiconductors, such as TiO₂, SrTiO₃, ZnO, SnO₂, WO₃, for photoelectrochemical water splitting are related to their chemical inertness in most environments, their ease of fabrication through sol-gel procedures and their low cost. However, band-gap values of nearly 3 eV or higher means that these materials don't meet the fundamental requisite of photon absorption in the visible spectrum, moreover, the problem encountered with colored oxides such as Fe₂O₃ and WO₃, is that the conduction band-edge is too low in energy to allow for hydrogen generation at useful rate, and an external positive bias must be applied[8-10].

The simplest configuration (scheme 1) involves a semiconductor/electrolyte junction electrically connected with a metal electrode: when the semiconductor is irradiated with photons of energy corresponding to the band-gap, electron-hole pairs are created and the Fermi level in the semiconductor is raised towards the flat band potential V_{fb} by an amount V_{ph} which is the photopotential generated.



Scheme 1

The maximum value the Fermi level can reach in the semiconductor is the flat band potential V_{fb} which, in many cases, is lower with respect to the H^+/H_2 redox couple (a).

This means that hydrogen evolution cannot take place at the metal electrode even at the highest irradiation intensity. For hydrogen evolution to occur, a positive bias must be applied to the semiconductor electrode. This bias, which is usually provided by an external voltage source, should also account for the necessary cathodic (η_c) and anodic (η_a) overvoltages in order to sustain the current flow (b). The use of a p-type semiconductor instead of a metal electrode can eliminate the need for an external bias, but, again, there are problems related to the choice of the p type semiconductor in terms of visible light harvesting efficiency and photoelectrochemical stability[11].

Sensitization of wide band gap semiconductor oxides, like TiO_2 , can offer an alternative approach to bulk semiconductors for photodriven hydrogen production. A surface bound sensitizer, S, acts as a light harvesting centre, collecting photons in the visible region and performing a photoinduced charge injection into the semiconductor which is merely an electron gathering medium. The Fermi level of the TiO_2 is sufficiently negative to allow for a direct hydrogen evolution at a metal (usually Pt) counter electrode without the need of a relevant external bias, however the hole, in this case located on the sensitizer, is not usually positive enough to perform direct water oxidation at any reasonable rate. As a consequence, a sacrificial electron donor with an appropriate potential has to be employed to obtain an effective S^+ reduction. This type of conceptually simple sensitized photo-electrolytic cell is schematized in Fig 5.1.

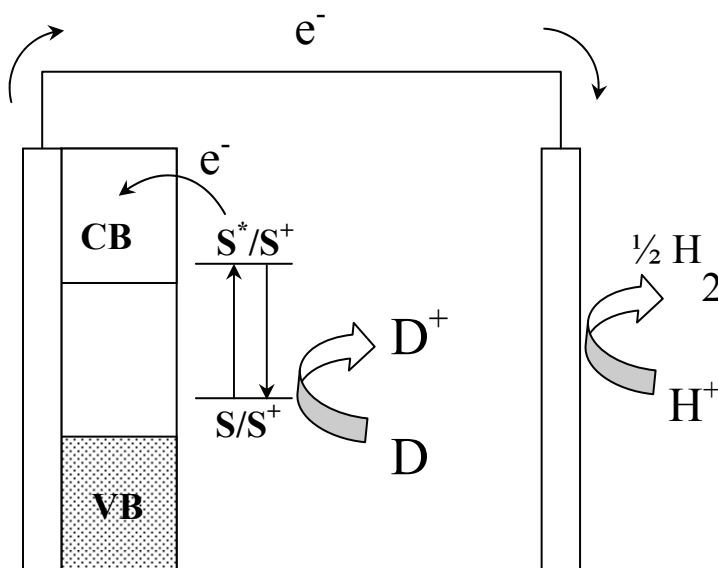


Fig 5.1. Working principle of a dye-sensitized photoelectrolytic device

In principle, D^+ could compete with the reduction of H^+ at the counter electrode, thus decreasing the hydrogen yield, however this process can be avoided, or at least minimized, by an appropriate choice of D (eg. irreversible couples, non electro-active oxidized species) or simply by operating the two electrodes in separate compartments connected by a glass frit, a proton permeable membrane or a salt bridge. Unless sensitizers capable of performing directly an efficient water oxidation are designed[12,13], the use of sacrificial agents, although disadvantageous, cannot be avoided. Nevertheless it must be noted that there is a potentially large number of relatively abundant easily oxidizable ions and organic species that could be consumed to produce hydrogen[14-22].

Recently, Bard and coworkers have shown that photoinduced water splitting can be achieved with a monolithic photoelectrochemical tandem cell containing bipolar WO_3/Pt and dye sensitized TiO_2/Pt panels, capable of vectorial electron transfer in presence of I_2/I^- in acetonitrile[23,24]. The system represents an interesting modification of a conventional DSSC²⁵⁻²⁷ and allow for a 1.9% H_2 production efficiency.

In an aqueous solvent the stability of the linkage between the molecular sensitizer and TiO_2 is crucial and requires the use of multiple anchoring groups. After a series of disappointing tests on dye molecules containing carboxylic acid functions, observed to undergo hydrolysis and desorption from the TiO_2 photoanodes, we decided to focus our studies on the series of dyes shown in Fig. 5.2, containing phosphonic acid functions.

In this paper we report the results of a photoelectrochemical and photophysical investigation on TiO_2 photoanodes sensitized with the molecular species **1-3** which display a remarkable adsorption stability and allow for visible light harvesting, charge injection and hydrogen production at a Pt counter electrode in aqueous solutions containing iodide, chloride, isopropanol or ascorbic acid as sacrificial donors.

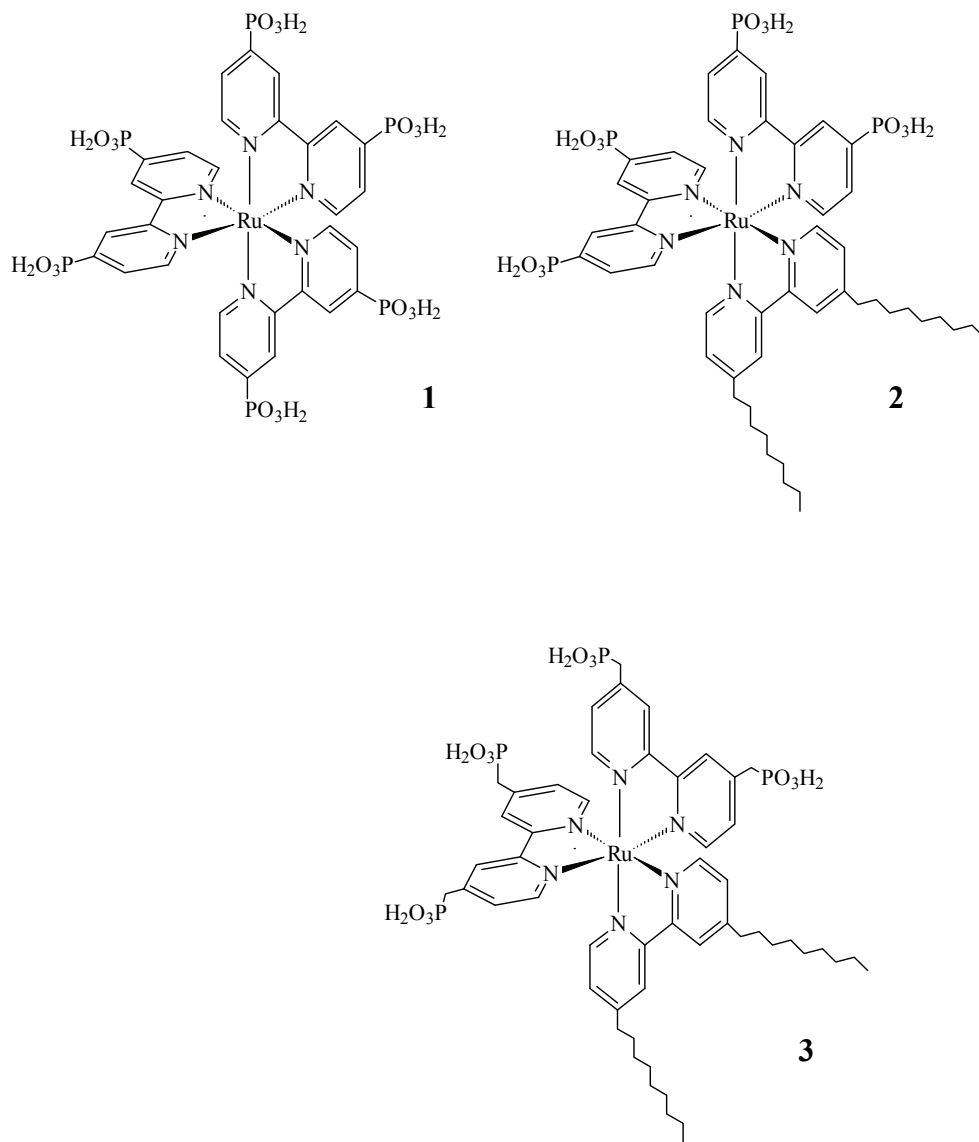


Fig. 5.2

5.2 Experimental Section

Materials. NaI, NaCl, Na₂SO₄, titanium tetra-isopropoxide (Ti(ip)₄), TiCl₄, 4,4'-dinonyl-2,2' bipyridine (dnbpy), dichloro (p-cymene)-Ru(II) dimer, spectroscopic grade acetonitrile (ACN), dimethyl-formamide (DMF), ascorbic acid, isopropanol, formic acid, sodium chloride, lithium chloride, were from Aldrich and Fluka. RuCl₃, was from Alfa Aesar. The phosphonic ligand 2,2'-bipyridine-4,4'-di-methylene-di-phosphonic ethyl-ester (bpy(CH₂PO₃(CH₂CH₃)₂)₂) was available from a previous work. The 2,2'-bipyridine-4,4' ethyl-ester (bpy(PO₃(CH₂CH₃)₂)₂) ligand was purchased from Hetcat. Sephadex LH 20 was provided by GE Healthcare Biosciences. Conductive glass sheets (Fluorine-Tin-Oxide, FTO) (8 Ω/□) were purchased from Hartford Glass. TiO₂ preparation, TiCl₄ treatment and electrode fabrication were performed according to previously published procedures[28]. Unless otherwise stated all chemicals were used as received.

Synthesis

[Ru(bpy(PO₃H₂)₂)₃]²⁺ (1). RuCl₃ x 3 H₂O, dissolved in DMF, was refluxed under nitrogen in the presence of a three fold molar excess of 2,2' bipyridine-4,4' diphosphonic ethyl ester. The progress of the reaction was monitored by TLC on silica gel (methanol as eluant) and UV-Vis spectroscopy. After completion of the reaction, testified by the disappearance of the purple spot corresponding to the intermediate (Ru(bpy(PO₃H₂)₂)₂Cl₂), the solvent was evaporated under reduced pressure and the crude product was dissolved in water and purified by size exclusion chromatography (LH 20/water). The desired product, corresponding to an intense orange band, was collected and refluxed in 6 M HCl for 12 hours to obtain the complete hydrolysis of the ethyl ester groups, which were found partially hydrolysed during the DMF stage.

A subsequent purification on an LH 20 column afforded the desired product with a good degree of purity.

Anal cal.cd for Ru(C₃₀H₃₀Cl₂N₆O₁₈P₆): H 2.7%; C 32.16%; N 7.5%; Found: H 2.67%; C 32.10%; N 7.48%.

¹H NMR 300 MHz (D₂O), δ (ppm): 8.5,d (6H); 7.6,m(6H); 7.36, m(6H)

ESI MS : 524 (M²⁺)

[Ru(dnbpy)(bpy(PO₃H₂)₂)]²⁺ (2): a 2.76·10⁻² g amount (4.5·10⁻⁵ moles) of di-chloro Ru(p-cymene) dimer dissolved in ca.10 ml of DMF, was reacted, under nitrogen, with (3.68·10⁻² g) (9·10⁻⁵) moles of dnbpy at 70 C° for 5 hours. After this time 8.2·10⁻² g (18·10⁻⁵ moles) of (bpy(PO₃(CH₂CH₃)₂)₂) were added and the resulting solution was refluxed for further 4 hours. The progress of the reaction was monitored by TLC and UV-Vis spectroscopy. After completion of the reaction, the solvent was evaporated under reduced pressure and the crude product was purified by size exclusion chromatography (LH 20/water). The desired product was collected and refluxed in 6 M HCl for 15 hours to obtain the complete hydrolysis of the ethyl ester groups.

A subsequent purification on an LH 20 column afforded the desired product with a good degree of purity.

Anal cal.cd for Ru(C₄₈H₅₄Cl₂N₆O₁₂P₄): H 4.53%; C 47.93%; N 6.99%; Found: H 4.50%; C 47.89%; N 7.01%.

¹H NMR 300 MHz (CD₃OD), δ (ppm): 8.95 d (4H); 8.7 s(2H); 8.05 m (4H); 7.4 m (4H); 7.25 d (2H); 7 d (2H); 2.9 m, broad (4H); 2.1 m, broad (4H); 1.2 m broad (24H); 0.9 m, broad (6H)

ESI MS: 577 (M²⁺)

[Ru(dnbpy)(bpy(CH₂PO₃H₂)₂)]²⁺ (3): this complex was prepared following the procedure described for (2), by using the bpy(CH₂PO₃(CH₂CH₃)₂)₂ ligand .

Anal cal.cd for Ru(C₅₂H₆₂Cl₂N₆O₁₂P₄): H 4.96%; C 49.61%; N 6.68%; Found: H 4.92%; C 49.58%; N 6.65%.

¹H NMR 300 MHz (D₂O), δ (ppm): 8.35 d (4H); 8 s (2H); 7.75 m (2H); 7.4 m (2H); 7.2 m (2H); 7.5 m (6H); 3.7 m, broad (4H); 3.05 s, broad (4H); 2.5 s, broad (4H); 1.35 m, broad (4H); 0.95 m, broad (24H); 0.55 m, broad (6H)

ESI MS: 562 (M²⁺)

TiO₂ sensitization. TiO₂ sensitization was carried out by immersion of the TiO₂ electrodes in a water/methanol 50/50 sensitizer solution (≈ 10⁻⁴ M) for 12 hours, in the dark, at room temperature. If needed, dye adsorption could be accelerated by moderate heating (50-60 C°). In such conditions adsorption was completed within 3-4 hours.

These photoelectrodes exhibited a strong absorption in the visible region, with optical densities ≥ 1.3 in correspondence of the MLCT maximum of the dye.

Apparatus and methods Electrochemical characterization of the ruthenium dye sensitizers in solution and anchored to an FTO surface was carried out by cyclic voltammetry in an aqueous 1 M Na_2SO_4 supporting electrolyte. IPCE[29] (Incident Photon to Current Conversion Efficiency) spectra were collected by focusing the monochromatic light generated by an Applied Photophysics monochromator (spectral bandwidth = 10 nm) onto the photoanode of a three electrode photoelectrochemical cell (Sensitized $\text{TiO}_2/\text{Pt}/\text{SCE}$) connected to an AMEL mod. 552 Potentiostat. The illuminated area was 0.5 cm^2 . Short circuit photocurrents were measured with an Agilent 34401A multimeter. Incident irradiance was calculated by means of a Centronic OSD 100-7Q calibrated silicon photodiode. J-V curves, photocurrent and photopotential transients were obtained under the white visible light generated by an HID lamp, filtered from its weak UV component by a 420 nm cut off filter, by using an EcoChemie PGSTAT 30 electrochemical workstation connected to a conventional three electrode cell. Incident white light irradiance was measured with a Moletron Powermax 5200 Power-meter and set to approximately $0.1 \text{ W}/\text{cm}^2$.

Photoelectrochemical experiments using a three compartment cell configuration were performed by immersing the photoanode (working electrode, WE) in a NaI/ACN solution while the reference and counter electrodes were immersed in 1 M HCl aqueous solution. Each electrode compartment was separated by a glass frit as shown in scheme 2.

Qualitative gas chromatographic detection of hydrogen was performed with a Varian CP 4900 Micro Gaschromatograph equipped with a molecular sieves column and a thermal conductivity detector.

Moles of produced hydrogen were calculated by measuring the volume of hydrogen gas collected in a 1 ml graduated syringe at $T = 287 \text{ K}$ (14 C°) and at $P = 1013 \text{ hPa}$. The electrolysis yield was calculated from the ratio between the moles of collected hydrogen and those predicted on the basis of the Faraday law.

Time resolved spectroscopic experiments were carried out in air by using carefully rinsed and air dried sensitized TiO₂ films (active area 4 X 1 cm) previously subjected to specific photo electrochemical experiments (see supporting information).

Conduction band electrons to dye cation recombination kinetics, observed at 450 nm (band pass \approx 21 nm), were obtained by excitation of the sensitized TiO₂ films with the second harmonic (532 nm) of a Nd-YAG laser (FWHM = 7 ns) using a transient absorption apparatus previously described[28]. Laser pulses were attenuated with a chemical filter (aqueous KMnO₄, 5% T @ 532 nm) and defocused with a plano-concave lens to achieve pulse energies of ca. 1 mJ/cm²/pulse. To avoid direct TiO₂ excitation, a 400 nm cut-off filter protected the sensitized TiO₂ photoelectrode sample from the exposure to the UV light contained in the probe beam. Under such conditions no sample degradation was detected over several repeated laser pulses. An interference filter oriented at 45 ° prevented laser stray light to reach the detector, avoiding possible artefacts originated by direct scattered laser light detection and/or photomultiplier blinding. Decays with a satisfactory signal-to-noise ratio were usually obtained by averaging 10 laser shots.

5.3 Results and Discussion

The stability of the bonding between the dye sensitizer and the TiO₂ surface in an aqueous medium is crucial and requires the use of multiple anchoring groups. Thus, the phosphonic groups have been selected for their strong interaction with the metal oxide due to their ability of forming a tripodal linkage[30]. Our attention has been focused on the Ru(II) tris-bipyridine type design with the following goals in mind: (i) reversible Ru(II)/(III) oxidative processes at anodic potentials ($E_{1/2} \geq 1V$ vs SCE); (ii) intense visible absorption bands ($\lambda < 600$ nm) associated to strongly reducing MLCT excited states; (iii) high photochemical stability in coordinating solvents.

All these requirements are oriented to obtain the necessary chemical and photochemical stability for operating the photoelectrode in aqueous media for long periods without dye decomposition, and allowing for charge injection into the TiO₂ conduction band while

maintaining a sufficient driving force for the oxidation of a potentially large number of sacrificial electron donors.

The nonyl substituents of complexes (**2**, **3**) have been introduced to enhance the stability against desorption phenomena thanks to the formation of an hydrophobic network originated by the interdigitated alkyl chains[31,32]. Moreover the steric hindrance of these chains contributes to slow down the electron recapture by the oxidised electron donor³³.

Both the adsorption and the photochemical stability of the complexes **1-3** on the TiO₂ surface are remarkable and are testified, as an example, by the comparison of the absorption spectra of **1** (Fig.5.3) recorded before and after one month of continuous immersion in a water/isopropanol 8/2 mixture, during which the photoelectrode was exposed to 240 hours of visible light irradiation ($\lambda > 420$ nm, ≈ 0.1 W/cm²) under short circuit conditions.

The electrolyte solution consisting in 0.1 M LiClO₄ in water/isopropanol 8/2 at pH 3 (HClO₄) was renewed on a daily basis and the photocurrent density was observed to be substantially stable, within 250 ± 20 μ A/cm².

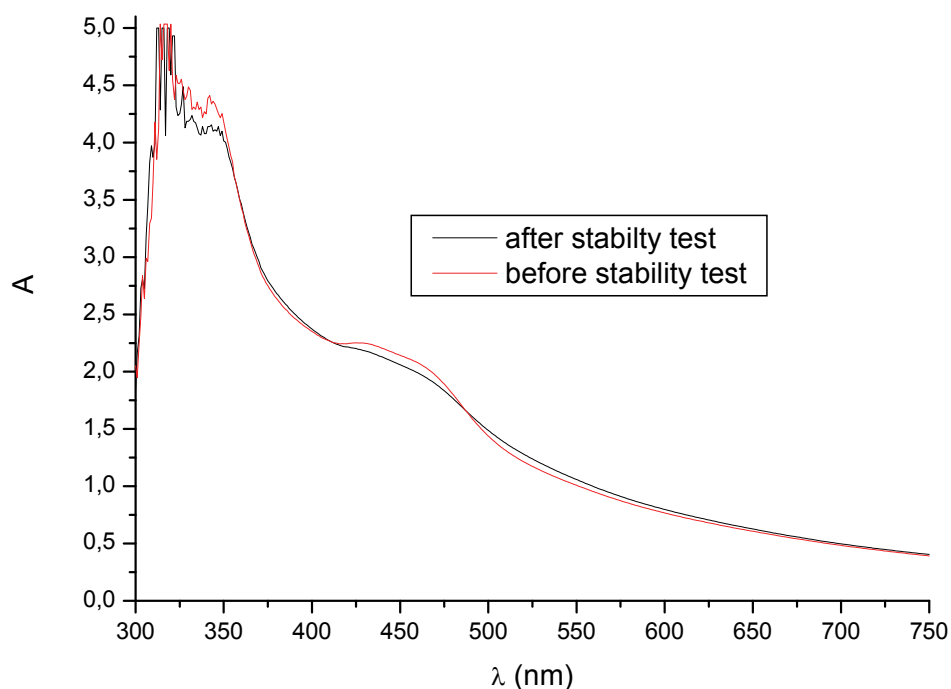


Figure. 5.3. Absorption spectra of **1** loaded on a transparent TiO₂ photoelectrode before (red) and after (black) immersion in 0.1 M LiClO₄ in water/isopropanol 8/2 electrolyte for 30 days.

The Ru(II)/(III) oxidation potentials of the selected dye sensitizers are decreasing in the order **1** (1.20 V vs SCE) > **2** (1.18 V vs SCE) > **3** (0.94 V vs SCE). The trend is expected on the basis of the substituents at the 4,4' positions of the bipyridines: in **3** the methylene spacers attenuate the electron withdrawing inductive effect of the phosphonates, leading to a destabilization of the metal $d\pi$ orbitals which results in an oxidation potential evidently less positive than **1** and **2**, which show energetically close processes. The wave separation is in all cases of the order of 80-100 mV, without cell resistance compensation, indicating a fast electron transfer, expected in the case of redox processes involving Ru(II-III) $d\pi$ orbitals[34].

5.3.1 Organic Sacrificial Agents

In the most favourable case (complex **1**), it was possible to observe the production of a photoanodic current in the presence of plain water/LiClO₄ 0.1M at pH 5 (HClO₄). However, despite a reasonable negative free energy difference for water oxidation (ca. 0.46 V, considering that the thermodynamic potential for oxygen evolution at pH 5 is 0.95 V vs NHE) the photocurrent was extremely small, ca. 5 $\mu\text{A}/\text{cm}^2$ (Fig.5.4a). Chronoamperometry under pulsed illumination (Fig.5.4b) revealed the presence of a fast relaxation from the initial value, reached as soon as the electrode was exposed to light, and the presence of dark cathodic features. Both characteristics are indicative of an inadequate dye regeneration efficiency which reflects in an interfacial hole accumulation leading to an effective photoinjected electron to Ru(III) recombination[35].

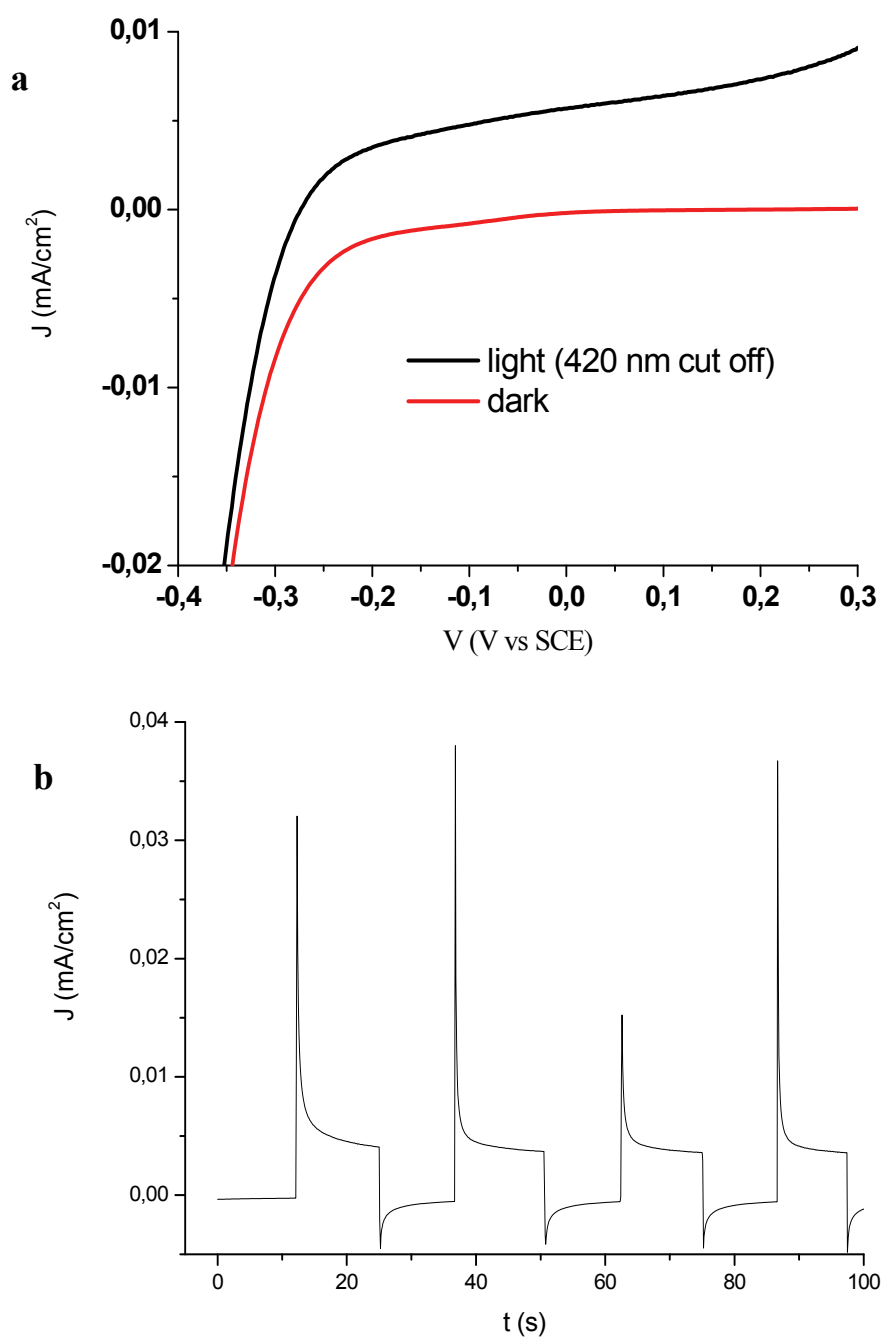


Figure 5.4 (a): J-V curves of **1** in water LiClO₄ 0.1 M at pH 5 (HClO₄); (b) photocurrent transients under 0 mV vs SCE potential bias.

Addition of isopropanol 20 % v/v leads to a general increase of the performances, allowing for the delivery of a maximum photocurrents density of $300 \mu\text{A}/\text{cm}^2$ in the case of **1**. The photoanodic current (Fig. 5.5) increases in the order $3 < 2 < 1$, in agreement with the relative Ru(II)/Ru(III) oxidation potentials. The photocurrent transients collected in the presence of a 0 mV vs SCE potential bias approach a more ideal rectangular shape, although both the initial relaxation and the cathodic features are still evident. These latter are, however, barely observable, indicating that isopropanol effectively acts as an electron donor, promoting Ru(III) reduction[36].

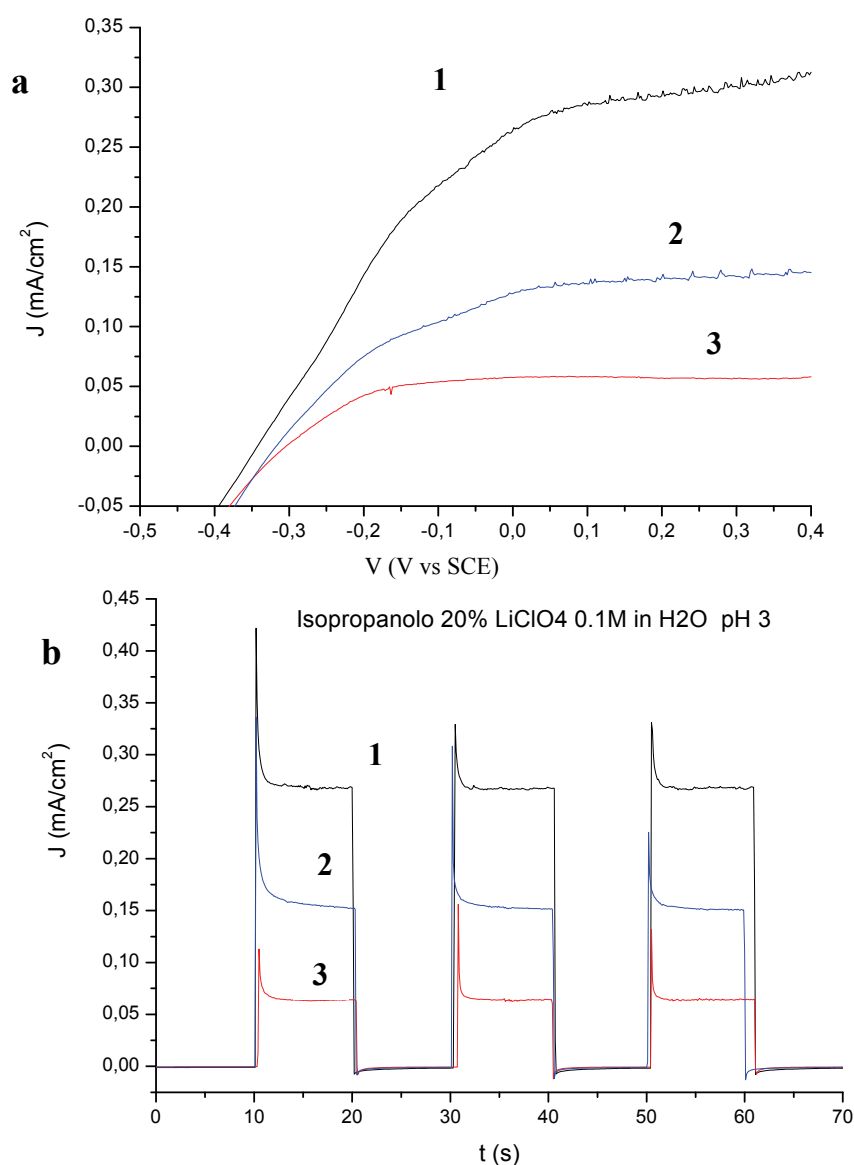


Figure 5.5. (a): J-V curves for the complexes **1-3** in water/isopropanol 8/2 v/v, LiClO₄ 0.1 M at pH 3 (HClO₄); (b) photocurrent transients under 0 mV vs SCE potential bias.

Ascorbic, citric and formic acid may represent an additional interesting class of water soluble sacrificial electron donors. In particular, ascorbic acid has been used as an electron donor in photocatalytic hydrogen evolving systems in homogeneous phase, some of which involved the use of Ru polypyridine complexes as light harvesting and photoreactive centres³⁷. Moreover the carboxylic function promote their adsorption on the titania surface, increasing the probability of interaction with the dye molecules. Ascorbic acid was found to be an effective electron donor, resulting in a maximum IPCE of 24% in the 430-500 nm region, with a photoaction onset at 675 nm (Fig.5.6).

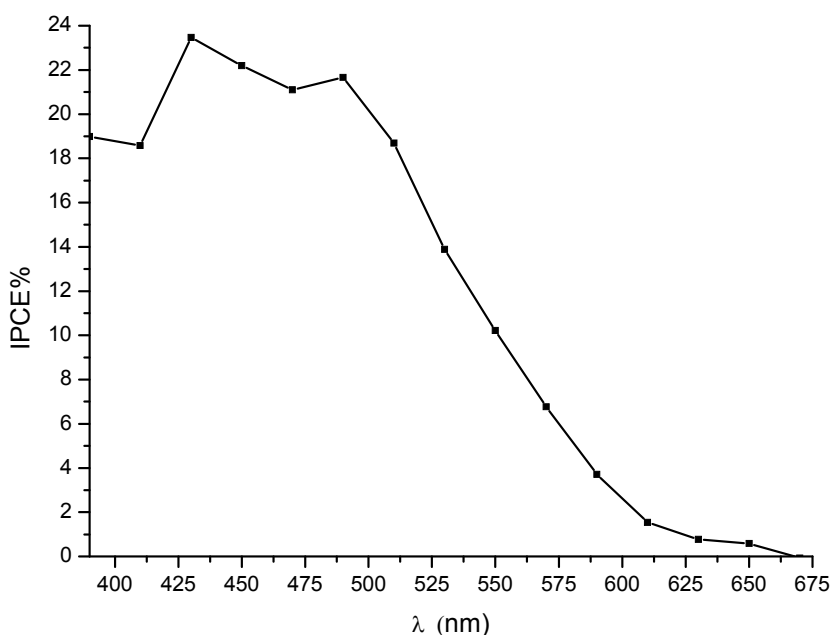


Figure 5.6 Photoaction spectrum of complex **1** in the presence of 1 M ascorbic acid and 0.1 LiClO₄ in water. Bias: 0 mV vs SCE.

Correspondingly, under white light irradiation, photocurrents higher than 2 mA/cm² were achieved with **1** at 0 mV vs SCE and a photoanodic plateau of ca. 3 mA/cm² was observed under a slightly positive bias (0.2 V vs SCE) (Fig. 5.7). Hydrogen collection experiments revealed a satisfactory electrolysis yield (96.7 %), which resulted in the production of 2.96 10⁻⁵ mol of H₂ in 2680 s (Fig 5.8).

Rectangular shaped photocurrent transients indicate a strongly decreased electron back recombination involving Ru(III) and a good reproducibility of the photoanodic processes. On the contrary, formic acid, which is known to be an effective hole scavenger for bare TiO₂ (upon direct band gap excitation), revealed inadequate for

regenerating the sensitizer, producing a marginal improvement over the pure water/ LiClO_4 electrolyte. This evidence is related to the exceedingly positive potential for formic acid oxidation, which could not be observed by cyclic voltammetry at a glassy carbon electrode in water/ LiClO_4 in the interval 0-1.2 V vs SCE; on the contrary, in the same conditions, ascorbic acid gave a clear irreversible oxidation wave with a peak at 0.36 V vs SCE.

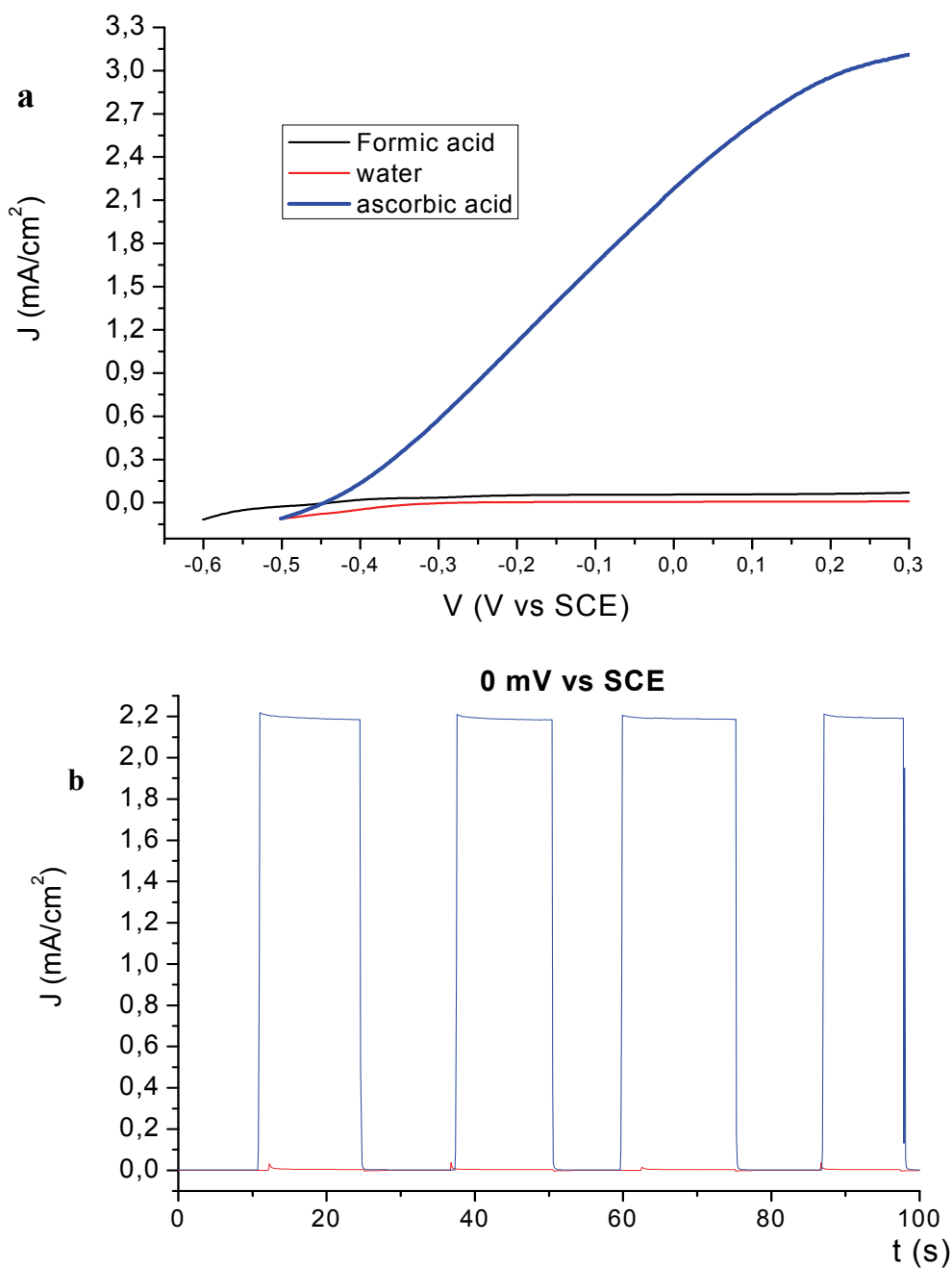


Figure 5.7 (a): J-V curves for the complexes **1** in water: 1M ascorbic acid/ 0.1 M LiClO_4 (blue); 1 M formic acid / 0.1 M LiClO_4 (black); 0.1 M LiClO_4 (red); (b) photocurrent transients under 0 mV vs SCE potential bias.

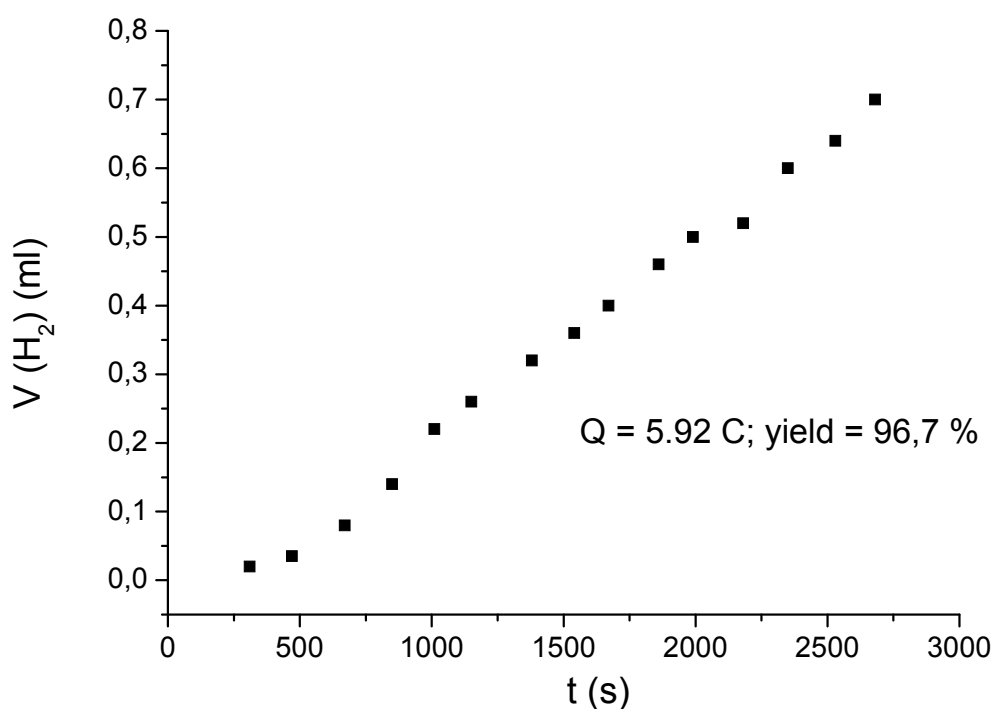


Figure 5.8. Volume of produced hydrogen as a function of time during the photoelectrolysis employing ascorbic acid as a sacrificial electron donor .

5.3.2. Halides

The use of chlorides as sacrificial agents in either aqueous or in organic media did not lead to relevant performances (Fig.5.9). The best results were obtained with complex **1**: in the presence of a positive bias of 0.4 V vs SCE photocurrents of $(120 \pm 20) \mu\text{A}/\text{cm}^2$ were measured. At 0 mV vs SCE **2** and **3** produce lower photoanodic currents (ca. $60 \mu\text{A}/\text{cm}^2$). The photocurrent transients recorded at 0 mV vs SCE (Fig.5.7b) indicate for all complexes an inefficient Ru(II) recovery most probably due to the small driving force for the Cl^- oxidation by Ru(III) ($E^0(\text{Cl}_2/\text{Cl}^-) = 1.1 \text{ V vs SCE}$)

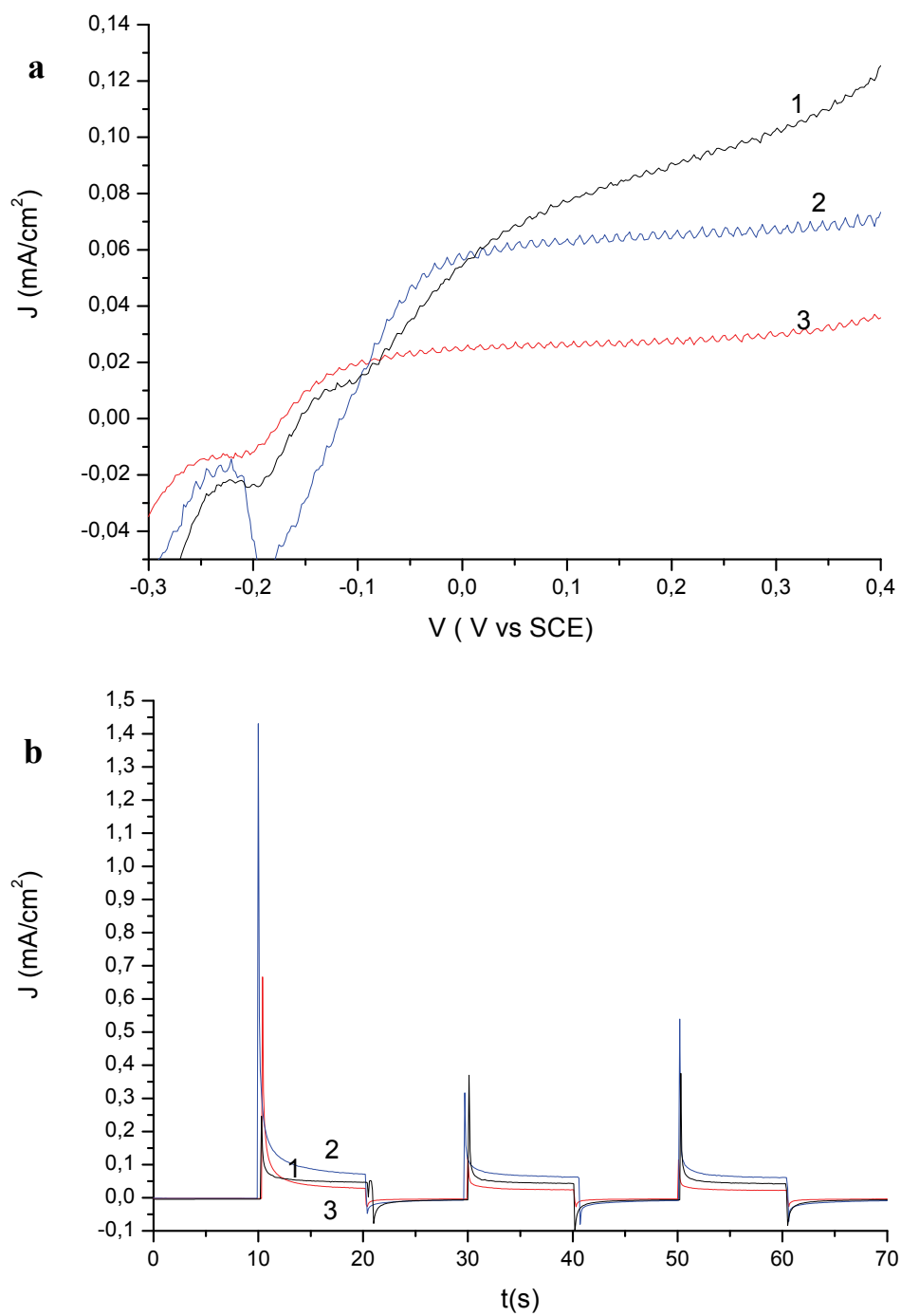


Fig.5.9. (a) J-V curves for the complexes **1,2,3** in aqueous 1 M NaCl at pH 3; (b) photocurrent transients under 0 mV vs SCE potential bias.

Iodide was expected to be a better hole scavenger since its formal oxidation potential is of the order of 0.4 V vs SCE; however the use of aqueous iodide solutions led to instability of the photoanodic response of the sensitized anodes, and the reasons of such behaviour were investigated in detail.

All complexes effectively sensitize transparent titania. As an example, complex **3** gives rise to photoelectrodes with a maximum visible absorbance of 1.5-1.7. The photoresponse in acetonitrile in the presence of I^-/I_3^- is substantially stable with time and the photoaction spectrum shows the usual and expected features, matching the dye absorption spectrum with a maximum IPCE of the order of 60 % (Fig. 5.10(a)). In aqueous media, initial maximum IPCE values of 30 % (Fig. 5.10(b)) were observed to decrease to maximum stationary values of the order of 5-6% in a time scale of a few seconds (Fig. 5.10(b, red line)) independently by pH and type of iodide salt (LiI, NaI, HI, KI). An entirely analogous behaviour extends to complexes **1** and **2**.

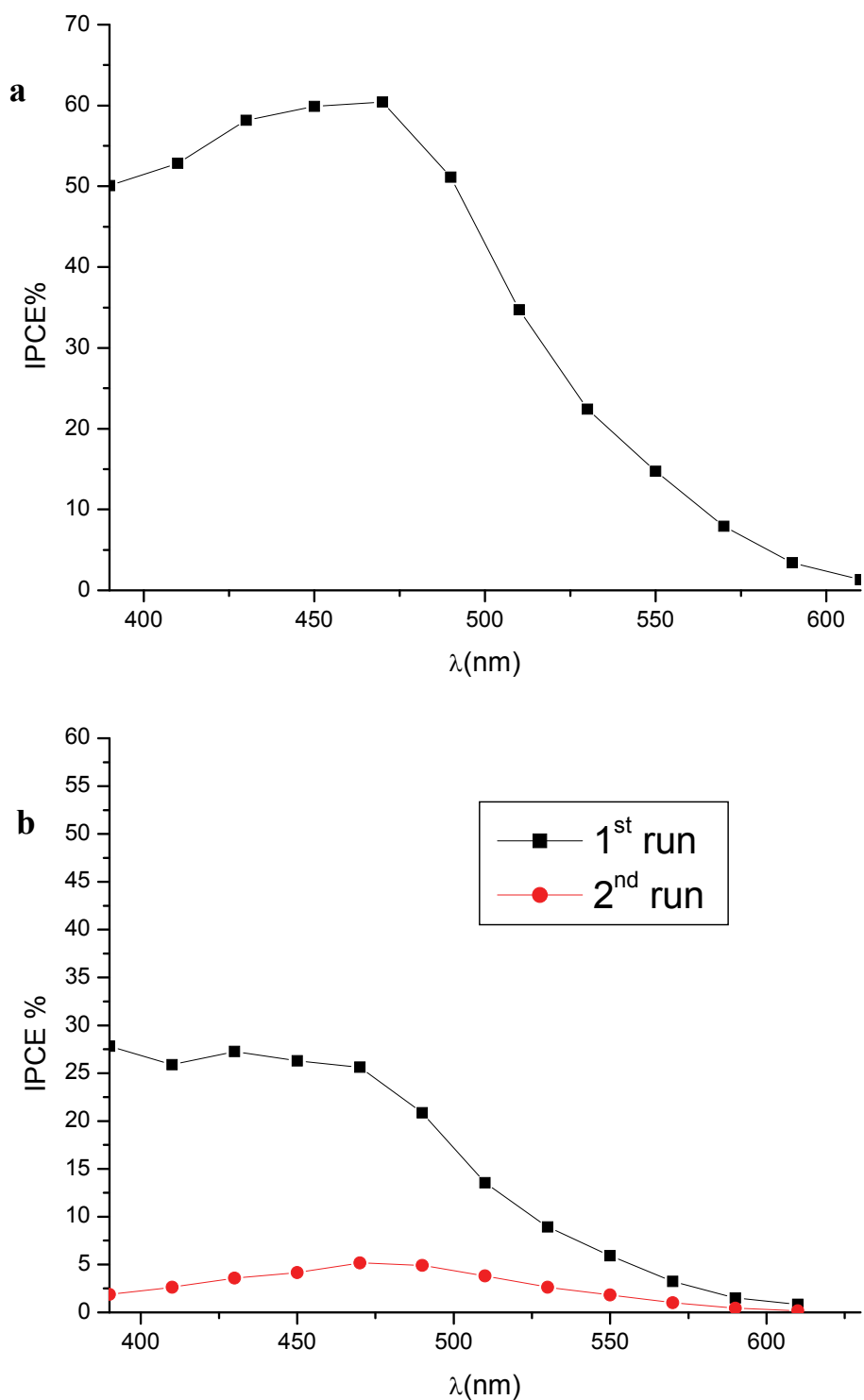


Figure 5.10. (a) Photoaction spectrum of complex (3) recorded in NaI 0.5 M in ACN; (b) photoaction spectra recorded in aqueous 1M NaI, pH 3(HClO₄). Black line: first run; Red line: second run sequentially obtained with the same photoelectrode. Potential bias: 0 mV vs SCE.

Photocurrent transients recorded in aqueous 1 M NaI at pH 3 (HClO₄) under 0.1 W/cm² white light irradiation confirmed the photoanodic instability: within a few seconds, the photocurrent decreases from an initial value of 5 mA/cm² to 0.5 mA/cm² without recovering to the initial value in subsequent irradiation cycles (Fig.5.11).

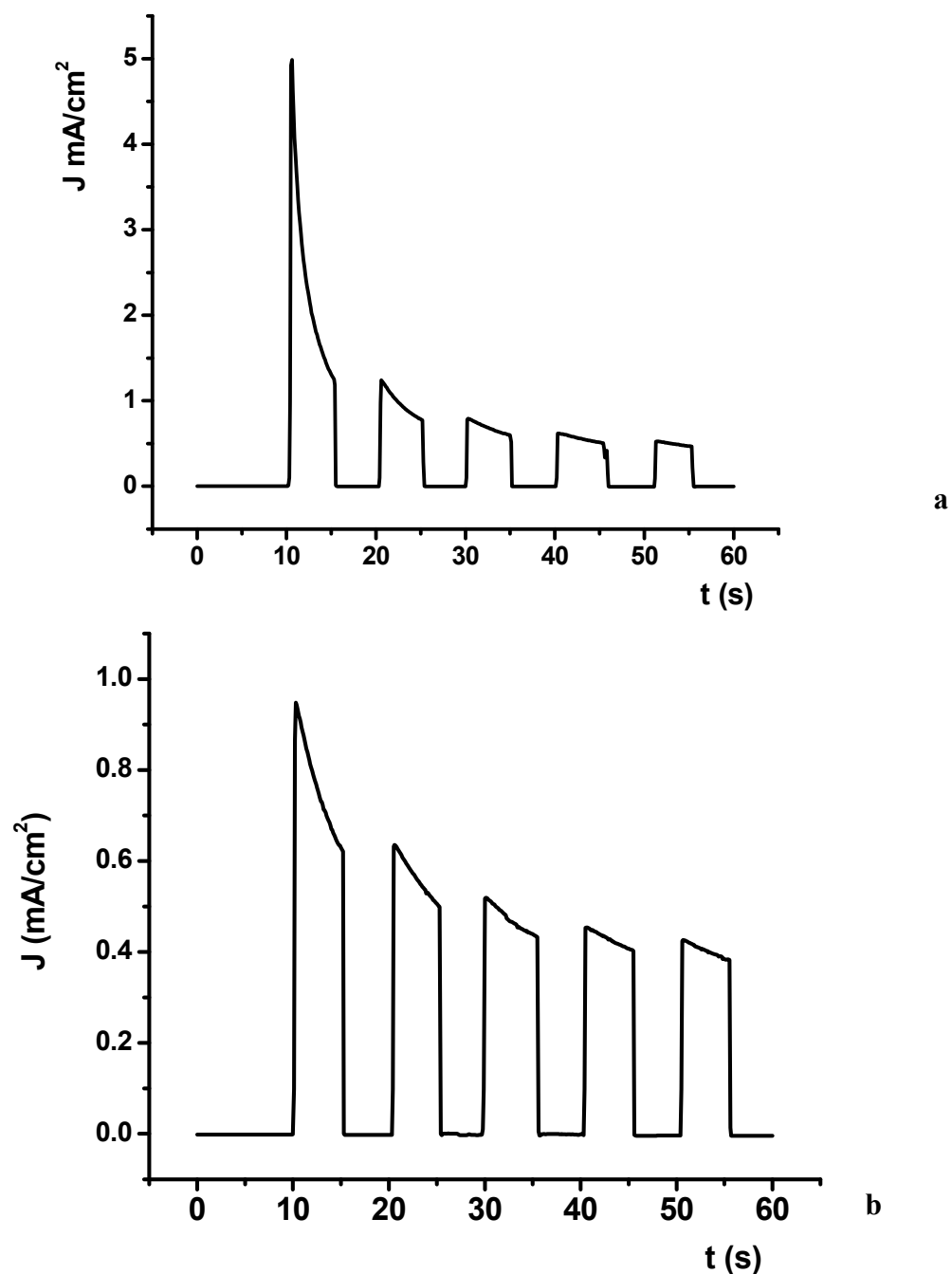


Figure 5.11. Photocurrent transients recorded in aqueous 1 M NaI, pH 3(HClO₄), 0 mV vs SCE. (a) First run; (b) second run after sitting in the dark for 10 min.

The J-V curves recorded on photoanodes sensitized with **3** under shuttered illumination (Fig. 5.12) show, in the 0- -300 mV interval, the expected decrease in photoresponse, determined by a combination of increased charge recombination from progressively filled higher lying TiO₂ states and to a decreased driving force for the charge injection process. In the - 300 – 500 mV range, however, enhanced photoanodic transients are followed by a fast decay and by sharp cathodic spikes when the light is turned off. This behaviour is consistent with the presence of surface adsorbed I₃⁻: at potentials approaching I₃⁻ reduction, a local surface excess of I⁻ is produced and readily intercepted by the photooxidised sensitizer, giving rise to the sharp photoanodic transients followed by cathodic features caused by efficient back recombination with I₃⁻. At potentials more negative than -500 mV vs SCE the photoanodic current is largely suppressed as the flat band potential of the semiconductor is approached.

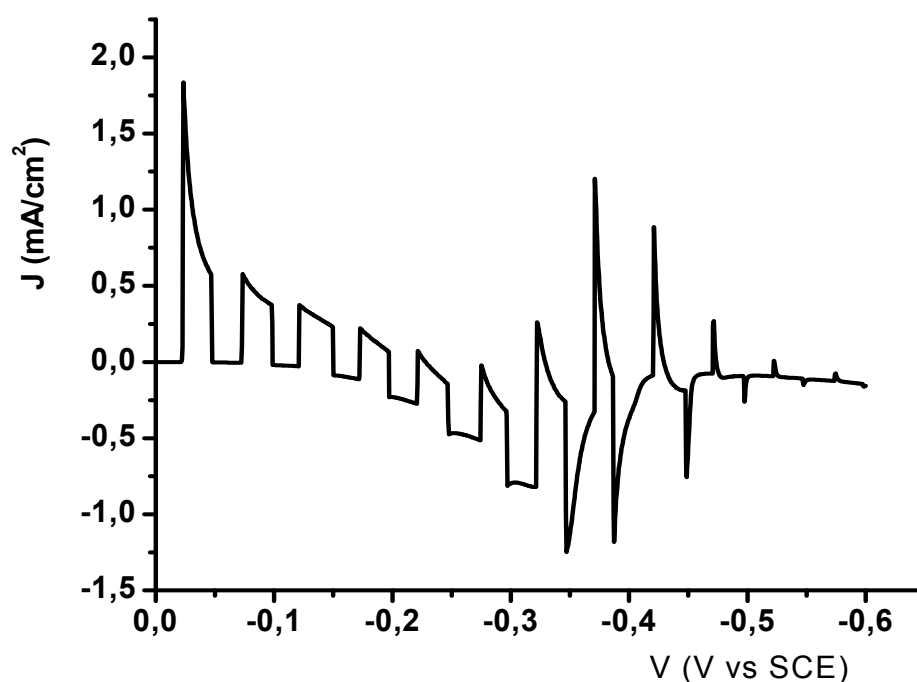


Figure 5.12. Photocurrent transients as a function of the applied potential for a photoanode sensitized with complex **3**. Scan speed 10 mV/s.

The hypothesis of triiodide adsorption is corroborated by cyclic voltammetry (CV) recorded in an aqueous NaCl supporting electrolyte, by using photoanodes previously irradiated (60s) under 0 mV vs SCE potential bias in a 1 M NaI solution (Fig. 5.13).

The CV recorded in NaCl solution using the freshly prepared photoelectrode shows the expected reduction peak due to the $Ti^{4+} \rightarrow Ti^{3+}$ process, evident for potentials more negative than -0.5 V vs SCE. The same electrode, after irradiation in NaI, (Fig 5.13 (B)) shows an intense, triangular shaped irreversible peak, with a maximum at -420 mV vs SCE, due to the adsorbed triiodide reduction. Triiodide is irreversibly consumed during the first scan and diffuses away from the electrodic surface. Indeed, upon a second scan only a minor residual amount is reduced, appearing as a small shoulder at the same potential. In agreement with the CV results, the initial photoelectrochemical performance of the photoelectrodes could be fully restored after a potentiostatic conditioning at -400 mV vs SCE for 100 s (Fig. 5.14).

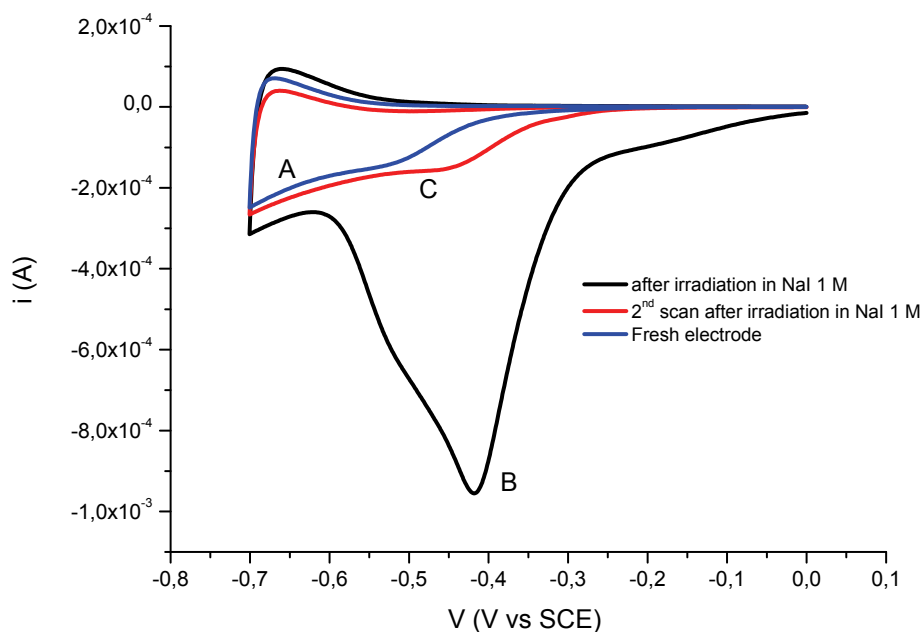


Figure 5.13. Cyclic voltammetry of a TiO_2 electrode sensitized with **3** in aqueous 1 M NaCl: (A) freshly prepared electrode (blue line); (B) after 60 second irradiation in 1 M NaI and water rinsing (black line); (C) same as in (B), 2nd scan. Scan speed 20 mV/s. Potentials referred to SCE.

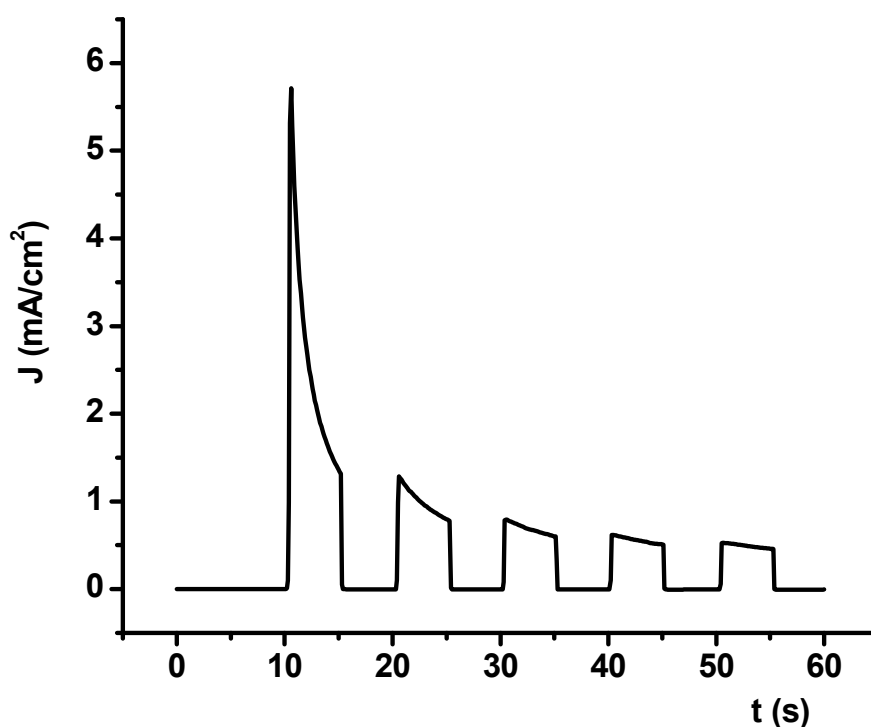


Figure 5.14. Photocurrent transients obtained after 100 s of electrochemical conditioning at -400 mV vs SCE. Same electrode and solution as in Fig. 5.12 .

Additional spectroscopic evidences of triiodide adsorption on the TiO_2 photoelectrodes have been obtained by time resolved laser experiments (Fig. 5.15).

The recovery of the photogenerated Ru(III) (red line) show a considerable dependence by the type of electrode pre-treatment. When the electrode is irradiated in aqueous NaI (Fig. 5.15 (A)) the Ru(II) recovery is complete within 1 microsecond from the laser pulse, while in the other investigated cases (Figs 5.15 (B, C)) it is much slower and follows a time evolution analogous to the reference.

This fact is consistent with adsorption of I_3^- taking place preferentially in the aqueous solvent.

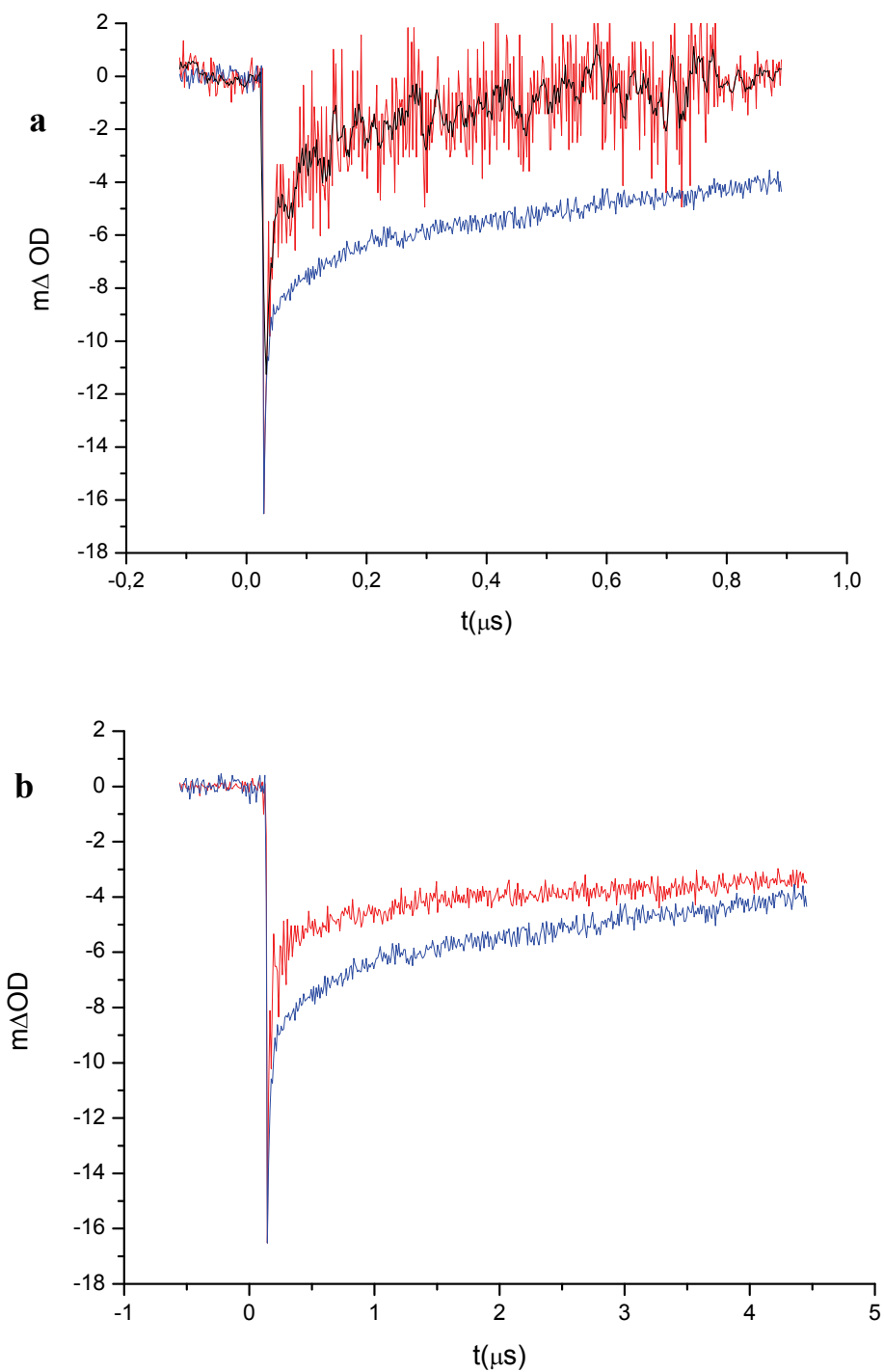


Figure 5.15. Charge recombination kinetics of treated electrodes (red line) compared to the reference electrode (blue line). **(a)** Electrode irradiated in 1M aqueous NaI; **(b)** electrode irradiated in 1M aqueous NaCl; **(c)** electrode irradiated in 1 M NaI in ACN.

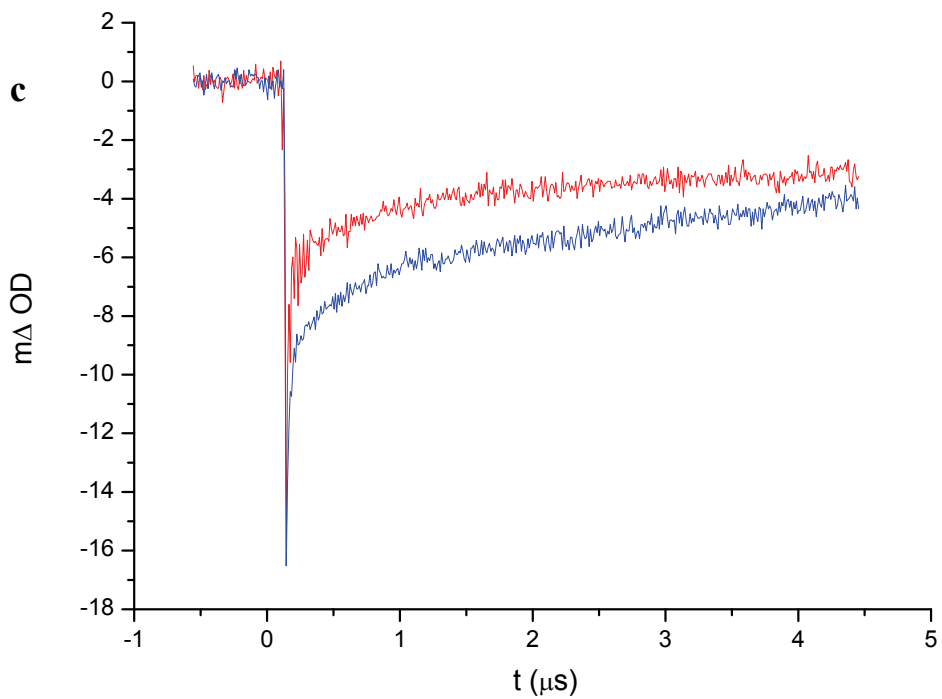
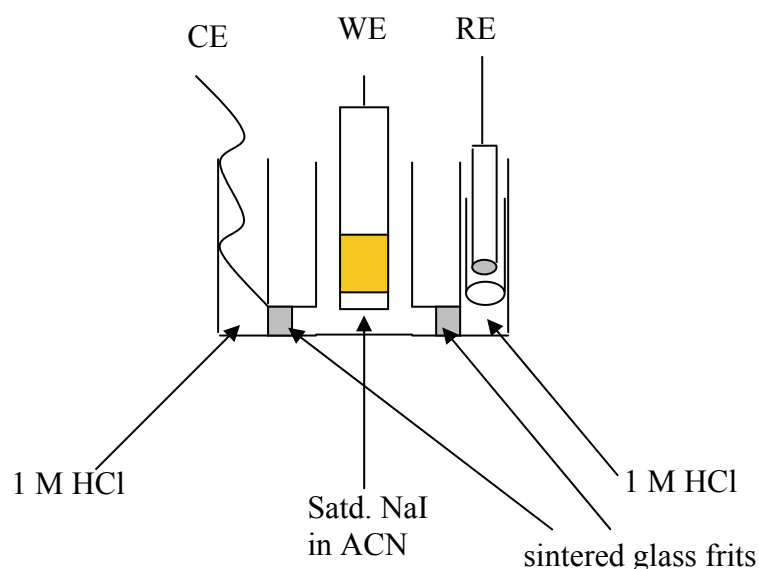


Figure 5.15. Charge recombination kinetics of treated electrodes (red line) compared to the reference electrode (blue line). **(a)** Electrode irradiated in 1M aqueous NaI; **(b)** electrode irradiated in 1M aqueous NaCl; **(c)** electrode irradiated in 1 M NaI in ACN.

Since adsorption of triiodide at the TiO_2 interface in aqueous solution was responsible for the observed drop in the photocurrent response, we have performed a series of photoelectrochemical experiments using a three compartment cell configuration where the photoanode was immersed in an NaI/ACN solution, while the counter electrode was immersed in an aqueous acidic solution (1 M HCl).



Scheme 2. Experimental set up for photoelectrolysis experiments with partitioned solvents.

The J-V characteristics (Fig.5.16 (a)), recorded under these conditions show the expected behaviour of an n-type semiconductor/electrolyte rectifying junction. The photoanodic transients decrease at increasingly negative potentials without the appearance of oscillations in the $-300 \text{ mV} - 400 \text{ mV}$ Vs SCE region. Upon subsequent irradiation cycles under a 0 mV vs SCE bias a photoanodic current of about $5.5 \text{ mA}/\text{cm}^2$ was recorded with good stability and reproducibility (Fig. 5.16 (b)). The apparent small decrease of the photocurrent is due to the filtering effect of the yellow I_3^- developing in few seconds, under such high current densities, in the anodic compartment. The triiodide production was paralleled by the evolution of hydrogen at the Pt cathode, resulting in $1.43 \cdot 10^{-5} \text{ mol}$ of H_2 collected in 1190 s, corresponding to an electrolysis yield of 86.6 % (Fig. 5.17). The production and accumulation of I_3^- at the anodic compartment of the cell results in a strong coloration which limits the light harvesting efficiency of the photoanode, leading to a slow decrease of the photocurrent, which, for example, in several hundreds seconds drops to less than 75% of the initial value. Thus

the hydrogen collection time has been limited with respect to the experiment carried out in the presence of ascorbic acid (Fig.9).

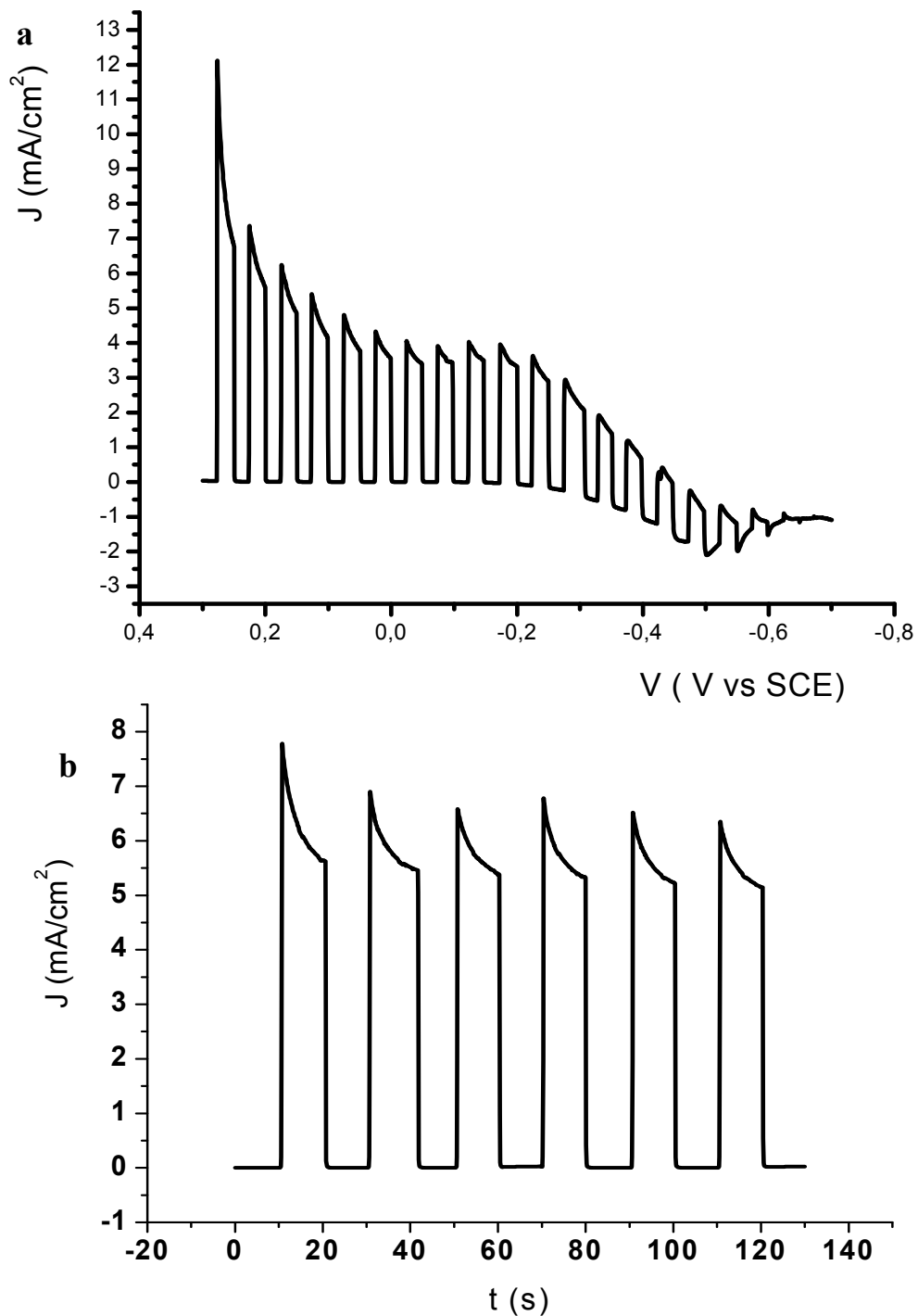


Figure 5.16. (a) J-V shuttered J-V curve recorded in satd. NaI in ACN using the cell arrangement of scheme 1. Scan speed 10 mV/s; (b) Photoanodic response upon subsequent irradiation cycles at 0 mV vs SCE

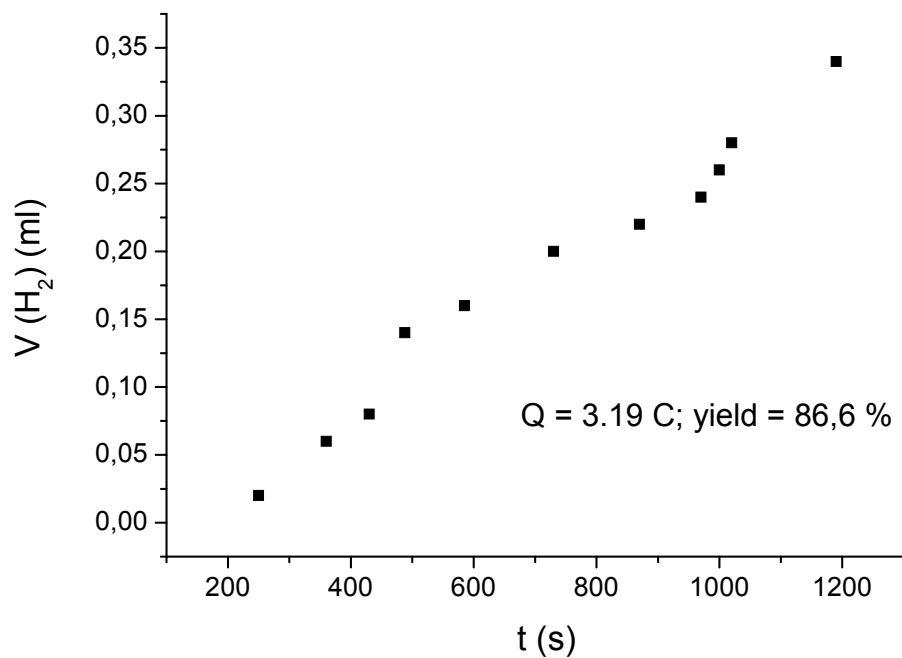


Figure 5.17. Volume of produced hydrogen as a function of time during the photoelectrolysis employing I^- as a sacrificial electron donor in the cell configuration represented in scheme 2.

5.4 Conclusions

In this preliminary work we have investigated the possibility of using TiO₂ sensitized photoelectrodes in aqueous solution containing sacrificial electron donors in order to produce hydrogen. The main goal was to explore the stability of the linkage between the light absorbing sensitizer and the surface of the wide band-gap semiconductor as well as the behaviour of different hole scavengers in photoelectrosynthetic devices operating under visible light irradiation at 0 V vs SCE.

A series of ruthenium (II) polypyridine complexes bearing phosphonic acid functions at the chromophoric ligands sustained 240 h of irradiation without undergoing appreciable hydrolysis and decomposition in aqueous environment at pH 3. Despite the demanding kinetics of water oxidation a reproducible photoanodic response of 5 $\mu\text{A}/\text{cm}^2$ was detected at pH 5. This fact is relevant and suggest that possible improvements could be obtained by assembling this type of dyes in a polymeric structure favouring concerted multielectron oxidation processes.

As expected, the use of organic sacrificial donors considerably enhanced the photoanodic response, while a common inorganic ion, largely present in nature, such as iodide, was found to limit the efficiency of the photoelectrosynthetic device due to the adsorption of the photogenerated I₃⁻ which favours charge recombination with conduction band electrons. However, experiments performed in a two compartment device, where the photoelectrode was in contact with an organic solvent limiting I₃⁻ adsorption, showed a remarkable photocurrent, corresponding to 1.5-1 $\mu\text{Mol}/\text{minute}/\text{cm}^2$ of produced hydrogen. This result is comparable to those obtained with the best TiO₂ supported photocatalysts so far reported by other authors.

5.5 Bibliography

- (1) Eisenberg, R.; Nocera, G. D. *Inorg.Chem.* **2005**, *44*, 6799-6801.
- (2) Khaselev, O.; Turner, J. A. *Science* **1998**, 425-427.
- (3) Nozik, A. J. *Appl.Phys.Lett.* **1976**, *29*, 150.
- (4) Nozik, A. J.; Fornarini, L.; Parkinson, B. A. *J.Phys.Chem.* **1984**, *88*, 3238-3243.
- (5) Tan, M. X.; Laibnis, P. M.; Nguyen, S. T.; Kesselman, J. M.; Stanton, C. E.; Lewis, N. S. In *Progress in Inorganic Chemistry*; John Wiley & Sons, 1994; pp 21-144.
- (6) Nozik, A. J.; Memming, R. J. *J.Phys.Chem.* **1996**, *100*, 13061.
- (7) Fujishima, A.; Honda, K. *Nature* **1972**, *238*, 37.
- (8) Sartoretti, C. J.; Alexander, B. D.; Solarska, R.; Rutkowska, A. I.; Augustynski, J. *J.Phys.Chem.B.* **2005**, *109*, 13685-13692.
- (9) Santato, C.; Ulmann, M.; Augustynski, J. *J.Phys.Chem.B.* **2001**, *105*, 936-940.
- (10) Santato, C.; Ulmann, M.; Augustynski, J. *J.Am.Chem.Soc.* **2001**, *105*, 936-940.
- (11) Grimes, C. A.; Varghese, O. K.; Ranjan, S. *Light, Water, Hydrogen*; Springer: New York, 2008.
- (12) Alstrum-Acevedo, J. H.; Brennaman, M. K.; Meyer, T. J. *Inorg.Chem.* **2005**, *44*, 6802-6827.
- (13) Youngblood, J. W.; Seung-Hyun, A. L.; Kobayashi, Y.; Hernandez Pagan, E. A.; Hoertz, P. G.; Moore, T. A.; Moore, L. A.; Gust, D.; Mallouk, T. E. *J.Am.Chem.Soc.* **2009**, *131*, 926-927.
- (14) Brown, G. M.; Brunshwig, B. S.; Creutz, C.; Endicott, J. F.; Sutin, N. *J.Am.Chem.Soc.* **1979**, *101*, 1298-1300.
- (15) Krishnan, C. V.; Sutin, N. *J.Am.Chem.Soc.* **1981**, *103*, 2141-2142.
- (16) Graetzel, M. *Acc.Chem.Res.* **1981**, *14*, 376-384.
- (17) Krishnan, C. V.; Brunshwig, B. S.; Creutz, C.; Sutin, N. *J.Am.Chem.Soc.* **1985**, *107*, 2005-2015.
- (18) Arakawa, H.; Abe, R.; Sayama, K.; Domen, K. *Chemical Physics Letters* **2001**, *344*, 339-344.

- (19) Arakawa, H.; Abe, R.; Sayama, K. *Chemical Physics Letters* **2002**, *362*, 441-444.
- (20) Arakawa, H.; Abe, R.; Sayama, K. *Chemical Physics Letters* **2003**, *379*, 230-235.
- (21) Dempsey, J. L.; Esswein, A. J.; Manke, D. R.; Rosenthal, J.; Soper, J. D.; Nocera, G. D. *Inorg.Chem.* **2005**, *44*, 6879-6892.
- (22) Abe, S.; Sayama, K.; Arakawa, H. *J.Photochem.Photobiol. A:Chemistry* **2004**, *166*, 115.
- (23) Park, J. H.; Bard, A. J. *Electrochemical and Solid State Letters* **2005**, *8*, G371-G375.
- (24) Park, J. H.; Bard, A. J. *Electrochemical and Solid State Letters* **2006**, *9*, E5-E8.
- (25) Graetzel, M. *Inorg.Chem.* **2005**, *44*, 6841-6851.
- (26) Hagfeldt, A.; Graetzel, M. *Acc.Chem.Res.* **2000**, *33*, 269.
- (27) O'Regan, B.; Graetzel, M. *Nature* **1991**, *353*, 737.
- (28) Cazzanti, S.; Caramori, S.; Argazzi, R.; Elliott, C. M.; Bignozzi, C. A. *J.Am.Chem.Soc.* **2006**, *128*, 9996-9997.
- (29) Nazeeruddin, M. K.; Kay, A.; Rodicio, I.; Humphry-Baker, R.; Mueller, E.; Liska, P.; Vlachopoulos, N.; Graetzel, M. *J.Am.Chem.Soc.* **1993**, *115*, 6382-6390.
- (30) Gillaizeau-Gautier, I.; Odobel, F.; Alebbi, M.; Argazzi, R.; Costa, E.; Bignozzi, C. A.; Qu, P.; Meyer, G. J. *Inorg.Chem.* **2001**, *40*, 6073-6079.
- (31) Zakeeruddin, S. M.; Nazeeruddin, M. K.; Pechy, P.; Quagliotto, P.; Barolo, C.; Viscardi, G.; Graetzel, M. *Langmuir* **2002**, *18*, 952.
- (32) Wang, P.; Zakeeruddin, S. M.; Comte, P.; Charvet, R.; Humphry-Baker, R.; Graetzel, M. *J.Phys.Chem.B* **2003**, *107*, 14336-14341.
- (33) Klein, C.; Nazeeruddin, M. K.; Di Censo, D.; Liska, P.; Graetzel, M. *Inorg.Chem.* **2004**, *43*, 4216-4226.
- (34) Balzani, V.; Juris, A. *Coord.Chem.Rev.* **1988**, *84*, 85-277.
- (35) Hammett, A.; Dare edwards M.P.; Wright, R.D.; Seddon, K.R. Goodenough J.B.; *J.Phys.Chem.* **1979**, *83(25)*, 3280-3290
- (36) Treadway, J. A.; Moss, J. A.; Meyer, T. J. *Inorg.Chem.* **1999**, *38*, 4386-4387.

- (37) Na, Y.; Wang, M.; Pan, J.; Zhang, P.; Akermark, B.; Suin, L. *Inorg. Chem.* **2008**, *47*, 2805-2810.

Publications

Photoelectrochemical Behavior of Sensitized TiO₂ Photoanodes in an Aqueous Environment: Application to Hydrogen Production

Stefano Caramori, Vito Cristino, Roberto Argazzi, Laura Meda, Carlo A. Bignozzi
Inorg. Chem. 2010, 49, 3320–3328

Photo-electrochemical properties of nanostructured WO₃ prepared with different organic dispersing agents

Laura Meda, Gabriella Tozzola, Alessandra Tacca, Gianluigi Marra, Stefano Caramori, Vito Cristino, Carlo Alberto Bignozzi
Solar Energy Materials & Solar Cells 94 (2010) 788–796

New Components for Dye-Sensitized Solar Cells

Stefano Caramori, Vito Cristino, Rita Boaretto, Roberto Argazzi, Carlo Alberto Bignozzi, Aldo Di Carlo
International Journal of Photoenergy Volume 2010, Article ID 458614, 16 pages

Modified Tungsten oxide and process for this preparation

Laura Meda, Alessandra Tacca, Carlo Alberto Bignozzi, Stefano Caramori, Vito Cristino
Patent WO 2011/012238 A1

Topics in water splitting

Hydrogen Production with Nanostructured and Sensitized Metal Oxides

Stefano Caramori, Vito Cristino, Laura Meda, Roberto Argazzi, Carlo Alberto Bignozzi

Efficient Photoelectrochemical Water Splitting by Anodically Grown WO₃ Electrodes

Vito Cristino, Stefano Caramori, Roberto Argazzi, Laura Meda, Gian Luigi Marra, Carlo Alberto Bignozzi
Langmuir – Submitted –

Ringraziamenti

Ringrazio il Prof. Carlo Alberto Bignozzi e il Dott. Stefano Caramori per avermi dato l'opportunità di svolgere questo dottorato.

Ringrazio la Dott.ssa Rita Boaretto per l'assistenza tecnica fornita, Daniela Palmeri del centro di Microscopia Elettronica dell'Università di Ferrara per le immagini SEM e Marco Carmosino per il supporto fornito.

Ringrazio l'ENI per aver finanziato questa ricerca.